The Effects of Microstructure and Microtexture Generated during Solidification on Deformation Micromechanism in IN713C Nickel-Based Superalloy

By

Gang Liu

College of Engineering,

Swansea University, U.K.

Supervised by Dr Soran Birosca

A dissertation submitted in fulfilment of the requirements for

the Degree of Doctor of Philosophy,

Swansea University

Acknowledgements

If there is only one person I need to express my gratitude, that would be my supervisor, Dr. Soran Birosca, for offering me the position at the very beginning when I was still a newcomer in materials science in China, for giving his guidance during the whole research progress (especially for the detailed corrections for every single word I wrote) and his kind suggestions in my daily life. His academic insight, his kindness, his friendliness, his sense of humour, his talkativeness, his industriousness, his always smiling face, and all in all, his charisma, is what I always admire and want to follow. Before I came to Swansea, my expectation for the PhD period was nothing but one paper to be published on Acta Materialia someday; Now I will probably have three in the upcoming months. (Although just one has been published for the moment, the data for the other two including one on Waspaloy are Acta-quality, at least I believe). I attribute this achievement to him. I have to say, he is the best supervisor I have ever met and the best supervisor I imagine I could meet.

I also would like to thank Jordi for his help and kindness to me, and Peter, for kindly deal with my complaint about the EBSD sessions, and Sean and Katie for their useful discussions throughout this project and their support for this project, and the friendship with Ali, Diween and Steve.

I am also grateful to my lovely and beautiful wife, for her company and sacrifice she did for me during the last three years, especially for lots of nights I stayed late in the lab. Hopefully all the promise I made for her will come true very soon.

Last, I am indebted to CSC (Chinese Scholarship Council) and College of Engineering, Swansea University, for their generous financial support for my PhD. And thanks also go to Cummins Turbo Technologies for providing the materials.

Abstract

Nickel-based superalloy IN713C produced by investment casting method are used for turbine blade of turbocharger in modern vehicles. IN713C alloy possesses good strength, fatigue, creep and high temperature oxidation resistance that make the alloy suitable to be used in harsh service environment such as in the heating part of turbocharger. However, this material suffers from microstructure and microtexture heterogeneity produced during solidification. This microstructure heterogeneity across the component will inevitably give rise to local stress and strain accumulation which may facilitate crack initiation and affect crack propagation. Fatigue, both LCF (Low Cycle Fatigue) and HCF (High Cycle fatigue) are the common failure modes of turbine blade component in turbocharger. It is of industrial and academic interests to identify and classify the features of fracture surface of each failure mode. The necessity of optimisation of fatigue property for the newly developed turbocharger component parts is becoming critical and a fundamental research for understanding fatigue deformation micromechanism and the influence of microstructure (dendrite structure, carbides / oxidised carbides, grain size, etc.) and microtexture (individual crystallographic orientation, cluster of grains, etc.) is required.

In the current investigation, LCF and HCF fatigue tests are conducted on real turbine blades as wel as on bars produced via investment casting. Various microstructure characterisation tools were used to identify the deformation micromechanics during LCF and HCF fatigue conditions. The results showed that in real turbine blades where there are much less casting defects than in the testing bar, the fatigue crack initiated from blade surface and crack propagation process was mainly dominated by oxidation-assistant process with oxidised carbides during LCF test. During the late stage of crack propagation, the interdendrite area was found to deform differently from the surrounding area to accommodate accumulated strain heterogeneity. Whilst for HCF, facet was initiated from slip planes with the highest Schmid factor and assisted by small porosity in most cases.

As for the fatigue tests conducted on test bars produced via investment casting, the dendrite structure played a vital role in crack propagation mechanism. Based on the observations throughout this study, a concept of ‘crack propagation unit (CPU)’ was proposed. From this proposed micro deformation mechanism, a new perspective of Hall-Patch effect of small grain size in casting alloys (containing dendrite structure) was further elucidated duirng both LCF and HCF.

Finally, solidification trials were performed to study the exact correlation between solidification cooling rate and microstructure evolution including grain size and structure, gamma prime, carbides and other phases.

Declaration

This work has not previously been accepted in substance for any degree and is not being concurrently submitted in candidature for any degree.

Signed ..... (candidate)

Date .....

STATEMENT 1

This thesis is the result of my own investigations, except where otherwise stated.

Other sources are acknowledged by footnotes giving explicit references. A bibliography is appended after each chapter.

Signed ..... (candidate)

Date .....

STATEMENT 2

I hereby give consent for my thesis, if accepted, to be available for photocopying and for interlibrary loan, and for the title and summary to be made available to outside organisations.

Signed ..... (candidate)

Date .....

Publications

[1] Gang Liu, J. Salvat Cantó, S. Winwood, K. Rhodes, S. Birosca, The effects of microstructure and microtexture generated during solidification on deformation micromechanism in IN713C nickel-based superalloy, Acta Materialia 148 (2018) 391-406. (**Chapter 5**)

[2] Gang Liu, S. Winwood, K. Rhodes, S. Birosca. The Effects of Dendritic Structure and Crystallographic Orientation on Fatigue Crack Propagation in IN713C Nickel-Based Superalloy, Acta Materialia (Under review) (**Chapter 6**)

[3] S. Birosca, Gang Liu, Rengen Ding, Cathie Rae, Jun Jiang, Ben Britton, Chris Deen, Mark Whittaker. The dislocation behaviour and GND development in nickel-based superalloy during creep, International Journal of Plasticity (Under reriew)

[4] Gang. Liu, W. Peng, Muriel Véron, Y.L. Xu, J. Li, X.S. Xiao, S. Birosca. η phase precipitation within γ' phase during long-term thermal exposure, Scripta Materialia (Submitted)

Table of Contents

List of Tables

List of Figures

Fig. 5.5 SEM images of Dendritic structure (a, e), optical micrographs of carbide network (c, g) and carbides size and morphology (d, h) in LCF and HCF failed specimens. Nb EDX maps for the area in (a, e), shown in (b, f), respectively, to signify the Nb element partition in dendritic structure.

Fig. 5.6 Typical oxides and semi-transformation of oxides from carbides in LCF failed specimen. (a) oxides change the second crack propagation direction and EDS maps show the chemical composition of red dashed rectangular area in the left; (b) second crack initiated from oxides; (c) inner short crack initiated from oxide and (d) semi-transformation of oxides from carbides with EDS maps for the red dashed rectangular area in (d).

Fig. 5.7 Near surface oxidised carbides in LCF failed specimen. (a) SE image of carbides and oxidized carbides; (b-d) selected EDS mapping for elements C, O and Nb in area (a); (e) EBSD-derived IPF//LD map of area (a); (f) GND (Geometrically Necessary Dislocation) map with step size of 200 nm.

Fig. 5.8 Three layer of the same area GND density maps in LCF failed specimen. (a), (c) and (e) are SE or BSE images; (b) and (f) are high-resolution GND maps with step size of 60 nm in the red rectangular area in (a) and (e), respectively; (d) is the GND map for (c); the inset of (b) is the same area of black rectangular area in (a), showing the γ' impeding carbide.

Fig. 5.9 GND density and their local distribution of carbides near crack initiation sites in LCF (a-c) and HCF (d-f) failed specimens. (a,d) SEM image; (b, e) EBSD-derived IPF//LD; (d,f) GND density maps using step size of 200 nm.

Fig. 5.10 GND density distribution in dendritic structure in LCF failed specimen. (a) Band contrast image of large area of interest; (b) GND density map for the same area in (a) with step size of 0.5μm; (c) fracture surface in crack propagation area revealing sharp and square shape dendritic structure and (d) EDS chemical elements maps for a selected area in (a).

Fig. 5.11 EBSD-derived IPF//LD across facet after serial sectioning on a HCF failed fracture surface. Sectioning position are indicated in dashed lines in (a,b,c), and are the same position indicated in red dashed lines in Fig. 3a. (d,e,f) are IPFs map //LD of cross section 1-3, respectively, parallel to LD-ND plane, and (b) is IPF//LD of LD-TD plane

shown in (b) and notice that they are cut and separately scanned due to very large area; (f) average grain size of these structures.

Fig. 6.2 Representative microstructure in received materials: (a) dendrite structure within three grains, dashed lines show grain boundaries; (b) carbides segregating in interdendrite area; (c) and (d) γ′ in dendrite area and interdendrite area, respectively; Magnified area in (c) shows very small γ′ in γ channels.

Fig. 6.3 Grain structure around actual fractured area in tested bars: IPFs in (c-e) for LCF and (f-h) for HCF; (a) a representative failed bar (L-C) with major dimension size; (b) schematic half fractured sample with sectioning planes showing EBSD scan position (only two scales shown here). To examine assumed transition structure, both half fractured samples are characterised and displayed. The results show no transition structure in the centre of the bar with 'nominal' transition structure. And the actual grain size might not fit well with assumed grain structure compared to Fig. 1.

Fig. 6.4 Fracture surface in LCF samples by optical microscope and SEM. (a-c) for L-T (LCF-Transition), (d-e) for L-E and (g-i) for L-C. Red arrows in (a) (d) (g) indicate crack initiation sites, white dashed lines distinguish crack propagation stages, yellow double arrows show crack propagation distance and red dashed lines indicate EBSD position. (c) and (f) show porosities in initiation sites (highlighted by yellow dashed circles) and (i) shows a large pore in the middle of fracture surface in L-C. (j) Fatigue life (cycles) for each sample and the crack propagation distance measured by the yellow double arrows; (k) Average grain size of each sample and average porosity size; (l) Grain structure with all Euler color for each sample.

Fig. 6.5 Fracture surface in HCF samples by optical microscope and SEM. (a-c) for H-T (HCF-Transition), (d-e) for H-E and (g-i) for H-C. White dashed lines in (a) (d) (g) distinguish crack propagation stages, yellow double arrows show crack propagation distance and red dashed lines indicate EBSD position. (c) and (f) show porosities in initiation sites (highlighted by yellow dashed circles) and (i) shows a large pore in the middle of fracture surface in L-C. (j) Fatigue life (cycles) for each sample and the crack propagation distance measured by the yellow double arrows; (k) Average grain size of each sample and average porosity size; (l) Grain structure with all Euler color for each sample.

Fig. 6.6 Cross section of porosities. (a-c) porosity of initiation site in H-C, sectioning line is shown in Fig.5i with red dashed line, (b) The magnified area of white dashed rectangular area in (a), and (c) GND map of (b). (d) The large middle porosity in Fig. 4i (EBSD position is shown with red dashed line), (e) and (f) show the EBSD area and GND map, respectively. (g) The position very close to initiation porosity in H-E, the sectioning position is shown with the red dashed line in Fig. 5f. IPFs are superimposed on scanning surface in (a), (d) and (g). Step size for GND mapping is 200 nm.

Fig. 6.7 General features in sequential crack propagation stages, exemplified from sample L-T. (a) schematically showing different propagation stages with striations (black curved lines) superimposed. (b) and (c) Part of whole fracture surface by OP and SEM, respectively. (d-g) Fatigue striations as major characteristics are shown in each stage corresponding to the area in (c). (h-k) γ' morphology immediately beneath the fracture surface in (d-g) individually. Very thin oxidation layer can be noticed, and the thickness are indicated by double dotted lines in (h) and (j).

Fig. 6.8 oxidation assisted crack propagation: oxidised carbides along secondary crack (a) and primary crack ((b) and (c)).

Fig. 6.9 Secondary dendrite structure and striation distribution. (a-d) from L-C, (e-h) from H-E and (i) from L-E. (a, b) and (e-g) show the dendrite structure on fracture surface; (c) and (h) show the striations in dendrite area; (d) Dendrite structure in the sample and the average size of secondary dendrite is comparable to dendrite size on fracture surface in (b).

Fig. 6.10 Primary dendrite structure and striation distribution. (a-c) from L-T, (d-h) from H-C. Primary dendrite are shown in red dashed circles in (a, b) and representative fine striations close to initiation site is shown in (c). Primary dendrites are shown by color contrast in (d) and striations are magnified in (f, h) from white dashed rectangular areas. (i) Schematically illustration of dendrite structure (both primary and secondary) and striation distribution. (j) Grain size dependence of crack growth rate, obtained from measurement of width of striations, as displayed in (c, f, h) and in other figures for example.

Fig. 6.11 Dendrite structure dependence GND density distribution based on EBSD datas. (a-c) from L-T and (d-f) from H-E. (a, d) IPFs show grain orientation grain structure; (b, e) Element mapping of Nb showing dendrite structure in the same area in

(a, d), respectively; (c, f) GND density mapping with grain boundaries superimposed by white lines, step size of 200 nm were used.

Fig. 6.12 dendrite structure dependence dislocation distribution based on TEM. (a-d) specimen from FIB (Focused Ion Beam) extracted site; (e-g) specimen from electric polishing. (c, d) BF (Bright Field) images of interdendrite area and dendrite area, respectively; (f, g) STEM-HADDF images of interdendrite and dendrite area, respectively. (e) BF image of intedendrite area showing dislocation around γ′

Fig. 6.13 Grain orientation and structure distribution across the fracture surface revealed by serial sectioning method in sample H-T (a, c) and H-E (b, d), parts of IPFs // LD are displayed corresponding to the red dashed sectioning lines in (a, b). Calculated slip traces for {111} slip planes in facet grain(s) are superimposed and the highest Schmid factor value for each slip plane are displayed for each facet grain in (c, d).

Fig. 6.14 Grain orientation and structure distribution across the fracture surface in sample H-C. Parts of IPFs // LD (c) are displayed corresponding to the red dashed sectioning lines in (a). (d-e) IPFs // LD of cross section (CS) 5, 7 and 8 without image distortion. Calculated slip traces for {111} slip planes in facet grains (G5, G6 and G7) are superimposed and the highest Schmid factor value for each slip plane are displayed for each facet grain in (d). (b) Both top and bottom half of fractured sample at some locations are sectioned and EBSD scanned to reveal the whole facet grain. (e) Intersection of three grains that produce the porosity; (f) Spatial grains position around fracture surface. (g) schematically shows grain size dependence of porosity size in the materials.

Fig. 6.15 Grain orientation and structure distribution across the fracture surface in sample L-T (a), L-E (b) and L-C (c). Parts of IPFs // LD (c) are displayed corresponding to the red dashed sectioning lines.

Fig. 6.16 Schematic showing the grain size dependence of crack propagation rate and the dendrite structure dependence of dislocation distribution. (a-c) for large single grain; (d-f) for small multi-grains. Individual dendrite area serves as crack propagation unit. The real dendrite structures are shown in the highlight of (a, d) and the real striation within dendrite area is shown in the highlight of (e). Dislocation segregated in interdendrite areas are proved both by GND mapping (the highlight in (c, f)) and HAADF images (the highlight in (b)).

Chapter 1: Introduction

Turbocharger is a critical accessory of diesel engines and have been widespread equipped in automotive industry especially in heavy duty vehicles. Turbocharger improve the efficiency of machine by taking advantage of the emission gas to rotate the turbine wheel blade at the speed as high as 100,000 rpm, and at the same time, rotate the compressor wheel to bring more air to the combustion chamber. The turbine wheel blades, which is directly in contact with the emission gas, thus experience harsh service conditions: high temperature (above 650°C), high stress (induced by high rotational speed) as well as the resonance effects due to operational speed range. Usually nickel-based superalloy is used to match the strict requirement of the materials used for turbine wheel blade. The most common and successful candidate for the choice of superalloy is Inconel 713C (IN713C) due to its good castability, suitable mechanical properties and microstructural stability at elevated temperatures. The turbine wheels are produced via investment casting method in a large industrial scale. During investment casting process, the geometrical irregularity in turbine wheels shapes leads to disparity in solidification parameters such as cooling rate in different positions of the wheel component, which inevitably results in inhomogeneous microstructure and microtexture in the component. Furthermore, strain distribution inhomogeneity and localised deformation might be induced due to these microstructural inhomogeneities and finally affect the alloy's performance and mechanical properties to different extend during service. During service, the most common failure mode is fatigue. Fatigue life evaluation and improvement are always the focus and interest in both industry/engineering and scientific aspects. What is more, it is expected to further increase the service temperature (say, to 700°C) to improve the turbocharger efficiency due to pressure of environment protection and carbon dioxide emission reduction. Both require the fundamental understanding of fatigue deformation mechanism and its correlation with material's microstructure and microtexture, which then can be used as guidance for microstructure / microtexture adjustment by controlling the casting process and/or tailoring the chemical composition.

This project is collaborated with Cummins Turbo Technologies (CTT) Ltd, Huddersfiled, UK, by providing Cummins in-house testing and supplying cast IN713C superalloy bars and complete and failed in service turbine wheels. The aim of this study

is to establish process / structure (microstructure, microtexture) / property relationships and identifying the key microstructure features that determine the fatigue crack initiation and propagation. Throughout this investigation, the fatigue tests (including LCF and HCF) were conducted on both real turbine blades and standard cast bars, followed by detailed material characterisation, using both 2-D and 3-D micro analytical tools. High Resolution (HR) SEM, HR-EBSD, TEM, STEM-HADDF techniques were utilised during this study. Furthermore, quantitative analyses including grain and grain boundary characteristics, strain distribution, geometrically necessary dislocation (GND) measurement, slip trace calculation, as well as chemical analyses were concluded to obtain comprehensive description of deformation micromechanism during fatigue failure.

The research presented here is organised in the following parts: literature review (Chapter 2) and experimental procedures (Chapter 3), fractography study of failed blades after in-house testing (Chapter 4), deformation mechanism analysis on real blade in in-house testing (Chapter 5), deformation mechanism analysis on standard fatigue test bars (Chapter 6), solidification trials (Chapter 7) and conclusions (Chapter 8).

In the chapter of literature review (Chapter 2), the basic information about nickel-based superalloy such as crystallographic structure, general function of each element, most common phases in superalloy…etc. will be first introduced. Following this, some specific information about the IN713C and recent research progress will also be reported. Then the basic mechanism of fatigue crack initiation and small crack propagation will be introduced, with more attention paid to some specific effects studied in recent years such as porosity, grain size, slip transfer and crystallographic orientation…etc. Furthermore, recent development of GND calculation and its application to interpret deformation mechanism will be highlighted.

In the experiment chapter (Chapter 3), in addition to the fatigue test conditions during both LCF and HCF using Cummins in-house test and standard bar fatigue test, the sample preparation prior to observation is described. The basic principle of EBSD is also introduced. Moreover, the EBSD data-based GND calculation and slip trace calculation principles will be reported.

In Chapter 4, detailed fractography study on failed turbine blades has been undertaken via OM (Optical Microscope) and SEM. Based on the characteristics of fracture surface,

a step-by-step guidance for distinguishing the LCF and HCF failure mode in turbine service (simulated service) condition is established.

In Chapter 5, further microstructure and microtexture analyses have been carried out on the cross section of the failed turbine blades utilising SEM and EBSD. In particular, a semi-3-D grain orientation distribution was studied using quasi-3-D EBSD construction for HCF samples by serial sectioning techniques. This could give a direct correlation between the fracture surface and the subsurface structure. Moreover, HR-EBSD and GND calculation have been used to analyse dislocation distribution. Finally, a microstructure sensitive failure mechanism for LCF and a microtexture sensitive failure mechanism for HCF are elucidated, respectively.

In Chapter 6, conventional fatigue test method using standard cast bars have been undertaken on the same material. The testing bars have been specially designed to possess three different grain structures, namely: transition, equiaxed and columnar. Following the test, the failed samples are proceeded with similar characterisation procedures with failed blades in Chapter 5. Based on the detailed observation of fracture surface via OM and SEM, verified by the dislocation density distribution which is calculated by both EBSD-based GND and STEM-based direct observation, a dendrite structure dependence of crack propagation mechanism and the notion of 'crack propagation unit (CPU)' are proposed. Moreover, the beneficial effect of small grain size on fatigue property together with a new perspective of Hall-Patch relation in casting alloys (containing dendrite structure) are further elucidated during both LCF and HCF tests.

In Chapter 7, the effects of cooling rate on the microstructure and microtexture of IN713C has been investigated through performing solidification trials. It was found that significant microstructure changes, such as grain size, γ', carbides and other phases can occur depending on the cooling rate applied during solidifications. The hardness test followed EBSD analysis also have been conducted to reveal the microstructure / property relationship. Furthermore, all the phases in the materials have been identified by means of TEM study.

The major contribution of this research in the deformation micromechanisms during LCF and HCF is reported in Chapter 8 where the general findings throughout this study is covered. The effects of carbides / oxidised carbides, dendrite structure, grain size and

crystallographic orientation on deformation are particularly elucidated. Chapter 9 summarise the main conclusions obtained throughout this investigation and Chapter 10 suggest the further study in this research field.

Chapter 2: Literature review

2.1 Industrial Background: Turbocharger

A turbocharger is an accessory to an engine which can be used to reduce emissions and fuel consumption whilst increasing its power. This is done by utilising the energy from spent exhaust gases to force more air into the engine, see Fig. 2.1. This improvement over a naturally aspirated engine's power output is because the compressor can force more air, and proportionately more fuel, into the combustion chamber than atmospheric pressure alone. Turbocharging an engine increases the power-to-weight ratio and power-to-volume ratio; a turbocharger will typically add 30% to 40% horsepower increase to an engine. A turbocharged engine will also improve engine performance at high altitude areas. Normally aspirated engines suffer at altitudes because of decreased air pressure whereas turbocharged engines will ensure the optimum amount of air is always available by running the turbocharger slightly faster.

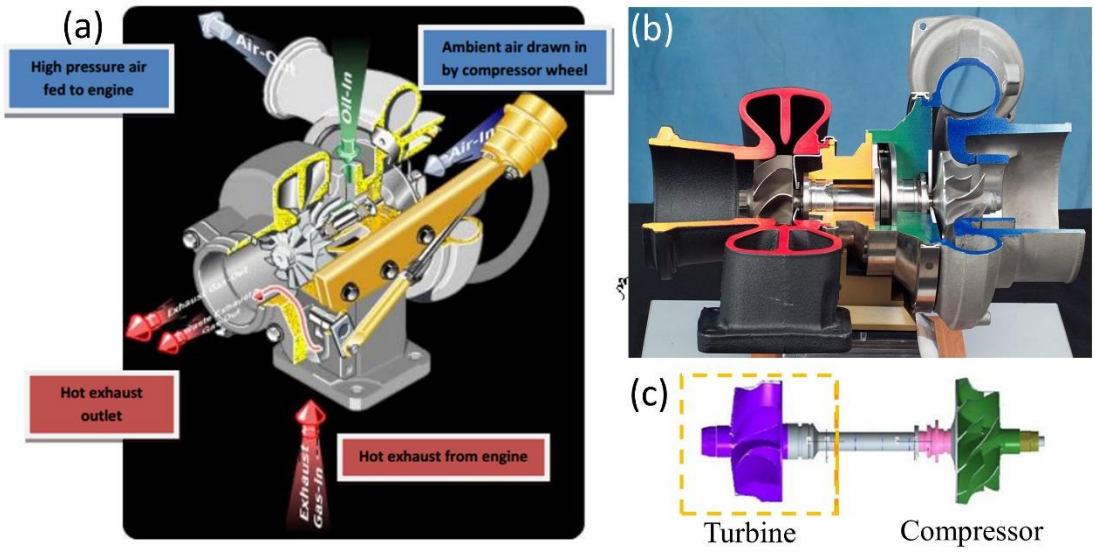

Fig. 2.1 (a) Schematic drawing of Air flow through a turbocharger; (b) Image of a turbocharger; (c) highlight of turbine wheel and compressor wheel in turbocharger. Image courtesy of Cummins Turbo Technologies Ltd.

Cummins Turbo Technologies builds and distributes a wide range of turbochargers to the commercial diesel engine market, with customers such as Scania, Volvo and Cummins Inc. There are three main types of turbochargers that Cummins Ltd.

manufacture, a fixed geometry turbo, a waste-gated turbo and the variable geometry turbo (VGT®).

The turbine wheel is a key component within the turbocharger. Its location and structure in turbocharger are shown in Fig. 2.1b,c. Its design must allow it to survive the high temperatures (~760 °C) and high rotational speeds (~150,000 rpm) that it experiences during the hostile operating conditions and strenuous duty cycles. The material currently used in the turbine wheel design is Inconel 713C, which is a precipitation hardenable, nickel-based cast superalloy. This alloy possesses excellent strength properties up to 780 °C, good castability, excellent resistance to oxidation and thermal fatigue, and good structural stability during operation [1].

The turbocharger turbine wheel differs from many aerospace turbine wheel designs in one major way in that the blades are permanently fixed to the hub. The size of the turbine wheels ranges from the smallest having a diameter of approximately 70 mm to the largest, 177 mm. A typical turbocharger turbine wheel has 10-13 blades which decrease in thickness toward the outer diameter of the wheel. Due to the material choice and high level of cast accuracy required the wheel is manufactured using a ceramic shell investment casting method at the supplying foundry, Cummins Ltd. receives the wheels in the as cast condition. Figure 2.2a shows a computer aided design (CAD) image of a typical turbine wheel with key regions identified. Fig. 2.2b shows an individual turbine wheel after chemical etching and Fig. 2.2c shows the grain structure across the blades with different grain size displayed by IPF (Inverse Pole Figure).

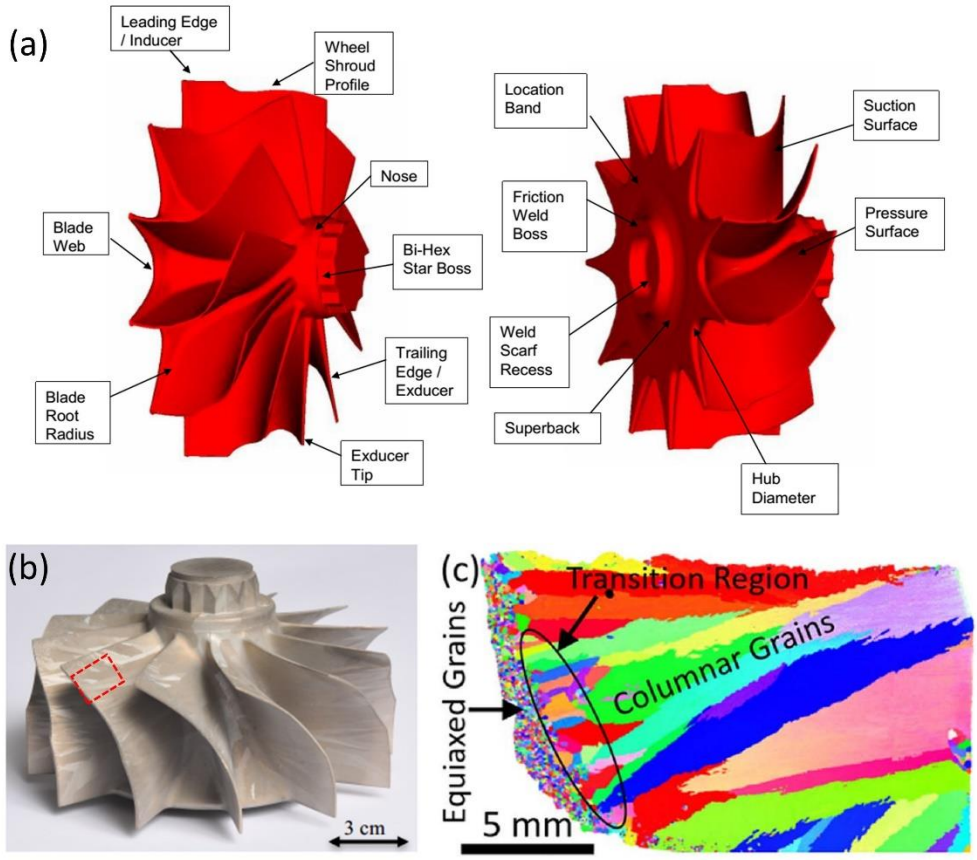

Fig. 2.2 (a) CAD image of a typical turbine wheel with key regions identified. Image courtesy of Cummins Turbo Technologies Ltd.; (b) real turbine wheel after etched; (c) Grain structure with different grain size across the turbine blade imaged by EBSD-IPF (Inverse Pole Figure). The imaged area is highlighted by the red rectangular area in (b).

The turbine wheel blades are thermally and mechanically loaded during the operation of the turbocharger. The mechanical loading is caused by centrifugal forces, and thermally induced mechanical loadings result from transient and inhomogeneous temperature fields within the blade [2]. With the objective to design safe components, it is necessary to understand the failure mechanisms of the employed materials under these complex loadings. Although different failure modes have been reported in literature, the two most prominent turbine wheel failure modes are Low Cycle Fatigue (LCF) and High Cycle Fatigue (HCF) [3, 4, 5]. It is also reported that the cyclical nature of the centrifugal stresses that the wheel experiences during service is responsible for fatigue crack growth [6]. During operation, these centrifugal stresses are amplified above design limits by the presence of a stress concentration, such as a defect in the

material. When the stress concentration at this defect exceeds a critical level, a fatigue crack can initiate and subsequently propagate under the influence of the stress cycles.

2.2 Nickel-Based Superalloys

2.2.1 Basic Structure of Nickel-Based Superalloy

The term superalloy came around World War II. The demand for this new class of alloys in aero-engines and turbine components increased rapidly because they retain their strength and oxidation resistance at high temperatures in contrast to most other material classes. The use of Co and Fe based superalloys is limited as compared to nickel-based superalloys primarily due to higher costs and lower corrosion resistance respectively.

The microstructure of most Ni-based superalloys consists of at least two phases: ordered γ′ and disordered γ. The fundamental properties of superalloys depend on these two common phases.

Gamma phase (γ): It is a continuous matrix, FCC Ni-based austenitic phase, in which other phases reside. The stability of the γ phase with respect to other possible crystal structures is very important since any phase transformations, either during thermal cycling or during extended periods of operation, would affect high temperature properties. It contains a high percentage of solid solution formers such as Co, Cr, Mo, and W, thereby giving rise to solid solution strengthening. The increase in strength depends on the differences in atomic sizes between the base Ni and substitutional atoms. Cr, Mo, and W are strong solid solution strengtheners. In contrast, Co, Fe, Ti, and Al have minor solid solution strengthening effects that contribute more to either improve the corrosion resistance or increase strength by precipitation strengthening [7].

Gamma prime phase (γ'): The γ' precipitate, an intermetallic compound of nominal composition Ni_3Al, can be obtained by ageing the solution treated alloys. It is the most important phase because it plays a significant role in strengthening of Ni-based superalloys by hindering the movement of dislocations. Its crystal structure consists of Al atoms at the unit cell corners and Ni atoms at the face centres (Fig. 2.3). Depending

on heat treatments and chemical compositions, different sizes of γ' precipitates, *i.e.*, fine, coarse, or duplex (both primary and secondary γ') can be formed.

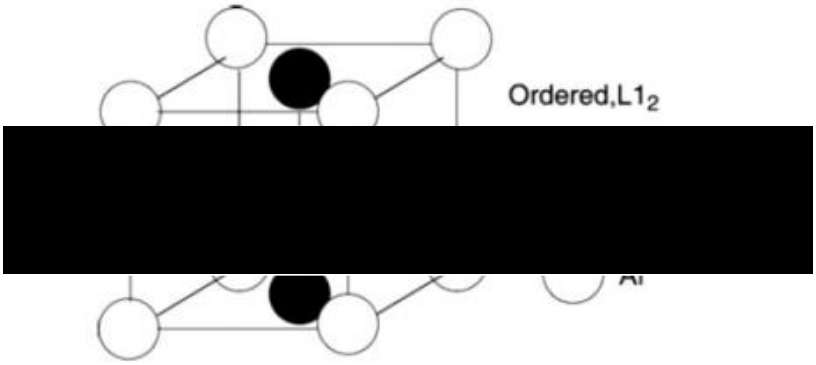

Fig. 2.3 Arrangements of Ni and Al atoms in the ordered Ni3Al phase [7].

Nickel in its pure form has poor mechanical properties such as resistance to corrosion despite its high melting temperature. To achieve the high temperature resistance and strength, nickel is alloyed with up to and/or beyond 10 various elements. This leads to the different element partition behaviours and different phase formations beside gamma prime. Furthermore, this alloying design results in different strengthening mechanism. The detailed information of some possible phases such as carbides and topologically close packed (TCP) phases in nickel-based superalloy are shown in Fig. 2.4 [8] and listed below in Table 2.1 [9], and the strengthening mechanism are briefly explained below.

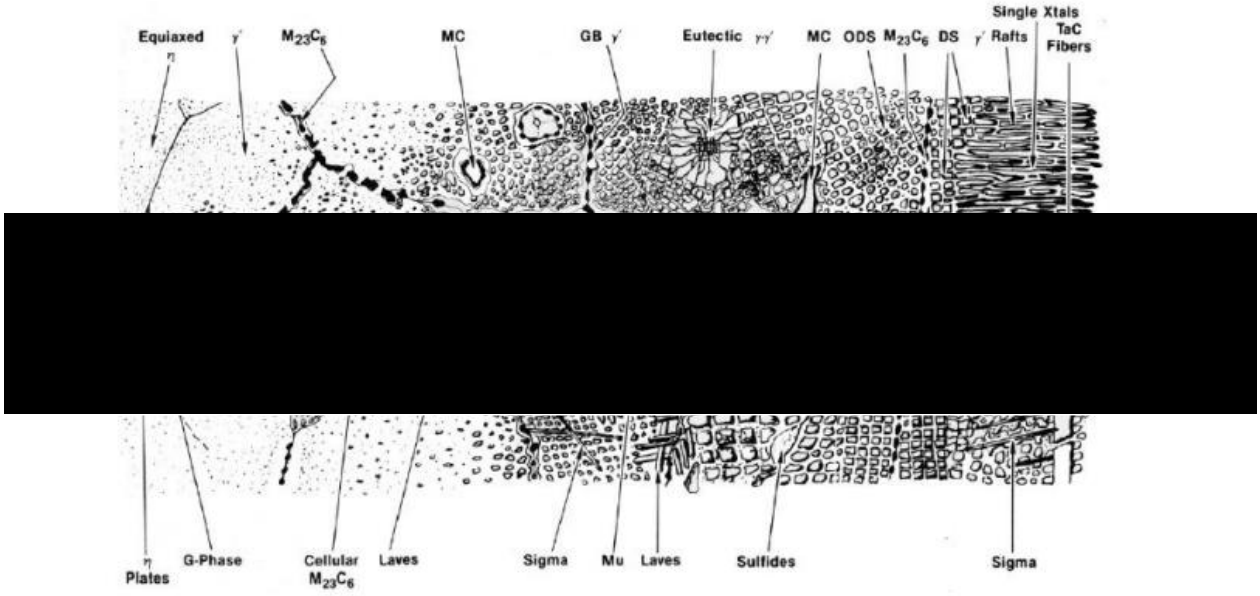

Fig. 2.4 Illustration of the possible phases observed within nickel-based superalloy [8].

Table 2.1 Phases observed in superalloys [9]

Phase	Crystal structure	Lattice parameter, nm	Formula	Comments
γ'	fcc (ordered $L1_2$)	0.3561 for pure Ni_3A1 to 0.3568 for $Ni_3(A1_{0.5}Ti_{0.5})$	Ni_3A1Ni_3(A1, Ti)	Principal strengthening phase in many nickel- and nickel-iron-base superalloys; crystal lattice varies slightly in size (0 to 0.5%) from that of austenite matrix; shape varies from spherical to cubic; size varies with exposure time and temperature. Gamma prime is spherical in iron-nickel-base and in some of the older nickel-base alloys, such as Nimonic 80A and Waspaloy. In the more recently developed nickel-base alloys, γ' is generally cuboidal. Experiments have shown that variations in molybdenum content and in the aluminum/titanium ratio can change the morphology of γ'. With increasing γ/γ' mis-
				thorium, or zirconium.
$M_{23}C_6$	fcc	a_0 = 1.050–1.070 (varies with composition)	$Cr_{23}C_6$ (Cr, Fe, W, Mo)$_{23}C_6$	Form of precipitation is important; it can precipitate as films, globules, platelets, lamellae, and cells; usually forms at grain boundaries; "M" element is usually chromium, but nickel-cobalt, iron, molybdenum, and tungsten can substitute.
M_6C	fcc	a_0 = 1.085–1.175	Fe_3Mo_3C Fe_3W_3C-Fe_4W_2C Fe_3Nb_3C Nb_3Co_3C Ta_3Co_3C	Randomly distributed carbide; may appear pinkish: "M" elements are generally molybdenum or tungsten; there is some solubility for chromium, nickel, niobium, tantalum, and cobalt.
M_7C_3	Hexagonal	a_0 = 1.398 c_0 = 0.4523	Cr_7C_3	Generally observed as a blocky intergranular shape; observed in alloys such as Nimonic 80A after exposure above 1000 °C (1830 °F), and in some cobalt-base alloys

(continued)

Phase	Crystal structure	Lattice parameter, nm	Formula	Comments
M_3B_2	Tetragonal	a_0 = 0.560–0.620 c_0 = 0.300–0.330	Ta_3B_2 V_3B_2 Nb_3B_2 (Mo, Ti, Cr, Ni, Fe)$_3B_2$	Observed in iron-nickel- and nickel-base alloys with about 0.03% B or greater; borides appear similar to carbides, but are not attacked by preferential carbide etchants; "M" elements can be
			Co_2Ta Co_2Ti	extended high-temperature exposure
σ	Tetragonal	a_0 = 0.880–0.910 c_0 = 0.450–0.480	FeCr FeCrMo CrFeMoNi CrCo CrNiMo	Most often observed in iron-nickel- and cobalt-base superalloys, less commonly in nickel-base alloys; appears as irregularly shaped globules, often elongated; forms after extended exposure between 540 and 980 °C (1005 to 1795 °F)

Solid solution strengthening: Impurity atoms or alloying elements are added to take substitutional or interstitial positions without any change in the crystal structure of the host material. Alloying elements either smaller or larger than the host atom impose lattice strains (tensile or compressive) on the surrounding atoms which restrict dislocation movement. Therefore, a greater applied stress is necessary in order to initiate and then continue plastic deformation resulting in the enhancement of strength and hardness. Higher concentrations of the impurity atoms provide stronger strengthening effects [8, 9]. Usually, Cr, Mo, and W are strong solid solution strengtheners in nickel-based superalloy.

Precipitation strengthening: The strength achieved through precipitation hardening is related to the degree of coherency between the precipitate particles and the matrix, which, in turn, depends critically on the lattice misfit. The misfit between γ′ and γ phases plays an important role in determining the morphology of γ′ precipitates whereas the morphology of γ′ precipitates plays an important role when considering dislocation-precipitate interactions.

The lattice parameters of γ′ and γ phases are very similar and the lattice misfit is small. These result in coherent γ/ γ′ interfaces that guarantee low interfacial energy which is essential for a stable microstructure and improves properties at elevated temperatures [9].

Precipitate cutting or Orowan looping are the two mechanisms that take place at γ′ particles during plastic deformation of Ni-based superalloys. When a mobile dislocation encounters a γ′ precipitate, the dislocation either shears the precipitate or bypasses it by Orowan looping. When the precipitate size is small, cutting or shearing is the dominant strengthening mechanism whereas Orowan looping or bypassing dominates at large precipitates. Careful control of the γ′ precipitates size results in the optimum hardness (strength) which is usually attained at the transition point between precipitate cutting and looping mechanisms. It is believed that both Orowan looping and particle cutting phenomena are at play at high temperatures to provide the observed strengthening effect [10, 11].

Grain boundary strengthening: Various carbides and borides segregate at γ grain boundaries. The actual type of carbides and borides depends on the alloy composition and processing conditions employed. Carbides and borides improve high temperature creep properties of the superalloys via the inhibition of grain boundary sliding [9].

2.2.2 IN713C Nickel-Based Superalloy

IN 713C nickel-based superalloy was developed by the International Nickel Company in the 1950s [1]. The alloy proved to possess a very good castability, good mechanical properties at elevated temperatures, and a high stability of the microstructure while being available at an acceptable price. The cost which is a very significant aspect (from the economical point of view) derives from the fact that the alloy does not contain the expensive cobalt. Today it is still used in large quantities, but mainly in the form of precision cast parts for hot-end turbocharger wheels in the automotive industry. The alloy is usually vacuum induction melted and conventionally cast into steel tubes in the form of cylindrical bars. The bars are remelted in foundries and cast into final shapes. Table 2.2 is the standard chemical composition of IN713C and the function of each element in the alloy are briefly explained below.

Table 2.2 Chemical composition of IN713C alloy (wt. %)

Ni	Cr	Al	Mo	Nb+Ta	Ti	C	Zr	B
Bal	12.50	6.10	4.20	2.20	0.80	0.12	0.10	0.01

Aluminium (Al): Al is the most important partitioning element for γ′ formation as both Ni and Al elements have the same crystal structure but exhibit two solid phases [7] outlined below.

i. A significant degree of directional, covalent bonding phase which gives a precise stoichiometric relationship between the number of nickel and aluminium atoms in each cell.

ii. A phase which contains crystals structures in which Ni-Al rather than Ni-Ni or Al-Al bonds are preferred. This results in a strong chemical order where typical structures include Ni_3Al, NiAl, Ni_2Al_3, $NiAl_3$ and Ni_2Al_9. The γ′ phase generally takes the form of Ni_3Al which is of ordered $L1_2$ with Al at the corners as seen in Fig. 2.3.

The ordered nature of the precipitate phase was reviewed in [7] where the ternary phase is of composition Ni-Al-X where X represents an element for example Co, Cr, Mo or W. For this ordered structure the γ' is extended in the direction which depends highly on the solubility of the element X in the γ' phase [7].

Titanium (Ti): Ti is also a strong γ′ former and can readily replace Al as a substitutional strengthener. Ti has also been seen to improve mechanical properties [12]. High additions of the element can decrease the melting temperature of the material and is detrimental to the oxidation resistance through the formation of rutile TiO_2.

Chromium (Cr): The addition of Cr improves the resistance to oxidation and hot corrosion through the formation of Cr_2O_3 [13]. The scale is protective and more importantly are adherent limiting the amount of spallation. The amount of Cr added is limited by the propensity of the σ TCP phase [14]. Whilst it is necessary that primary MC carbides are stable to ensure a reduction in Cr levels within the gamma matrix does not occur.

Carbides (C): With concentration of C of up to 0.2 wt. %, MC carbides are formed where the M refers to a metallic element such as Nb, Ti, Ta or Hf [15]. Carbides precipitate at high temperatures which can be higher than the γ′ solvus temperature. This is beneficial in the controlling grain growth during high temperature heat treatment processes. In processing, or during normal service temperatures, these MC carbides may decompose into other species such as $M_{23}C_6$ (Cr-rich) and M_6C (Mo and W-rich) via the following reactions.

$$MC + \gamma \rightarrow M_{23}C_6 + \gamma'$$

$$(Ti,Mo)C + (Ni,Co,Al,Ti) \rightarrow Mo_3(Ni,Co)_3C + Ni_3(Al,Ti)$$

Generally, the carbides which are rich in Cr, Mo and W are often found in interdendritic regions with no distinct orientation or relationship with the matrix [1]. They sit on the γ/γ grain boundaries and act to pin the boundaries from dislocations. Whether the carbides play beneficial or detrimental role depends on their morphologies and distributions. For instance, large fractions of carbides can result in a continuous film along grain boundaries which leads to alloy embrittlement. However, a fine dispersion of carbides can be seen within the γ matrix which can have a strengthening effect but can also lead to a decrease in ductility. The presence of discontinuous carbides decorating grain boundaries aids in restricting grain boundary sliding and improves resistance to creep. In alloys containing Nb, the concentration of C is monitored due to its propensity to form Nb carbides and thus reduce the benefits of Nb.

Molybdenum (Mo): Mo strengthens the γ phase and aids creep resistance due to its faster diffusion than Ni. Mo is a TCP former and can also be detrimental to oxidation resistance. Mo lowers the solvus temperature significantly when substituted for W. This suggests that Mo acts as a γ-stabiliser. In opposing findings showed Mo and V moderately increase γ′ solvus temperature and both act to stabilise the γ′-phase.

Niobium (Nb): Nb is the weakest of the γ' formers but is often added due to its benefit to oxidation resistance as grain boundary δ-phase acts as diffusion barrier. Additions of Nb also stabilises the γ' phase in a similar way to that of Ta. Meanwhile, Nb additions need to be carefully considered to deter the formation of the delta, δ, phase.

Tantalum (Ta): Ta is a γ' former and acts to increase the lattice parameter of the phase. Addition of Ta increases the solvus temperature of the alloy to approximately 1373K. This in turn increases the volume fraction of γ′ precipitates due to the higher solvus temperature. Ta has larger atomic radii than nickel and provides strong solution strengthening [14]. It also acts to increase the hardness of the material and slightly improve oxidation. It is a dense element and so has significant effects on alloy density.

Borides (B): Similar to C, B combines with elements such as Cr and Mo to form M_3B_2 borides which also sit on the γ grain boundaries with optimum concentrations around 0.003 wt. % [12]. Their presence in polycrystalline alloys has shown to inhibit grain

boundary sliding and increase the creep performance such as rupture strength, creep ductility and Low Cycle Fatigue (LCF) behaviour.

Zirconium (Zr): Zr is thought to 'clear' any undesirable or detrimental tramp elements such as sulphur and phosphorous, with both elements acting as getters of oxygen [12]. Zr has been seen to delay the precipitation of the $M_{23}C_6$ at grain boundaries and hinders the formation of continuous carbides [16].

The cast microstructure of IN713C normally consists of coherent γ' precipitate in a γ dendritic matrix, with carbide phase distributed along the dendrite arm and grain boundaries and the γ'-γ eutectic generally occupying remote interdendritic regions, as shown in Fig. 2.5 [17], which also shows interdendritic MC carbides at grain boundary (Fig.2.5b).

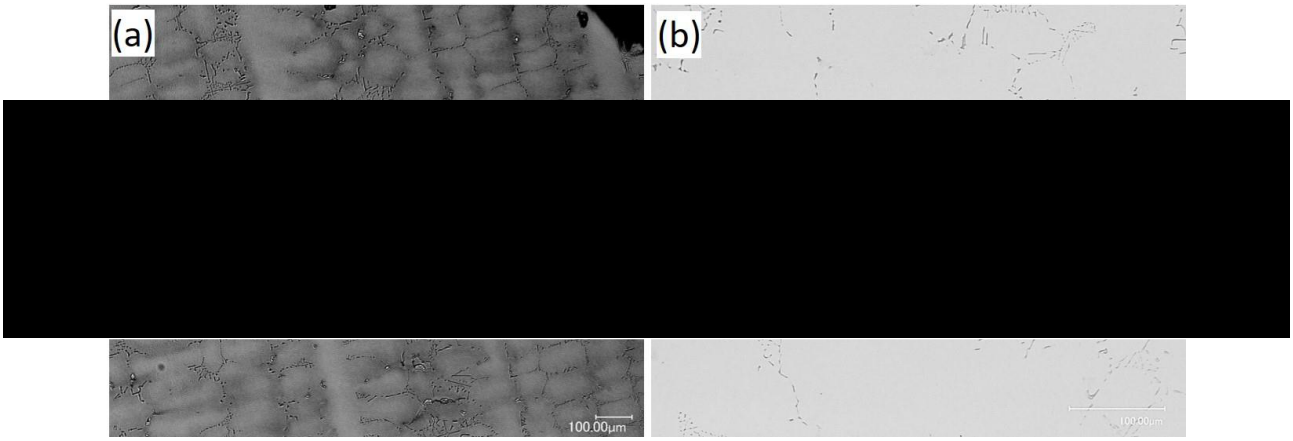

Fig. 2.5 The microstructure of as cast IN713C [17].

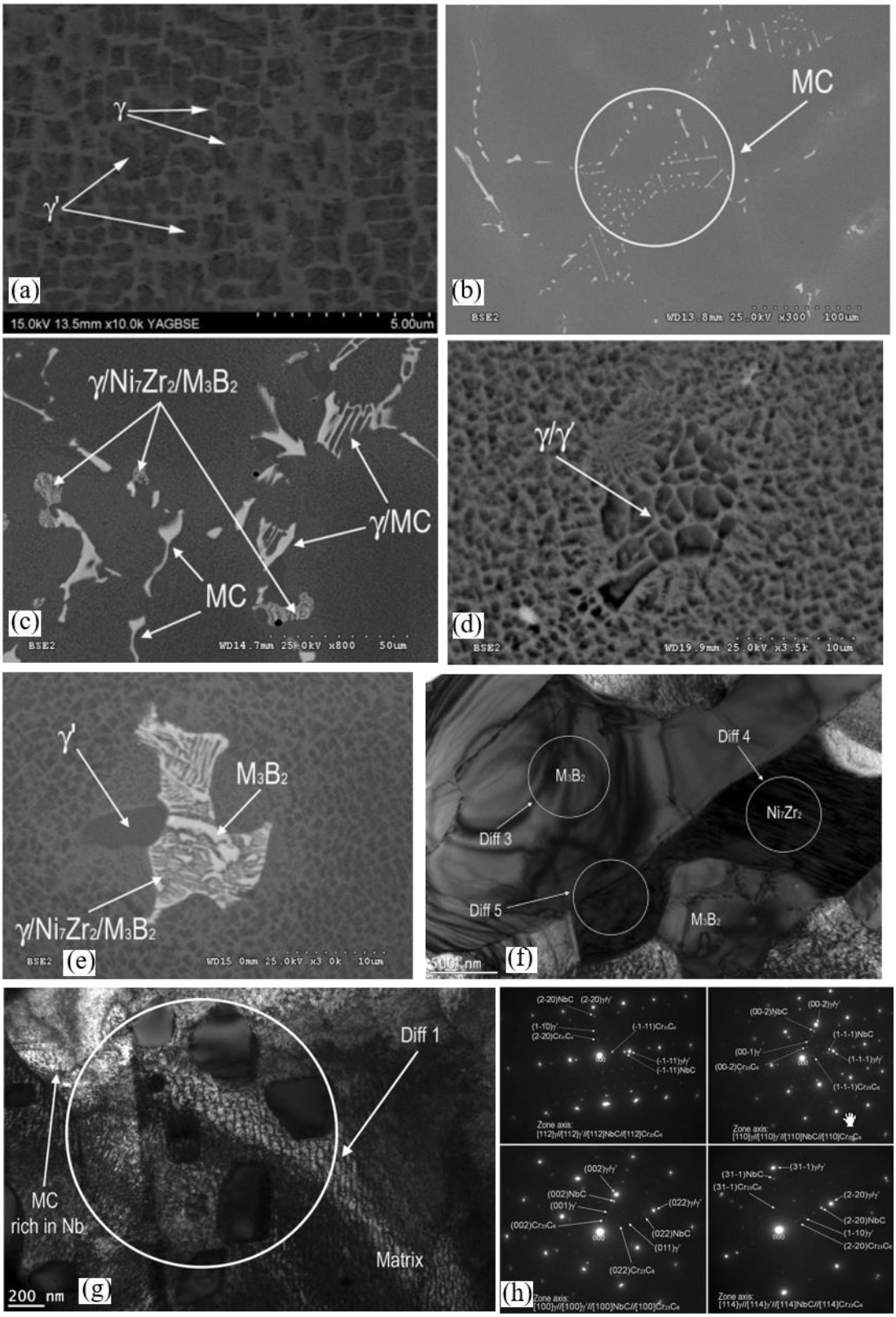

Fig. 2.6 Microstructure of IN713C in as-cast condition (a-f) and after stress-rupture at 980 °C/150 MPa (g, h) [1].

Dendritic growth in nickel-based superalloys gives rise to micro-segregation that greatly affects the formation and distribution of various secondary phases in the as-cast alloy. Piearcey et al. [18] have found that in Mar-M200 dendrite arm boundaries are richer in chromium, titanium, and nickel, whereas dendrite cores are richer in cobalt and tungsten. No difference was found in micro-segregation at boundaries between two columnar or between two equiaxed grains.

The occurrence of γ′-γ eutectic in cast nickel-based superalloys is a manifestation of micro-segregation. This eutectic is degenerate, with γ′ as the major phase appearing in the form of large particles separated by thin lamellae of γ phase. In a columnar ingot of Mar-M200 alloy the volume fraction of γ′-γ eutectic was found to increase from 0.25% at the chill to 3% at the top of the ingot and microprobe analysis showed that nickel, aluminum and titanium contents were higher in the eutectic than in the adjacent matrix, whereas cobalt, tungsten and chromium contents were lower [18]. The eutectic microconstituent is highly undesirable since it retains large amounts of alloying elements that otherwise would have been strengthening the matrix. It has been shown that γ'-γ eutectic can be dissolved by a solution treatment at a temperature at which incipient melting of the alloy could occur. In other superalloys such as IN100 it was established that, if the alloy is very slowly cooled from the liquid plus solid region to the solidus temperature, the eutectic microconstituent can be eliminated or, at least, greatly reduced.

The nature of carbide phases that are desirable in polycrystalline nickel-based superalloys for grain boundary strengthening depends on the composition of the superalloy. In the as-cast condition these carbides are usually of the MC type. MC carbides have a NaCl-type FCC structure. In as-cast Inconel 713C alloy there are two different carbide phases: 1) Normal MC with a lattice parameter of about 4.40 Å and; 2) A small amount of MC with a lattice parameter of 4.43 Å. The carbide with the large parameter contains larger amounts of Zr. In the as-cast alloys no orientation relationship is usually observed between MC carbides and the matrix. However, when studying the microstructure of cast IN713C before and after stress rupture test at 980 °C/150 MPa, Hubert et al. suggested that γ/γ′, NbC and $Cr_{23}C_6$ exist a 'cube-cube' crystallographic relationship, as shown in Fig. 2.6 g, h [1]. They also reported that besides the precipitate of Nb-rich MC carbides during solidification, three eutectics: (γ/NbC), (γ/γ′), and (γ/Ni_7Zr_2/M_3B_2) coexist after solidification (Fig. 2.6 a-f).

Among MC carbides, TaC and NbC are very stable. Multicomponent carbides of the MC-type encountered in many nickel-based superalloys are metastable with a tendency towards dissolution or dissociation after long service at high temperature. However, during slow solidification, as in slowly grown crystals of Mar-M200, MC carbides precipitate out as equilibrium phases. Normal MC carbide in Inconel 713C was found to be stable between 1030 to 1255 K, as well as between 1090 to 1150 K. High parameter MC carbide was found to be completely unstable between 1198 to 1420 K, forming $M_{23}C_6$.

The formation of γ′ is largely by solid state precipitation, though a small amount of this phase may precipitate out directly from the liquid as primary γ′ and is contained in the γ-γ′ eutectic. The average molecular composition of γ′ in Inconel 713C is: $Ni_{2.95}Cr_{0.95}Al_{6.78}Ti_{0.06}Nb_{0.06}Mo_{0.66}$ and the weight percent composition is: 80.4 Ni, 3.4 Cr, 9.7 Al, 2.7 Mo, 1.2 Ti, 2.6 Nb. The weight percent composition of γ is: 66.8 Ni, 22.6 Cr, 3.9 Al, 6.6 Mo, 0.1 Ti. The particle size of γ′ basically depends on the cooling rate of the solid after completion of solidification and has been observed in the as-cast material to be as small as 2 nm or as large as 10 μm. Generally, a coarse and a fine generation of γ′ coexist in the same cast nickel-based superalloy, with the coarse generation precipitating out at higher temperature. The size of coarse γ’ is finer along the center-line of the dendrite arm and becomes coarser near the dendrite arm boundary, presumably because of the effect of compositional variations on coarsening. The average volume fraction of γ’ is a function of comaposition and locally varies across the dendrite arm. The effect of cooling rate on γ’ size, shape and distribution has been studied in unidirectionally solidified Mar-M200 and has been found to be insignificant within the range of cooling rates achieved by this casting technique.

2.3 Fatigue in Nickel-Based Superalloys

In this section, some basic and important concepts such as persistent slip bands (PSB), and some general effects such as loading mode, temperature, microstructure on general fatigue mechanism will be briefly introduced, The concepts and mechanisms reported here may also be applicable to other nickel-based superalloy. The specific topics will be focused on in the next sections are: the effect of oxidation assistant fatigue crack

growth, the effects of carbides and oxidised carbides on crack initiation, the recent progress on deformation mechanism utilising GND theory and the 3-D study of fatigue cracks.

2.3.1 Some Important Concepts and General Effects on Fatigue Mechanism

Irreversible slip and PSB. During cyclic loading in fatigue deformation, cyclic strain localisation and fatigue crack initiation are closely related to the irreversible slip of dislocations. This irreversible slip results from the fact that the displacement imparted by the motion of dislocation in the forward loading cycle is not completely recovered in the reverse loading cycle [19, 20]. This irreversible slip of dislocation will cause the inhomogeneous distribution of plastic deformation or cyclic strain localisation, which will further lead to permanent fatigue damage. Among all the microstructure changes, persistent slip band (PSB) formation is the most significant one and is believed to be the major cause for crack initiation especially in defect-free samples [21]. Macroscopically, the local deformed zone due to PSB end on the specimen surface in the so-called intrusion and extrusion morphology in single crystal and surface grains (if in polycrystals). The PSBs exhibit different structures in different alloys, such as the typical ladder structure of PSB in copper, see Fig. 2.7a, and bands structure in single crystal nickel-based superalloy CMSX-4 [22], see Fig. 2.7b. All these structures present high dislocation density within the PSB compared to that of the surrounding areas, which indicates the severe strain localisation within the PSB.

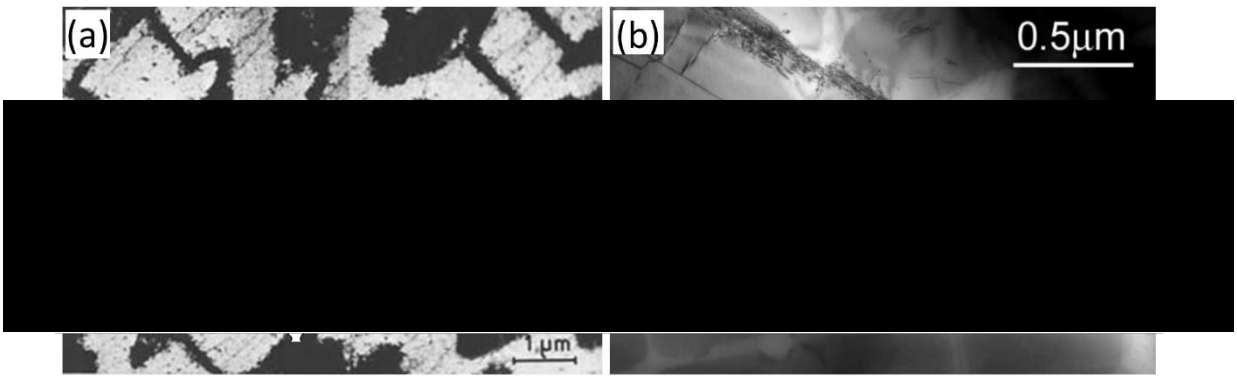

Fig. 2.7 (a) TEM micrograph of persistent slip bands in fatigued copper [19]; (b) TEM image of persistent slip band in single crystal nickel-based superalloy CMSX-4 fatigued at 850°C [22].

Loading modes. In nickel-based superalloys, fatigue cracks initiate not only from metallurgical defects such as pores and inclusions [23-25], but also from microstructure via cyclic strain localisation. These microstructural inhomogeneities such as microtexture and grain boundary character can cause local stress concentrations that contribute to cyclic strain localization. In the regime of low cycle fatigue (LCF), under high loading stresses, most of grains can be plastically deformed. The effect of such microstructure heterogeneities would, therefore, be expected to be very small. However, in the high cycle fatigue (HCF) and/or very high cycle regime, under very low loading stresses, only a small fraction of grains is actively involved in the fatigue deformation process. The deformation then becomes much more localized [26]. This effect of microstructure heterogeneity on fatigue crack initiation and fatigue life is expected to be more prominent in the regime of very high cycle fatigue (VHCF) where deformation is primarily elastic over most of the material volume.

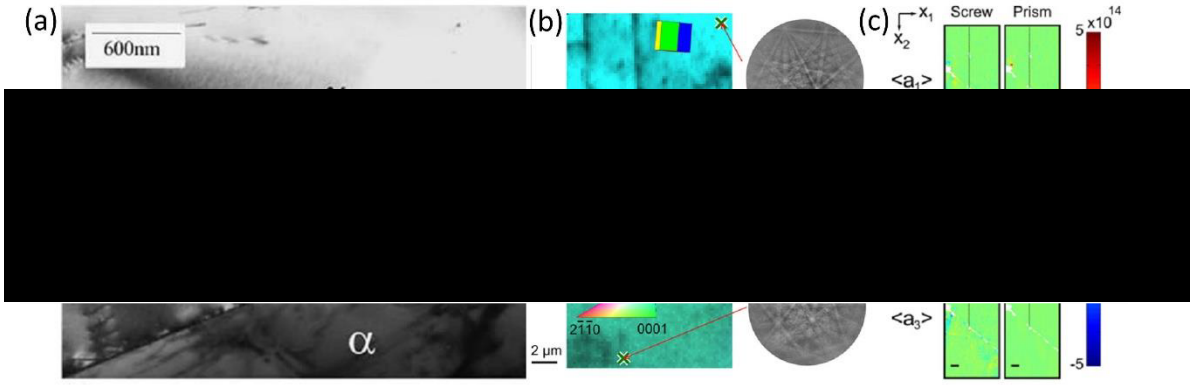

Fig. 2.8 Dislocation pile-ups at grain boundary. (a) Transmission electron micrograph of dislocation pileup at a γ/α phase boundary in AISI F51 duplex steel after cyclic deformation [28]. (b) Conventional EBSD map showing combined image quality and normal direction inverse pole figure map with coloured crystal inserts and reference EBSPs in deformed titanium [29]. (c) Calculated distributions of three <a> screw and three edge <a> on prism planes using Nye's analysis [29].

Grain size. The effect of grain size on mechanical properties and tailoring of grain size is quite a classical research topic, and many efforts have been devoted to fatigue crack study in terms of grain size. The classical empirical Hall-Patch relationship indicating the beneficial effect of smaller grain size has been successfully applied to many

metals/alloys and still been widely used nowadays. The classical explanation for this relationship is either dislocation pile-up at grain boundaries as crack barriers in small size grains or large local stress by dislocation accumulation causing neighbouring grain slip activation in large size grains [27]. Fig. 2.8a shows dislocation pileups at a γ/α phase boundary in AISI F51 duplex steel after cyclic deformation when transmission of plasticity is hindered, e.g., by a large misorientation between the neighbouring slip systems [28]. Many recent researches on slip transmission [29, 30] or dislocation transmission [31] across grain boundary confirmed and further developed this theory. Fig. 2.8c shows the calculated distributions of three <a> screw and three edge <a> on prism planes using Nye's analysis (GND) along a grain boundary in deformed titanium along with the IPFs shown in Fig. 2.8b. This confirmed the pile-up of dislocations at the intersection of slip bands and grain boundary, and further validate a dislocation mechanics by revealing elastic stress state ahead of the pile-up [29]. Furthermore, Shao et al. [32] developed a gradient grain (GS) size structure sample in TWIP (twining induced plasticity) steel by torsion and anneal treatment. This GS structure sample exhibited a better LCF performance than both fine grain and coarse grain samples. This improved fatigue property of GS is attributed to the large generation of geometrically necessary dislocations (GNDs) and the formation of hard core and soft-shell structure during cyclic loading, as schematically shown in Fig. 2.9. Nevertheless, as Hall-Patch relationship usually apply to homogeneous single-phase materials, it is yet to be answered if it is still applicable in heterogeneous multi-phase system like casting superalloy and what is the difference in the micromechanism of dislocation.

Fig. 2.9 Schematic illustration of stress gradient in a deformed gradient structure (GS) sample in TWIP (twinning induced plasticity) steel. This sample contains small size grains in out-surface area and big size grain in the centre [32].

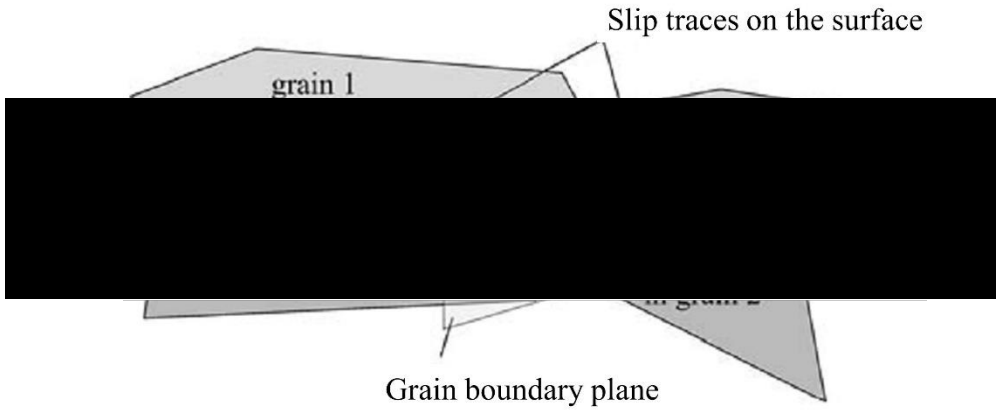

Fig. 2.10 The configuration of tilt (ϕ) and twist (ζ) misorientation across a grain boundary [27]

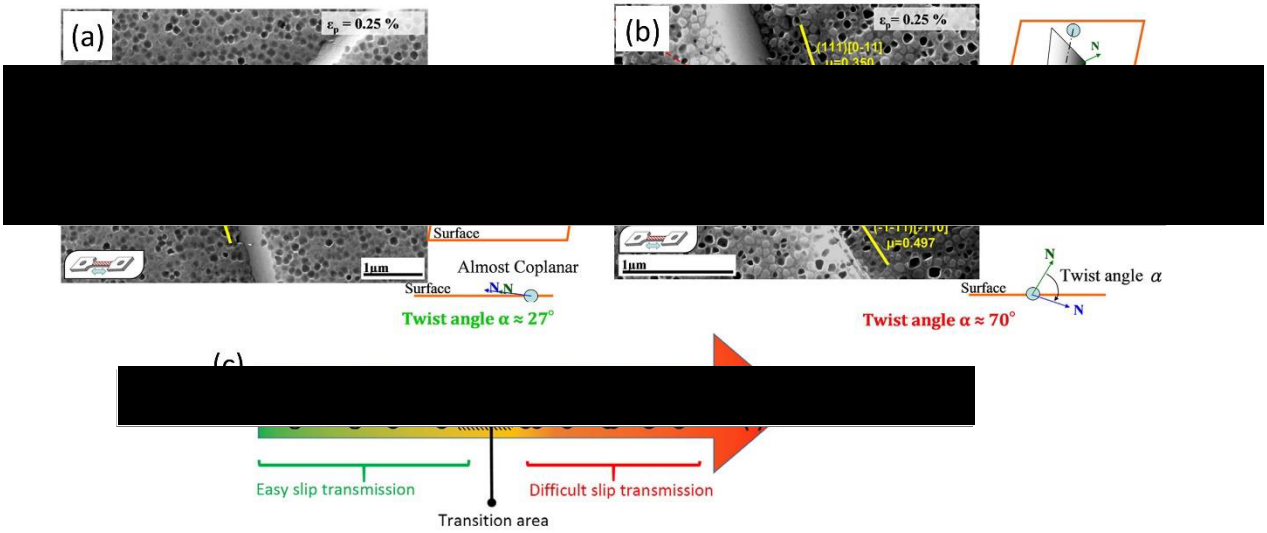

Fig. 2.11 Two opposite geometrical configurations of slip planes on both side of the grain boundary associated to an easy slip transmission (a) and a difficult slip transmission with the development of a micro-volume and of the first stages of micro-cracking (b); (c) Impact of the twist angle value on the slip transmission between neighboring grains [34].

Crystallographic orientation. Crystallographic orientation and microtexture also determine not only the crack initiation but also crack propagation. It is realised that not only the tilt misorientation angle that can be observed from surface operated slip trace, but also the twist misorientation angle within the grain boundary plane [33, 34] and the structure of the grain boundary itself [35] determine the barrier strength of a grain boundary from the spatial misorientation perspective. Fig. 2.10 shows these two misorientations across a grain boundary. Larrouy et al. [34] reported that the difficulty

of slip transfer across grain boundary largely depends on the twist misorientation angle. Fig. 2.11a and b present an easy slip transfer when the angle was less than 60° and a difficult slip transfer when the angle is large, respectively [34]. One difficulty of such study is to provide such 3-D vision of orientation distribution. Another big challenge is to correlate these microstextures to the crack propagation route and features in 3-D perspective, as striations are essentially formed by the alternative slip activation and blunting on different slip systems which depend on crystallographic orientations [36, 37].

Other effects on fatigue property such as temperature [38-41], frequency [42], the size of γ' [41], etc. can be found in other literatures and will not detailed here.

2.3.2 The Effect of Oxidation on Fatigue Crack Growth

The effect of oxygen on the time dependence of high-temperature crack growth has been well documented in literature. Most of which focus on the intergranular time-dependent crack in superalloys which is known to be promoted by oxygen-rich environments at high temperatures (typically >500 °C) in combination with sustained loads or certain low frequency fatigue cycles. This is in contrast to the transgranular cycle-dependent behaviour observed in environments with low oxygen content (e.g. vacuum or inert gas environments such as Ar), lower temperatures or at higher fatigue frequencies (typically >10 Hz) [43].

In the literature, two main mechanisms are often proposed: dynamic embrittlement (DE) and stress accelerated (sometimes also termed strain-assisted) grain boundary oxidation (SAGBO). Dynamic embrittlement is stated to occur by grain boundary diffusion of oxygen ahead of a crack tip, causing decohesion and consequently cracking of the grain boundary under load. Oxidation is suggested to take place only following cracking by DE. Conversely, SAGBO advocates fracture of an oxidized grain boundary ahead of a crack tip, that is, through the preferential formation of grain boundary oxides at, or ahead of, the crack tip. Crack advance is subsequently promoted by the cracking of these oxides [44-47].

Andrieu et al. [44] observed a change in the fracture mode in their study on the crack-tip oxidation mechanisms of Inconel 718 from completely intergranular to completely

transgranular when the testing environment changed from air to vacuum. These results indicate the predominant effect of the environment on the crack growth properties. The effect of testing environment on the crack growth behaviour was conducted by Ghonem and Zheng [45]. It was observed that the crack growth rates were considerably higher for the material tested in air as compared to the material tested in vacuum. A short-range diffusion mechanism with the formation of spinel-oxide interface by a protective chromia layer was established to illustrate the increases in crack propagation rates.

In recent years, with the development of high-resolution techniques, such as HR-TEM (EDS) and APT (Atom Probe Tomography), it's possible to investigate the effect of oxygen on the local crack tip microstructure and chemistry down to atomic level [46, 47]. Kitaguchi et al. [46] investigated the oxide intrusions which formed ahead of the intergranular crack tip in an advanced nickel-based superalloy (containing 18.5 wt. % Co) after exposure to air at 650 °C. They reported that the intrusions were consisted of layered oxides in the thermodynamic sequence of CoO, NiO, Cr_2O_3, TiO_2 and Al_2O_3 along the crack or at the intrusion tip in the condition of dynamic crack or hold stationary crack, as shown in Fig. 2.12. Moreover, these oxide layers seem "sealed" intrusions and can prevent large quantities of oxygen from penetrating the alloy. Similar observation was made by Viskari et al. [47] when studied the intergranular crack tip oxidation at 700 °C under sustained tensile load in Allvac 718Plus (containing 9.1 wt. % Co and 9.5 wt. % Fe), which shows Ni-rich oxide, Ni/Fe-rich oxide an Cr-rich oxide from oxide to metal (Fig. 2.13). Using the technique of APT, they also found the alloy matrix does not oxidize in the same way as the Ni_3(Al, Nb)-γ' precipitates, which was oxidised to NiO (the green area in Fig. 2.13a).

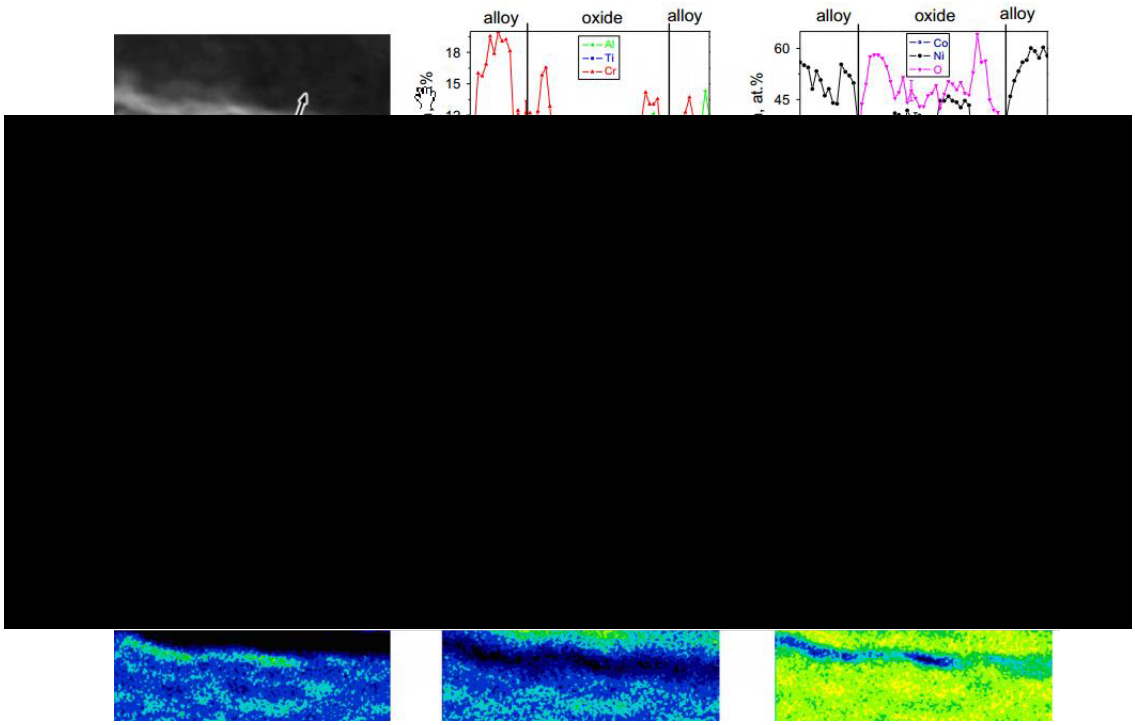

Fig. 2.12. A bright field STEM image, EDX maps and linescans obtained from a region that is close to the crack tip of a growing crack in an advanced polycrystalline superalloy. The relative concentration in the EDX maps increases from low to high in the sequence: black, blue, green, yellow, orange and red [46].

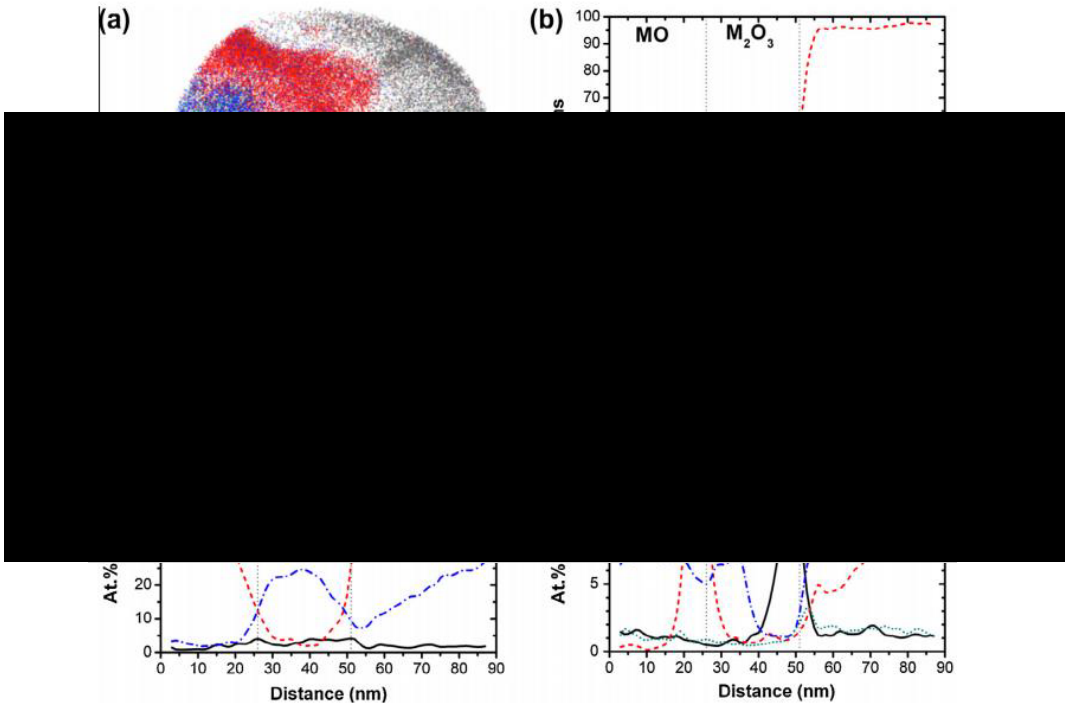

Fig. 2.13 APT reconstruction showing the interface region between metal and a crack tip oxide in Allvac 718Plus. (b-d) Concentration profiles according to the respective legends along the direction shown in (a) [47].

2.3.3 Effects of Oxidised Carbides on Fatigue Crack Initiation and Propagation

IN713C contains relatively high concentration of C and Nb elements as listed in Table 2.2. This leads to the high-volume fraction of MC carbides precipitation during solidification process, especially in interdendrite areas due to element segregation (Fig. 2.5). This microstructure inhomogeneity resulted from the distribution and morphology of carbides are supposed to have some effects on the fatigue property. Carbide sometimes act as crack initiation sites by its brittle nature itself. Moreover, during service in high temperature such as in turbocharger, the carbides are easily oxidised. The carbides and/or oxidised carbides related deformation and their effects on fatigue crack initiation and propagation have been recently reported [48-53]. But their contributions to fatigue deformation micromechanism are yet to be established.

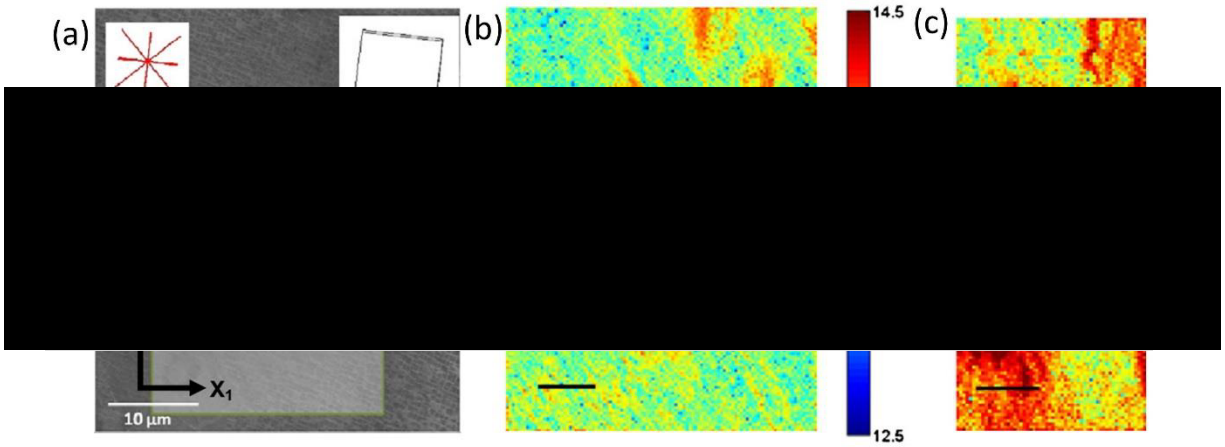

Fig. 2.14 (a) Secondary electron image of a carbide particle in superalloy Mar-M-002 with insets showing the crystal orientation and the trace of <110> slip directions in the surface plane. Total density of GNDs around carbide particle: (b) thermally induced, and (b) after subsequent compression by around 6%. The scale bars in (b, c) are 5 µm long and the colour scale gives log GND density in lines per meter square [48].

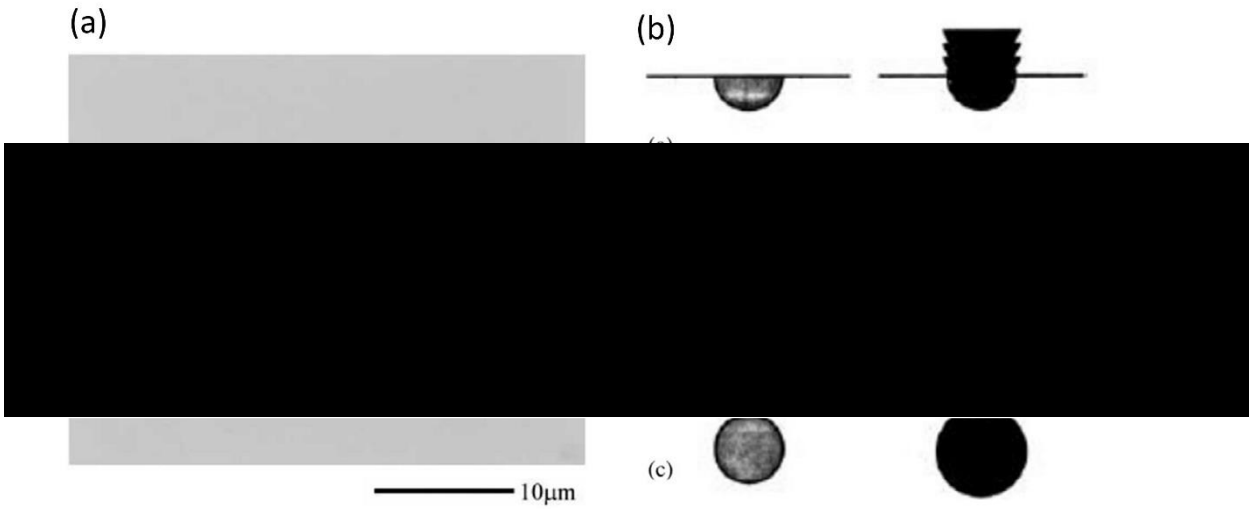

Fig. 2.15 (a) Irregular surface eruption of oxidised (Nb,Ti)C [49]. (b) schematically illustration of this carbides oxidation in different types [50].

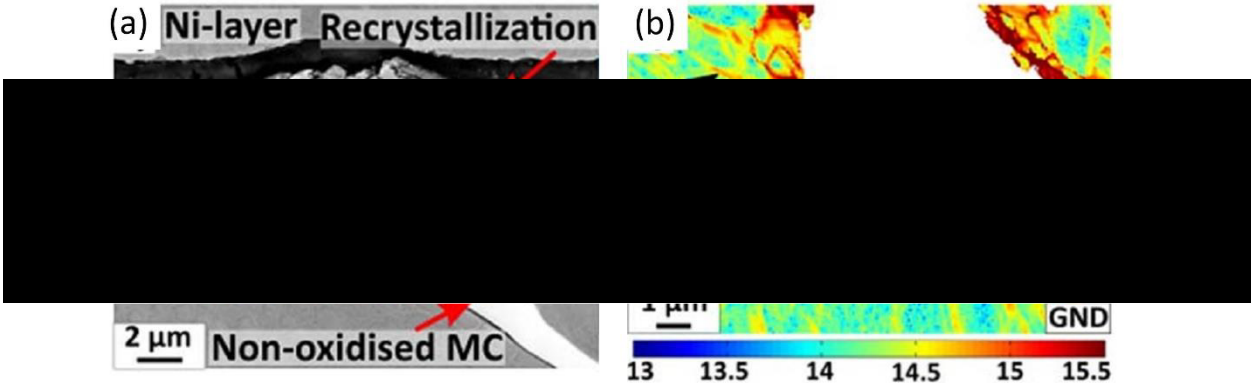

Fig. 2.16 (a) Backscattered SEM image showing recrystallization in the vicinity of an intragranular oxidised MC carbide connected to the surface in polycrystalline superalloy IN792. (b) HR-EBSD strain map from the region as denoted in Fig. 2.12a by the red dashed box, showing the GND density map with the scale bar in log10 scale of dislocation lines m^{-2}. Black arrows in Fig. 2.12b indicate high GND density in γ channels and correspond to the black arrows in Fig. 2.12a. [53]

Karamched and Wilkinson [48] revealed a high GND (Geometrically Necessary Dislocation) density around an individual MC-type carbide in a directionally solidified superalloy MAR-M-002, as shown in Fig. 2.14a, b. The high strains induced surrounding carbide by thermal treatment (solidification) is attributed to the lower

thermal expansion coefficient of the carbide inclusions compared to that of the matrix. In addition to elastic strains the mismatch was sufficient to have induced localised plastic deformation in the matrix leading to high GND densities in regions around the carbide. Furthermore, following the three-point bending tests, the markedly high GND density were found near the carbides particles (Fig. 2.14c) which are majorly generated by the large strain gradients produced around the plastically rigid inclusion during mechanical deformation. Conolley *et al.* [49] have reported the short fatigue crack initiation due to carbides oxidation in detail in IN718 [49]. It is observed that many of the cracks initiated at bulge-like features formed by volume expansion of oxidised (Nb,Ti)C particles. In unstressed samples, oxidation of MC carbides occurred readily, producing characteristic surface eruptions, as shown in Fig. 2.15a and schematically illustrated in Fig. 2.15b [50]. They also estimated the volume expansion factor between Nb_2O_5 and NbC may varies from 2 to 2.4. The volume expansion factor is defined as: $\delta_V = \frac{V_{Nb_2O_5}}{2V_{NbC}}$. Moreover, they also claimed that this type of oxidation process can lead to a localised γ deformation around the oxidised carbides. This type of local deformation of γ matrix is mainly induced by the volume expansion during carbides oxidation. This volume expansion-induced localised deformation during phase transformation also have been reported in other alloys [51], for instance, the volume expansion during austenite-to-martensite transformation in dual steels that cause adjacent ferrite matrix to deform [51]. Surface carbides oxidation has also been studied by Kontis *et al.* [52] recently when comparing the different effects of MC carbides and M_5B_3 borides on tensile property of a nickel-based superalloy at elevated temperature. In addition to surface eruption and volume expansion, pores around oxidised carbides have also been observed by them and supposed to cause microcracks. Recently, Kontis *et al.* [53] reported the higher GND density around cross-sectioned oxidised carbides, see Fig. 2.16. They also reported suspected softer area of recrystallization adjacent to oxidised carbide and caused by elements diffusion through dislocations, which might also contribute to the weakening of oxidised carbides areas [53].

2.3.4 Recent Progress on Deformation Mechanism Utilising GND Theory

The roles of microstructure, grain boundary characteristics and local texture are becoming predominant factors in crack initiation and propagation with the

advancements in materials processing techniques and heat treatments [54, 55]. Moreover, it vital to study local plastic and/or elastic strain distributions as well as lattice distortions near specific features, if the deformation mechanism are to be well understood from a fundamental level. For these purposes, Transmission Electron Microscopy (TEM) and X-ray or neutron diffraction have been widely utilised but with their own shortcomings in length scales. However, by means of high-resolution Electron BackScatter Diffraction (HR-EBSD) which developed rapidly in recent years, it is possible to capture lattice distortions and dislocation arrangement at the mesoscopic and microscopic length scales, thus bridging a balance between analysis of individual defects in TEM and volume-averaged densities via X-ray methods. In particular, local changes in the lattice orientation reflect lattice curvature and can be further used to calculate Geometrically Necessary Dislocation (GND) densities. The concept of GND originally based on the assumption that during plastic deformation, a strain gradient necessitates the creation of minimum dislocation networks to maintain the geometric continuity of the material [56]. This strain gradient often is produced in materials that have two phases that have different deformation ability or adjacent grains with different orientations in polycrystalline alloys [57]. The strain gradient results in orientation gradient and the later can be derived from misorientation across grains, thus the ability of probing orientation of grains in EBSD making the calculation of GND density across grains possible. This type of calculation and measurement by means of HR-EBSD have contributed greatly in better understanding of dislocation arrangements in intra/inter grains [55, 58] and within local microstructure features in nickel-based superalloys. For instance, Soran et al. [55] investigated the influence of local texture on fatigue initiation and propagation by measuring plastic strain present in RR1000 nickel-based superalloy microstructure following thermo-mechanical fatigue tests. The result revealed that cube (<001> // loading direction) and near cube orientations (φ_1, Φ, φ_2: 0, 0-15,0) behaved as “soft” grains with a high Schmid factor and contained low geometrically necessary dislocation (GND) density. While the brass grains (<111> // loading direction) acted as “hard” grains that have the lowest Schmid factor with the highest Taylor factor and GND density. Moreover, the detailed GND map of each grain give indications of the strain hardening state and deformation stages in hard and soft grains, as shown in Fig. 2.17. In a research on crack nucleation in a polycrystal nickel-based superalloy containing non-metallic inclusion in three points fatigue tests, Jiang et al. [59] reported a clear link between crack initiation sites / crack growth area and high GND density

distribution, as shown in Fig. 2.18, the 5% top GND density are marked as red dots and were found fit well with the short cracks. Furthermore, by utilising HR-EBSD and/or High Resolution Digital Image Correlation (HR-DIC) technique, Jiang *et al.* [60] revealed the dual roles of GND in a micro-fracture process: on the one hand, providing local stress amplifications to drive cracking; on the other hand, forming the GND wall ahead of the crack tip and cause blunting of the crack. Here, HR-EBSD-based GND calculation seems to be a promising tool in understanding the relationship between strain inhomogeneity, orientation gradients and dislocation accommodations as well as their interactions with microstructures during plastic deformation.

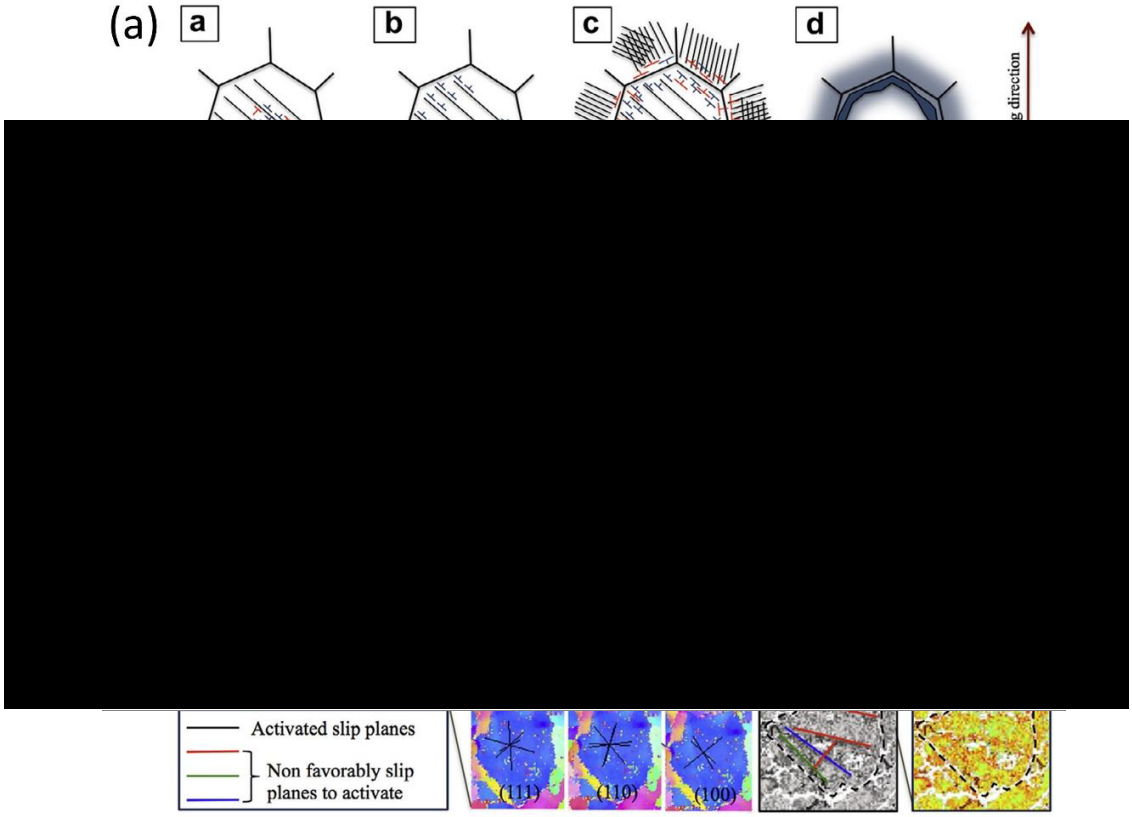

Fig. 2.17. The development of GND accumulation model in soft (above) and hard (below) grains in RR1000 nickel-based superalloy following thermo-mechanical fatigue tests [55].

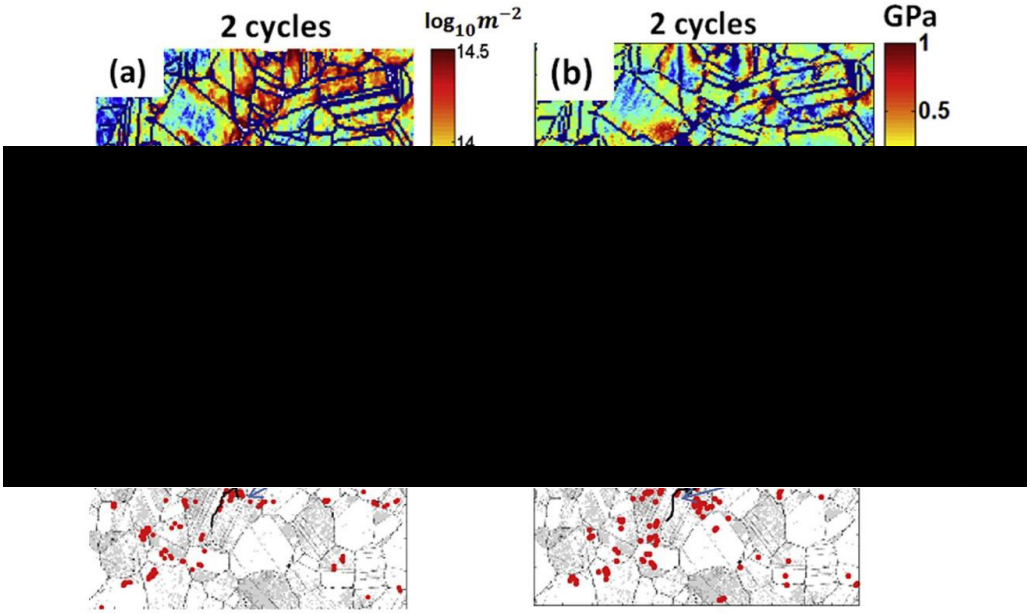

Fig. 2.18 GND and stress map in a polycrystal nickel-based superalloy containing inclusion in three-point fatigue test [59]. (a) GND density map and (b) grain normalised in-plane shear stress map at 2 cycles. The dark blue lines represent grain boundaries. The top 5% of (c) GND density and (d) the grain normalised in-plane shear stress maps at cycle 2 are selected and plotted as red dots and overlaid with the image quality map in which the crack path is clearly marked.

2.3.5 3-D Study of Fatigue Cracks

It is easy to understand that an exhaustive analysis of (short) fatigue cracks would require information on microstructure, microtexture (grain shape and orientation) and crack propagation rate in 3-D. By combining diffraction and phase-contrast X-ray tomography technique, Herbig *et al.* [61] made the first attempt to correlate fracture surface and grain orientation and propagation rate in 3-D in an in-situ and non-destructive way. Fig. 2.19 shows the fracture surface orientation along loading axis (Fig. 2.19a) and the local growth rate da/dN (Fig. 2.19b). Amongst destructive and post-mortem way for fatigue research, serial sectioning method can give 3-D information either by focussed ion beam (FIB) milling [62] or mechanical serial polishing [63], from which 3-D images of short cracks can be reconstructed. Fig. 2.20 shows the 3-D reconstructed fatigue crack path in aluminium by serial sectioning with FIB [62]. It is found that the crack (indicated by black arrows in Fig. 2.20a) continues below the particle, mainly inside of the grain that also contains the particle. It does not follow any obvious grain or subgrain boundary. The crack extends into a number of differently

oriented grains, as indicated by the white arrows Fig. 2.20a. A 3-D view of 2-D KAM (Kernel Average Misorientation) maps is shown in Fig. 2.20c to reveal the dislocation related information along the crack. Example of 3-D fatigue map produced by manually serial sectioning technique is shown in Fig. 2.21 in compacted graphite iron after thermal-mechanical fatigue [63]. It is found that crack growth is enhanced by the presence of graphite particles, and the density of graphite particles on the fracture plane is more than double as high as in any other arbitrary plane of the structure. Moreover, the obtained results did not indicate a crystallographic preference of fracture plane [63]. However, both FIB technique and diffraction / phase contrast technique has the disadvantage of very limited studied volume. What is more, a direct link between fracture surface and grain orientation and microstructure in 3-D is yet to be explored.

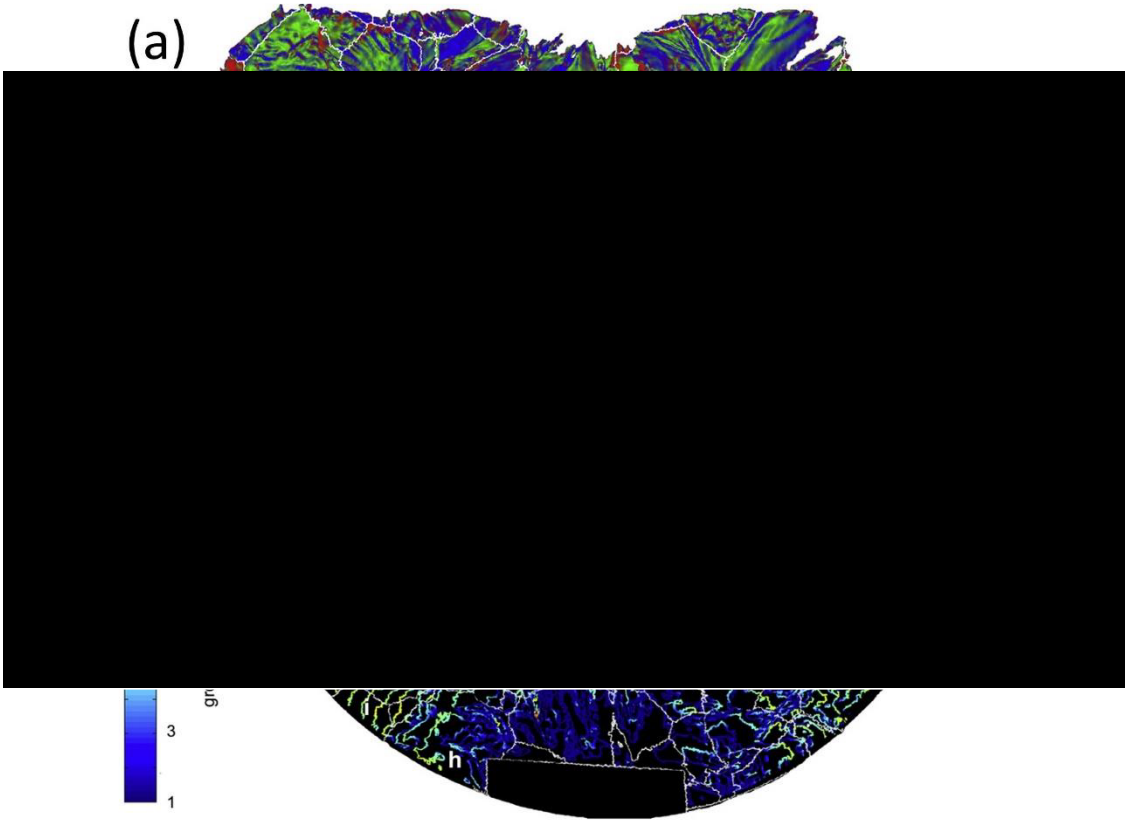

Fig. 2.19 A 3-D view of fracture surface orientation and in-situ local crack growth rate by combining diffraction and phase-contrast X-ray tomography technique [61]. (a) View along the loading axis of the 3-D triangular mesh which represents the fracture surface. White lines indicate intersections of the crack with the grain boundaries. The triangle colours represent the orientation of the fracture surface in the crystallographic system (crystallographic orientation) as defined on the colour map/stereographic triangle on the right. The positions of the slip planes

reported for bcc {1 0 1}, {1 1 2}, {2 1 3} are labelled. (b) Local growth rate da/dN shown with a logarithmic colour code.

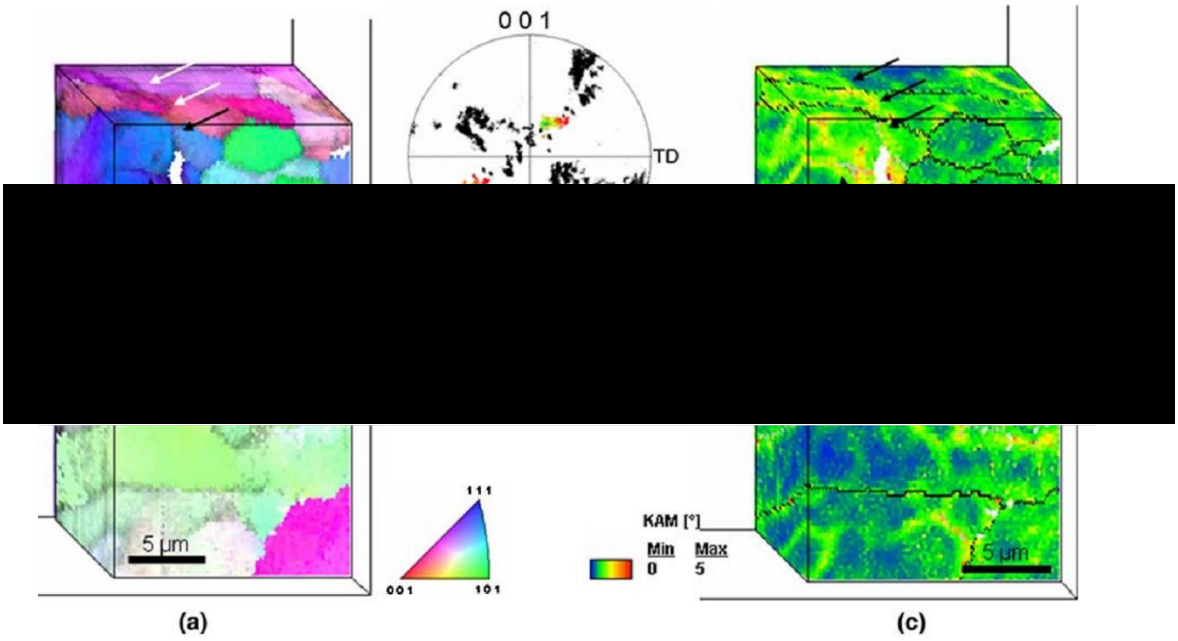

Fig. 2.20 3-D reconstructed fatigue crack by FIB sectioning. (a) 3-D view of the part of the investigated volume close to fatigue crack path in aluminium. Colours according to the IPF for the rolling direction. (b) Pole figure of the front slice of the present view. The orientation of the main grain containing the crack path (indicated by black arrows) is indicated by colour. (c) KAM map. Arrows indicate those areas of high KAM values that are due to cracks. Other areas of high KAM values are due to small-angle grain boundaries [62].

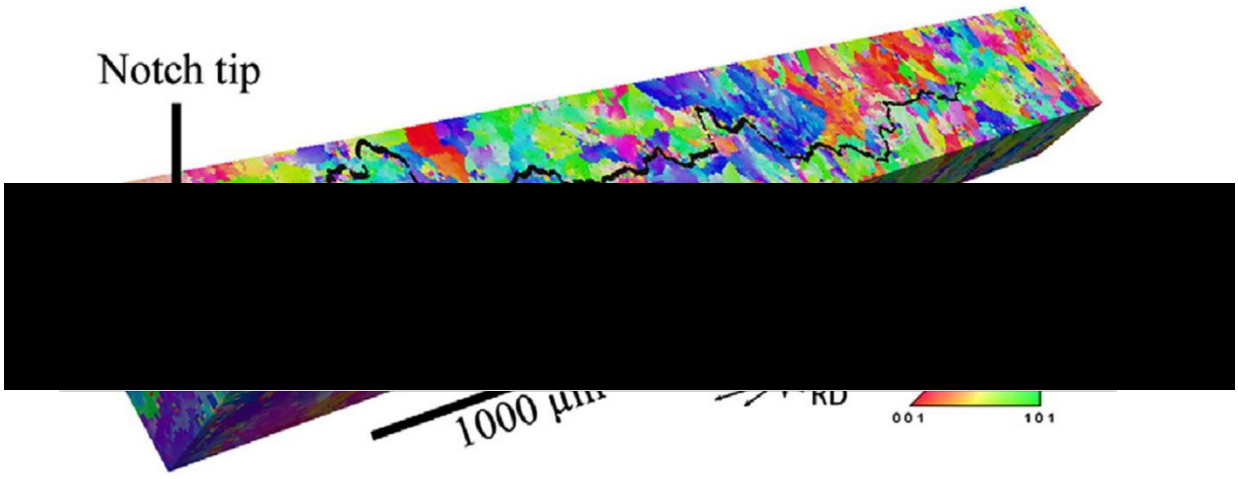

Fig. 2.21 Reconstructed 3-D microstructure of thermo-mechanical fatigue crack in compacted graphite iron. Samples are prepared by manual serial sectioning technique (totally 31 layers were made). Crack is highlighted as black [63].

2.3.6 Fractography of Fatigue Fracture

Compared with other fracture modes, fatigue fracture has its own characteristics because of its loading history and deformation process. As discussed above, number of test conditions such as frequency will affect the fatigue behaviour, which will be reflected on the feature of fracture surface, *i.e.* the fractography. The accumulated experimental knowledge on the micro-fractography of different fatigue tests will be helpful to distinguish the fatigue mode, *i.e.* HCL or LCF, and even tell the details of the deformation history.

Although fatigue fracture can occur in a perfectly smooth, polished specimen via persistent slip bands as discussed above, the crack initiation process is considerably facilitated by irregularities in the surface. Regions of localised plastic deformation or of stress concentration are often observed to be the initiation sites for fatigue fracture: inclusions at the free surface, impressed foreign particles, and crack formed by sand-blasting or shot-blasting, corrosion pits, scratches and surface damage caused by fretting. In addition, phases with low fatigue strengths are often suspected of causing crack initiation.

2.3.6.1 Fatigue Crack Propagation

After crack initiation (usually termed as Stage I) which usually involves 45° propagation in a zone usually comprising one or two grains, fatigue crack propagates at right angles to the direction of the tensile stress (usually termed as Stage II). During this stage, the crack advances by a certain distance with each load cycle. The process leaves a series of striations on the fracture surface, depending on the fatigue mode and condition. Macroscopically, crack propagation in Stage II shows characteristic propagation patterns. These are indicated by the beach marks on the fatigue fracture surface and by the crack front at the transition to final catastrophic fracture. The beach marks, lying parallel to the fatigue striations, form due to changes in loading and/or due to changes in the crack tip environment and the surface layers which subsequently form.

Fatigue cracks propagate predominantly in a ductile manner. Each load cycle results in intensive plastic deformation taking place around the crack tip. This process occurs in a transcrystalline manner. In the case of polycrystalline micro-structures, the crack front is subdivided locally onto a number of separate planes. This results in the formation of the microscopically visible structure consisting of many parallel crack paths.

The profiles of the individual striations depend on the material and the loading conditions. The model of crack propagation proposed by C. Laird and G. C. Smith is generally accepted (Figure 2.22). According to this model, the striations result from the successive opening and closing of crack flanks. During opening, the crack advances, but during closing, the plastically deformed material at the crack tip is compressed, with the deformation of upsetting folds which stand out subsequently in the form of the striation pattern. The profile varies with the intensity of loading and with the ease of slip deformation of the material at the crack tip. In this process, the limitation of compression caused by the meeting of the crack flanks plays an important role.

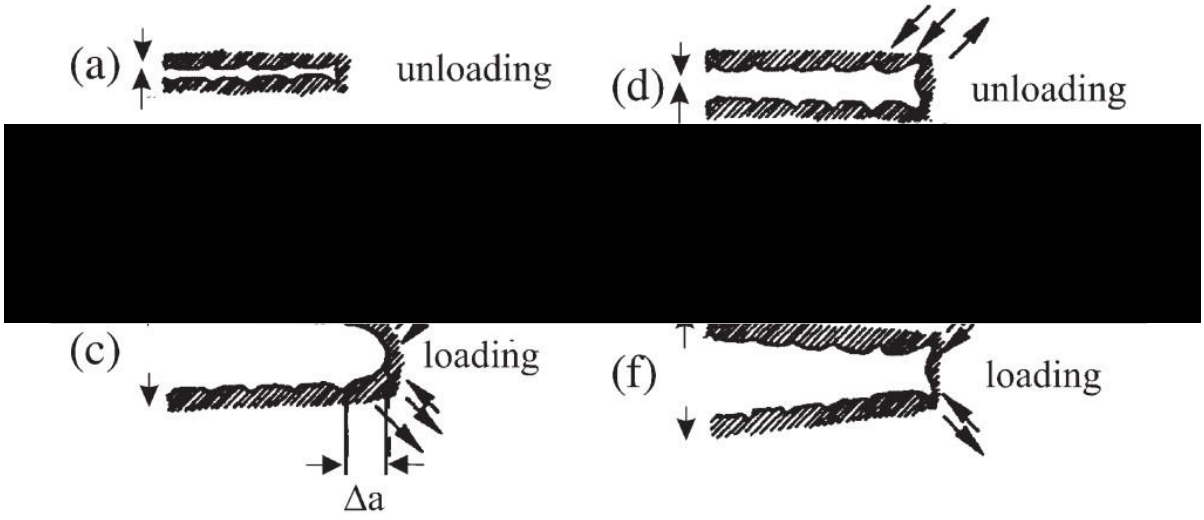

Fig. 2.22 Schematic representation of the model of Laird [64, 65] for one complete unloading (a, e, e) and loading (b, c, f) cycle

2.3.6.2 Fatigue Striations and its Evaluation

Fatigue striation is generally considered to be conclusive proof for fatigue fracture characteristics and in some particular cases, they can be quantitatively analysed. The total number of load cycles to fracture can be extrapolated from measurements of

striation width at a number of points on the fracture surface. Some points that should be remembered when making a quantitative evaluation of fatigue striations are summarised as follows:

(a) The incubation period for fatigue fracture, i.e. Stage I, does not lead to the formation of fatigue striations. As a result, the evaluation of fatigue striations leads to a minimum figure for the number of load cycles to which the material has been subjected.
(b) It is possible that fatigue crack progresses by such small steps that these do not show up as striations. This must be the case when the step width is of the same order of magnitude as the lattice spacing, i.e. in the region of a few nm. In addition, in SEM, only striations greater than 10 nm in width can be resolved.
(c) The striation width varies with the structure of the underlying metal. As a result, the number of measuring position must be large.
(d) It is impossible to follow the fatigue striations continuously from the beginning to the end of a fracture surface because a polycrystalline metal structure results in discontinuities in crack propagation, e.g. where the crack jumps forward by overload or catastrophic fracture mechanisms.

The width of the striations depends on the localised maximum stress and the stress amplitude. Thus, for in-service fractures, the striations in the initiation zone are usually narrower than those in the final fracture zone, since as a rule, decreasing cross-sectional area of the component leads to an increase in the maximum stress at the crack tip.

Irregularities in the striation width can result from periodic changes in the load. If the maximum load remains constant and only the load amplitude varies, then the striation width may change but without any particular dependence on the new amplitude. If, with a constant amplitude, the load shows a periodic increase, then the first load cycle of each period produces a particularly wide striation.

2.4 Microstructure Development during Investment Casting

2.4.1 Investment Casting Process

Investment casting (also known as ‘lost wax casting’or ‘precision casting’) has been a widely used process for centuries. It is known for its ability to produce components of excellent surface finish, dimensional accuracy and complex shapes. It is especially useful for making castings of complex and near-net shape geometry, where machining may not be possible or too wasteful. It is also considered to be the most ancient process of making art castings. Technological advances have also made it to be the most modern and versatile one among all the metal casting processes [66].

Investment cast superalloys are usually nickel-based and cobalt-based. Polycrystalline casting technology for superalloys has been thriving for 60 years, since the cobalt alloys were adapted to the gas turbine engine. In the latter half of the past century, investment casting became the only way to produce required parts from modern high-strength nickel-base superalloys that operate in the gas paths of turbines.

In general, during investment casting, a ceramic slurry is applied around a disposable pattern, usually wax, and allowed to harden to form a disposable casting mold (shell). The disposable pattern is typically removed by steam, leaving a hollow cavity inside the ceramic shell into which molten metal can be poured. Molten superalloy metal is poured into the mold and allowed to solidify under various practices. When no special heat control or other metal solidification control is exercised, the casting that is produced is polycrystalline (PC). If special techniques are used in conjunction with directional heat removal (directional solidification, or DS), columnar grain (CG) or single crystal (SC) products result.

The details of modern shell mold investment casting process consists of a number of steps and explained below, as indicated schematically in Fig. 2.23 [8]

:

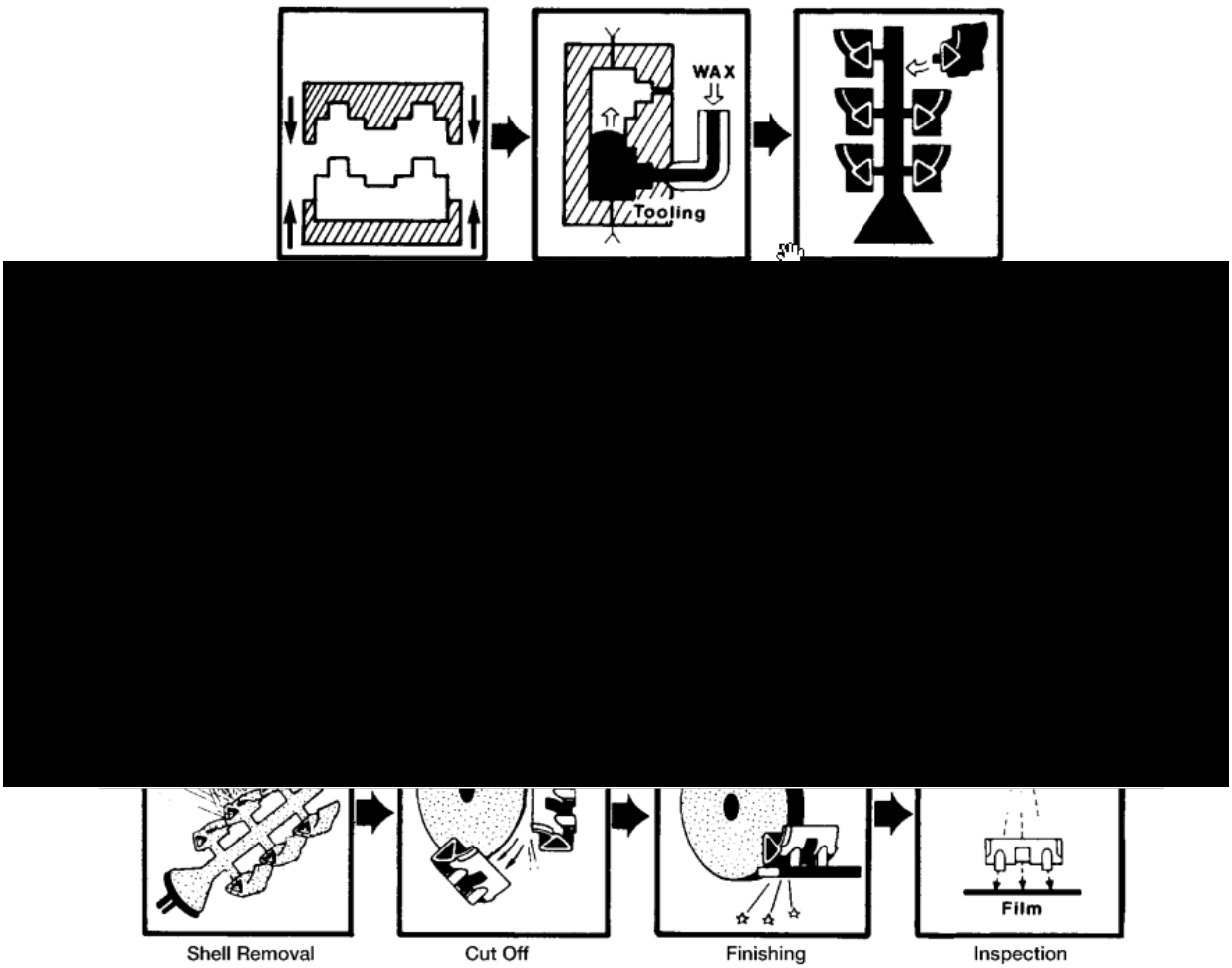

Fig. 2.23. Schematic illustration of the investment casting process [8].

• Construct a die or tool that has at least one internal cavity that corresponds to the external geometry of the article to be produced. One must allow for shrinkage, and more than one cavity might be constructed in the tool.

• Set, in the tool, an appropriate core to form the internal geometry of the article to be produced.

• Inject an appropriate pattern material (usually wax) into the tool to produce a pattern. Many duplicates of the pattern usually will be produced.

• Join one or more of the patterns together on a tree, with wax runners and so on, with the desired gating arrangement to form a wax assembly or cluster.

• Invest the wax cluster in various ceramics, using slurries of the same. This amounts to alternately subjecting the wax assembly to different ceramic slurries, followed by periods of drying, until a sufficient (thickness/strength) green shell has been built up.

The first application is the face coat, which significantly affects the grain size (PC cast alloys) and surface finish of the cast parts. Subsequent to the slurry coat(s), coarser ceramic stucco is built up. At the present time, the procedure is automated, but for many years, all dipping processes were by hand.

• Remove all or most of the pattern, often using a steam autoclave (this process allows the reclamation of the wax pattern material as well), then heat to elevated temperature in a furnace to complete pattern removal by burnout. This process fires the green shell or prefires it before the shell is transferred to a higher-temperature furnace for final firing of the ceramic to produce a cured and strong shell.

• Place the mold in a can, often surrounded by insulating ceramic, and then in a furnace for preheating before pouring.

• Pour liquid superalloy into the mold, often through a dross filter. Solidify the mold either by conventional heat transfer (yielding a PC part) or by directional heat transfer processes (DS), leading to a CG or SC part dependent on the use of selectors to get a single grain or just a water-cooled copper plate to initiate directional growth.

• Remove the mold from the casting furnace and from the can. Break out the raw casting from the mold, usually removing the ceramic shell by mechanical means or a combination of mechanical and chemical means (caustic solution in an autoclave at elevated temperature).

• Cut the sprues, gates, and risers from the article and eliminate any residual gate material.

• Possibly solution heat treat the article at this point, especially if it is a DS product that might have unfavourable recrystallized surface grains created by a combination of stress from mechanical processing and the temperatures of solution heat treatment.

• Clean and finish the article surfaces using methods that may include grinding, polishing, blasting, and/or media finishing.

• Inspect the part to standards set by the caster and by the consumer. Inspection consists of all or most of the following: visual, fluorescent penetration, radiography, ultrasonic (for wall thickness in hollow parts), and dimensional gaging. If the article is DS, then

crystallographic orientation of the article or the orientation differences of grains or subgrains may be checked by x-ray diffraction.

Grain size in PC parts is controlled by an appropriate primary dip coat in the investment, along with manipulation of the moldmetal pour temperatures and use of selective mold insulation to adjust heat flow. An example is the microcast-X method, which makes fine-grained (ASTM 5 to 3) PC superalloys by using a very low superheat (low pour temperature) and a heated mold.

Technically, the grain control, e.g., size, shape and orientation in CGDS or SCDS products is achieved by use of special furnaces that provide appropriate thermal gradients and by selective filters and/or starter nucleation sites. Cores in DS parts may need to be modified in chemistry, because the long-time of solidification exposes them to more heat and increases the possibility of warping. Grain size cannot be significantly altered, owing to the directional nature of the solidification process and the need to avoid any nucleation events that might introduce spurious grains.

2.4.2 Microstructure Evolution during Casting

The microstructure of a casting is of great importance since many material properties, especially mechanical properties, depend on the grain shape and grain size. Furthermore, segregation resulting from solute partitioning during solidification can have significant effects. In this section, the fundamentals of dendrite study including, dendritic structures and dendrite primary spacing, will be reviewed to better understand the evolution of solidification structure. The competitive growth mechanism during solidification will also be discussed.

2.4.2.1 Dendritic Structure Evolution

Dendrites are the most prevalent structure in casting alloys, and the pattern of dendrites determines the final properties of castings [67-69]. Generally, two distinct forms of dendritic structures, columnar and equiaxed dendrites, exist in castings. The structure is called columnar if the growth is preferentially oriented in a direction close to the heat flux, whereas equiaxed grains are growing in all directions, leading to a material with

more isotropic macroscopic mechanical properties and a more homogeneous composition field than those with columnar microstructure.

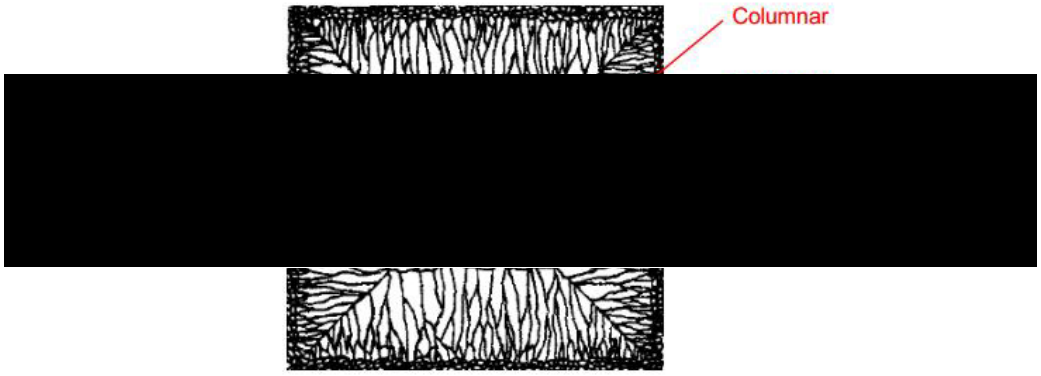

Fig. 2.24 Columnar-to equiaxed transition in casting process [70].

In casting of metallic alloys, a transition from columnar grain structure to equiaxed grain structure can be observed (Fig. 2.24) ([70]. This columnar-to-equiaxed transition is of high technological relevance both from the metallurgical point of view and for the understanding of the fundamentals related to physical phenomena, since the dendrite structures in cast alloys contribute significantly to the final properties of components manufactured from them [68-75]. Fig. 2.25 [76] shows the 3D columnar dendritic morphology in single crystal (SX) superalloys used for turbine blades. All the primary dendrites are aligned with the same direction and free of high angle boundaries, resulting in a great improvement in the creep rupture life.

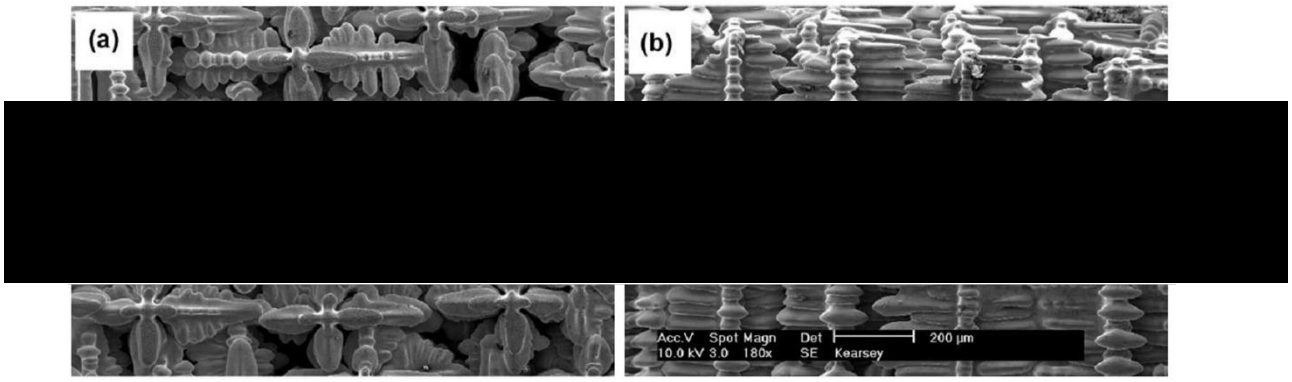

Fig. 2.25 Scanning electron image showing the 3D dendritic morphology of single crystal Ni-based superalloy for both (a) transverse and (b) longitudinal directions [76].

To achieve the columnar dendrite structure, high temperature gradients in front of the solid/liquid (S/L) interface and low solidification velocities are used to prevent the formation of equiaxed grains [77].

2.4.2.2 Primary Spacing in Dendrites

Dendrites have many characteristic structural length scales such as dendrite tip radius and primary and secondary dendrite spacing as illustrated in Fig. 2.26.

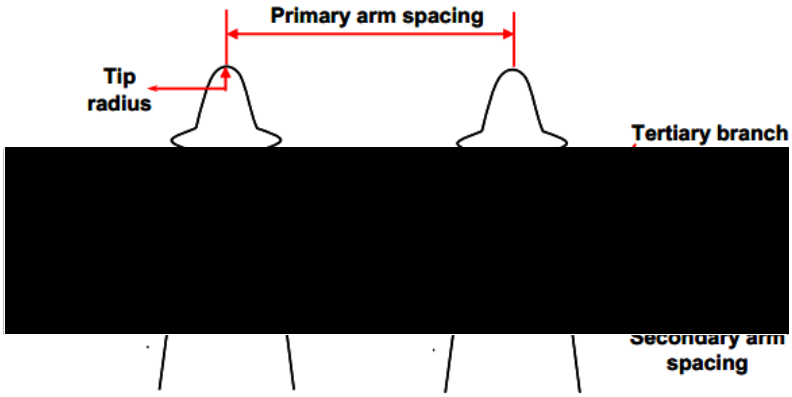

Fig. 2.26 Length scales used in dendrite study [76]

For directional solidification applications where the structure is mainly columnar dendrites, the primary spacing (λ_1) characterizes the maximum length scale for the segregation of alloying elements [69]. As shown in Fig. 2.27 [76], the bright colour stands for the dendrites while the dark colour stands for the interdendritic regions. During solidification, some elements like Re and W prefer to accumulate to the dendrite core while the other elements like Al, Ti and Ta prefer to accumulate in the interdendritic region. The primary spacing (λ_1) indicates the maximum length scale for the segregation and will affect solutioning time afterwards. In general, solutioning time is proportional to the square of primary spacing (λ_1). This means if the dendrite primary spacing (λ_1) can be decreased to half, the required solutioning time will be reduced to a quarter, which will significantly reduce the cost in heat treatment. It has also been found that the primary dendrite arm spacing affects both the processing of alloys and the final thermal mechanical properties of the component [78]. Therefore, a fine spacing

is sought to reduce the propensity for casting defects, minimise heat treatment time, and improve mechanical properties.

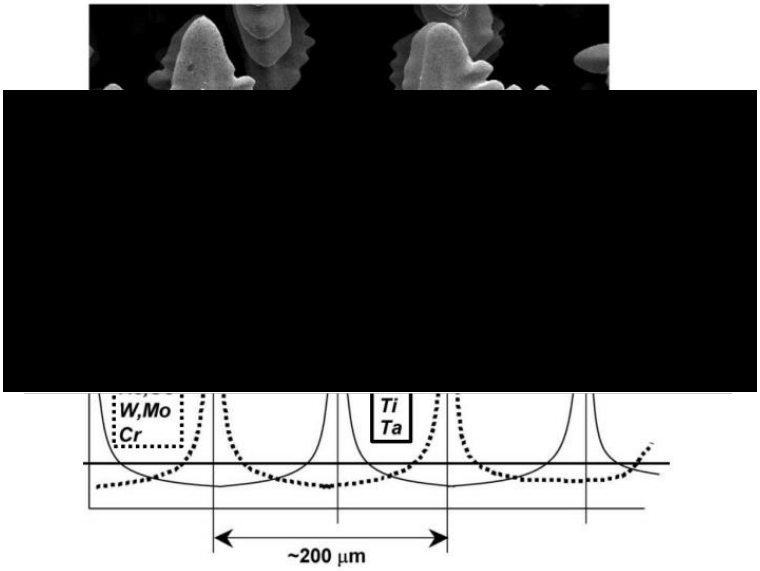

Fig. 2.27 Illustration of micro-segregation in the transverse section of Ni-based single crystal superalloy [76].

Early studies characterised the spacing as a unique value for a given condition [69], but later studies have illustrated that a range of primary spacings are possible for any given set of growth conditions and a small range of dendrite primary spacings can be present in a directionally grown sample [79].

Experimental observations suggested that the spacing range is governed by over growth at the minimum end and branching at the maximum end of the range. If a member of the dendrite array has a spacing which is too small, it will be overgrown by its neighbours (Fig. 2.28a). If the spacing is too large a new primary dendrite will form by the growth of a tertiary arm (Fig. 2.28c).

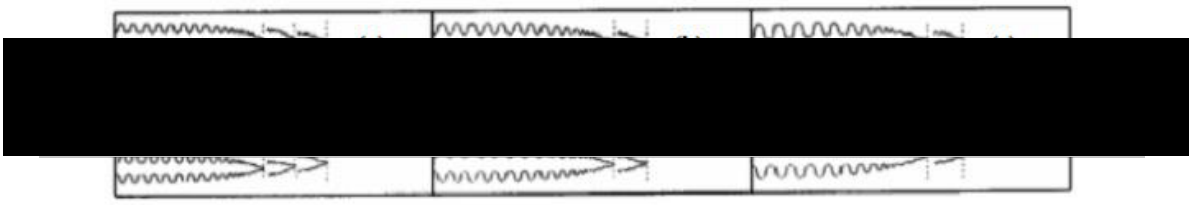

Fig. 2.28 A schematic diagram showing the primary spacing change mechanisms for dendrites: (a) overgrowth; (b) steady state; (c) branching [79]

Stability analysis of the solid/liquid interface by perturbing the solidification front [80] predicted the lower bound in an allowable velocity range, but not the upper bound. Calculations from a numerical model developed by [81] also suggested a solute interaction limit to determine the lower band of spacing. Again, branching was not included in this model, and therefore the upper limit was estimated to be twice as the lower limit. To gain a better understanding of the primary spacing, a model which is capable of simulating branching is required.

Since structure control during single crystal investment casting depends strongly on the competitive growth of dendrites, understanding the underlying mechanism becomes vital. Fig. 2.29 illustrates the schematics of the competitive growth during solidification [82].

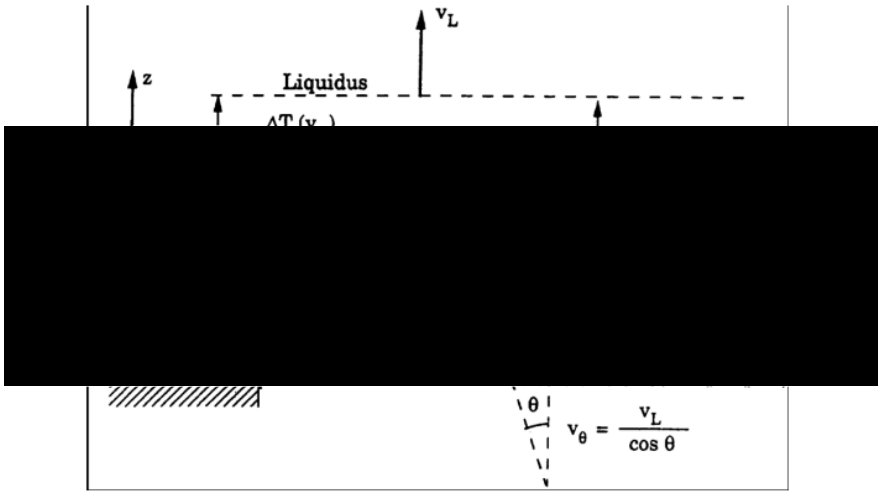

Fig. 2.29 Schematic representation of dendrite growth illustrating the mechanism of competitive growth during directional solidification [82]

As shown in Fig. 2.29, grains on the left and right contain dendrites with preferred growth direction <001> well-aligned with the thermal gradient and they grow with the same rate, v_L, as the velocity of the liquidus isotherm. The grain shown in the middle

has a mis-aligned angle of θ with respect to the direction of thermal gradient. To keep up with the better aligned neighbours, it must grow with a larger growth rate: $v_\theta = v_L/\cos\theta$. Since the growth rate during solidification is determined by the local tip undercooling [79], the mis-aligned grains in the middle then are characterized by a larger undercooling ($\Delta z_\theta > \Delta z_0$). This difference in undercooling makes the mis-aligned grains fall behind and creates the competitive growth mechanism in two situations: converging and diverging.

In a converging case which is shown on the left in Fig. 2.29, it is difficult for the secondary arms to develop from the primary dendrites because of the strong solute interaction. Since the mis-aligned grains are behind the well-aligned grains due to the local undercooling, the dendrite tips of mis-aligned grains will hit the side of well aligned grains and be blocked, generating a grain boundary which is always in the same direction as the growth direction of the well- aligned grains [82].

However, recent experimental analysis on bi-crystal samples during directional solidification [83] shows that the mis-aligned grain was able to overgrow the well-aligned grain by blocking its primary dendrite chunks by branching at different longitudinal planes.

In a diverging case shown on the right in Fig. 2.29, the open space between the two grains offers the opportunity for the secondary arms of mis-aligned dendrites to develop, and then the tertiary arms will branch from the secondary arms to adjust the dendrite spacing and to compete with exist other primary dendrite arms during solidification. As a result, the well-aligned grain will eventually overgrow the mis-aligned grain and generate a grain boundary with an inclined angle which is equal to one third of the angle difference between these two touching grains [83].

2.4.3 Influence of Cooling Rate on the Microstructure Development during Nickel-Based Superalloy Casting

To control the solidification of castings, especially for equiaxed grains, the investment caster has several tools at his disposal: facecoats that encourage grain nucleation, the pour temperature of the metal, preheat temperature of the shell, shell thickness, part orientation and spacing, gating locations, insulation of wrap the shells, pouring speed,

and shell agitation. However, among these methods, the adjustment of cooling rate seems more available and have been widely studied on the solidification structure of nickel-based superalloys [84-87].

One of the wide interest in the early study of cooling rate on solidification is its effect on the carbides formation. Bhambri [84] showed that the shape of MC $(Nb_{0.63}Ti_{0.31}Mo_{0.06})C$ carbide in IN713C alloy depend greatly on :1) the G/R (thermal gradient and growth rate, respectively) at the solid-liquid interface, i.e. under planar front growth conditions the carbide particles were octahedral, under cellular growth conditions they were plate-like, elongated along the cellular growth direction, and under dendritic growth conditions they were irregularly shaped; 2) the local cooling rate, ε, when γ′ was dendritic, with a transition from octahedral to dendritic with increasing ε. The size of MC carbide was also found to be controlled by coarsening and to become finer with increasing ε. What's more, the composition of MC in this alloy was found practically independent of local cooling rate [84].

A great academic interest has also been paid to the effect of cooling rate on the morphology change and size distribution of γ′. The morphology of γ′ particles depends not only upon the elastic energy associated with the lattice misfit between γ′ and γ but also upon the nucleation rate. When the initial density of γ′ is high so that the overlap of diffusion fields occurs, the supersaturation is reduced and γ′ grows in a stable manner. In this condition the precipitates undergoing Ostwald ripening will assume the equilibrium shapes of spheres, cubes, octocubes, aligned cubes, doublets of cubes and plates depending on γ′ size, lattice misfit and thermal processing conditions [7]. On the other hand, when the nucleation rate is low, the precipitates grow to large sizes in the supersaturated matrix, developing solid-state morphological instability. In this condition, when the misfit is high, γ′ precipitates develop cruciform dendrites and flower-like dendrites when the misfit is nearly zero [85]. A typical morphology and size change of γ′ in nickel-based superalloy is shown in Fig. 2.30, where Zhang et al., [86] investigated microstructure evolution with a wide range of cooling rates in an experiment nickel-based superalloy, using the spray casting and melt spinning process to reach high cooling rate (~10^3 k/s and 10^5~10^6k/s, respectively). When cooling rate is very slow (below 0.035 k/s), γ′ exhibit irregular patterns, while it's too high (10^5~10^6 k/s), γ′ exhibit spherical shape. In the medium of range, it shows cuboidal shape and moreover, within this medium of cooling rate, γ′ shape experience irregular cuboidal,

regular cuboidal and near cuboidal patterns with increasing cooling rate. Also in this study, the microstructure changed from plannar, cellular, dendritic, the dendritic growth suppressed features with increasing cooling rate, as shown in Fig. 2.31.

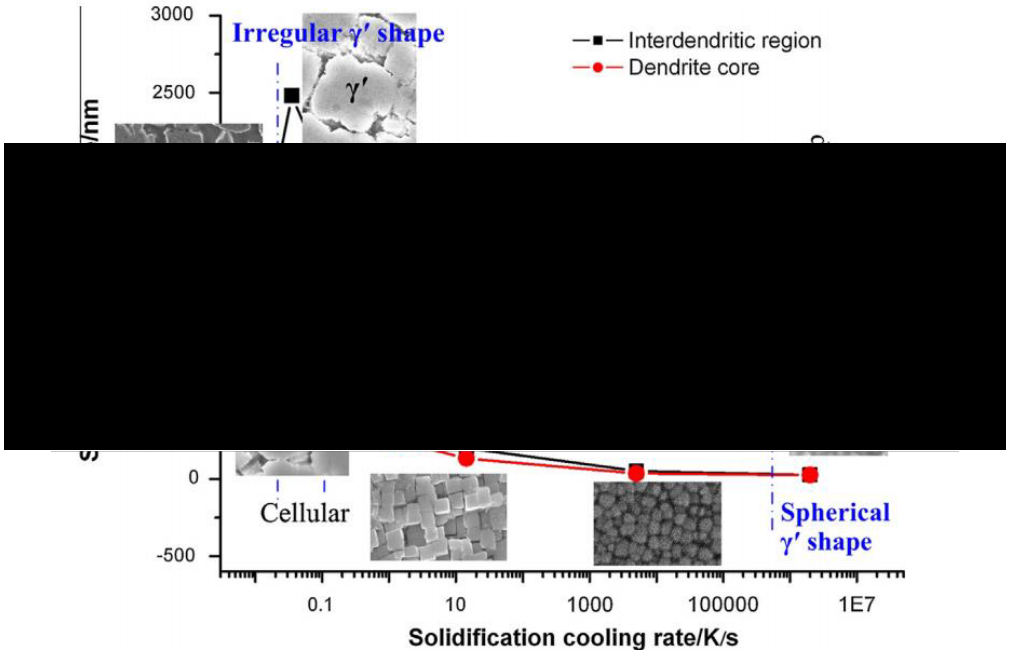

Fig. 2.30 Evolution of microstructure with wide range of solidification rate in Nickel-based superalloy [86].

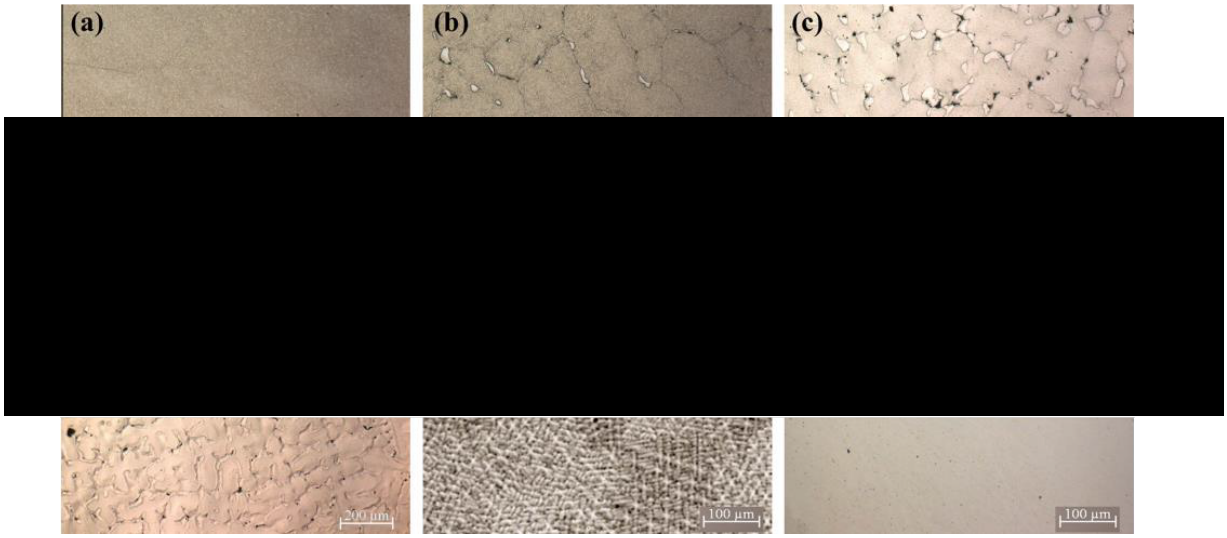

Fig. 2.31 Microstructure evolution with solidification cooling rate: (a) 0.012 k/s, (b) 0.035 k/s, (c) 0.15 k/s, (d) 0.65k/s, (e) spray casting sample (~10^3 k/s), and (f) melt spinning sample (10^5~10^6k/s) [86].

Similar observation was made by Srdjan et al., [87] when studied the effect of the cooling rate on microstructure and hardness of MAR-M247 Nickel-based superalloy, their studies showed that small cooling rate (0.25 k/s) resulted in cellular microstructure and high cooling rate (1.5 and 10 k/s) resulted in dendritic microstructure. Moreover, the secondary dendritic arm spacing decreased and the hardness increased with the increase in the cooling rates from 1~12 k/s as shown in Fig. 2.32.

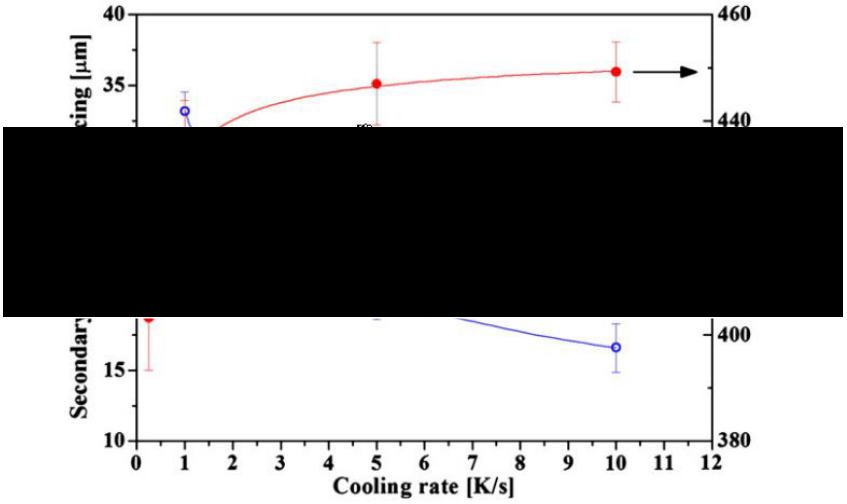

Fig. 2.32 Secondary dendrite arm spacing and microhardness of the MAR-M247 alloy as a function of the cooling rate [87].

According to Bhambri [84] the inter-particle spacing as well as the particle size of γ′ precipitate varied only under conditions of high cooling rate (like in chill-cast rods and next to the chill in unidirectional cast material. There was practically no variation in inter-particle spacing and particle size at other locations in the unidirectional cast ingot where cooling rate was lower. Thus, when the cooling rate was low the normally expected coarser particle size with decreasing cooling rate was not present.

2.5 Summary of Literature Review

In this Chapter, up-to-date literature and available data, concepts and theorises of deformation mechanism in nickel-based superalloys have been reported and reviewed. In general, the literature review in this chapter included: the industrial background of this project (turbine blade in turbocharger wheel), the brief introduction to nickel-based superalloy, the composition and typical microstructure of IN713C that is used for

turbine blade, the principle of investment casting process, the typical effects of cooling rate on microstructure during solidification and some important factors affecting fatigue deformation in superalloys. Particularly, the recent research progress on dislocation analysis and fatigue deformation micromechanism based on HR-EBSD and GND calculation, and progress on 3-D investigation of fatigue deformation have been reviewed. From the literature review, it is clear that although a general fatigue deformation mechanism reported in literature can be validated in many cases in superalloys (for instance, the effect of grain size, grain boundaries and grain orientation), the fatigue deformation micromechanism in IN713C can be completely different due to its inhomogeneous microstructures, e.g., dendrite structure and large grains generated during solidification. For instance, the pioneering work about the possible effects of dendrite structure on fatigue life was conducted by Horstemeyer et al. [88] in a die cast magnesium alloy. They noticed the variation in HCF life might be affected by average secondary dendrite arm spacing in addition to the drastic difference in nucleation site size and average grain size. However, as the most prominent characteristic of casting materials, many dendrite structure related questions remain unanswered, such as to what extend it affects crack propagation? What is the deformation micromechanism related to this structure? And which stage of fatigue process it really affects? The effect of grain size on mechanical properties and tailoring of grain size is another example, although many efforts have been devoted to fatigue crack study in terms of grain size [27]. The classical empirical Hall-Patch relationship indicating the beneficial effect of smaller grain size has been successfully applied to many metals/alloys and still been widely using nowadays. The classical explanation for this relationship is either dislocation pile-up at grain boundaries as crack barriers in small size grains or large local stress by dislocation accumulation causing neighbouring grain slip activation in large size grains [27]. Nevertheless, as Hall-Patch relationship usually apply to homogeneous single-phase materials, considering heterogeneous multi-phase system like casting superalloy would inevitably give rise to the following questions: is Hall-Patch rule still applicable? If so, is it the same micromechanism of dislocation as in other alloys? And what is the difference or are they the same mechanism in LCF and HCF mode for possible beneficial effect of smaller grain size?

Therefore, the influence of dendrite structure, carbides/oxides, grain size and crystallographic orientation on fracture mechanics, i.e., fatigue crack initiation and propagation, which has little been reported in casting superalloy before, are investigated here. The aim of this project is to examine the deformation behaviour and micromechanism of IN713C nickel-based superalloy using different geometry (turbine wheel blades or cast bars) and loading modes (HCF or LCF). The objective here is to establish a correlation between the microstructure and microtexture and deformation mechanisms.

References:

[1] H. Matysiak, M. Zagorska, A. Balkowiec, B. Adamczyk-Cieslak, R. Cygan, J. Cwajna, J. Nawrocki, K.J. Kurzydłowski, The Microstructure Degradation of the IN 713C Nickel-Based Superalloy After the Stress Rupture Tests, J. Mater. Eng. Perform. 23(9) (2014) 3305-3313.

[2] P. Moraal, I. Kolmanovsky, Turbocharger Modeling for Automotive Control Applications, (1999).

[3] H. Nguyen-Schäfer, Rotordynamics of automotive turbochargers, Springer2015.

[4] M. Petrenec, K. Obrtlík, J. Polák, Inhomogeneous dislocation structure in fatigued INCONEL 713 LC superalloy at room and elevated temperatures, Mater. Sci. Eng. A 400-401 (2005) 485-488.

[5] D. Gelmedin, K.-H. Lang, Fatigue behaviour of the superalloy IN 713C under LCF-, HCF- and superimposed LCF/HCF-loading, Procedia Engineering 2(1) (2010) 1343-1352.

[6] S.D. Arnold, Turbocharging technologies to meet critical performance demands of ultra-low emissions diesel engines, SAE Technical paper, 2004.

[7] R.C. Reed, The superalloys: fundamentals and applications, Cambridge university press, 2008.

[8] W. Betteridge, Nickel and Its Alloys. Northcote House Publishers Ltd., 1977.

[9] M.J. Donachie, S.J. Donachie, Superalloys: a technical guide, ASM international2002.

[10] A. Baldan, Review progress in Ostwald ripening theories and their applications to nickel-base superalloys Part I: Ostwald ripening theories, Journal of materials science 37(11) (2002) 2171-2202.

[11] A. Baldan, Review Progress in Ostwald ripening theories and their applications to the γ′-precipitates in nickel-base superalloys Part II Nickel-base superalloys, Journal of materials science 37(12) (2002) 2379-2405.

[12] A. Suzuki, T.M. Pollock, High-temperature strength and deformation of γ/γ′ two-phase Co–Al–W-base alloys, Acta Mater. 56(6) (2008) 1288-1297.

[13] A. Pineau, S.D. Antolovich, High temperature fatigue of nickel-base superalloys–a review with special emphasis on deformation modes and oxidation, Eng. Fail. Anal. 16(8) (2009) 2668-2697.

[14] M. Hardy, B. Zirbel, G. Shen, R. Shankar, Developing damage tolerance and creep resistance in a high strength nickel alloy for disc applications, Superalloys 2004 (2004) 83-90.

[15] Y. Xu, Q. Jin, X. Xiao, X. Cao, G. Jia, Y. Zhu, H. Yin, Strengthening mechanisms of carbon in modified nickel-based superalloy Nimonic 80A, Mater. Sci. Eng. A 528(13-14) (2011) 4600-4607.

[16] R.F. Decker, J.W. Freeman, The mechanism of beneficial effects of boron and zirconium on creep-rupture properties of a complex heat-resistant alloy, (2000).

[17] D.S. Kang, K.D. Woo, D.G. Kim, S.M. Kim, D.Y. Kim, W.J. Kang, E.J. Jo, Heat Resistant Turbine Wheel Development of Automobile, Advanced Materials Research 658 (2013) 372-375.

[18] B. Piearcey, B. Kear, R. Smashey, Correlation of structure with properties in a directionally solidified nickel-base superalloy, ASM Trans Quart 60(4) (1967) 634-645.

[19] H. Mughrabi, Cyclic slip irreversibilities and the evolution of fatigue damage, Metallurgical and Materials Transactions B 40(4) (2009) 431-453.

[20] Suresh S, Fatigue of materials, Cambridge: Cambridge University Press; 1991.

[21] M. Risbet, X. Feaugas, C. Guillemer-Neel, M. Clavel, Use of atomic force microscopy to quantify slip irreversibility in a nickel-base superalloy, Scr. Mater. 49(6) (2003) 533-538.

[22] P. Lukáš, L. Kunz, Role of persistent slip bands in fatigue, Philos. Mag. 84(3-5) (2004) 317-330.

[23] J. Hyzak, I. Bernstein, The effect of defects on the fatigue crack initiation process in two P/M superalloys: Part I. Fatigue origins, Metall. Trans. A 13(1) (1982) 33-43.

[24] J. Hyzak, I. Bernstein, The effect of defects on the fatigue crack initiation process in two p/m superalloys: part ii. surface-subsurface transition, Metall. Trans. A 13(1) (1982) 45-52.

[25] E.S. Huron, P.G. Roth, The influence of inclusions on low cycle fatigue life in a P/M nickel-base disk superalloy, Superalloys 1996 (1996) 359-368.

[26] P. Lukáš, L. Kunz, Specific features of high-cycle and ultra-high-cycle fatigue, Fatigue & Fracture of Engineering Materials & Structures 25(8-9) (2002) 747-753.

[27] U. Krupp, Fatigue crack propagation in metals and alloys: microstructural aspects and modelling concepts, John Wiley & Sons2007.

[28] O. Düber, Ausbreitungsverhalten kurzer Ermüdungsrisse in einem austenitischferritischen Duplexstahl, Dissertation, Universität Siegen, 2006.

[29] T. Benjamin Britton, A.J. Wilkinson, Stress fields and geometrically necessary dislocation density distributions near the head of a blocked slip band, Acta Mater. 60(16) (2012) 5773-5782.

[30] Z. Zheng, D.S. Balint, F.P.E. Dunne, Investigation of slip transfer across HCP grain boundaries with application to cold dwell facet fatigue, Acta Mater. 127 (2017) 43-53.

[31] R. Ding, J. Gong, A.J. Wilkinson, I.P. Jones, A study of dislocation transmission through a grain boundary in hcp Ti–6Al using micro-cantilevers, Acta Mater. 103 (2016) 416-423.

[32] C.W. Shao, P. Zhang, Y.K. Zhu, Z.J. Zhang, J.C. Pang, Z.F. Zhang, Improvement of low-cycle fatigue resistance in TWIP steel by regulating the grain size and distribution, Acta Mater. 134 (2017) 128-142.

[33] T. Zhai, A.J. Wilkinson, J.W. Martin, A crystallographic mechanism for fatigue crack propagation through grain boundaries, Acta Mater. 48(20) (2000) 4917-4927.

[34] B. Larrouy, P. Villechaise, J. Cormier, O. Berteaux, Grain boundary–slip bands interactions: Impact on the fatigue crack initiation in a polycrystalline forged Ni-based superalloy, Acta Mater. 99 (2015) 325-336.

[35] Lee, I. Robertson, H. Birnbaum, AnIn Situ transmission electron microscope deformation study of the slip transfer mechanisms in metals, Metall. Trans. A 21(9) (1990) 2437-2447.

[36] C. Bowles, D. Broek, On the formation of fatigue striations, Int. J. Fract.Mech. 8(1) (1972) 75-85.

[37] H. Cai, A. McEvily, On striations and fatigue crack growth in 1018 steel, Mater. Sci. Eng. A 314(1-2) (2001) 86-89.

[38] V. Singh, M. Sundararaman, W. Chen, R. Wahi, Low-cycle fatigue behavior of NIMONIC PE16 at room temperature, Metall. Trans. A 22(2) (1991) 499-506.

[39] K. Obrtlík, M. Petrenec, J. Man, J. Polák, K. Hrbáček, Isothermal fatigue behavior of cast superalloy Inconel 792-5A at 23 and 900 C, Journal of materials science 44(12) (2009) 3305-3314.

[40] B. Lerch, V. Gerold, Room temperature deformation mechanisms in Nimonic 80A, Acta Metall. 33(9) (1985) 1709-1716.

[41] B.A. Lerch, N. Jayaraman, S.D. Antolovich, A study of fatigue damage mechanisms in Waspaloy from 25 to 800 C, Materials Science and Engineering 66(2) (1984) 151-166.

[42] F. Organ, M. Gell, The effect of frequency on the elevated temperature fatigue of a nickel-base superalloy, Metallurgical Transactions 2(4) (1971) 943-952.

[43] L. Garimella, P. Liaw, D. Klarstrom, Fatigue behavior in nickel-based superalloys: a literature review, JOM Journal of the Minerals, Metals and Materials Society 49(7) (1997) 67-71.

[44] E. Andrieu, R. Molins, H. Ghonem, A. Pineau, Intergranular crack tip oxidation mechanism in a nickel-based superalloy, Mater. Sci. Eng. A 154(1) (1992) 21-28.

[45] H. Ghonem, D. Zheng, Depth of intergranular oxygen diffusion during environment-dependent fatigue crack growth in alloy 718, Mater. Sci. Eng. A 150(2) (1992) 151-160.

[46] H.S. Kitaguchi, H.Y. Li, H.E. Evans, R.G. Ding, I.P. Jones, G. Baxter, P. Bowen, Oxidation ahead of a crack tip in an advanced Ni-based superalloy, Acta Mater. 61(6) (2013) 1968-1981.

[47] L. Viskari, M. Hörnqvist, K.L. Moore, Y. Cao, K. Stiller, Intergranular crack tip oxidation in a Ni-base superalloy, Acta Mater. 61(10) (2013) 3630-3639.

[48] P.S. Karamched, A.J. Wilkinson, High resolution electron back-scatter diffraction analysis of thermally and mechanically induced strains near carbide inclusions in a superalloy, Acta Mater. 59(1) (2011) 263-272.

[49] T. Connolley, P.A.S. Reed, M.J. Starink, Short crack initiation and growth at 600 °C in notched specimens of Inconel718, Mater. Sci. Eng. A 340(1–2) (2003) 139-154.

[50] A. Pineau, D.L. McDowell, E.P. Busso, S.D. Antolovich, Failure of metals II: Fatigue, Acta Mater. 107 (2016) 484-507.

[51] M. Calcagnotto, D. Ponge, E. Demir, D. Raabe, Orientation gradients and geometrically necessary dislocations in ultrafine grained dual-phase steels studied by 2D and 3D EBSD, Mater. Sci. Eng. A 527(10) (2010) 2738-2746.

[52] P. Kontis, E. Alabort, D. Barba, D.M. Collins, A.J. Wilkinson, R.C. Reed, On the role of boron on improving ductility in a new polycrystalline superalloy, Acta Mater. 124 (2017) 489-500.

[53] P. Kontis, D.M. Collins, A.J. Wilkinson, R.C. Reed, D. Raabe, B. Gault, Microstructural degradation of polycrystalline superalloys from oxidized carbides and implications on crack initiation, Scr. Mater. 147 (2018) 59-63.

[54] M. Coleman, H. Alshehri, R. Banik, W. Harrison, S. Birosca, Deformation mechanisms of IN713C nickel-based superalloy during Small Punch Testing, Mater. Sci. Eng. A 650 (2016) 422-431.

[55] S. Birosca, F. Di Gioacchino, S. Stekovic, M. Hardy, A quantitative approach to study the effect of local texture and heterogeneous plastic strain on the deformation micro-mechanism in RR1000 nickel-based superalloy, Acta Mater. 74 (2014) 110-124.

[56] J. Nye, Some geometrical relations in dislocated crystals, Acta Metall. 1(2) (1953) 153-162.

[57] M. Ashby, The deformation of plastically non-homogeneous materials, Philos. Mag. 21(170) (1970) 399-424.

[58] M. Calcagnotto, D. Ponge, E. Demir, D. Raabe, Orientation gradients and geometrically necessary dislocations in ultrafine grained dual-phase steels studied by 2D and 3D EBSD, Mater. Sci. Eng. A 527(10) (2010) 2738-2746.

[59] J. Jiang, J. Yang, T. Zhang, F.P.E. Dunne, T.B. Britton, On the mechanistic basis of fatigue crack nucleation in Ni superalloy containing inclusions using high resolution electron backscatter diffraction, Acta Mater. 97 (2015) 367-379.

[60] J. Jiang, J. Yang, T. Zhang, J. Zou, Y. Wang, F.P.E. Dunne, T.B. Britton, Microstructurally sensitive crack nucleation around inclusions in powder metallurgy nickel-based superalloys, Acta Mater. 117 (2016) 333-344.

[61] M. Herbig, A. King, P. Reischig, H. Proudhon, E.M. Lauridsen, J. Marrow, J.-Y. Buffière, W. Ludwig, 3-D growth of a short fatigue crack within a polycrystalline microstructure studied using combined diffraction and phase-contrast X-ray tomography, Acta Mater. 59(2) (2011) 590-601.

[62] S. Zaefferer, S.I. Wright, D. Raabe, Three-Dimensional Orientation Microscopy in a Focused Ion Beam–Scanning Electron Microscope: A New Dimension of Microstructure Characterization, Metallurgical and Materials Transactions A 39(2) (2008) 374-389.

[63] H. Pirgazi, S. Ghodrat, L.A.I. Kestens, Three-dimensional EBSD characterization of thermo-mechanical fatigue crack morphology in compacted graphite iron, Mater. Charact. 90 (2014) 13-20.

[64] C. Laird, G. Smith, Crack propagation in high stress fatigue, Philos. Mag. 7(77) (1962) 847-857.

[65] C. Laird, The influence of metallurgical structure on the mechanisms of fatigue crack propagation, Fatigue crack propagation, ASTM International 1967.

[66] S. Pattnaik, D.B. Karunakar, P.K. Jha, Developments in investment casting process—A review, J. Mater. Process. Technol. 212(11) (2012) 2332-2348.

[67] J. Hunt, Steady state columnar and equiaxed growth of dendrites and eutectic, Materials science and engineering 65(1) (1984) 75-83.

[68] T. Pollock, W. Murphy, E. Goldman, D. Uram, J. Tu, Grain defect formation during directional solidification of nickel base single crystals, Superalloys 1992 (1992) 125-134.

[69] W. Kurz, D.J. Fisher, Fundamentals of solidification, trans tech publications Aedermannsdorf, Switzerland,1986.

[70] J. Campbell, Castings, Elsevier2003.

[71] O. Dogan, Columnar to equiaxed transition in high Cr white iron castings, Scr. Mater. 35(2) (1996).

[72] M. Gäumann, R. Trivedi, W. Kurz, Nucleation ahead of the advancing interface in directional solidification, Mater. Sci. Eng. A 226 (1997) 763-769.

[73] F. Hua, R. Grugel, Direct observation of the columnar to equiaxed zone transition in an undercooled melt, Scr. Mater. 34(4) (1996) 573-577.

[74] W. Kurz, C. Bezencon, M. Gäumann, Columnar to equiaxed transition in solidification processing, Sci. Technol. Adv. Mater. 2(1) (2001) 185.

[75] W. Kurz, B. Giovanola, R. Trivedi, Theory of microstructural development during rapid solidification, Acta Metall. 34(5) (1986) 823-830.

[76] R.M. Kearsey, J.C. Beddoes, P. Jones, P. Au, Compositional design considerations for microsegregation in single crystal superalloy systems, Intermetallics 12(7–9) (2004) 903-910.

[77] H.B. Dong, P.D. Lee, Simulation of the columnar-to-equiaxed transition in directionally solidified Al–Cu alloys, Acta Mater. 53(3) (2005) 659-668.

[78] M. McLean, Directionally solidified materials for high temperature service, (1983).

[79] H. Weidong, G. Xingguo, Z. Yaohe, Primary spacing selection of constrained dendritic growth, J. Cryst. Growth 134(1-2) (1993) 105-115.

[80] J.A. Warren, J. Langer, Stability of dendritic arrays, Phys. Rev. A 42(6) (1990) 3518.

[81] J. Hunt, S.-Z. Lu, Numerical modeling of cellular/dendritic array growth: spacing and structure predictions, Metallurgical and Materials Transactions A 27(3) (1996) 611-623.

[82] M. Rappaz, C.-A. Gandin, Probabilistic modelling of microstructure formation in solidification processes, Acta Metall. Mater. 41(2) (1993) 345-360.

[83] Y.Z. Zhou, A. Volek, N.R. Green, Mechanism of competitive grain growth in directional solidification of a nickel-base superalloy, Acta Mater. 56(11) (2008) 2631-2637.

[84] A. Bhambri, T. Kattamis, J. Morral, Cast microstructure of Inconel 713C and its dependence on solidification variables, Metall. Trans. B 6(4) (1975) 523-537.

[85] S. Behrouzghaemi, R.J. Mitchell, Morphological changes of γ′ precipitates in superalloy IN738LC at various cooling rates, Mater. Sci. Eng. A 498(1–2) (2008) 266-271.

[86] Y. Zhang, Y. Huang, L. Yang, J. Li, Evolution of microstructures at a wide range of solidification cooling rate in a Ni-based superalloy, J. Alloys Compd. 570 (2013) 70-75.

[87] S. Milenkovic, I. Sabirov, J. Llorca, Effect of the cooling rate on microstructure and hardness of MAR-M247 Ni-based superalloy, Mater. Lett. 73 (2012) 216-219.

[88] M.F. Horstemeyer, N. Yang, K. Gall, D.L. McDowell, J. Fan, P.M. Gullett, High cycle fatigue of a die cast AZ91E-T4 magnesium alloy, Acta Mater. 52(5) (2004) 1327-1336.

Chapter 3: Experimental Procedures

3.1 Materials Used in this Study

This study focuses on the fatigue behaviour and deformation micromechanism of nickel-based superalloy IN713C in the form of wheel blade used in turbocharger and standard fatigue bars in terms of their relationship with microstructures and microtexture. Furthermore, to understand the effects of cooling rate on the microstructure and microtexture, we undertake the solidification experiment to simulate the casting process. The materials, in the form of broken blades or in the form of cast bars which are specially made, are provided by Cummins Turbo Technologies Ltd. and, are made of nickel-based superalloy IN713C. The chemical composition of this alloy is given in Table 2.2.

3.2 Fatigue Test in In-house Testing

Various components failed in in-house testing were received from Cummins Turbo Technologies. Most of the failure were under the two most prominent turbine wheel failure conditions, namely: low cycle fatigue (LCF) and high cycle fatigue (HCF). Below is the description of both fatigue failure conditions.

3.2.1 Real Turbine Wheel Failed under Low Cycle Fatigue (LCF)

Failures associated with lives of less than 10^5 cycles, when the components are subjected to stresses above that of the general yield of the material, are commonly known as LCF failures. LCF failures at Cummins for turbine blades are categorised as initiating from a stress concentration either at the surface or in the bulk of the material. The stress concentration typically arises as a result of casting defects. Casting defects commonly come in the form of gas porosity, shrinkage porosity, oxide defects and shell inclusions. It is these defects that add significantly to the variation in life cycles often observed in the stress vs life (S-N) data of cast components.

The cyclical nature of the centrifugal stresses that the wheel experiences during service is responsible for fatigue crack growth. These centrifugal stresses are amplified above

design limits by the presence of a stress concentration, such as a defect in the material. When the stress concentration at this defect exceeds a critical level, a fatigue crack can initiate and subsequently propagate under the influence of the stress cycles that the wheel is subjected to. Moreover, the cyclic loading of the turbine wheel results from the ever-changing speed of the engine. When the speed of the engine is increased, the mass flow of exhaust gases through the engine and turbine wheel are increased, resulting in an increase in the turbine wheel speed and hence the associated centrifugal stresses. The stresses in the turbine wheel increase as a function of the square of its angular velocity. Constantly varying speed cycles causes varying centrifugal stresses throughout the turbine wheel with the peak stresses occurring in the blade roots as confirmed by FE modelling.The inlet gas temperature is 600 °C and up to 100,000s cycles of damage been applied during testing.

Wheels are tested using a wide speed range and maximum speeds are typically >100 krpm. These speed range represent speed cycles that could occur in service. As for testing cycles, ~3 sec ramp from min to max speed (~6 sec cycle), so completing a test series can take several months. It's estimated that induced centrifugal stresses are generally below yield strength of material and local yielding may occur in specific regions in some designs. After test the failed wheels will be used for failure analysis.

3.2.2 Real Turbine Wheel Failed under High Cycle Fatigue (HCF)

Failures occurring after $\approx 10^5$ cycles, when the components are subject to stresses below that of the general yield of the material, are commonly known as HCF failures. Cummins' definition of HCF for turbine blades were mainly refers to a failure induced through resonance. Each blade on a turbine wheel has a natural frequency determined by the material and geometrical properties of the design. When the wheel spins at speeds that coincide with blade natural frequencies. As a result, excessive strains are produced at certain areas of the blades. Each time the wheel experiences these speeds microstructural damage accumulates at the antinodes.

The blades of the turbine wheel can experience a mode excitation (natural frequency) at several speed orders. The orders are a result of the turbine wheel housing geometry. As the turbine wheel increases in speed it will run through several orders before

reaching the speed limit. The vibration excitation occurs when the modal frequency is intersected by the excitation order.

Certain speed orders are of greater concern to Cummins and these orders can be particularly detrimental to the turbine wheel life when they hit the modal frequencies within the speed range of the turbocharger. For these orders the vibration excitation can result in high stresses in the blades causing the wheel to fail. When a failure of this nature occurs, it is usually identified as a high cycle fatigue (HCF) failure.

In the HCF test, one full turbocharger turbine wheel is tested per session, using a gas stand. The outstanding features in HCF test is that pins are added to the exhaust flow path close to the turbine wheel. These pins cause large pressure variations around the volute. When the blade of a spinning wheel passes through these pressure changes it will experience a 'push-pull' force. When the push-pull forces occur at a rate that matches the resonant frequency of the blade, the blade will accumulate fatigue damage at a very high rate (blade resonant frequency, kHz). Previously, frequency survey test identifies the resonant frequency of the turbine wheel blades. The speed range for the test is chosen so that all blades will experience resonance during a half cycle (min to max speed), i.e. ~6 min ramp from min to max (~12 min per cycle). The total amount of damaging fatigue cycles is unknown, but the speed ramps are counted to give us a base for comparison. The induced strain has not been measured. The inlet gas temperature is also 600 °C. Failure analysis on test wheels confirm that HCF test failures are similar to 'HCF' driven failures in Service.

The example of the in-house test set up for HCF (Fig. 3.1a), an example of failed wheel after in-house LCF test (Fig. 3.1c) and turbine wheel before test (Fig. 3.1b) are shown in Fig. 3.1. More details about the test procedures and received materials after tests can be found in Chapter 4 and Chapter 5.

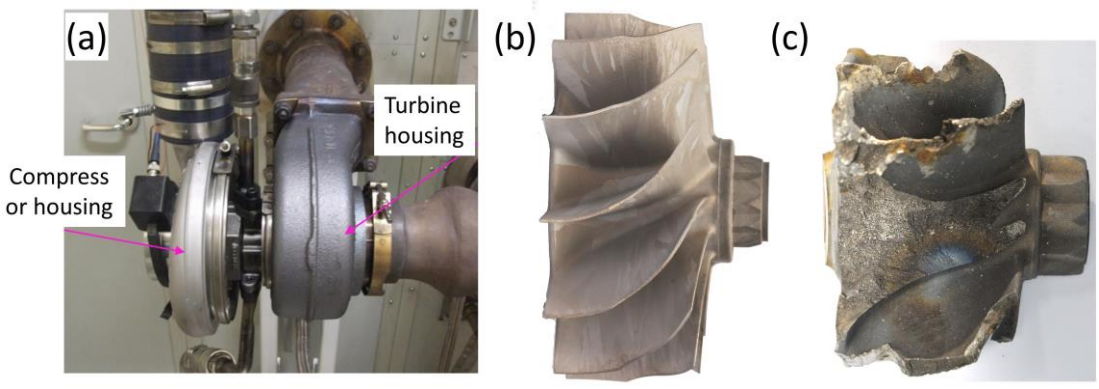

Fig. 3.1 (a) The test set up for in-house HCF; (b) An example of turbine wheel before test and the surface has been etched showing the grain structure; (c) An example of failed wheel blade after in-house LCF test.

3.3 Standard Fatigue Tests

In the casting process for turbocharger turbine blades, complex geometrical configuration leads to local different solidification parameters such as cooling rate, finally resulting disparity of grain structure across the blade, i.e., columnar grain area with large grain size in the most part of blade, equiaxed grain area with small grain size at blade tip and transition area between them (Fig. 2.2c). In order to study the effects of these grain structure on fatigue property, specially designed samples with three grain structure were produced using investment casting. Detailed manufacturing process for the samples can be found in [1]. The representative structures of samples for three grain structure, i.e., transition, equiaxed and columnar, are shown in Fig. 3.2a. The IPFs (Inverse Pole Figures) and ODFs (Orientation Distribution Functions) show no significant texture for each structure. IPF of Transition structure is shown in Fig. 3.2c as an example.

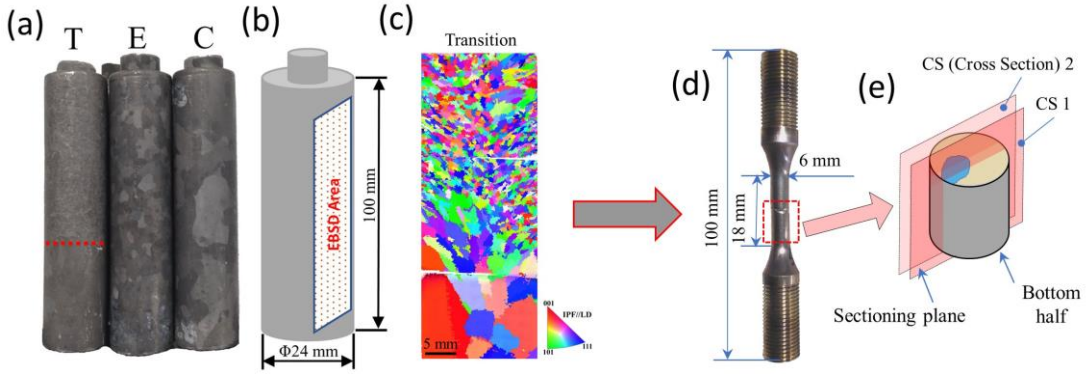

Fig. 3.2 (a) Received bars with three grain structures: transition (T), Equiaxed (E) and Columnar (C); (b) Dimension of the bars; (c) IPF//Y of Transition structure showing the grain structure; (d) Machined bars for fatigue test and its dimension; (e) Schematic illustration of serial sectioning of failed sample

The received casting materials are cylinder bars. The grain structure type (transition, equiaxed or columnar) are determined by the surface appearance as shown in Fig. 3.2a.

The bars with different grain structure was then chosen followed by machining to fatigue specimens. The geometry of the specimens for both LCF and HCF is shown in Fig. 3.2d, with a gauge length of 18 mm and a gauge diameter of 6 mm. The LCF tests were conducted according to ASTM E606 standard and under strain control with maximum strain of 0.4%, and this value is particularly chosen from previous LCF results [1] to balance the expected fatigue life and research purpose of this study. Whilst the HCF tests were conducted according to ASTM E466 standard and under stress control, and the maximum stress values were obtained by tensioning the samples to 0.2% strain and were around 335 MPa for all the samples. The test frequency for LCF and HCF were 0.5 Hz and 30 Hz, respectively. Both kind of tests were conducted at the R-ratio of -1, with sinusoidal waveform and at 650 °C. Only one sample with each microstructure was tested in both LCF and HCF and totally six samples have been tested. After tests, the failed samples are first under fractography investigation and then analysed using serial sectioning technique. The schematic illustration of sectioning process is shown in Fig. 3.2e.

3.4 Solidification Experiment

To simulate and study the effects of cooling rate during solidification on the microstructure (dendritic, grains, carbides and gamma prime), solidification experiment was undertaken with different cooling rate using induction furnace with Ar gas protection. The raw materials were cut from the received bars. The material was first heated up to 1550°C within 15 mins and hold for 15 min, then cooled down with different cooling rate (controlled by heating system) in a crucible ring with the size of Ø12×24 mm. Fig. 3.3 shows the dimension of the crucible ring (Fig. 3.3a) and the temperature evolution during cooling for four cooling rate (Fig. 3.3b and c): 4°C/s (AC, Air Cooling), 2.8 °C/s (2C), 1.2 °C/s (3C) and 0.3 °C/s (4C). Afterwards, the solidified sample were cut through the longitudinal direction (solidification direction). The cross-section surface was then mounted, grinded and polished and further for harness test and EBSD scanning.

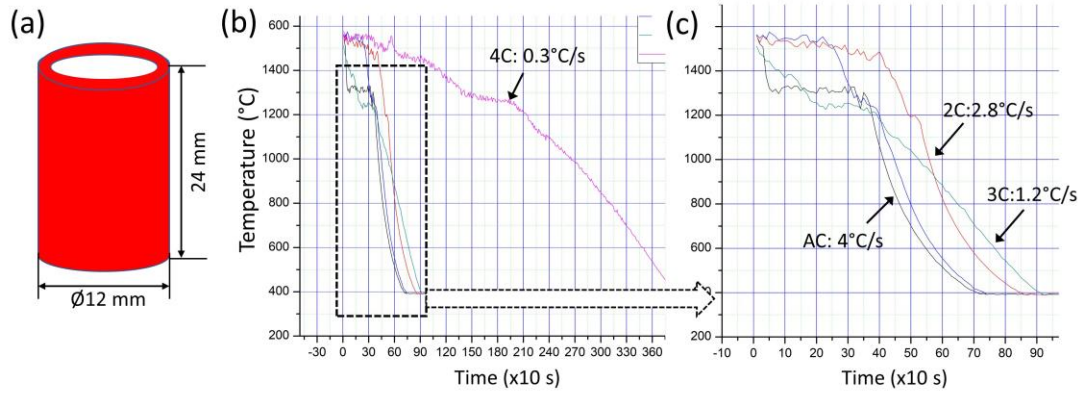

Fig. 3.3 (a) Dimension of the crucible cylinder ring for solidification; (b) Temperature versus time during cooling and (c) cooling rate of enlarged area in the black box in (b). Four different cooling rates are averaged and superimposed in the figure: 4°C/s (AC, Air Cooling), 2.8 °C/s (2C), 1.2 °C/s (3C) and 0.3 °C/s (4C).

3.5 Micro-analytical techniques

Various characterisation techniques were used to investigate the fracture surface, microstructure and microtexture of the tested (or failed) samples for different research purposes. These include optical microscope (OP), scanning electron microscope (SEM), electron backscatter diffraction (EBSD) and transmission electron microscope (TEM) based at AIM (Advanced Imaging of Materials) in Swansea Univeristy.

3.5.1 Optical Microscopy

The preparation of samples for observation using optical microscopy or SEM routinely consist of grinding and polishing, after mounting in conductive phenolic compound. The grinding disc used here is MD-Piano, which is a diamond disc for grinding materials of HV> 150. It is available in variety of grades. After grinding on MD-Piano, the finish is comparable to that obtained using SiC-paper with the same respective grit size, *i.e.* grinding on MD-Piano 120 is comparable to grinding on SiC-paper #120. After the grinding process of MD-Piano 4000, polishing process is carried on with diamond polishing compound of 1 micron. Afterwards, if need to do EBSD scanning, further polishing will be made with non-crystallizing colloidal silica polishing suspension of

0.04 micron. For optical microscopy and SEM image observation, it is better to etch the sample to observe the grain structure, second phase such as particles and carbides, cracks and precipitates (γ′). Both chemical etching and electric etching are used. The chemical etching solution of Kalling's No.2 (5 g of $CuCl_2$ per 100 mL of HCl and 100 mL of C_2H_6O) is used to remove γ' precipitate. The electric etching solution of 10% phosphoric acid (H_3PO_4 +H_2O) is used to remove γ matrix.

Optical microscopy was initially used to study the macrostructure as well as microstructure and sometimes was used as marking tools for SEM observations. Initial investigation of any failed specimen is conducted by means of non-destructive means (optical and electronic microscopy). It is important that a record is made of the as-failed specimen as secondary investigation requires preparation methods such as sectioning which may disturb or contaminate the fractured surface.

3.5.2 Scanning Electron Microscope (SEM)

SEM is the major tool used in the present research to observe the microstructure of materials. There are two types of SEM equipment available in AIM in Swansea University. One is Zeiss-EVO which fits large size specimen and mainly used to observe the fracture surface of failed turbine blades or bar samples. The other one is JEOL 7800 field emission SEM, which possesses the very high resolution both for image and EBSD. Both machines are equipped with EDS and EBSD detectors. The JEOL mainly is used to do high resolution microstructure characterisation such as γ′ morphology and distribution, high resolution chemical composition distribution and high resolution EBSD (HR-EBSD). The voltage used for imaging usually range from 10KV to 20KV, with working distance of 6mm to 15 mm.

3.5.3 Electron Backscatter Diffraction (EBSD)

Electron backscatter diffraction (EBSD) is a technique which is combined with SEM to provide quantitative microstructural information about the crystallographic nature of materials. Available information from traditional EBSD techniques also includes grain size distribution, Schmid factors, variations (gradients) in lattice orientation, and GB

misorientations. EBSD patterns are collected in a SEM. As the electron beam is held in one spot, high energy, back-scattered electrons diffract on their way back out of the sample. The resulting back scattered diffraction pattern is collected using a CCD (charge coupled device) camera and stored electronically. This process is illustrated in Fig. 3.4.

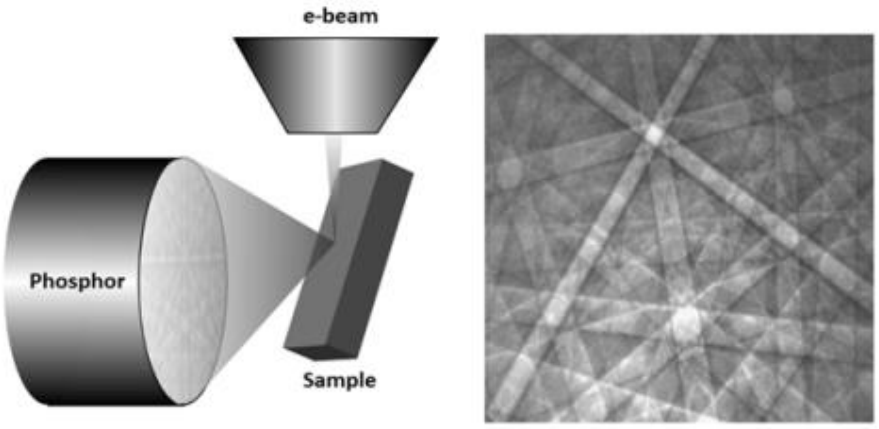

Fig. 3.4: Schematic of EBSD microscope set-up (left) and an example of an EBSD pattern from a silicon sample (right).

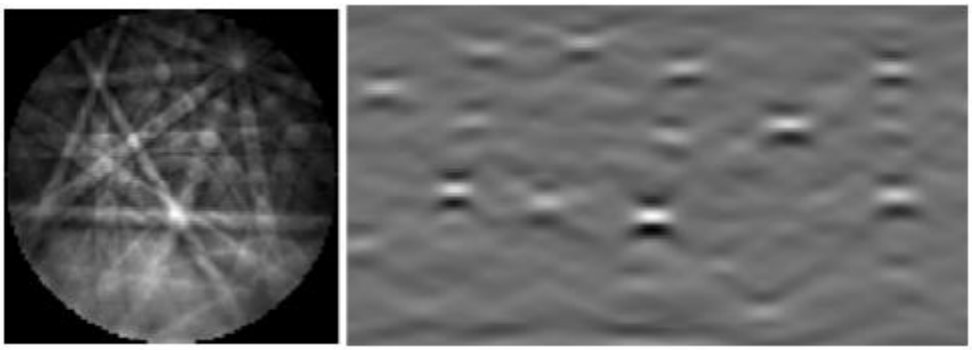

Fig. 3.5 An EBSD pattern (left) and its corresponding Hough transform map (right). Each peak in the Hough transform corresponds to a band in the EBSD pattern.

These techniques employ the Hough transform as a computer vision technique to accurately index (determine the orientation of) these patterns. A number of alternate indexing methods have also been developed, but the original, Hough-based techniques dominate the commercial market for EBSD indexing software.

The Hough transform is an integral transform that works by taking a line integral across an image. Each point on the Hough transform represents the line integral across the

original image at a certain angle and intersect. Thus, the distinctive band patterns on EBSD patterns show up as peaks on the Hough transform map. An EBSD pattern and its Hough transform are shown in Figure 3.5. Each band corresponds to a diffracting plane in the investigated lattice, and once precisely located, several bands may be used to determine the orientation of the lattice to within about a half a degree. This information may be used to approximate a distortion gradient. This distortion gradient may then be used to resolve dislocation content.

Crystallographic information about fatigue behaviour can be measured in nickel-based superalloy using modern EBSD techniques. EBSD provides the ability to extract a myriad of metrics for input into a machine learning framework. Additionally, in recent years high resolution EBSD (HR-EBSD) techniques have been developed to extract even more information from the collected EBSD data.

3.5.4 TEM

The phase identification and dislocation density close to initiation sites and beneath fatigue striations are also studied using FIB-TEM and STEM-HAADF (Scanning Transmission Electron Microscope-High Angle Annular Dark Field) with FEI Talos 200F. The TEM specimen beneath striation was used FIB lift-out technique. Other TEM specimens close to initiation sites were first cut out as thin plate along loading direction and then grinded and polished to 100 μm in thickness. After punching into 3 mm diameter foils, they were further polished to 50 μm, followed by twin-jet electronic polishing (Struers Tenupol III). An electrolyte of 10 vol.% perchloric acid in methanol was used at -20 ºC and 20 V.

Literature

[1] J.S. Cantó, S. Winwood, K. Rhodes, S. Birosca, A Study of Low Cycle Fatigue Life and its correlation with Microstructural Parameters in IN713C Nickel Based Superalloy, Mater. Sci. Eng. A (2018).

Chapter 4: Fracture Surface Investigation of Failed Wheel Blades during Cummins In-house Testing

4.1 Introduction

The turbine wheel blades in turbocharger failed in service generally either due to centrifugal stress or vibration, which has been introduced in Chapter 3. For simplicity and convenience, the former fatigue mode is termed 'LCF' and the latter 'HCF (VHCF)'. The presence of a small stress concentration, such as shrinkage porosity, coincident with a location of high HCF stress can increase the likelihood of HCF failure, so it is not uncommon to have a HCF failure initiating from an inclusion. In general, when a larger inclusion type defect is found to be the initiator of a failure, it is often difficult to conclude whether or not it is classed as HCF or LCF, as HCF type failures will preferentially initiate at a defect if it happens to be in a region of high vibration induced stress. In some cases, HCF can be indicated by a shorter life and an initiator located at certain 'islands' on the blade where the high vibrational stresses are known to occur. LCF can be distinguishable by a longer life and an initiator located toward the blade root, where the centrifugal stresses are higher. When there are features of both failure mechanisms within one fracture it is often difficult to accurately label the failure mode and it may be misdiagnosed upon entry into the Service Database of Cummins Turbo Techologies. Therefore, one of the aim of current study is to investigate the fracture surface and failure microstructure characteristics of High Cycle Fatigue (HCF) and Low Cycle Fatigue (LCF) failed wheels during in-house durability tests. The objective is to reliably distinguish the turbocharge wheels that failed in service under LCF and HCF loading conditions.

4.2 Experimental Procedure

All the tests including LCF and HCF tests were conducted in Cummins Turbo technologies. The details of the Cummins in-house LCF and HCF tests are reported Section 3.2.1 and Section 3.2.2, respectively.

4.3 Results

13 pieces of fractured blades were received without labelling or classification as whether LCF or HCF failed specimen by Cummins Turbo Technologies in Huddersfield. At the early stage of the analyses, the observation and thereafter classification of the features are purely based on observation itself in a 'black box' way, without any other testing information about these fracture samples. This information was later informed and can be found in Chapter 3 and Chapter 5. Therefore, this fractographic study is only the summary and classification of fracture surface features based on pure observation by utilising optical microscope and SEM. At the end of complete analyse the results was reported to Cummins to be compare to their analyses. It is concluded that there were 9 pieces failed during HCF loading and 4 during LCF loading condition. The test classification (LCF or HCF type) is Swansea University was matched 90% of the Cummins classifications. This was an indication that the recognised LCF and HCF fracture surface features are characteristics and unique for specific loading condition. The loading conditions are reported in Section 3.2. It should be noted that the complete fracture mechanism and deformation mechanism will be discussed for the same samples in Chapter 5. Here, major differences in fracture surface between HCF and LCF are listed as following:

1. The macroscopic images of turbine wheel and failed blades (6 out of 9 blades from HCF, and 4 blades from LCF, 9 blades from HCF are labelled as H1, H2…etc., and LCF samples as L1, L2…etc.) are shown in Fig. 4.1. The figure shows that most of failure sites in HCF are at upper position of the blades while nearly all the failure sites in LCF are at the root position of the blades.

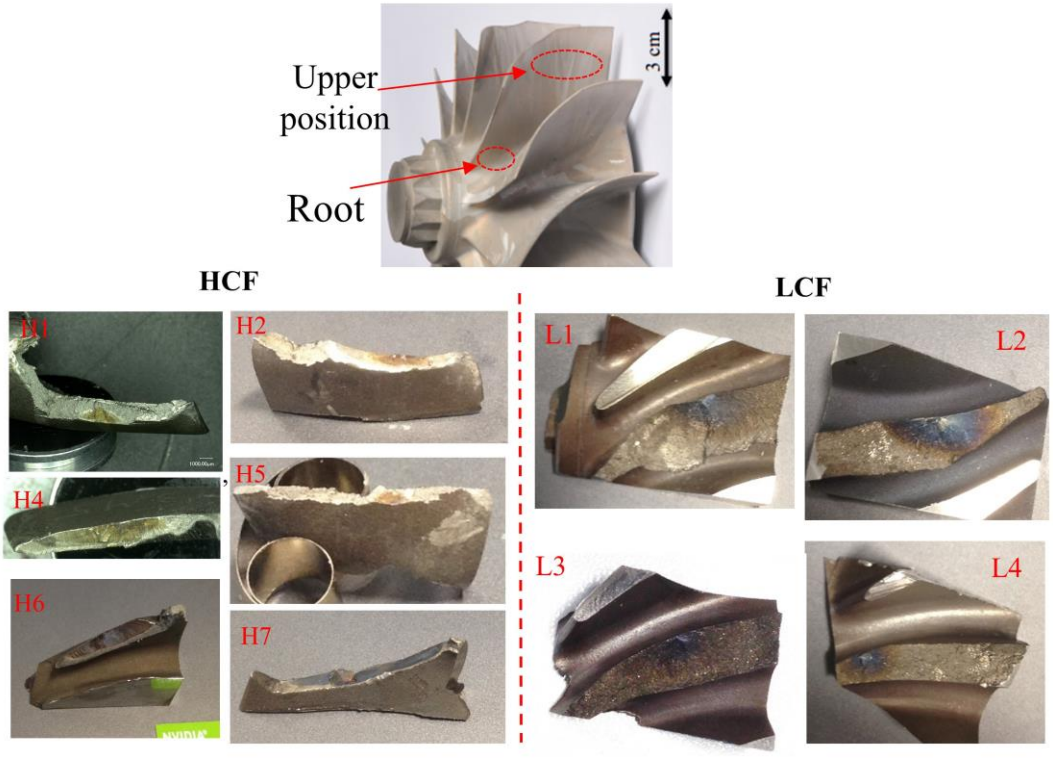

Fig. 4.1 Macroscopic images of turbine wheel and failed blades. It shows turbine wheel (blades) image before loading, 6 of 9 failed blades in HCF and all 4 failed blades in LCF. The upper position and root position of the blades are indicated, and the sample numbers are superimposed on the figure. ('H' stands for 'HCF' and 'L' stands for 'LCF', samples from LCF are labelled as L1, L2…etc., and samples from HCF are labelled as H1, H2…etc.)

2. Macroscopically, the major difference of fracture surface is that in propagation areas (stage II of fatigue fracture), HCF samples show evident beach marks or clam shells, usually with a large crack propagation area according to colour contrast in OM or SEM. While in LCF samples these marks can hardly be seen. Fig. 4.2 shows all the fracture surface from HCF samples by OP, some beach marks are indicated in the figures. Some beach barks or large striations in the rectangular area on the left are magnified in the SEM images on the right side. Fracture surface imaged by the OP for LCF failed blades are shown in Fig. 4.3, exhibiting the abrupt crack propagation process and rough fracture surface.

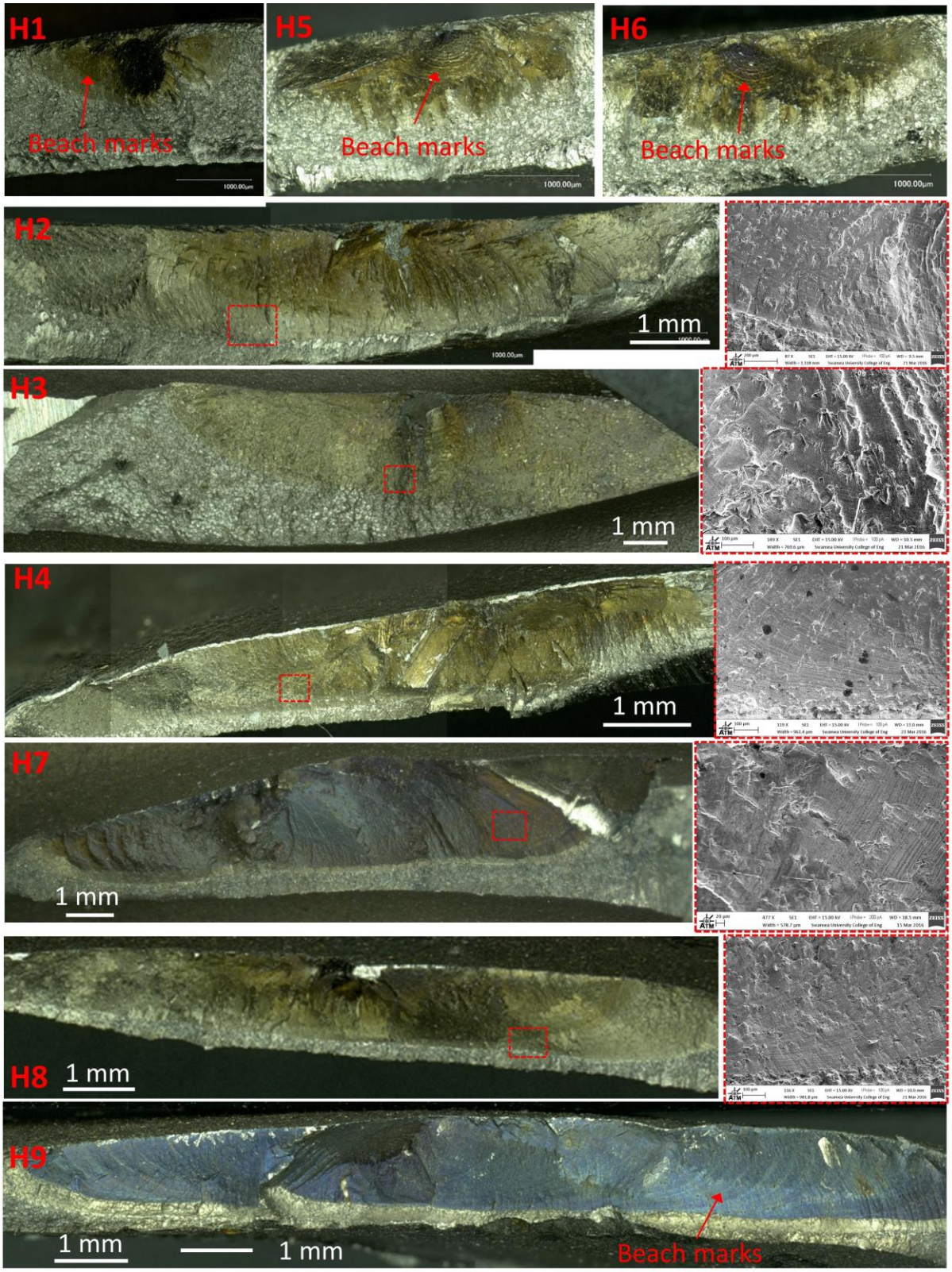

Fig. 4.2 Optical images of fracture surface in all 9 HCF failed blades, showing the beach marks on the surface and usually large crack propagation areas. Some SEM images on the right are the magnified images of red rectangular areas on the left, showing the beach marks or striations.

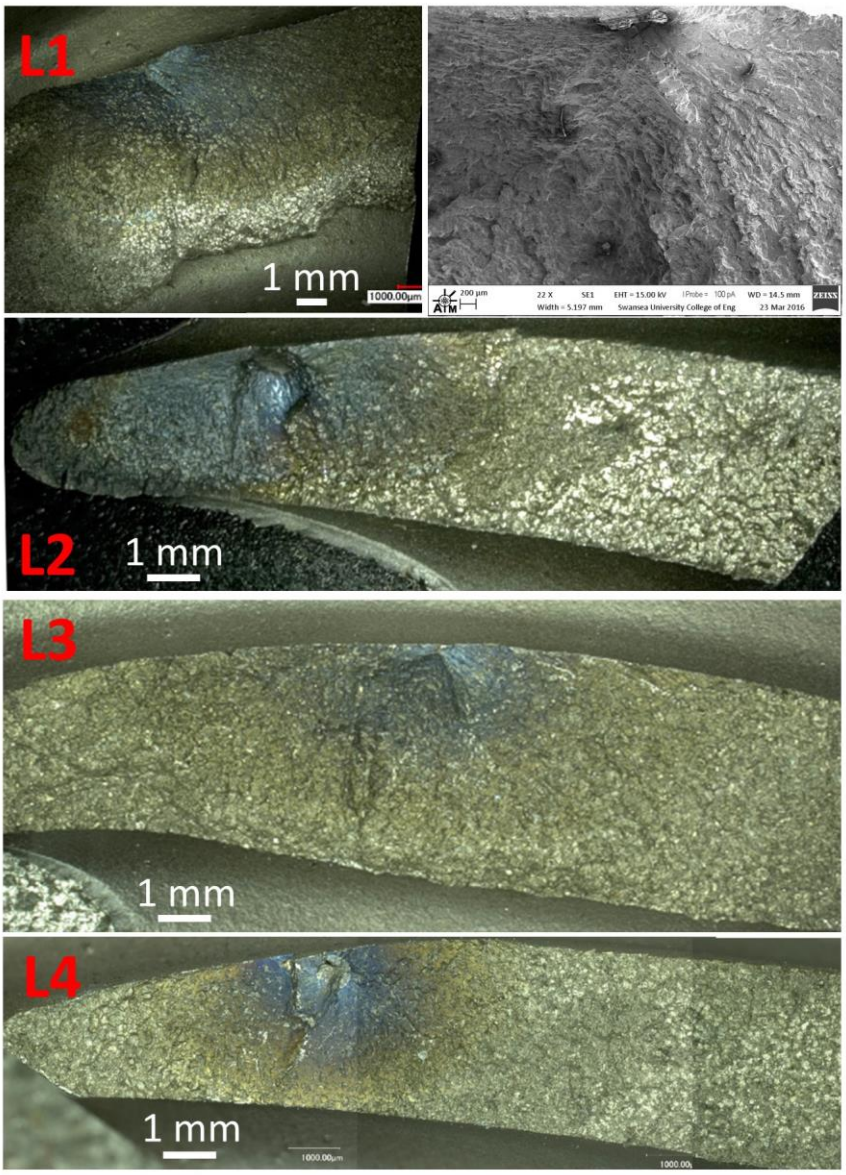

Fig. 4.3 Optical images of fracture surface in all 4 LCF failed blades, showing the small crack propagation areas rough surface. A low magnification SEM for L1 is also listed.

3. In the stage I of fatigue, *i.e.* initiation of fracture, HCF samples usually have brittle appearance of cleavage fractures (except H2) which is usually termed ‘facet’, while no such feature can be found in LCF failed samples. Fig. 4.4 shows all the facets in 8 HCF samples. The facet either initiated on the casting defects (most of them are porosities) such as in H1, H2 and H4, or on the blade outside surface such as in H5 and H6. Initiation sites from LCF failed samples are shown in Fig. 4.5, and no such facet feature can be observed, and it is hard to identify the exact initiation causes in some cases.

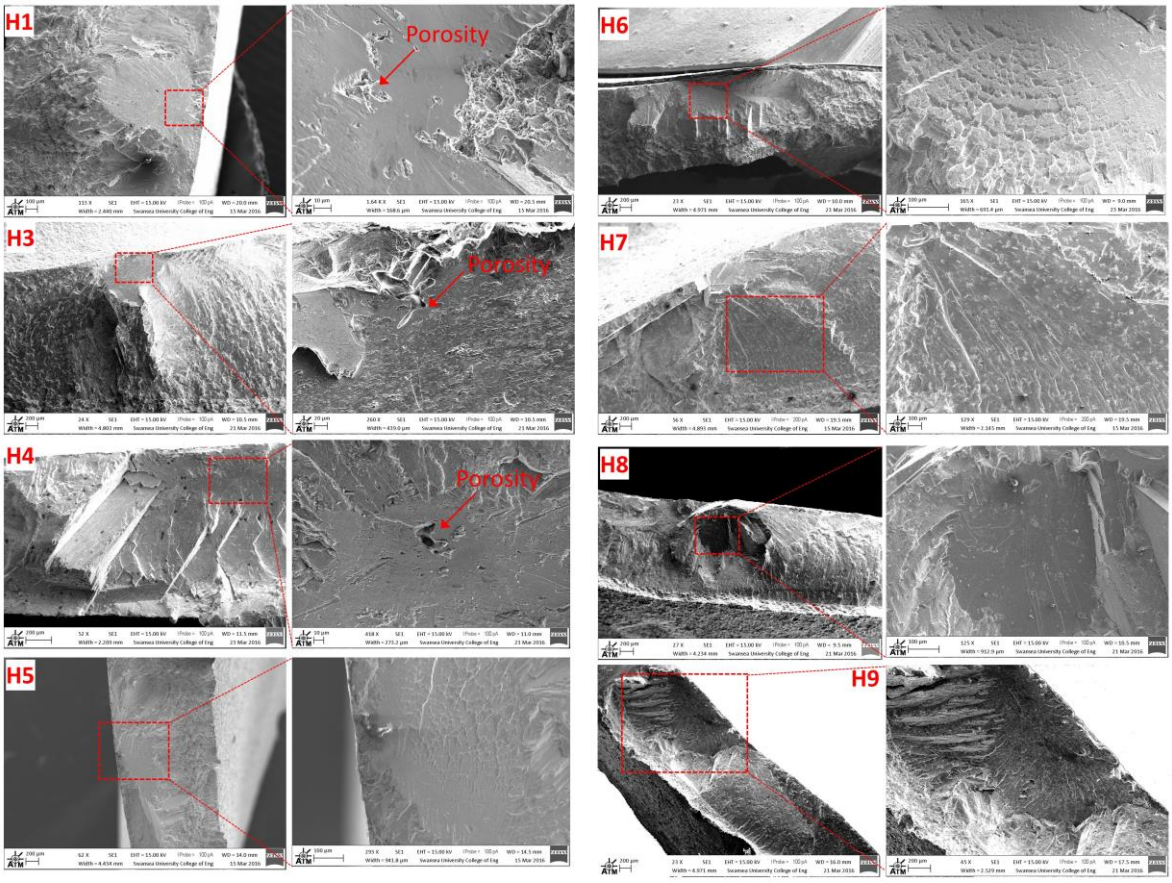

Fig. 4.4 Facet and crack initiation site (usually porosity) in HCF samples.

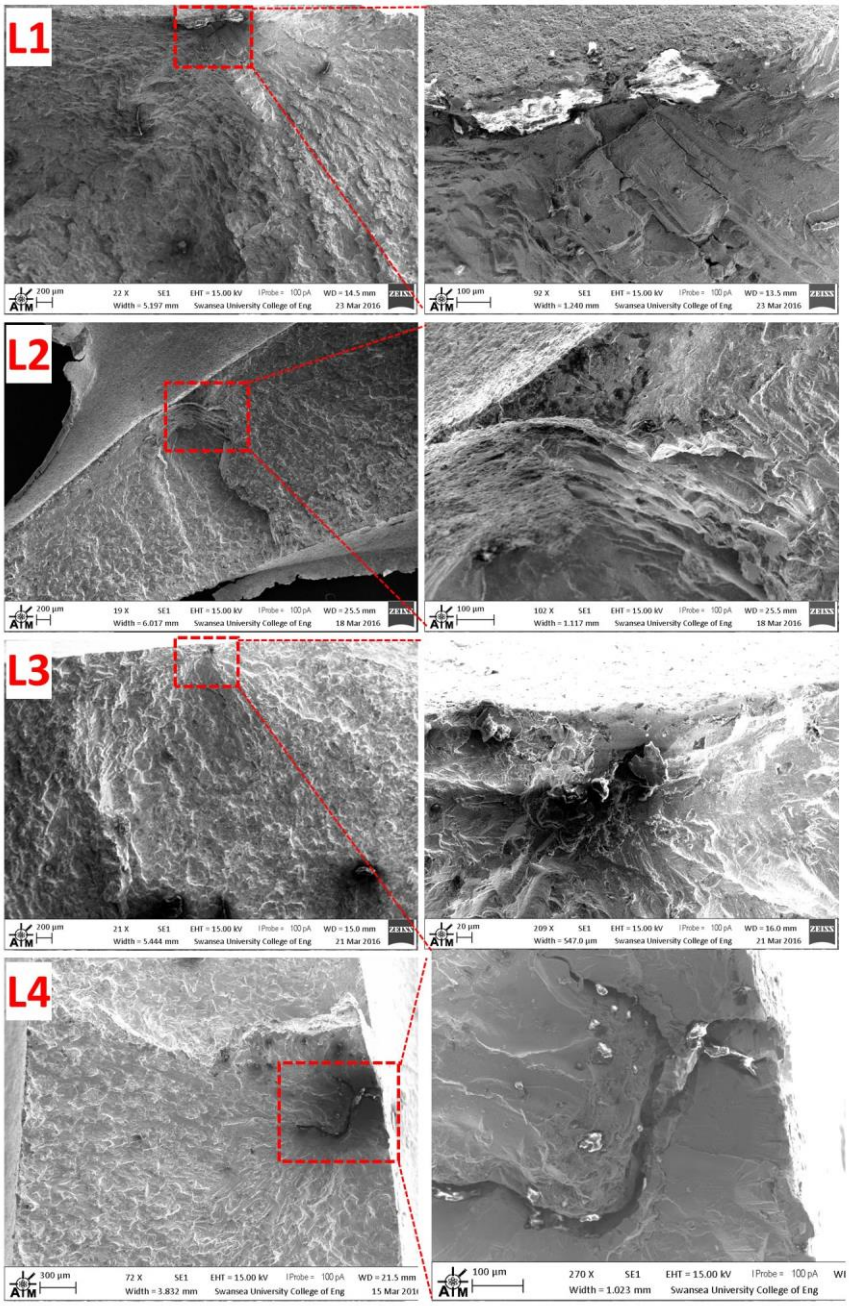

Fig. 4.5 Crack initiation sites in LCF samples (The white spots in L1 and L4 are contaminations).

4. The most significant difference is the morphology and distribution of fatigue striations. Striation, as a unique feature of fatigue deformation can be observed in both LCF and HCF. However, at the stage II, HCF samples usually show continuous well-defined striations, especially at the end of stage II propagation areas, In the contrast, there is no such continuous striations in LCF samples, only local and sometime vague striations can be found. Fig. 4.6 exhibits the

representative striations in all the HCF samples. The rough locations of these striation are shown in the left and well-defined striations are shown in the right after two times of magnification. They have slightly different morphologies but well-defined and are easy to identify. Instead, local striations (L3) and faint striations (L1) can be observed in LCF samples, which is shown in Fig. 4.7.

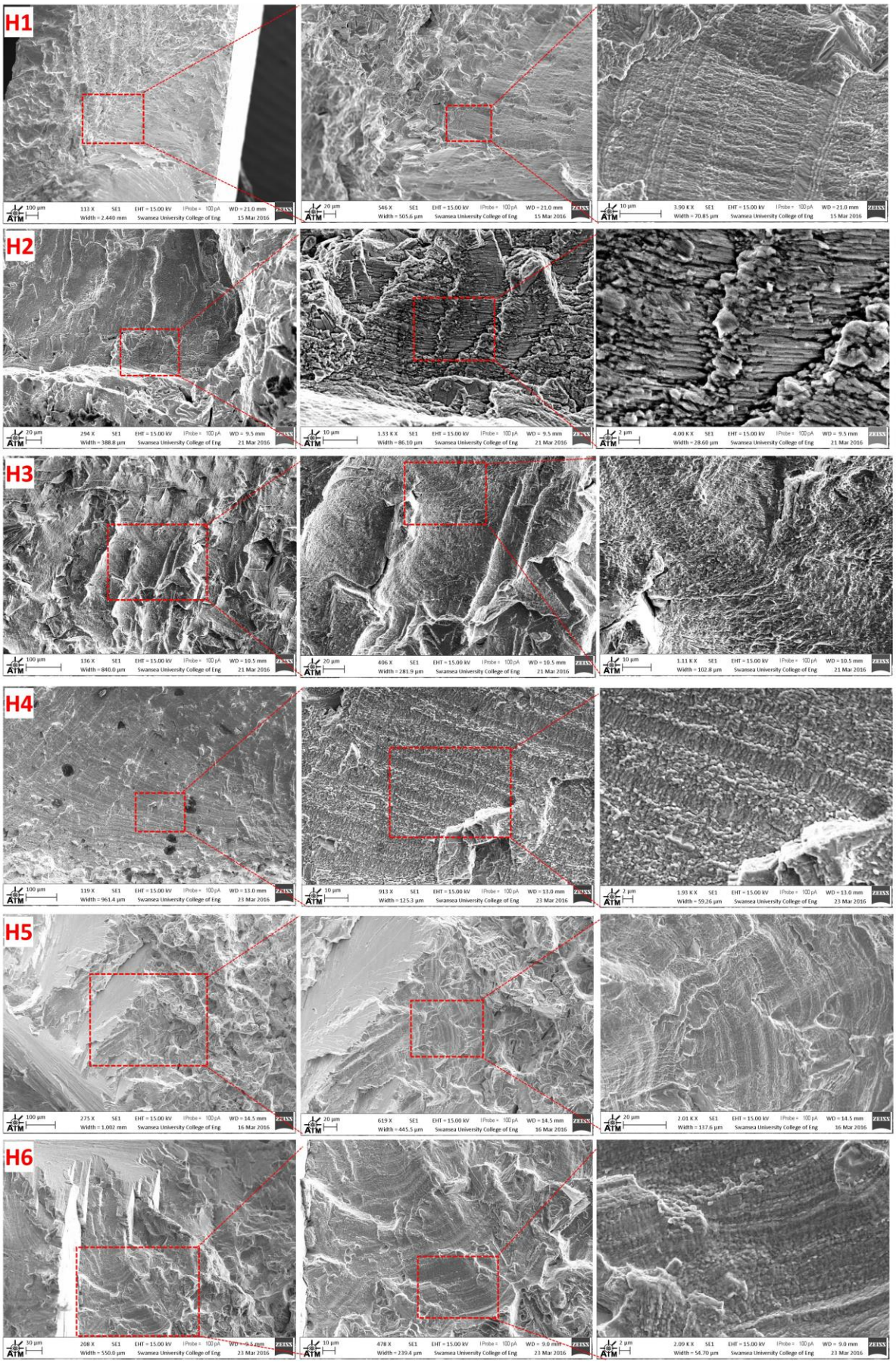
H1
H2
H3
H4
H5
H6

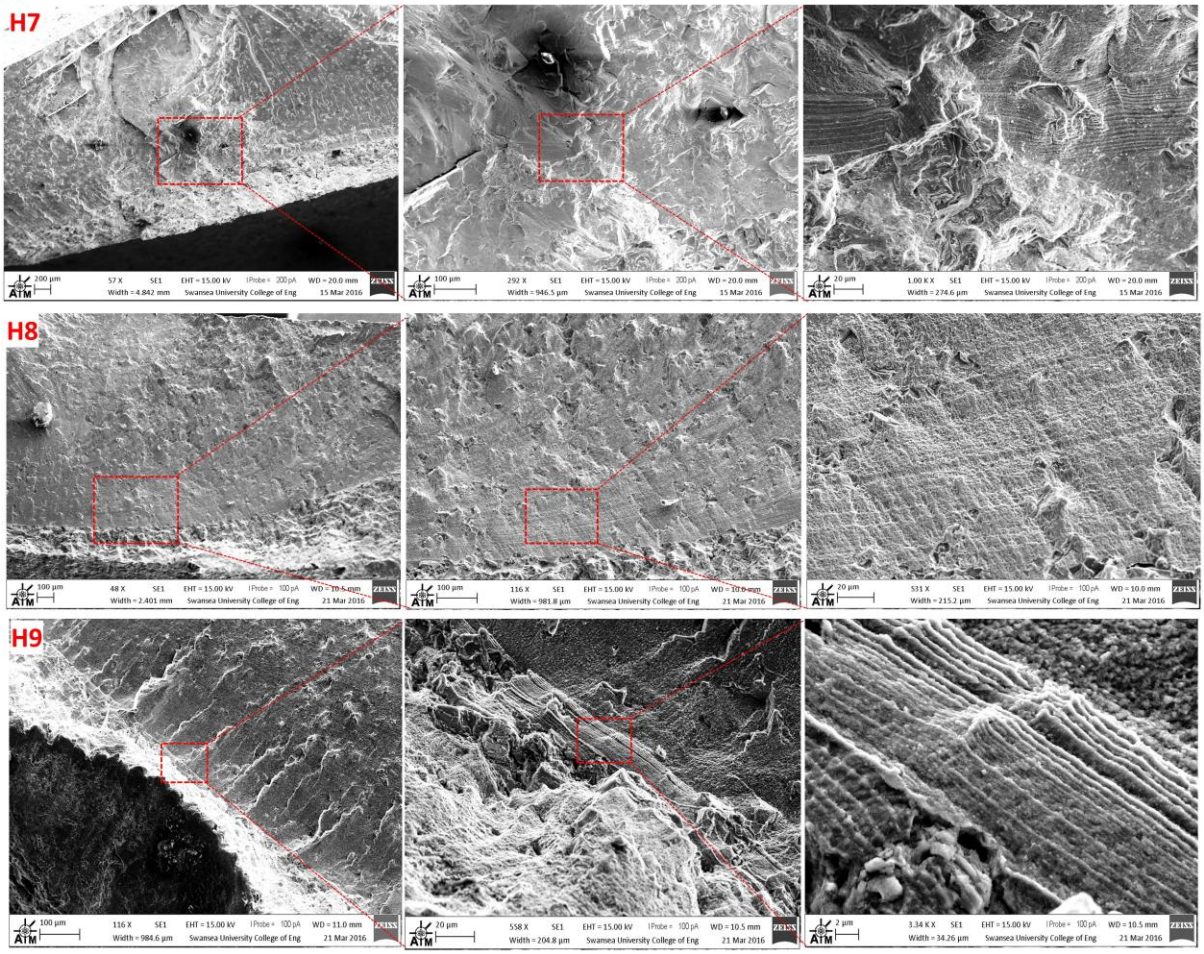

Fig. 4.6 Representative long continuous fatigue striations in HCF samples.

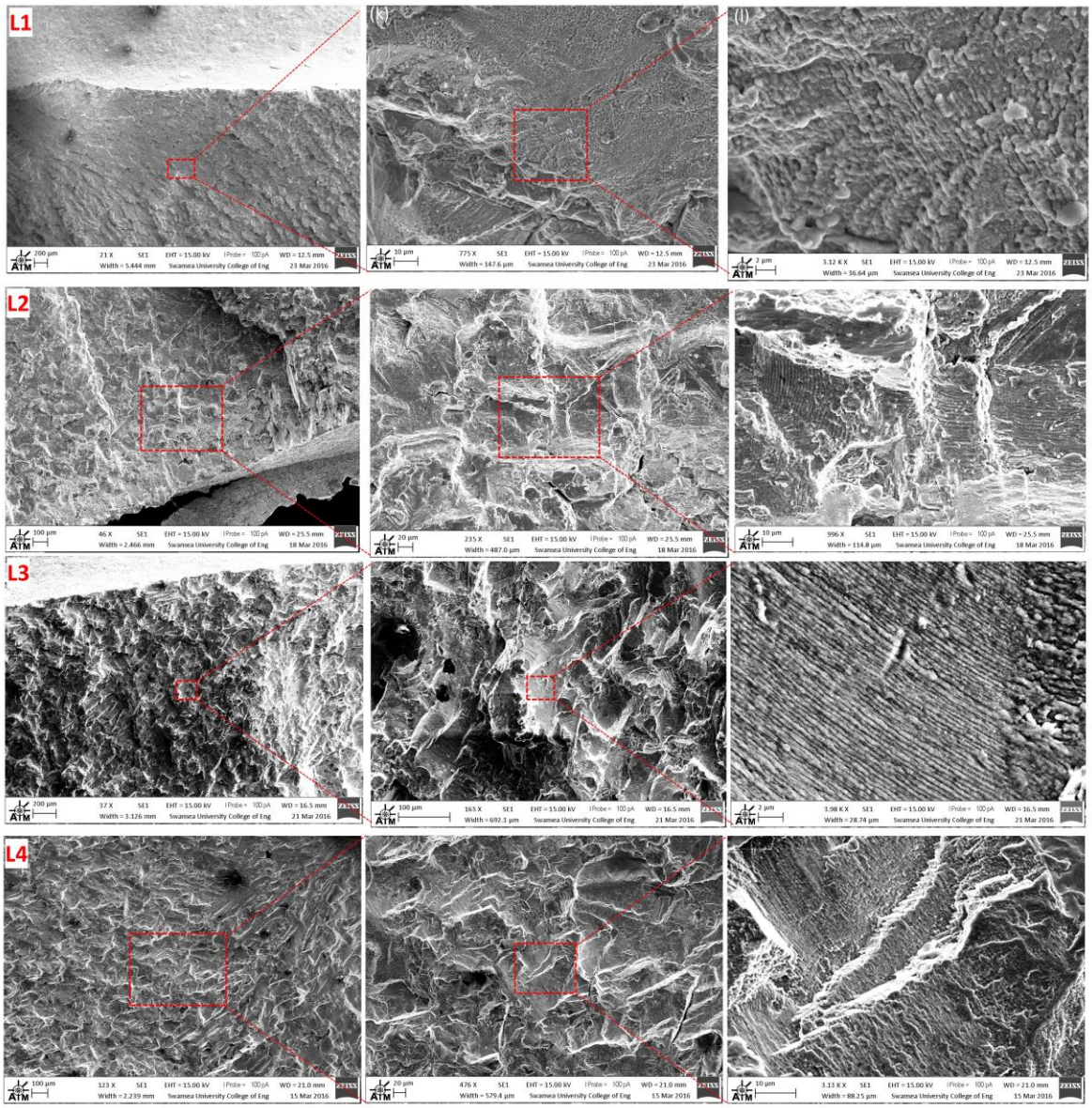

Fig. 4.7 Representative local, weak fatigue striations in LCF samples.

5. Because the propagation area (stage II) in HCF is macroscopically and/or microscopically flat and smooth, there is usually a distinctive transition between propagation area and rough final catastrophic fracture area (overload stage or stage III), while in LCF samples, as the propagation area is restricted and rough or rugged, the transition between stage II and stage III is not obvious. Fig. 4.8 gives three examples of HCF and two examples of LCF to exemplify this difference.

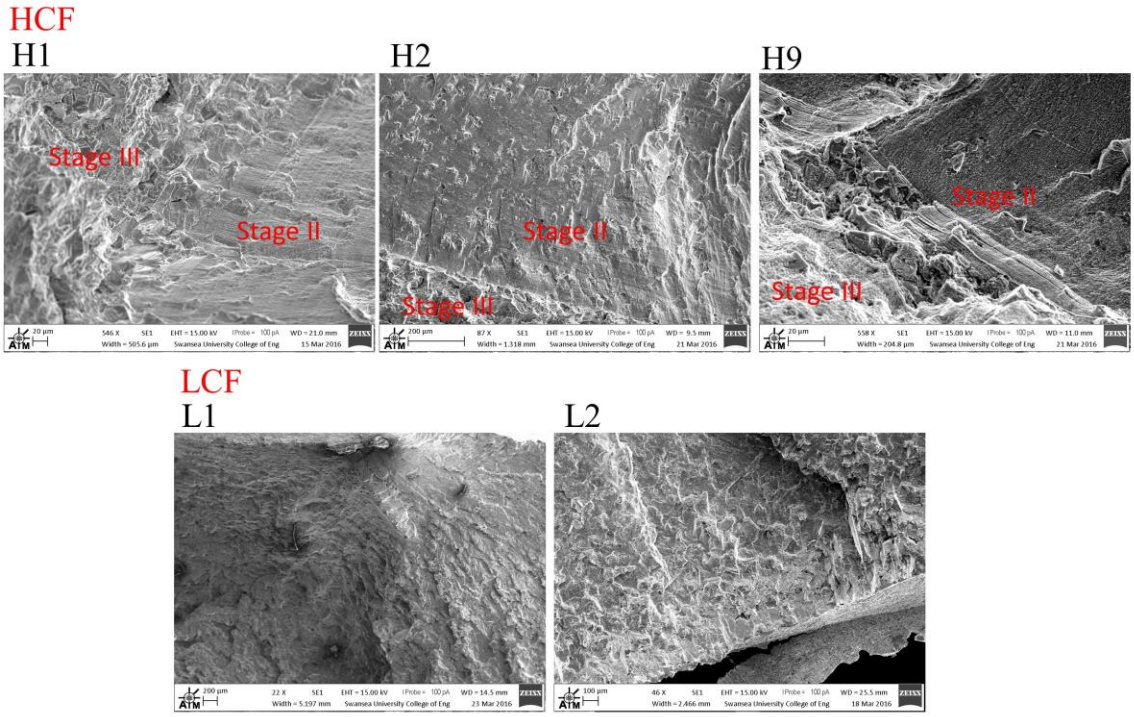

Fig. 4.8 Transition areas between crack propagation stage and final overload stage in representative HCF and LCF samples.

6. In the early stage of LCF, dendrite structure and lots of secondary cracks can be observed, showing a strong microstructure sensitiveness. While this feature is not identified in HCF samples. Fig. 4.9 show two examples from LCF samples (L1 and L2).

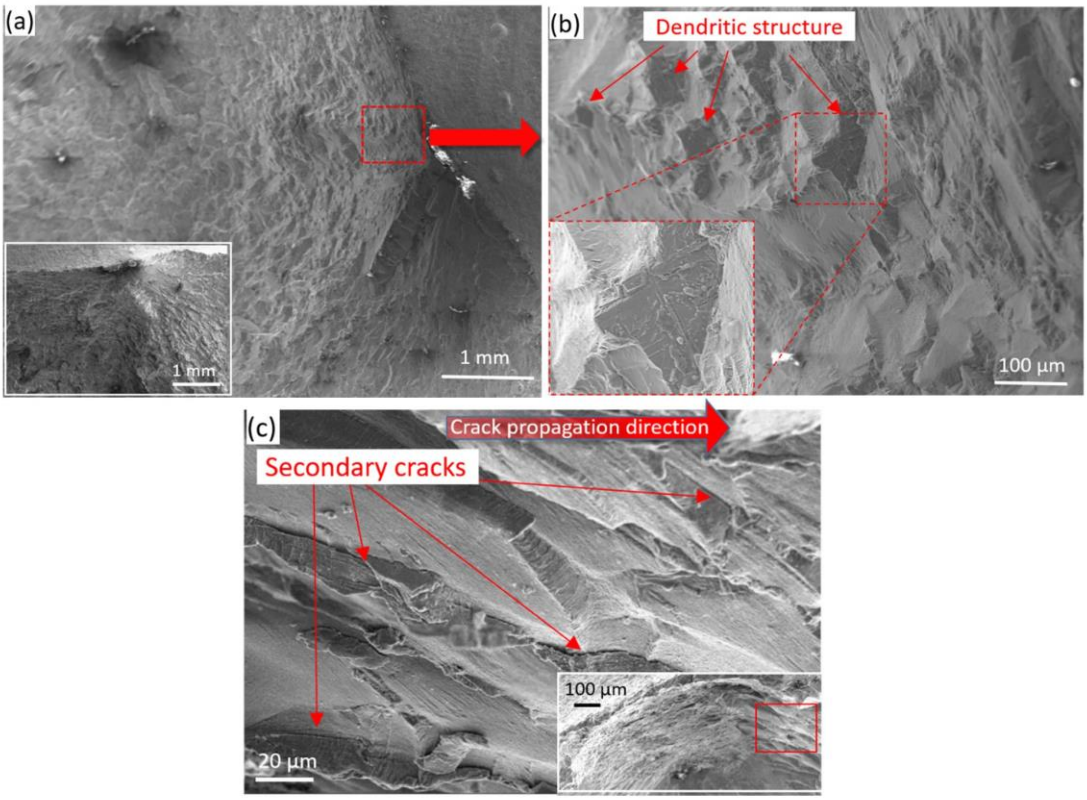

Fig. 4.9 Dendrite structure and secondary cracks in LCF samples: (a, b) L1 and (c) L2.

4.4 Conclusion

Based on these differences in fracture surface features, a step by step guideline has been formed to distinguish the fracture mode of failed blades in the service, as shown in Fig, 4.10. The samples failed during LCF and HCF can be differentiated using the guidelines obtained from optical and SEM observations. For instance, the basic observation by means of optical microscope is as follow: the location of the failure is critical. Observing the failure close to blade root is an indication of LCF occurrence. While failure site at the middle or tip of the blade probably indicates HCF failure mode. Similarly, if the crack initiate from the blade surface, it is highly chance to be LCF mode; whilst the crack initiate from the bulk of blade, it probably belongs to HCF failure mode. If there is a big facet on the fracture surface, the crack can be classified as HCF failure mode for sure, as faceting is the unique feature of HCF mode. Another feature that can be relatively easily observed by optical microscope is beach mark which is the indication of HCF failure mode. By means of SEM, if long continuous striations can be observed, the crack should be caused by HCF mode. Furthermore, if dendrite

structure or secondary cracks can be observed close to initiation sites, the crack are most likely caused by LCF failure mode. Because HCF cracks are usually initiated from porosities, if in SEM, porosities can be detected in initiation sites, the cracks probably belong to HCF failure mode.

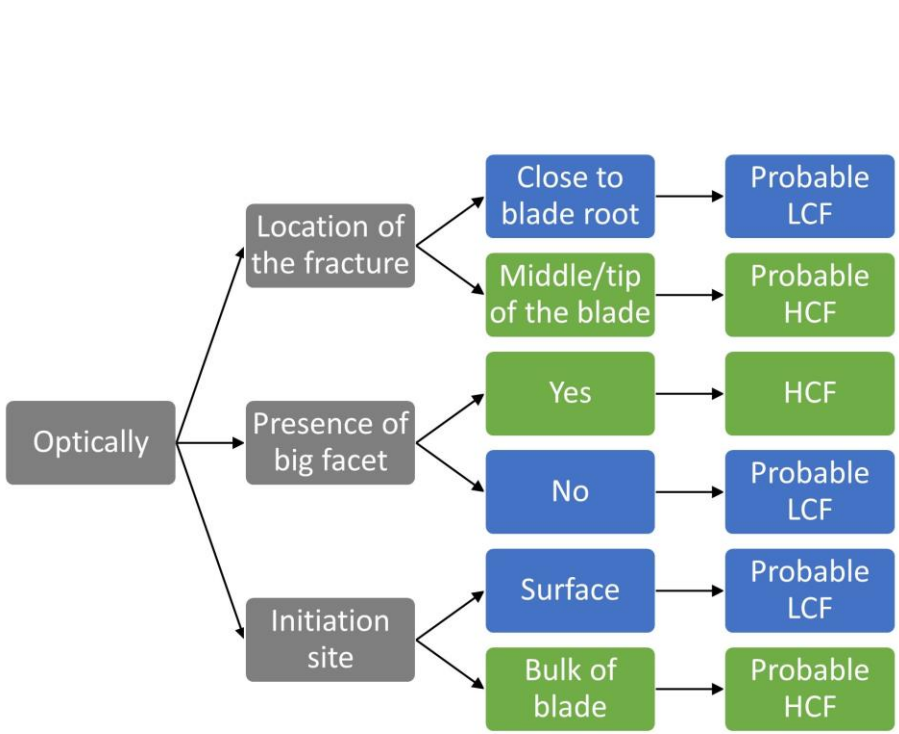
Optically
Location of the fracture
Close to blade root
Probable LCF
Middle/tip of the blade
Probable HCF
Presence of big facet
Yes
HCF
No
Probable LCF
Initiation site
Surface
Probable LCF
Bulk of blade
Probable HCF

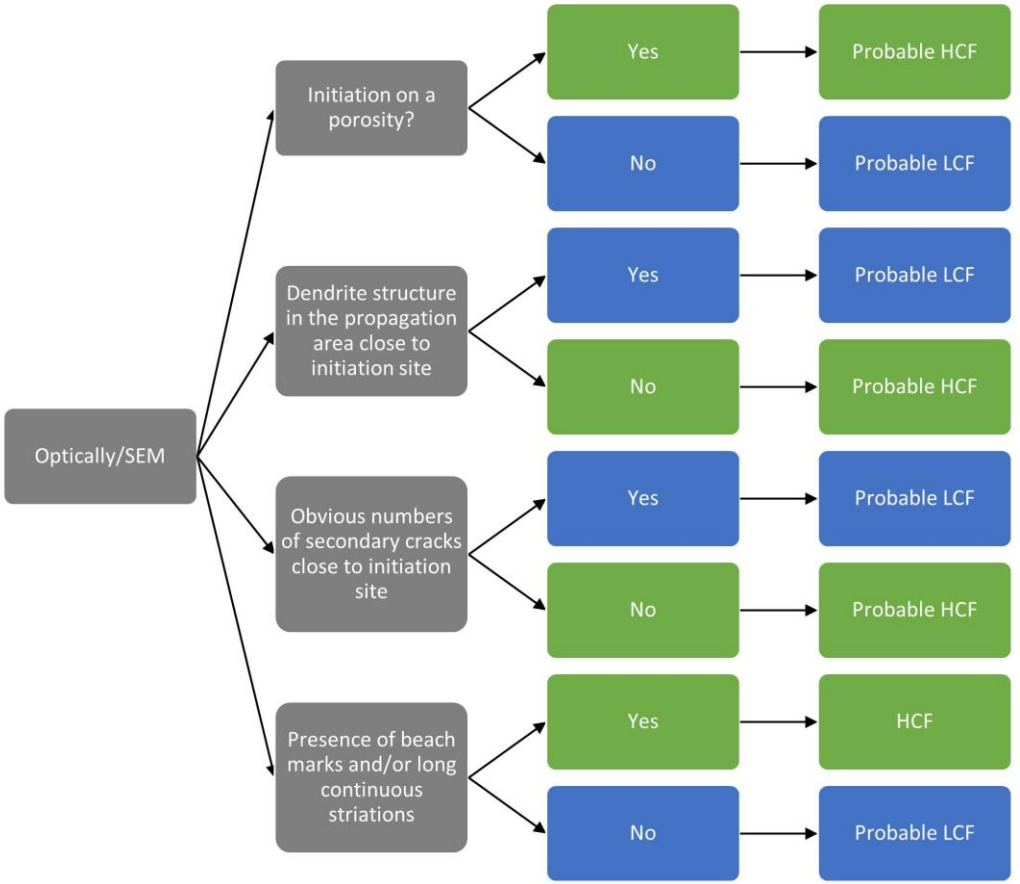
Optically/SEM
Initiation on a porosity?
Yes
Probable HCF
No
Probable LCF
Dendrite structure in the propagation area close to initiation site
Yes
Probable LCF
No
Probable HCF
Obvious numbers of secondary cracks close to initiation site
Yes
Probable LCF
No
Probable HCF
Presence of beach marks and/or long continuous striations
Yes
HCF
No
Probable LCF

Fig. 4.10 Step-by-step flow chart to guide how to distinguish LCF and HCF failure mode.

Chapter 5: Deformation Micromechanism of IN713C Used for Turbine Wheel Blades

Abstract

Nickel-based superalloy IN713C produced through investment casting route is widely used for turbocharger turbine wheels in the automotive industry. The produced microstructure and microtexture are not homogeneous across the turbine component due to geometrical factors and localised cooling rate during the casting process, which give rise to inhomogeneous deformation during service. In the present paper, two kinds of in-house fatigue tests, Low Cycle Fatigue (LCF) and High Cycle Fatigue (HCF), were conducted at 600°C in attempt to simulate the actual fatigue conditions experienced by turbine wheels in turbocharger. From Geometrically Necessary Dislocation (GND) distributions and strain analyses, it is concluded that microstructure heterogeneity such as carbide precipitates distribution within dendritic structure network determine the failure micromechanics during LCF tests. In the early stage of LCF loading, crack principally initiated within near surface carbides that have been oxidised during high temperature exposure. The higher GND density at the tip of carbide precipitates due to oxidation volume expansion are found to facilitate easy cracks initiation and propagation. Moreover, the cluster-like carbides network and its distribution can accelerate oxidation process and crack growth effectively. Furthermore, in the later stage of crack propagation during LCF, the weak interdendrite areas rotate to accommodate increased strain leading to faster cracks propagation and hence final catastrophic failure. Serial section technique for 3-D visualisation was employed to investigate crystallographic grain orientation correlation with fracture mechanics during HCF tests. It appears that the microtexure and grain orientations are more critical than the alloy microstructure in an area with a relatively uniform carbides distribution and weak dendrite structure where HCF failure occurred. Based on the slip trace analysis, it was found that most faceting happened in Goss grains (<110>//LD) and on slip system with the highest Schmid factor. It is concluded that cracks were initiated on planes with high Schmid factors and assisted by the presence of porosity.

5.1 Introduction

IN713C is a γ′ precipitation hardened cast nickel-based superalloy that was developed by the International Nickel Company in the 1950s [1]. This alloy is still used in large quantities nowadays, because of its good castability, suitable mechanical properties and microstructural stability at elevated temperatures. However, IN713C alloys are mainly used in the form of precision cast parts for hot-end turbocharger wheels in the automotive and power generation industries. During investment process casting, the geometrical irregularity in turbine wheels shapes leads to disparity in solidification parameters such as cooling rate in different positions of the wheel component, which inevitably results in inhomogeneous microstructure and microtexture in the component. For instance, two different grain morphologies exist in the wheel blades, *i.e.* small equiaxed grains at blade tips and columnar grains in the bulk of the blades [2]. Furthermore, strain distribution inhomogeneity and localised deformation might be induced due to these microstructural inhomogeneities and finally affect the alloy's performance and mechanical properties to different extend during service [2].

The turbine wheel blades are thermally and mechanically loaded during the operation of the turbocharger. The mechanical loading is caused by centrifugal forces and thermally induced mechanical loadings result from transient and inhomogeneous temperature fields within the blade. Conventionally, low cycle fatigue (LCF) and thermomechanical fatigue behaviour, which both may be significant during start-up and shut down of the engines, garner major research attention concerning the fatigue performance. In addition to the fatigue resulting from centrifugal force and wheel rotational speed during service, the fatigue caused by resonance is also found critical failure mode in turbine blade. In the later form, the high frequency of the blades may coincide with the wheel spinning at specific speeds (range), and cause 'VHCF (Very High Cycle Fatigue)'. In recent years, several works [3-7] concerning fatigue of IN713LC have been carried out to investigate the deformation behaviour and failure mechanism in both LCF [3] and HCF [3-5] conditions. Furthermore, Coleman et al., studied the microtexture correlation with turbine blade properties [2]. Most of these studies pay attention to defects in cast specimen [5], localised dislocation structure in small scale [6], and fracture surface analysis [7]. However, a comprehensive description of crack initiation and propagation is yet to be established for industrial benefit and scientific understanding. Moreover, the conducted experiments in the above studies

used cylindrical button-end specimens from cast rods, which will inevitably result in a failure mechanism deviating from the real wheels, considering the geometrically complexity and inhomogeneous microstructure of the wheels and blades variation between the two.

In general, researchers agree that the major source of crack nucleation during fatigue test of nickel-based superalloys are casting defects such as porosity [5], inclusions such as carbides [8, 9] and persistent slip bands (PSBs) formation [6]. For alloys subjected to high temperature fatigue loading, crack initiation in terms of surface oxidation and stress assisted intergranular oxidation have received considerable academic attention [10]. In particular, since fatigue cracks initiated by oxidised carbides were observed by Connolley *et al.* [11], the importance of carbides oxidation has been reported [12] and its effects on local lattice and chemical changes in adjacent areas have been studied in detail recently in [13, 14]. However, with the advancements in materials processing techniques and heat treatments, cast defects have been reduced and their influence on the fatigue life have been greatly minimised. Consequently, the roles of microstructure, grain boundary characteristics and local texture have subsequently become predominant factors in crack initiation and propagation [2, 15]. Moreover, it vital to study local plastic and/or elastic strain distributions as well as lattice distortions near specific features, if the deformation mechanism are to be well understood from a fundamental level. For these purposes, Transmission Electron Microscopy (TEM) and X-ray or neutron diffraction have been widely utilised but with their own shortcomings in length scales. However, by means of high-resolution Electron BackScatter Diffraction (HR-EBSD) which developed rapidly in recent years, it is possible to capture lattice distortions and dislocation arrangement at the mesoscopic and microscopic length scales, thus bridging a balance between analysis of individual defects in TEM and volume-averaged densities via X-ray methods. In particular, local changes in the lattice orientation reflect lattice curvature and can be further used to calculate Geometrically Necessary Dislocation (GND) densities. This type of calculation and measurement by means of HR-EBSD have contributed greatly in better understanding of dislocation arrangements in intra/inter grains [15, 16] and within local microstructure features in nickel-based superalloys. For instance, Birosca *et al.* [15] proposed distinctive dislocation evolution models in soft and hard grains based on the GND distribution in RR1000 superalloy during thermo-mechanical fatigue. Karamched

et al. [17] first reported high resolution strain and GND distribution around carbides after heat treatment and deformation in a solidified superalloy. Britton *et al*. [18] confirmed the pile-up of dislocations at the intersection of slip bands and grain boundary, and further validate a dislocation mechanics by revealing elastic stress state ahead of the pile-up. By utilising HR-EBSD and/or High Resolution Digital Image Correlation (HR-DIC) technique, Jiang *et al.* [19, 20] revealed a direct relationship between dislocation density and fatigue crack nucleation in nickel-based superalloy containing non-metallic inclusions. Thus, HR-EBSD seems to be a promising tool in understanding the relationship between strain inhomogeneity, orientation gradients and GND accommodations as well as their interactions with microstructures during plastic deformation.

In the present study, in-house LCF and HCF (caused by resonance) tests are applied to real turbocharger wheels. Detailed post-mortem analysis including fractography, microstructure and microtexture characterisations of failed areas have been conducted. Moreover, the relationship between deformation micromechanism and microstructural heterogeneity has been investigated utilising HR-EBSD. The theoretical models of failure mechanics during LCF and HCF conditions are established throughout this study.

5.2 Experimental Procedures and Material Used

The turbocharger wheels produced via investment casting route were tested using Cummins in-house fatigue testing machines at Cummins Turbo Technologies Ltd/Huddersfield/UK. The tested turbine wheels were made of IN713C with a chemical composition shown in Table 2.2. An example of a general condition and geometry of the turbine wheels prior and post testing are shown in Fig. 5.1a and 5.1d, respectively. The wheels subjected to both LCF and HCF loading conditions. However, using in-house testing method the exact condition of LCF and HCF are slightly different from standard fatigue test as it is described below. The in-house testing focus on crack initiation, path and propagation and final fracture of the alloys rather than the total number of cycles to failure. The design of the LCF test here is based on the crack initiation from a high stress concentration points either at the surface, subsurface or in the bulk of the material. Whilst, the HCF test is designed to emulate the resonance effect on the blade failures. As shown in Fig. 5.2a, a standard turbine wheel housing is used

for both LCF and HCF tests with the wheel connected to a controlled high rotating speed motor. The end of the housing is connected to an environmentally controlled chamber to supply a gas stream to the turbine housing. The inlet gas temperature in both tests was 600 °C. During the LCF test, the wheels were rotated with a wide speed ranges with maximum speeds above 100 krpm. Fig. 5.2b shows a typical LCF speed cycles during the in-house test. From the same figure, it appears that tension-tension LCF loading condition is applied in such a test. The cyclical loading caused by the applied centrifugal stress to the turbine blades result from the ever-changing speed of wheels during the LCF test. It is estimated that induced centrifugal stresses that cause the alternating loading are generally below the yield strength of IN713C alloy, but with the presence of stress concentration local yielding may occur in specific regions of the wheel. A typical turbine speed versus time figure during HCF tests is shown in Fig. 5.2c. For HCF tests, by changing the wheel blade speed cycle/range and the inner housing structure, a 'push-pull' force is introduced around the tip of blades. when the push-pull forces occur at a rate that matches the resonant frequency of the blade, the blade will accumulate fatigue damage at a very high rate. The speed range for the test is chosen so that all blades will experience resonance during a half cycle. Fig. 5.2d and Fig. 5.2e also show the typical stress distribution during LCF and HCF, respectively. They demonstrate the high stress at blade root area in LCF and high stress at blade tip area in HCF.

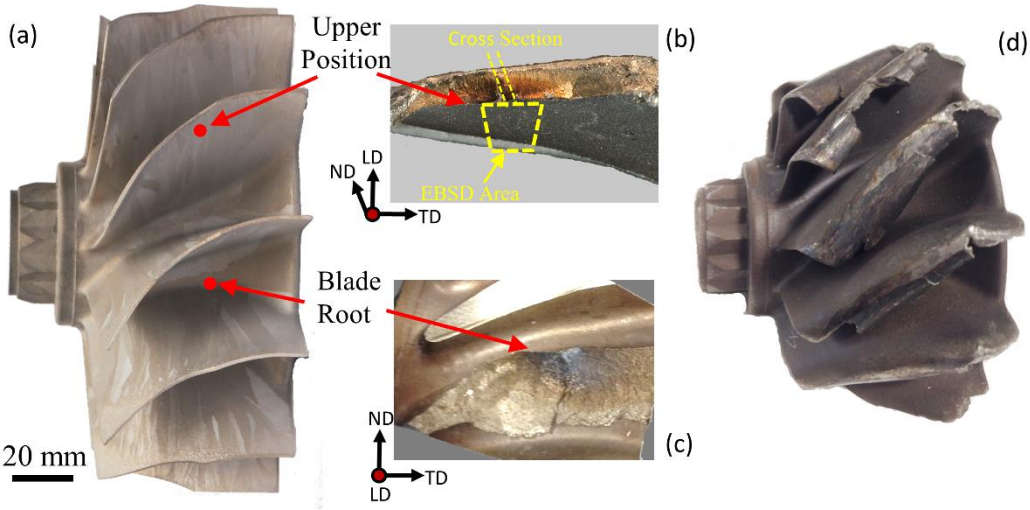

Fig. 5.1 Turbine wheel blade prior (a) and post (d) testing at 600ºC, typical failure location during HCF (b) and LCF (c) tests.

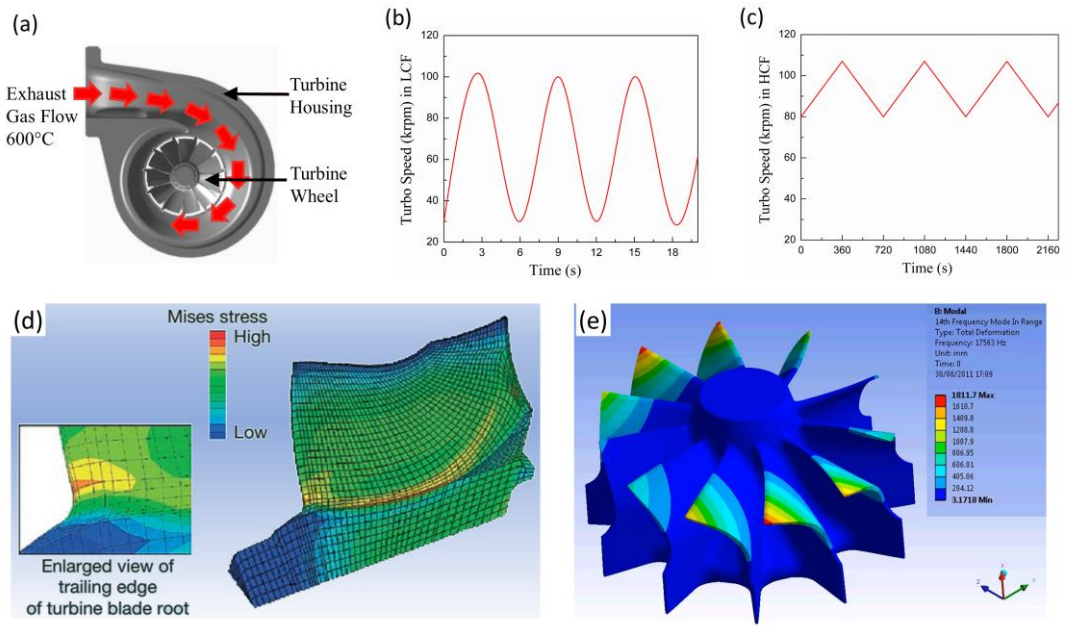

Fig. 5.2 Test schematic for LCF and HCF test (a) and turbo speed versus time during LCF (b) and HCF (c) tests. By changing turbo speed range and inner turbine housing structure, wheel blade failed by resonance in HCF test. (d) and (e) Typical stress distribution in LCF and HCF, respectively.

Following the fatigue tests, the failed specimens were cleaned by ultrasonic bathing in detergent solution for 20 minutes and then in ethanol for 20 minutes in order to optimize fracture surfaces feature observations. Fracture surface study was then carried out for the failed blades using Keyence light microscope and Zeiss (EVO) Scanning Electron Microscope (SEM). The failed blades were then mounted and the surface parallel to loading direction (radial direction) metallographically is prepared. The standard procedure was followed for the sample preparation, culminating with 0.05 µm Colloidal Silica for 20 min. For further microstructure observations, the specimens were etched in Kalling's No. 2 solution (5g $CuCl_2$, 100 ml hydrochloric acid and 100 ml ethanol). After complete fracture surface characterisation, sectioning of failed fatigue samples was performed in order to observe regions surrounding crack initiation sites. This allowed complete characterisation of critical microstructure features controlling fatigue crack initiation and the early stage of small crack growth. Metallographic sectioning planes were parallel to TD-LD plane (Fig. 1b) and the loading axis in both LCF and HCF failed samples. Moreover, for HCF failed specimens, serial sectioning was also conducted across fracture surface (parallel to ND-LD plane) to reveal three-

dimensional view around the cracked areas. Following each high-resolution imaging and EBSD scanning on each section surface, the mounted samples were then demounted to locate the exact location of the sectioning surface that has been characterised. High resolution imaging and EBSD were performed using a JEOL 7800F field emission gun SEM equipped with AZTEC data acquisition and analysis software and a Nordlys EBSD detector. To optimise the image or diffraction patterns quality, the SEM operating voltage used was 10~15 kV for imaging and 20 kV for EBSD scan with a current of ~ 14nA. A binning of 4×4 and Hough resolution of 85 were chosen to balance the time consumed and quality required, leading to an exposure time of 150 ms per pattern. The EBSD date analysis was conducted using standard HKL-EBSD Channel 5 software package.

The concept of GND originally based on the assumption that during plastic deformation, a strain gradient necessitates the creation of minimum dislocation networks to maintain the geometric continuity of the material [21]. This strain gradient often is produced in materials that have two phases that have different deformation ability or adjacent grains with different orientations in polycrystalline alloys [22]. The strain gradient results in orientation gradient and the later can be derived from misorientation across grains, thus the ability of probing orientation of grains in EBSD making the calculation of GND density across grains possible. The detailed mathematical description of GND is given by Arsenlis and Parks [23]. The basic equation for this calculation is dislocation density tensor α_{ij}, which quantifies the content of dislocations in the lattice was:

$$\alpha_{ij} = \sum_{t} b_i^t \, l_i^t \delta(\vec{x} - \overrightarrow{x^t}) \quad (1)$$

Where Burger vector $\vec{b}$ characterise the displacement, dislocation line vector $\vec{l}$ indicates their direction, *t* denotes the type of dislocation and position vector $\vec{x}$. In the present study, we use a Python code to calculate GND which is reported in detail previously [15]. First the Euler angles were converted to a quaternion unit for each point, which were further used to calculate misorientation quaternion. It is worth noting that the misorientation quaternion is calculated for each point along with its adjacent neighbour rather than central point of the grain. Then misorientation vector maps can be obtained, from which only five out of nine Nye dislocation tensor components can be derived as only 2D EBSD orientation date are available. For each type of dislocation

from the 18 types of dislcoations in fcc crystal, we use a combination of five Nye components to resolve at each point and thus, different combinations of dislocation types are selected to solve the equations. The sum of the absolute values of all components of the dislocation density tensor yield the total dislocation density [24]:

$$\rho_{gnd}^{tot} = \frac{1}{b}\sum_{i=1}^{3}\sum_{j=1}^{3}|\alpha_{ij}| \qquad (2)$$

from which the minimum total GDN density was chosen.

In the current study, the step size of EBSD mapping used for GND calculation varied from 60 nm to 300 nm as well as 0.5 micron in order to balance between the microscopically relevant and EBSD noises. It should be noted here that the error in dislocation density calculation will increase as the step size decreases [25, 26]. For the GND calculation in IN713C, a Burgers vector value of **b** = 0.254 nm was used [27]. All GND maps were plotted in logarithmic scale and total dislocation density per μm^2 unit area was used for GND measurements in this study.

For HCF failed specimen, slip trace was also determined in faceted and surrounding grains around crack initiation sites. From the crystallographic orientation data acquired by EBSD, the slip plane traces angle with LD were calculated. In the present study, we aligned the blade LD with the SEM *Y*-axis when inserting the sample into SEM chamber, see Fig. 1b and used the sample reference of *X*-axis = ND (note that the cross section is used for calculation), *Y*-axis = LD and *Z*-axis = TD. Following the quaternion conversion of Euler angles as mentioned above, all possible (111) slip plane traces then can be calculated using the cross product of the slip plane normal and the surface normal. Furthermore, the Schmid factors for each grain were calculated with Eq. (3):

$$S^{\alpha} = (gl \times n^{\alpha})(gl \times S^{\alpha}) \qquad (3)$$

where (g) is the orientation of each grain, (l) is the loading axis, n^{α} is the unit normal to the (111) slip planes and s^{α} is unit slip direction along <1-10>, in which α =1, 2, …12. Following this calculation, the angle between the slip trace and the unit LD (*l*) is determined by [28]:

$$Angle(°) = cos^{-1}[(gm \times \bar{n}) \times (gl)] \quad (4)$$

where $\bar{n}$ is the slip plane normal and *m* is the free unit normal. The detail of both GND and slip trace determination can be found in [15].

5.3 Results

5.3.1 Fractography Observations

In the current study fractography, *i.e.*, fracture surface study, was used to identify the main difference between LCF and HCF fracture surface features. Fig. 5.3 and Fig. 5.4 both give three representative examples of fractographies of HCF and LCF samples after failure, respectively. Macroscopically, nearly all HCF failures occurred in the upper position of blades, see Fig. 5.1b and it appears that the fatigue failure occurred following three stages, as indicated in Fig. 3a and magnified in Fig. 5.3b-d, *i.e.*, Stage 1: crack initiation on a specific grain plane, see Fig. 5.3c; Stage 2: relatively flat and large crack propagation area with characteristic of striations, see Fig. 5.3b and d; and Stage 3: tensile overload area which suffers catastrophic mechanical failure with ductile fracture features (dimples). The other two examples are shown in Fig. 5.3e-f and g-h, respectively, showing the same three failure stages as in Fig. 5.3a-d. Although the same faceting phenomenon had occurred in stage 1 in all the specimens, the crack initiation sites were differed. The crack sometimes was initiated in the vicinity of casting defects such as porosity (Fig. 5.3c) or inclusions (Fig. 5.3e, f), or from the sample surface as shown in Fig. 5.3g. In Fig. 5.3g, another characteristic of fatigue, beach marks, can also be clearly seen on the facet plane.

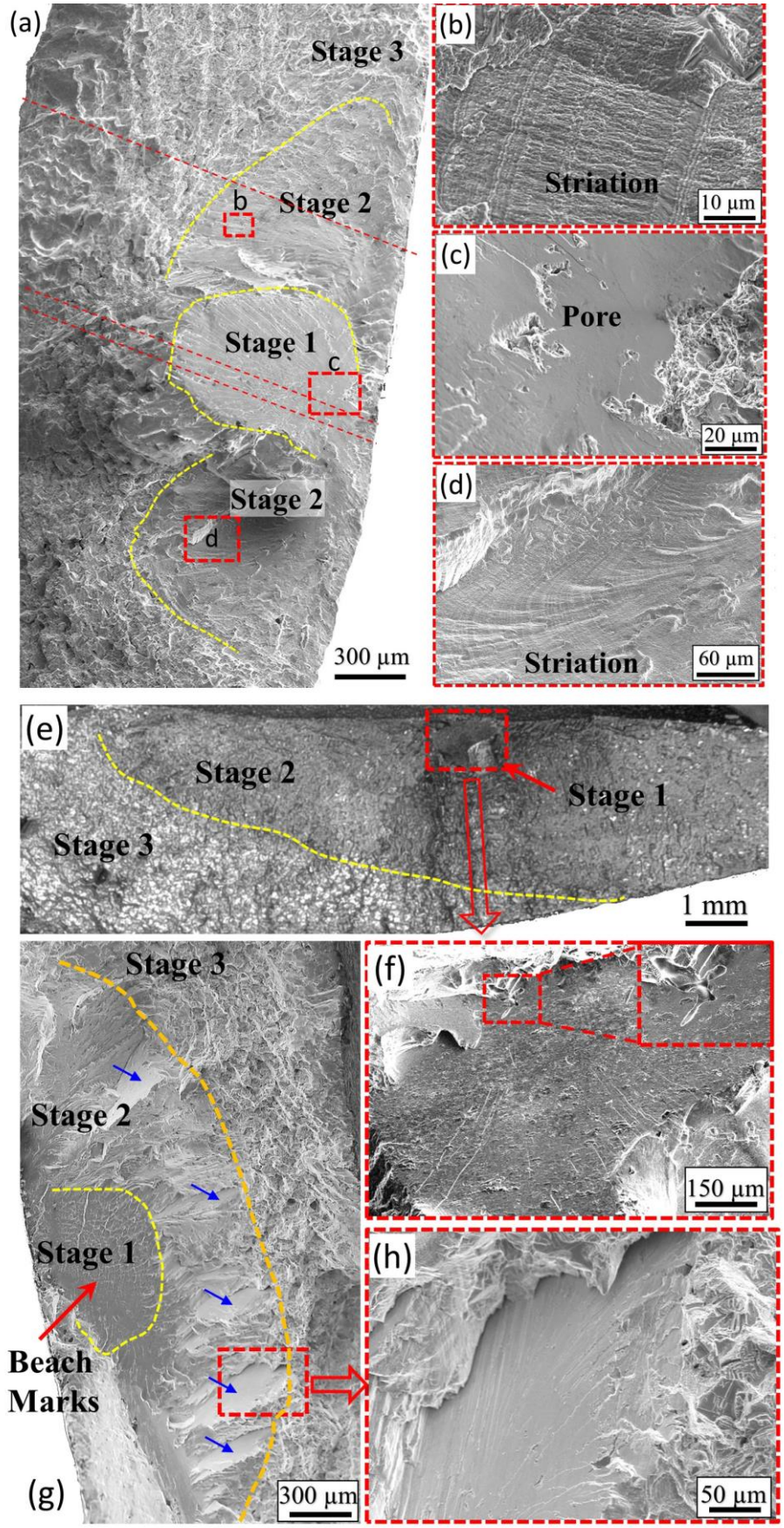
(a)
Stage 3
b
Stage 2
Stage 1
c
Stage 2
d
300 µm
(b)
Striation
10 µm
(c)
Pore
20 µm
(d)
Striation
60 µm
(e)
Stage 2
Stage 3
Stage 1
1 mm
Stage 3
Stage 2
Stage 1
Beach
Marks
(g)
300 µm
(f)
150 µm
(h)
50 µm

Fig. 5.3 Typical fractography of HCF test specimen. Three failed specimens are shown here. (a-d) Specimen 1, (e, f) Specimen 2, and (g, h) Specimen 3. ((b,c,d) are magnified image in red rectangular areas in (a). (f) and (h) are magnified images in red rectangular areas in (e) and (g), respectively. Three stages of crack initiation and propagation are indicated.

For LCF cases, the failure occurred on the blade root, see Fig. 5.1c. The predominant features in LCF failed samples are (1) dendrite structure as indicated in Figs. 5.4a and 5.4b, and (2) secondary cracks as indicated in Fig. 5.4c, both of which are close to initiation sites, indicating that the dendrite structure play an important role in crack propagation, as once the crack initiated during LCF, it can propagate in other directions depending on the dendrite morphology and structure. Moreover, the microstructurally crack propagation areas were not clear on the fracture surface, see Fig. 5.4e. In other words, there was no clear transition between crack propagation area and tensile overload area as was observed for HCF. This might indicate a faster crack propagation during LCF than in HCF. Microscopically, in HCF samples, long continuous striations, which are the most eminent features of fatigue can be found in the propagation areas, especially at the end of crack propagation areas, see Figs. 5.3b and 5.3d, and this is in agreement with most striations observations [29]. Although no such long and continuous striations was found in LCF samples, many local striations with different directions can be clearly observed in the propagation area, see Fig. 5.4d. Moreover, oxidised striations were also observed near crack initiation site, see Fig. 5.4f. It appears that the most contrasting difference between HCF and LCF is that the initiation sites in HCF is highly orientation dependent. Although most of cracks in HCF samples initiated directly from casting defects such as pores (Fig. 5.3c) and inclusions (inset of Fig. 5.3f) which are stress concentration locations, they are all located in grain planes with specific orientations. These planes on the surface of which feature with cleavage fractures are generally known as ‘facet’, are not unusual to be observed in HCF failed specimens. It is generally believed that the facet planes possess a specific angle with loading direction that favourable for slipping during external loading. As shown in Fig. 5.3g, not only did the crack start from a facet, but the propagation of crack also depended on specific oriented planes (indicated by blue arrows in Fig. 5.3g with one of area enlarged in Fig. 5.3h). Further microanalyses show that the dendritic structure and secondary cracks are found close to crack initiation site in LCF failed specimen, see

Fig. 5.4b, which is rare case in HCF sample and this aspect will be further investigated in the next section.

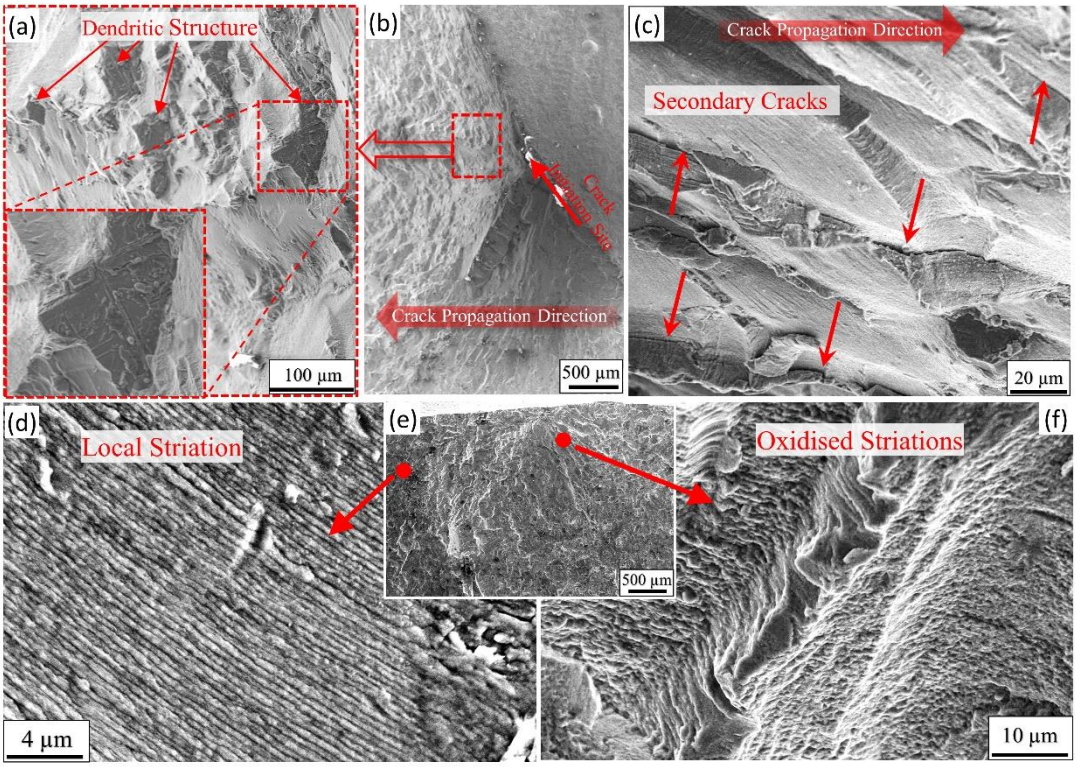

Fig. 5.4 Fractography of 3 LCF test specimens. (a, b) Specimen 1, (c) Specimen 2, and (d-f) Specimen 3. (a) Magnified image of the red rectangular area in (b) showing dendritic structure close to initiation site. (b) Crack initiation site and propagation area in Specimen 1. (c) secondary cracks close to initiation site in Specimen 2. (d) local striations in propagation area in the Specimen 3 (e), (f) oxidised striations close to initiation site in (e).

5.3.2 The Effect of Blade Geometry and Local Microstructure on Crack Initiation Site during LCF and HCF failures

The microstructure of cast IN713C generally consists of dendritic structure with MC type carbides that are rich in Nb, Mo, Ti trapped within interdendritic channels [1, 30]. For turbocharger wheel blades produced via investment casting, the irregular geometry give rise to different cooling rates and thermal gradients, that leads to further microstructure disparity in different locations within the wheel blades. Fig. 5.5 shows the microstructures of the failed blades during both LCF, close to blade root, see Fig. 5.5a-d, and HCF, upper position of the turbine blade, see Fig. 5.5e-h. As can be clearly

seen in the figures, the major differences lie in the dendritic structure, as well as the size, morphology and distribution of MC-type carbides. Based on high resolution EDS analysis used in the current study, all the carbides throughout blades have the stoichiometric ratio of $(Nb_{0.7}Ti_{0.2}Mo_{0.1})C$, which is in agreement with previous reports [1, 30]. It is well established that Mo and Ti generally partition in γ and they are carbides formers. However, unlike Mo and Ti, Nb is mostly diffused and segregated in MC carbides, making Nb-rich carbides all along the interdendritic areas. Based on this consideration, the Nb EDS map was used to identify the carbides location and their distribution as well as to reveal the dendritic structure. As shown in Figs. 5.5b and 5.5f, almost all the carbides precipitate in interdendritic areas, except a few numbers observed along γ grain boundaries. It is evident form Fig. 5.5a-d that the dendrite structure is more apparent with wider primary and secondary arms in the area where LCF occurred. Whereas finer primary arms were observed in the areas where HCF occurred, see Fig. 5.5e-g. Moreover, well defined and characteristic secondary arms can be clearly seen in the area where LCF occurred, see Fig. 5.5b. These microstructure characteristics indicate a faster cooling rate, and/or a high thermal gradient exhibited in upper location of blade where HCF failure took place.

In general, the carbides chemical composition and their trapping in interdendrite channel were the same in the locations where LCF and HCF took place. It is clear from Figs. 5.5c and 5.5g that the carbides show Chinese script and cluster morphology in the area where LCF failure occurred. Whilst the carbides show more uniform and granular shape in the area where HCF failure occurred. Although it is difficult to quantitatively analyse carbides size and their distribution due to the connectivity in 3D of some carbides (particularly in LCF sample), it is obvious that carbides in LCF specimen are much larger in size than that in the HCF specimen, with 5~40 μm in the former and 1~10 μm in the latter. Despite the obvious difference in MC carbide size and shape, the total volume fraction of carbides in two locations are almost the same with 1.8%, which seems less affected by cooling conditions. The effects of cooling parameters on microstructure including carbides and dendrite in casting superalloys have been widely studied. The shape and size of carbides in IN713C was reported depend on solidification parameters such as thermal gradient, growth rate and local cooling rate where a higher cooling rate leads to finer carbides size [30]. It is worth noting here that besides the disparity in carbides size and morphology, the connectivity of carbides

clusters in LCF specimen as mentioned earlier, see Fig. 5.5c, might affect the low cycle fatigue property, which will be discussed in Section 5.4.2.

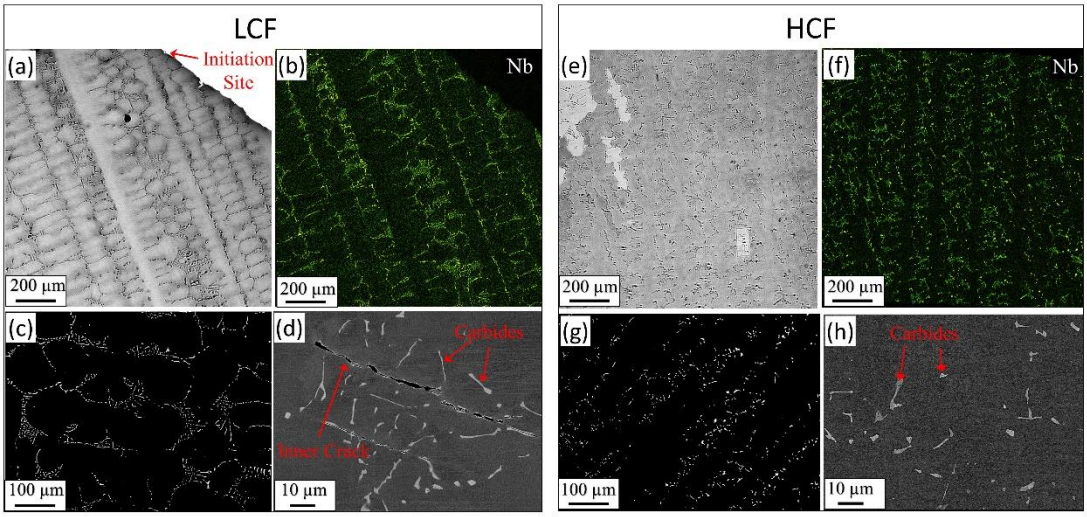

Fig. 5.5 SEM images of Dendritic structure (a, e), optical micrographs of carbide network (c, g) and carbides size and morphology (d, h) in LCF and HCF failed specimens. Nb EDS maps for the area in (a, e), shown in (b, f), respectively, to signify the Nb element partition in dendritic structure.

5.3.3 Near-Surface Carbides Oxidation and GNDs Heterogeneous Distribution in LCF Failed Specimens

Detailed microstructure observations revealed a prevailing oxidation phenomenon of carbides close to fracture surface in LCF failed specimen as shown in Fig. 5.6. The EDS mapping of carbides and oxides in the inset of Fig. 5.6a clearly identify that some $(Nb_{0.7}Ti_{0.2}Mo_{0.1})C$ carbides in the vicinity of specimen surface had been oxidised. The oxides share a similar stoichiometric composition with carbides as $(Nb_{0.7}Ti_{0.2}Mo_{0.1})O$. Furthermore, semi-oxidised carbides were also found near the failed sample surface, see Fig. 5.6c, d. It is evident that the oxidation process initially started from the centre of carbide precipitates, see the same EDS maps for Fig. 5.6d. Fig. 5.6 clearly demonstrates that oxidised carbides can play a vital role in secondary cracks formation and its behaviour, causing secondary crack deviation and undulation, Fig. 5.6a; forming new secondary cracks, Fig. 5.6b; initiating short (inner) cracks within γ matrix, Figs. 5.6c and 5.6d. It should be noted that in addition to the stress assisted intergranular oxidation [10], these types of near-surface carbide oxidation and their effects on fatigue

property received scientific attention recently in single as well as polycrystalline superalloys that contain high content of Nb during high temperature exposure [11-13]. It is suggested the tensile stress resulted from volume expansion of carbides oxidation leads to the short crack initiation [11]. However, as clearly shown in Figs. 5.6c and 5.6d, all the small initiated cracks are perpendicular to the loading direction, indicating the stress assisted effects on short cracks initiation within the oxidised carbides. From current investigation, it is established that carbides are brittle precipitates and can act as preferable sites of crack initiation. However, they are less susceptible to cracks than the oxidised carbides.

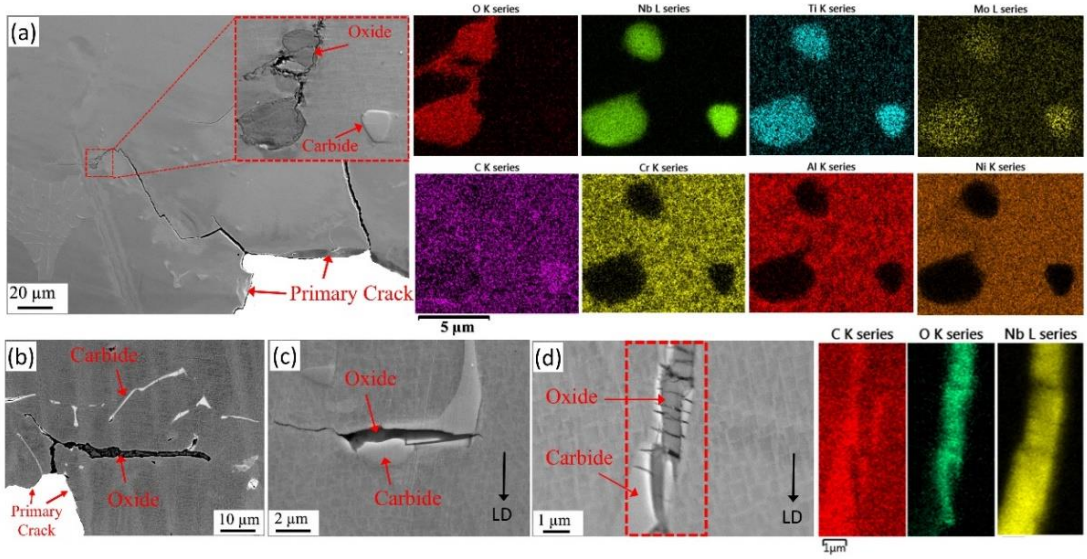

Fig. 5.6 Typical oxides and semi-transformation of oxides from carbides in LCF failed specimen. (a) oxides change the second crack propagation direction and EDS maps show the chemical composition of red dashed rectangular area in the left; (b) second crack initiated from oxides; (c) inner short crack initiated from oxide and (d) semi-transformation of oxides from carbides with EDS maps for the red dashed rectangular area in (d).

Fig. 5.7 shows continuous carbide and oxide along a short crack. It is clear from EDS maps (O, C, Nb, Fig. 5.7b-d) that only the carbides within the opened crack were oxidised, see the non-oxidised carbide away from the crack in the white dashed ellipse shape on Fig. 5.7a and 5.7d. It shows that the short cracks initiated at the tip of oxidised carbides and perpendicular to the loading direction. Figs. 5.7e and 5.7f show EBSD-derived IPF//LD map and GND map, respectively. Form the IPF map the carbides as well as oxidised carbides along the crack are all within one big grain. From the same

figures, it appears that the carbides have slightly different orientation from the γ matrix, see the white dashed ellipse in Fig. 5.7e. It appears that carbides have an FCC crystal structure and similar lattice parameters to γ matrix. This is in good agreement with the Transmission Electron Microscope (TEM) observation in [1]. Looking at the GND density distribution around the oxidised carbides in Fig. 7f, it is not surprising to find higher GND density around oxidised carbides. This is due to different deformation behaviour, hardness and volume expansion coefficient between carbides and the γ matrix that cause strain heterogeneity and GND accumulation. However, it is clear that the GND density at the end of oxides (where small cracks initiate) and ahead of the cracks (see the rectangular areas 1, 2 in Fig. 5.7f) are much higher (about two orders of magnitude) than those in the γ matrix. It seems the GND accumulation along crack direction or perpendicular to the loading direction. Moreover, it is safe to assume that high GND density ahead of the small cracks can promote further propagation.

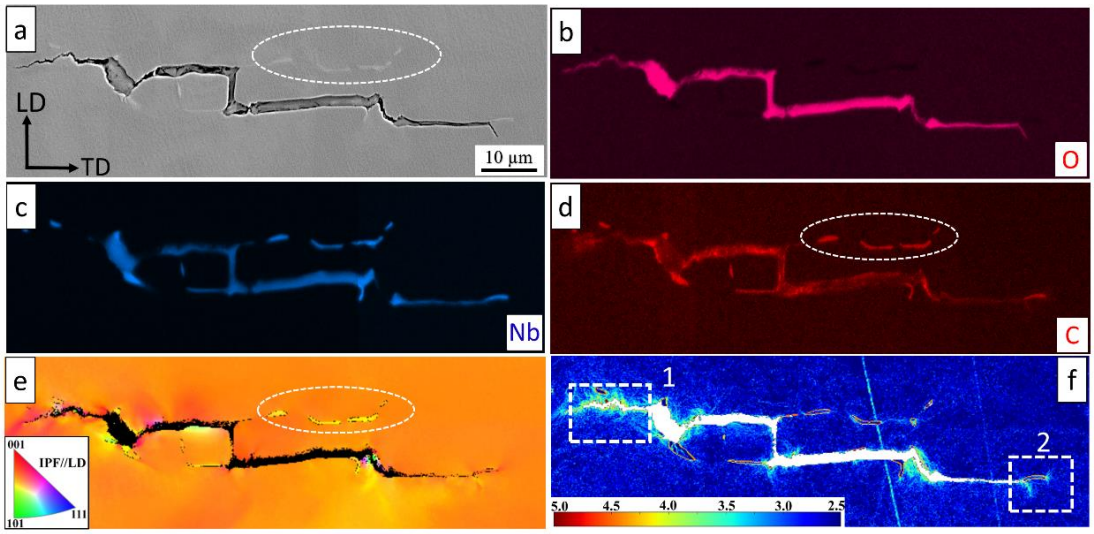

Fig. 5.7 Near surface oxidised carbides in LCF failed specimen. (a) SE image of carbides and oxidized carbides; (b-d) selected EDS mapping for elements C, O and Nb in area (a); (e) EBSD-derived IPF//LD map of area (a); (f) GND (Geometrically Necessary Dislocation) map with step size of 200 nm.

To investigate carbide and oxide connectivity as well as secondary and primary crack networks within the bulk sample, a three-dimensional imaging was performed using layer-by layer grinding and polishing method. Fig. 5.8 shows only 3 sections of the 3D observation: LD-TD plane surface in Fig. 8a which is the same plane surface in Fig.

5.7a, 20 and 40 microns away from the surface in Fig. 5.8c and 5.8e, respectively. The micro-crack in Fig. 8a appear as an isolated crack within the bulk sample, however, looking at other sections in Fig. 5.8c and 5.8e, it is evident that the crack was connected to the primary surface crack. This 3D connection provided sufficient oxygen amount to be diffused from the sample surface to deep inside the material in order to oxidise the carbides during 600 °C fatigue test. Moreover, it is evident that the small crack shown in the inset of Fig. 5.8a grew along the oxide/carbide boundary with the carbide been continually oxidised along the crack. This is because the oxide/carbide was directly bordered by a γ', see the black dashed rectangular area in Fig. 5.8a and enlarged in Fig. 5.8d, and the crack was finally arrested when it encountered by γ', however, after leaving a large GND accumulation at the tip of the crack which indicates strong γ' resistance to crack propagation, see Fig. 5.8b.

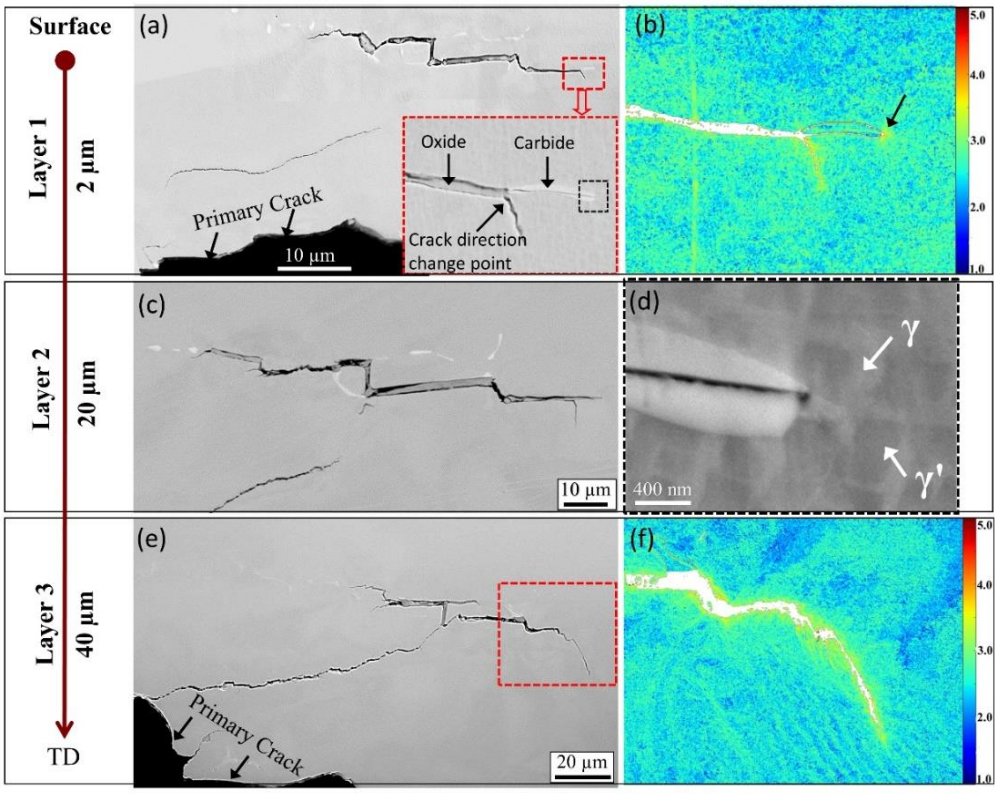

Fig. 5.8 Three layer of the same area GND density maps in LCF failed specimen. (a), (c) and (e) are SE or BSE images; (b) and (f) are high-resolution GND maps with step size of 60 nm in the red rectangular area in (a) and (e), respectively; (d) is the GND map for (c); the inset of (b) is the same area of black rectangular area in (a), showing the γ' impeding carbide.

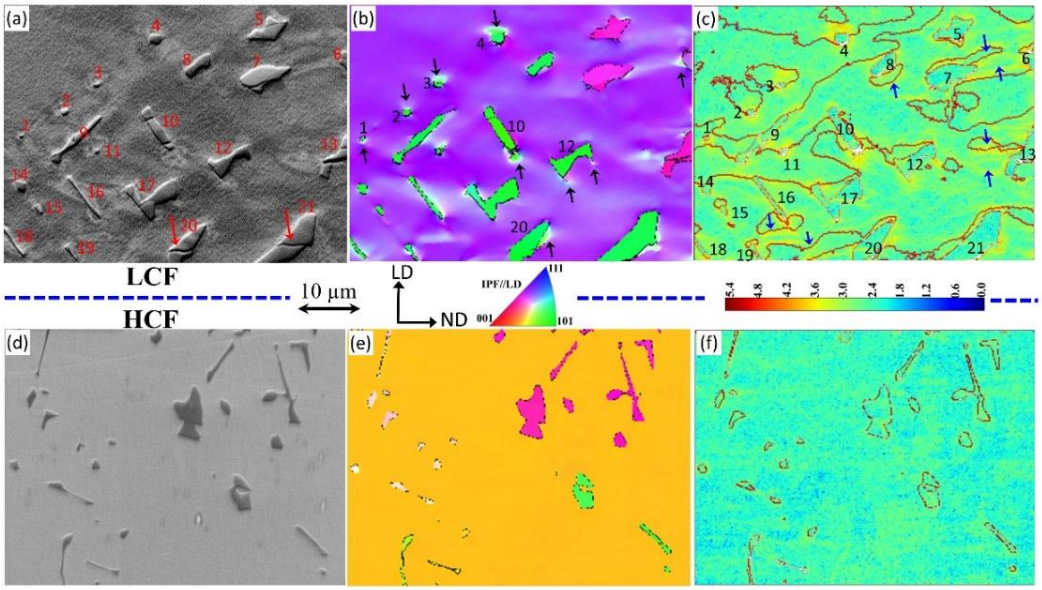

Fig. 5.9 GND density and their local distribution of carbides near crack initiation sites in LCF (a-c) and HCF (d-f) failed specimens. (a,d) SEM image; (b, e) EBSD-derived IPF//LD; (d,f) GND density maps using step size of 200 nm.

Further investigation was carried out in order to obtain a comprehensive description of carbide and oxide effects on crack formation and propagation in LCF and HCF failed specimens. For the statistical reliability purpose a large number of individual carbides (~ 100) in a depth of 200 µm away from the fracture surface and close to initiation sites were analysed by means of EBSD and GND density calculations. As shown in Fig. 5.9a-c, 21 carbides are identified in the LCF failed specimen with size ranging from 0.5 to 11 µm and large strain accommodation around them. It is clear from the EBSD-derived IPF//LD map in Fig. 5.9b that some of the carbides have completely different orientation from γ and γ' phases, *i.e.*, γ has a <112>//LD orientation while most carbides have <110>//LD and some close to γ orientation. Furthermore, the strain heterogeneous distributions are quantitatively analysed as shown in GND density map in Fig. 5.9c. It is clear from the GND map that higher GND density was observed surrounding areas of carbides, due to the different deformation behaviour between carbides and matrix during loading. The high GND density on carbides/matrix boundaries is more related to plastic strain incompatibility between the γ matrix and MC carbide, where these two phases were strain hardened in different rate and level during deformation. However, care should be taken when dealing with the concept of strain hardening where another

type of dislocation, *i.e*., statistically stored dislocation (SSD), that can also contribute in strain hardening is not measured here. It is well established that SSD evolves from random trapping processes, and GND is correlated to lattice curvature [15-16, 21-23]. A closer observation in the current study suggested that the high GNDs around carbides were not uniform. This observation was more evident in the IPF map in Fig. 5.9b. As shown in the figure, the white areas indicated by arrows correspond to high GND density in Fig. 5.9c. This GND accumulation is partly due to the shape and sharp edges of carbides, see carbide 10, 12, 20 in Fig. 5.9b. Furthermore, the loading conditions might have a direct effect on this type of GND accumulation, see carbides 1-4 in the same figure. Further analyses showed that the high GND density also exist in areas away from carbides (indicated by blue arrows in Fig. 5.9c). Considering the 3D network of carbides distribution mentioned above, it appears that these extra high GNDs reflect the strain accommodation surrounding the tip of carbides just below the current observed surface. In contrast to the high GND density surrounding carbides in LCF, the GND density map for HCF shows low density variation around carbides in upper position of blades failed during HCF test, see Fig. 5.9e and 5.9f. Similar GND measurements around carbides were performed by Karamched and Wilkinson [17] on a high Ta-containing directionally solidified Ni based superalloy. They found that the average GND density around carbides increased with increasing applied strain levels during three-point bending test. They also argued that this increase is slightly attributed to the pre-existing plastic residual deformation caused by thermal mismatch between carbide and nickel matrix [17]. However, the thermal mismatch appears to have little effect on the GNDs density in the present study as no obvious increases in GND density was evident between carbide and γ matrix, see Fig. 5.9f. On the other hand, by comparing the GNDs density in LCF and HCF, see Fig. 5.9c and 5.9f, respectively, it is clear LCF are imposed higher strain than in HCF, with average GNDs density of order of $10^{3.8}$ μm^{-2} (6.3×10^{3}) around carbides in LCF while ~$10^{2.4}$ μm^{-2} (2.5×10^{2}) in HCF.

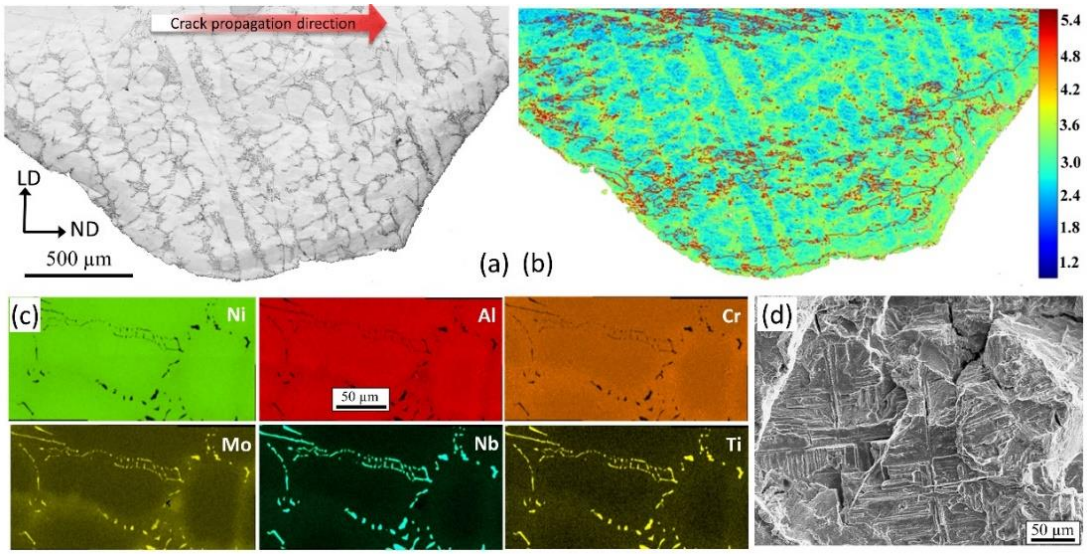

Fig. 5.10 GND density distribution in dendritic structure in LCF failed specimen. (a) Band contrast image of large area of interest; (b) GND density map for the same area in (a) with step size of 0.5µm; (c) fracture surface in crack propagation area revealing sharp and square shape dendritic structure and (d) EDS chemical elements maps for a selected area in (a).

Table 5.1 Segregation ratio and composition of elements in dendrite structure of the LCF failed specimen

	Ni	Al	Cr	Ti	Nb	Mo	Ta
Segregation ratio	0.96	0.98	1.12	1.42	1.47	1.34	1.78
Elements in dendrite	68.59	12.43	13.88	0.6	0.62	2.07	0.14
Elements in interdendrite	65.98	12.29	15.51	0.85	0.91	2.77	0.25

It was interesting to note that the GND density within carbides was much less than the GND density in the surrounding areas, for instance, see carbide number 5, 7, 8, 10, 12, 21 in Fig. 5.9c. It appears that GND density in the carbide was slightly less than the average GND density of γ matrix, which indicates in the hard and brittle nature of carbides. The reduced ductility of carbide lead to inhomogeneous deformation and less strain accumulation, hence less dislocation generation during LCF loading. It should be emphasized here, that during HCF loading, the GND density within the carbides seems to be rather uniform with the rest of matrix, see Fig. 5.9f. This is mainly due to overall lower GND density of γ matrix in HCF failed sample which were exposed to less

straining during HCF loading. However, in general in both LCF and HCF cases, the carbide contained much less GND density than the matrix.

Further GND measurement was conducted to investigate the GND density and their distribution in the dendrite structure within large area of the blade. Fig. 5.10a-b show the GND density in a large area for the same LCF failed specimen as in Fig. 5.9a-c. The plane area of interest in both Figs. 5.9a and 5.10a was parallel to LD-ND plane, which was parallel to main crack propagation direction of the primary crack, see also Fig. 5.1c. It is obvious from Fig. 5.10a-b that the dendritic structure has a great effect on the GND density distribution in LCF. The figure shows much higher GND density in interdendrite area (averagely $10^{3.7}$ μm^{-2}) than in dendritic area (~$10^{2.3}$ μm^{-2}). This GND density disparity imply the heterogeneous strain accommodation caused by the dendrite structure during plastic deformation. These dendrite structures are generated during the investment casting solidification process. However, essentially, they are the consequence of microsegregation of the alloying elements at the solidification front. Fig. 5.10c shows the EDS mapping of six major elements in the material in local dendrite/interdendrite structure. It is clear from the images that Ni and Al enriched and partitioned in dendrite area while Cr, Mo, Nb and Ti enriched in interdendrite areas. Moreover, among the latter four elements, only Cr uniformly distributed across the entire interdendrite area and did not diffuse or segregate into the carbide precipitates, see Cr EDS map. Whilst large quantity of Nb, Ti and Mo are merely partitioned and segregated into MC-type carbides. However, Mo shows a slightly wider diffused area in the EDS map compared with Nb and Ti segregation in carbide. The segregation ratios, defined as the maximum concentration in interdendritic areas over minimum concentration in dendrite core for each element, are determined and shown in Table 5.2. Fig. 5.10d shows a typical example of dendritic structure in the crack propagation area in the LCF failed sample. Moreover, secondary cracks can also be found along the dendritic structure. These prevailing dendritic structure along primary cracks and secondary cracks along dendritic structure clearly signify the weakening effect on LCF properties and this effect closely related with the heterogeneous strain distribution that identified by GND measurements.

5.3.4 The Effect of Grain Orientation on Crack Formation and Propagation during HCF Loading Condition

The microstructure of fracture location following HCF tests including the dendritic structure, carbides distribution and morphology as well as GND density across the sample were performed and compared to LCF failure mechanism. It is demonstrated in Section 5.3.1 that faceted fracture nature was exhibited at the initiation site in HCF failed blades. In this section, we mainly focus on the effects of microtexture and grain orientation on crack initiation and propagations using serial sectioning across and around the facets on the fracture surface. After each sectioning, secondary electron (SE) images were taken to precisely locate the actual section positions on the fracture surface plane. Fig. 5.11 and Fig. 5.12 show the orientation and grain size/shape distribution across the fracture surfaces in two typical HCF failed blades. The fracture surface shown in Fig. 5.11 is the same one as in Fig. 5.3a in which crack initiated from a porosity. The topographic features in Fig. 5.12a are very similar to those in Fig. 5.3g and crack initiated from blade surface. Both serial IPF//LD along cross section, *i.e.* parallel to LD-ND plane, see Fig. 5.11d-f and Fig. 5.12b, and IPF//LD along profile, *i.e.* parallel to LD-TD plane, see Fig. 5.11b and Fig. 5.12b-c, are illustrated to give a comprehensive view of the grain orientations and grain distribution near the failed areas. The critical points, *e.g.* grain boundary along section lines are also indicated by numbers or letters in red in fracture images and IPFs, see Fig. 5.11c-f and Fig. 5.12a-c. It can be clearly seen that these HCF failed blades consist of large grains, with 2 or 3 grains along ND and 1~3 mm along LD. In the first example, the crack initiated and facet formed in the Goss grain (<110>//LD), and the facet ended at the grain boundary, see points 3 and 2 in Fig. 5.11c, d. The same situation applies to the second example, where facet also formed in a Goss grain, which is roughly circled by points D-E-I-M-L, see Fig. 5.12a, b. The facet also ended at the encountering grain boundary, see points I and E in Fig. 5.12a, e, f. The results clearly show that facet area correspond well with the grain size.

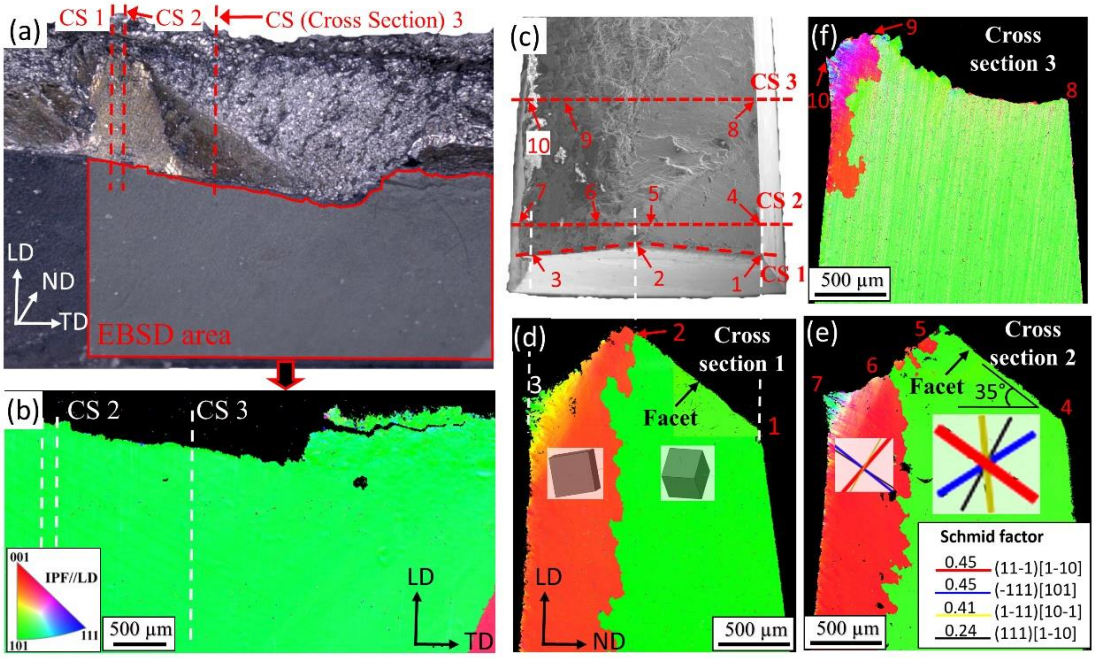

Fig. 5.11 EBSD-derived IPF//LD across facet after serial sectioning on a HCF failed fracture surface. Sectioning position are indicated in dashed lines in (a,b,c), and are the same position indicated in red dashed lines in Fig. 3a. (d,e,f) are IPFs map //LD of cross section 1-3, respectively, parallel to LD-ND plane, and (b) is IPF//LD of LD-TD plane indicated as red line enclosed area in (a). {111} Slip traces and 3D-view of crystal are superimposed on IPF maps in (e) and (d). Schmid factor values for each slip system in facet grain are listed in the inset of (e).

As shown in Fig. 5.11e and Fig. 5.12d, the (111) slip traces are superimposed on IPFs, and Schmid factors for each slip systems in facet grain (Goss grain) are also calculated and presented. These figures show that facet plane is parallel to the slip plane with highest Schmid factor among all slip systems available, *i.e.* (11-1) [1-10] in the first sample and (1-11) [10-1] in the second sample, see the slip trace line in red in Fig. 5.11e and Fig. 5.12d, respectively. It should be noted here that the highest Schmid factor in the faceted grain in Fig. 5.11, although already high with 0.45, is slightly lower than the one in Fig. 5.12 (0.49). Since the first facet initiated from a pore while the second one started from surface, it is reasonable to deduce that the stress concentration induced by porosity might reduce the critical sheer stress needed for slip system activation. In other words, when Schmid factor is high enough, the slip of that plane can occur without an assistant of the presence of defects such as porosity or inclusions. The angle between

the facet and horizontal plane (TD-ND plane) are around 35° in both cases. The degree of deviation of faceted grain away from ideal Goss orientation are determined using ODF (Orientation Distribution Function) and shows ~7° away from ideal Goss in the both cases, representatively shown in Fig. 5.12e. For crack propagation stage in the first HCF fracture surface, where featured as visible striations, propagation area was found within the same Goss grain, although changed into different lattice planes after faceting, see Fig. 5.11. Whilst for the second fracture surface, after faceting in Goss grain 'H-I', fatigue crack further propagates in adjacent grain 'I-J, E-F'. In this fractured specimen, Schmid factors of two other surrounding-faceted grains have also been calculated and listed in Fig. 5.12f. It shows that neither the highest nor average values of Schmid factor for the two grains are lower than that in the faceted grain, especially in Brass grain (grain 3), in which two of four available slip systems were almost zero. The low Schmid factor of the grains indicate on unfavourable crystallographic orientation to activate {111}<110> slip system. The different values of Schmid factor together with the grain size and distribution are believed to have great effect on the crack initiation and propagation during HCF as will be discussed in the Section 4.

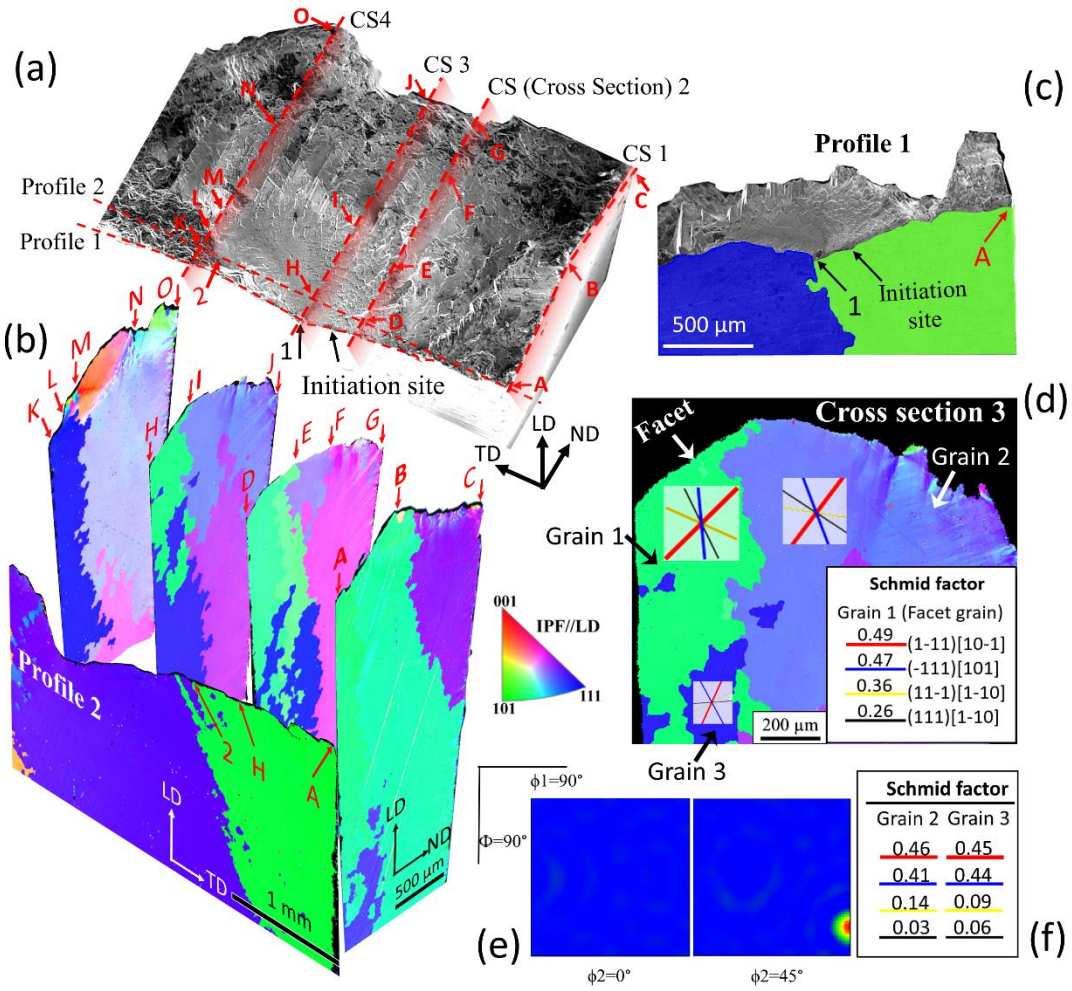

Fig. 5.12 3-D view of the microstructure, grain orientations around a facet for a HCF failed specimen. (a) SE-SEM image of the fracture surface; the section direction along ND (CS) and TD (profile) are indicated in red dashed lines.; (b) selected EBSD-derived IPF of Cross Sections (CS) on and near facet plane. (c) IPF//LD of the section plane parallel to LD-TD plane (profile 1), IPF//LD of profile 2 are shown in (b); (d) part of IPF//LD of cross section 3 on facet grain. Slip trace maps for three grains (Grain 1-3) are superimposed on the IPF. (e) ODF (Orientation Distribution Function) of facet grain (Grain 1); Schmid factor values are for three grains listed in (d) and (f).

5.4 Discussion

5.4.1 On the Role of MC Carbides and MC Oxide in LCF Deformation Mechanism

It is demonstrated in Section 5.3.3 that MC carbides in IN713C alloy plays a vital role in determining the LCF properties. It was also observed that the MC carbides' size,

shape, edges and prevailing precipitation distribution across γ matrix as well as their coherency and different deformation nature from γ have a great influence on LCF failure mechanism. On the one hand, as a second phase particle, carbide strengthen IN713C via precipitate strengthening by resisting dislocation motion (both SSD and GND) and dislocation fostering (Fig. 5.9c). On the other hand, when the strain that is resulted from heterogeneous deformation between carbides and matrix is accumulatively sufficient, can lead to carbides cracking, see the arrows in Fig. 5.5d and Fig. 5.9a. This is one of the major source of small crack formation and micro crack propagation as found in the centres of the brittle MC carbides.

It is clear that the most deleterious effect of carbides on fatigue property is observed upon their transformation to oxides. Connolley *et al.* [11] estimated the volume expansion factor between Nb_2O_5 and NbC may varies from 2 to 2.4. The volume expansion factor is defined as: $\delta_V = \frac{V_{Nb_2O_5}}{2V_{NbC}}$. As stated earlier the composition of carbides in the current study is found to be complex stoichiometric formula of $(Nb_{0.7}Ti_{0.2}Mo_{0.1})C$. However, the volume expansion due to different volume expansion coefficient in carbides and oxides is highly expected during carbides oxidation. It has been also reported that in stress free condition prior to deformation, sub-surface carbides can readily be oxidised with a characteristic surface eruption. It is also claimed that this type of oxidation process can lead to a localised γ deformation around the oxidised carbides [11]. This type of local deformation of γ matrix is mainly induced by the volume expansion during carbides oxidation. This volume expansion-induced localised deformation during phase transformation also have been reported in other alloys [16], for instance, the volume expansion during austenite-to-martensite transformation in dual steels that cause adjacent ferrite matrix to deform [16]. Surface carbides oxidation has also been studied by Reed *et al.* [13] recently when comparing the different effects of MC carbides and M_5B_3 borides on tensile property of a nickel-based superalloy at elevated temperature. In addition to surface eruption and volume expansion, pores around oxidised carbides have also been observed by them and supposed to cause microcracks. The similar observation of higher GND density around cross-sectioned oxidised carbides has been made by Kontis *et al.* [14] recently. They also reported suspected softer area of recrystallization adjacent to oxidised carbide and caused by elements diffusion through dislocations, which might also contribute to the weakening of oxidised carbides areas [14].

In general, during deformation, geometrically necessary dislocations (GNDs) are required for maintaining lattice continuity [21, 22] and statistically stored dislocations (SSDs) evolve from random trapping processes. However, except at the tip of long oxidised carbides, it appears there is no significant GND density increase was found around oxidised carbides compared to the GND density around the non-oxidised carbides, see Fig. 5.9c and Fig. 5.7f. Considering the long irregular script-like shape carbides in LCF failed specimen (Fig. 5c and 5d), it is likely that the volume expansion and stress accumulation near MC and MC oxides mainly occur in the high geometrical curvature sites such as the edges and the tip of carbides parallel to the loading direction. Moreover, it appears that the volume expansion may not cause a uniform deformation near oxidised carbides in all directions, but instead, the generated strain, hence stress, parallel to the external loading axis, caused a localised deformation in the geometrically weak sites and could lead to microcracks initiation. It should be noted here that the geometrically weak site is refers to carbide edges and corners. After such transformation-induced deformation, residual stresses remain due to the inhomogeneous plastic deformation and can further facilitate crack growth. The non-uniform and inhomogeneous distribution of GNDs around carbides in all directions is demonstrated in Section 5.3.3 and shown in Fig. 5.9c. This phenomenon is also reported in [17], where sharper corners tend to possess higher density of GNDs than the curved corners. In order to study the inhomogeneous distribution of effective strain and GNDs around non-metallic inclusion, an elastic finite element (FE) model has been generated and suggested that geometry of inclusion is responsible for the stress/strain conditions and hence GNDs accumulation in different directions [17].

Recently, GND concept is used widely to understand the deformation mechanism, strain hardening and recrystallization in various materials such as pure copper [31], titanium [18] and nickel-based superalloys [19]. It has also been reported that there is direct correlation between high GND density and LCF crack initiation and propagation in inclusion-containing superalloys [19, 20]. According to Stroh [32], the dislocation pile-up leads to crack nucleation as they increase the local shear stress which facilitates nucleation of a micro-cracks. However, it is argued that dislocations cannot be a sole criterion for crack initiation as high GND are not limited to crack initiation sites [19]. Based on the concept and evaluation of stored energy [33], the dual role of GNDs in fracture process was proposed by Jiang *et al*. [19]: On one hand, GNDs accumulation

can lead to local hardening and increasing the critical resolved shear stress. The stored energy is therefore increased and their dissipation lead to crack nucleation; On the other hand, GNDs can foster ahead of cracks and may have blunting effect as driving force for crack growth decreases. Both effects of GNDs were observed in the present study. First, as shown in Fig. 5.7f, high GND density at the tips of oxidised carbides could initiate micro-cracks, and secondly, the blunting effect could be clearly observed by the formation of the GNDs wall ahead of the small cracks (see the two rectangular areas in Fig. 5.7f). It is therefore concluded that GND fostering and accumulation can be an indication of plastic zone formation at the tip of the crack, and/or represent a strong driving force for crack propagation during loading. Thus, the GND calculation and strain mapping should be carefully utilised in deformation mechanism study. Therefore, the authors of this study believe that the local plasticity and stress state should be considered to understand the contribution of GND on strain hardening and fracture mechanics. Furthermore, GND density is not represent the total number of the dislocation as SSD cannot be measure or calculated by merely EBSD data. Thus, SSD contribution on dislocation fostering and accumulations should be also considered in this aspect.

Great attention in the current study was paid to understand the carbides oxidation and in particular, oxygen transportation through precipitate hardened IN713C alloy. In general, oxygen has limited ability for diffusion in nickle based superalloy [34], thus the lattice diffusion cannot be a major oxygen transportation channel for oxidation to occur. As proposed in Section 5.3.3 and shown in Fig. 8, the oxygen transportation was mainly through primary and secondary cracks that are formed during loading. Many observations supported this particular postulation in this study. First, all the LCF failure found in this study occurred on the surface of the blade root (Fig. 5.1c). Once the initial micro-crack forms, either under external stress or from surface oxidised carbides, oxygen can readily channel through the crack to sub-surface carbides, providing carbide network as discussed previously. Moreover, once the carbides have been oxidised, the MC oxides themselves can act as medium for further oxygen transportation. The connecting cluster-like carbides distribution shown in Fig. 5.5c can provide carbides bridging for oxygen transportation. Secondly, carbides oxidation was rarely found in HCF failed sample under the same temperature and testing condition. It appears that the dominant factor is that most of HCF cracks initiated inside the upper position of

blades (Fig. 5.3). Thus, diffusion of oxygen through γ matrix shows negligible effect compared with the crack channelling on oxygen transportation as discussed earlier. In conclusion, it is well known that oxides are more brittle than carbides due to crystallographic nature, and together with the strain induced by volume expansion during oxidation transformation as described earlier, it is established that the oxidised carbides are much more susceptible to microcracking than carbides.

5.4.2 On the Role of Dendritic and Interdendritic Structure in LCF Deformation Mechanism

The interaction between individual carbides/oxidised carbides and small cracks discussed in previous section underline the damage mechanism at microscopic scale at the early stage of crack initiation and propagation. Macroscopically, however, these damage accumulations lead to the weakening of large interdendrite areas where accommodate most of carbides and might accelerates crack propagation afterwards. Fig. 5.13 illustrates such weakening of interdendrite and its effects on failure mechanics. The dendrite structure is shown in Fig. 5.13a with area of interest been indicated by red rectangular inset and higher magnification of the area of interest are shown in Fig. 5.13b and 5.13c. The dark contrast of interdendrtite area in the EBSD band contrast images, see Fig. 5.13b, indicate lattice distortion and high local misorientation in that area. IPF in Fig. 5.13e shows that the original grain has a Brass orientation (<111>//Loading Direction (LD)) while the interdendrite shows Cube orientation (<100>//LD). In general, Brass oriented grains are regarded as hard grains with low Schmid factors and hence the slip system is difficult to be activated. Therefore, grain rotation is necessary in order to accommodate further external strain. Clearly a lattice rotation indeed happened in the area studied, but instead of the rotation of whole Brass grain, only weakened interdendrite rotated, specifically, about 55° along <110> axis from Brass to near Cube orientation, see Fig. 5.13e. In other words, at this stage of crack propagation, during loading of hard Brass grains, only the interdendrite area was rotated toward a soft orientation, *i.e.*, Cube with higher Schmid factor (Fig. 5.13d) so that can facilitate an easy slip system activation and hence crack propagation. This type of local lattice rotation would eventually lead to grain fragmentation and fracture of the blade in this area. This is further demonstrated in Fig. 5.13c, where a crack formed at the dendrite-

inderdendritic boundary. This is analogous to dislocation motion theory which replace the whole bulk shear during plastic deformation of alloys. The high GND density in Fig. 13f and severe deformed γ' in the interdendritic area shown in Fig. 5.13c as well as long cracks along dendrtite/interdendrite interface are the result from the lattice distortion and hard Brass grain fragmentation.

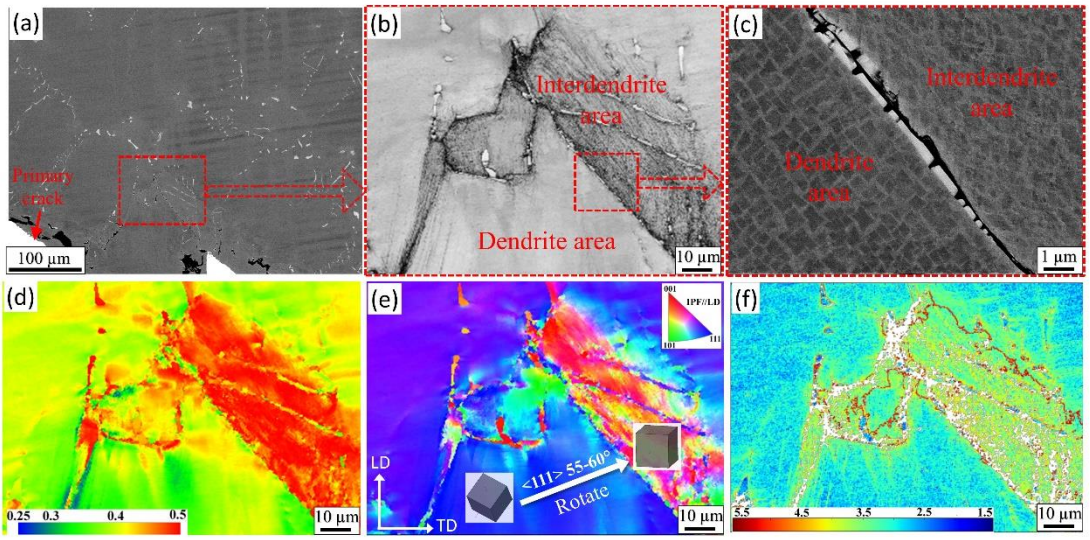

Fig. 5.13 Illustration of dendritic weakening during LCF failure. (a) Low magnification image shows the dendritic structure, (b) Band Contrast (BC) map of the red rectangular area in (a); (c) SE image of the red rectangular area in (b) showing the γ' structure in dendrite and interdendrite areas; (d) Schmid factor map, (e) EBSD-derived IPF//LD and (f) calculated GND density map of area in (b) with step size of 300 nm.

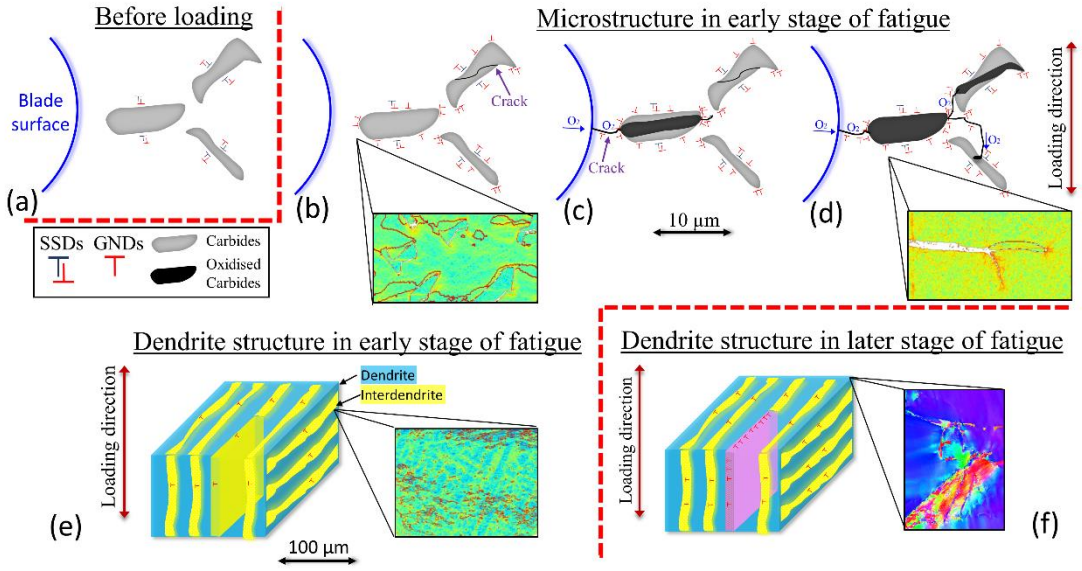

Fig. 5.14 Schematic showing the failure mechanism of crack initiation and propagation in the early (b-d) and later (f) stage of LCF test, and the effects of both carbides/oxides (microscopically, b-d) and (dendrite structure e-f) on crack initiation and propagation process.

Table 5.2 Schmid factors for slip systems in four typical grain orientations

Slip plane	Slip direction	<100>//LD	<-101>//LD	<112>//LD	<111>//LD
(111)	[-110]	**0.408**	0	0	0
	[0-11]	0	0	0.272	0
	[-101]	**0.408**	0	0.272	0
(-11-1)	[011]	0	0	**0.408**	0.272
	[-101]	**0.408**	0	0.136	0
	[110]	**0.408**	0	0.272	0.272
(-111)	[0-11]	0	**0.408**	0.136	0
	[101]	**0.408**	0	**0.408**	0.272
	[110]	**0.408**	**0.408**	0.272	0.272
(-1-11)	[011]	0	**0.408**	0	0.272
	[101]	**0.408**	0	0	0.272
	[-110]	**0.408**	**0.408**	0	0

Based on the experimental observations discussed above, it is proposed that the failure of turbocharger wheel blades under LCF condition is followed a sequence of events as schematically drawn in Fig. 5.14. It is reasonable to assume that prior to the LCF test, only a limited amount of SSDs and low density of GND existed around the large size carbides in the cast IN713C, see Fig. 5.14a. When the cast alloy subjected to LCF loading (cyclic centrifugal stress), large quantities of GNDs generated around carbides in order to accommodate the local strains as a result of heterogenous strain distribution, especially at the tip of carbides. As discussed earlier the tip represent geometrical irregular site that can be a preferential site of strain accumulation and dislocation fostering with a possibility of some carbides may crack due to inner stress, see the highlight in Fig. 5.14b and Fig. 5.9c. As cyclic loading continues, high stress concentration site at the blade root surface initiates small cracks (either by persistent slip band or surface carbides/oxidised carbides interface failure). Once the cracks form, oxygen can diffuse through the crack and readily oxidise the sub-surface carbides, which induce more GNDs at the tip of carbides due to volume expansion and lead to further crack propagation, see Figs. 5.14c and 5.14d. As oxygen continue to be channelled through oxidised carbides and cracks, the adjacent carbides would be oxidised along the crack length, see Fig. 5.14d. Considering the cluster-like and

connecting structure of carbides distribution in the blade root area as shown in Fig. 5.5b, 5.5c and Fig. 5.10, this oxidation-crack-oxidation interaction are expected to continue consequently.

Fig. 5.14b-d show the early stage of fatigue failure microscopically. Moreover, in a larger scale, the effects of dendritic/interdendritic morphology as well as carbide network and distribution on deformation micromechanics during LCF loading is demonstrated in Fig. 5.14e. It is evident in the figure that interdendrite accommodate much higher GND density than in dendrite areas. As the damage accumulate further, at the late stage of crack propagation during LCF failure, the weakened interdendrite area will first rotate to accommodate increased strain and facilitate further crack propagation, see Fig. 5.14f, which lead to the blade failure via grain fragmentation process as discussed earlier.

5.4.3 On the Role of Grain Orientation and Grain Morphology in HCF Crack Initiation and Propagation Mechanism

The crystallographic facets observation on the crack surface plane in nickel-based superalloys have been widely reported and generally attributed to the slip behaviour on {111} slip system in materials with FCC crystal structure during loading [4]. In the present study, facets have been found not only in grains with orientation of near Goss (<-101>//LD) as shown in Fig. 5.11 and Fig. 5.12, but also in Cube (<100>//LD) and Copper (<112>//LD) orientation grains. Table 5.3 shows Schmid factors of all the 12 slip systems in these grains including Brass (<111>//LD) oriented grains for comparison purposes. Illustrations of {111}<110> slip systems with some highest Schmid factor values in the ideal Cube, Goss and Copper orientations are shown in Figs. 5.15b, 5.15c and 5.15d, respectively. In the figures, the plane of (-111)[101] slip system is indicated in green and slip direction in blue. The red planes shown in the same figures are the perpendicular planes to the Loading Direction (LD) in each of the ideal orientations studied here. For instance, in Goss grain, the angle between loading direction and slip plane normal is 35.25°, see Fig. 15c, and with a slight grain rotation, the actual Schmid factor of this slip system can increase greatly. This specific case appeared to happen to create faceted grains in the two HCF fracture surface shown in Figs. 5.11 and 5.12. As shown in the figures, the facets are parallel to (-111) slip planes

in both samples. The measured angle between loading direction and facet normal is ~35° and the deviation from ideal Goss orientation is ~ 5° (see the faceted grain in Fig. 11) in the first HCF sample and ~7° in the second sample (see faceted grain or Grain 1 in Fig. 5.12e). As a result, the Schmid factor for the (-111)[101] slip system in the Goss grains increased from 0.408 to 0.45 and 0.49, respectively in the two samples.

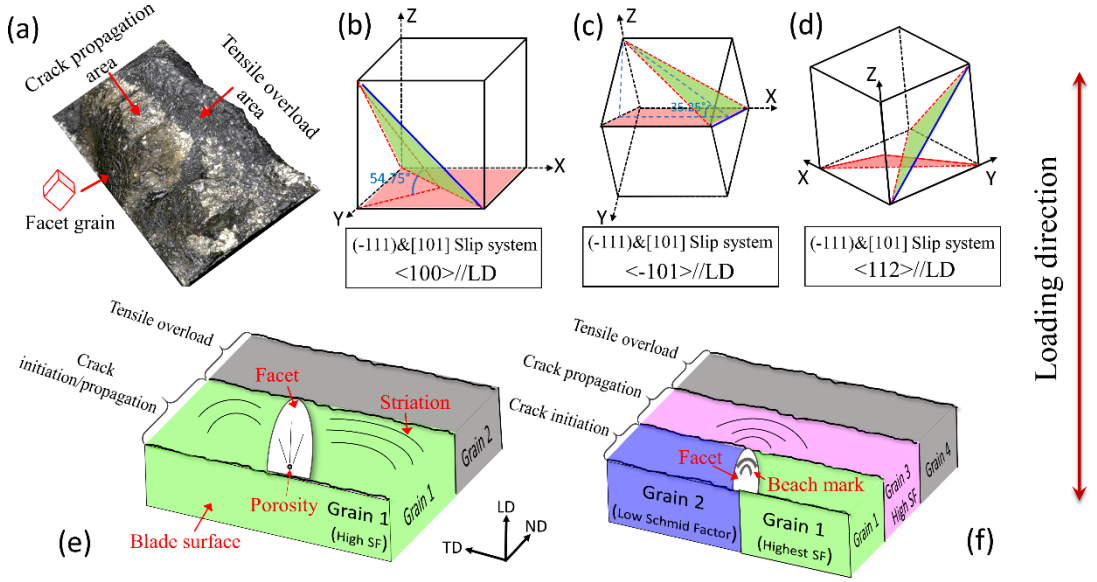

Fig. 5.15 Schematic showing the failure mechanism of crack initiation and propagation during HCF test. (a) a fracture surface of a failed sample, showing facet formation and rack propagation stages. (b-d) ideal facet plane orientation in different orientations. (111)<110> slip system with high Schmid factor (0.408) in <100>//LD, <110>//LD and <112>//LD grains are shown. Red planes are normal plane to loading direction (LD) and green planes are {111} slip planes with high Schmid factor. (e) and (f) two macroscopical fracture modes during HCF test, note the number, size, structure of grains and their correlation with crack stages in two modes.

The requirement of high Schmid factor for slip system activation and the formation of crystallographic facets has been proposed not only in nickel-based superalloys [35], but in other engineering alloys such as titanium alloys [36]. Recently, much of attention has been paid to the correlation between facet (plane) formation and grain orientation or microtexture in Ti–6Al–4V alloy, and generally believe that facet cracks preferentially form in grain oriented with a c-axis misorientation between 15° and 40° from loading direction. Dislocations along slip systems with highest Schmid factor and microcrack induced by the slip have also been observed using transmission electron microscope (TEM) [36]. In studying the VHCF in a polycrystalline nickel-based

superalloy, Miao *et.al* [35] observed that slip plane with highest resolved shear stresses is parallel to both the facet plane and the Σ3 twin boundary, suggesting that one of two criteria for facet formation is slip plane with high Schmid factor parallel to twin boundary.

It was evident from the current study, that the crack initiated in a grain that possesses highest average Schmid Factor value among surrounding grains. Comparing three observed grains in Fig. 5.12d, *i.e.*, Grain 1, Grain 2, Grain 3, it appears that in addition to the higher value of Schmid factor of favourable activated slip system in faceted grain (0.49 in Grain 1) compared to the Grain 2 and Grain 3 (0.46 and 0.45 in Grain 2 and Grain 3, respectively), the Schmid factor of other available not-activated slip systems in Grain 1 (0.47, 0.36 and 0.26) are much greater than in Grain 2 and Grain 3 (0.41, 0.14, 0.03 in Grain 2 and 0.44, 0.09, 0.06 in Grain 3). Moreover, within the faceted grain, the crack occurred on a {111}<1-10> octahedral slip with a highest Schmid factor value among all the available slip system. Here, in Grain 1, the Schmid factor of 2nd rank favourable slip system (0.47) is slightly smaller than the 1st rank activated slip system (0.49). It should be noted that the Schmid factor calculation here is based on the validity of the external uniaxial stress state within individual grains without considering additional local stresses. Although it has been reported that the effective Schmid factors might be affected by local stress states which maybe generated by a present of precipitates such as carbides, adjacent grains or residual stress [37]. However, as discussed previously, the carbides in HCF failed areas were relatively small and homogeneously distributed. Moreover, it should be noted that the microstructure of the failed HCF specimens consist of very large size grains (order of mm), where the entire fracture surface consists of only two and three grains along ND direction as shown in Fig. 5.11 and Fig. 5.12, respectively. Furthermore, in the current study, most of the Schmid factor calculations matched well with the effective slip plane (faceted plane). Therefore, the local stress effect is likely to be negligible in this study. It has also been reported [38] that at relatively small plastic strains under fatigue conditions, the crystalline interaction does not essentially affect the local stress within the grains. Nevertheless, high Schmid factor value alone may not sufficient for dislocation accumulation and slip system activation if cyclic stress level is relatively low. In that case, casting defects such as porosities can provide stress concentration zone and lead

to cyclic plastic strain localisation, which further lead to the accumulation of dislocations along slip plane and eventually microcracks formation.

Based on the 3D serial sectioning observations in Figs. 5.11 and 5.12, two schematic models for crack initiation, facets formations and crack propagation mechanisms are presented in Figs. 5.15 e and f. As discussed and demonstrated in Fig. 5.15a and Fig. 5.3, there are three stages during HCF failure, that is, crack initiation stage characterised as facet (Fig. 5.3c), crack propagation stage characterised as striation (Fig. 5.3b) and mechanical rupture stage of tensile overload (Fig. 5.3a). The main difference between the two failure models in Fig. 5.15 is strongly dependant on the microstructure cluster. The first failure mode observed on a fracture surface with only two grains demonstrate the fracture mode observed in Fig. 5.11 and schematically presented in Fig. 5.15e, the second fracture mode represent a HCF failure crack within multi-grain cluster as presented in Fig. 5.15f and demonstrated in Fig. 5.12b. It appears that the direct effect of grain size on fatigue crack formation is the size of the facet. As demonstrated in Fig. 5.15e-f, the radial dimension of the facet along Normal Direction (ND) is the same length of the grain diameter (grain 1 in Fig. 5.15 e and f). This clearly demonstrates that the crystallographic facet in a favourably oriented grain for octahedral slip system activation can provide unrestricted slip plane and an easy crack propagation until reaching the grain boundary and encountering neighbouring grains. In addition, the most distinguished fatigue crack feature is that in mode 1 with large grain size, the crack initiation and propagation areas are both confined in the same grain, see grain 1 in Fig. 5.15e. Whilst in mode 2 with smaller grains, the crack initiates and grows in Grain 1 (high Schmid Factor) and propagates through encountering neighbouring grain (Grain 3), due to the impediment effect and crack propagation resistance from Grain 2 (low Schmid Factor Brass oriented grain). It is clear that microstructure cluster, *i.e.*, the orientations and microtexture of the grain cluster (surrounding grains around crack initiation plane), have a great effect on fatigue initiation and propagation during HCF failure. Thus, the microstructure cluster can play a vital role in crack acceleration or retardation depending on the cluster configuration of hard and soft grains.

5.5 Conclusions

Based on detailed microstructure/microtexure analysis and fractography observations of failed turbocharger wheel blades during in-house LCF and HCF tests, together with strain mapping and GND density calculation via high-resolution EBSD, distinct deformation and failure mechanism for LCF and HCF are proposed and influence of predominant internal structure heterogeneity in terms of carbides, dendrite and grain orientation are demonstrated and verified.

1. Different fatigue cracks initiation and propagation mechanisms for LCF and HCF of wheel blades during in-house tests are established. The failure mechanism was greatly affected by loading conditions, microstructure and geometrical factor of wheel blades.
2. HCF failure usually occurred on the upper position of turbine wheel blades and the fracture surface features consist of facet, beach marks and clearly-defined striations. Whilst LCF failure occurred on the surface of blade root where highest stress concentration exists, and numbers of secondary cracks and dendrite structure can be found close to the crack initiation sites.
3. The microstructures across the turbine wheel blades is not homogenous due to different cooling rate along the blade during investment casting process. In upper position of blades, relatively uniform microstructure is produced with weak dendrite structure as well as fine and evenly distributed carbides. Whilst in the blade root area, well connected dendrite network with larger dendrite arm size and large cluster-like carbides are observed.
4. During LCF, once cracks initiated due to high applied stress level, cracks propagated via oxidised carbides paths, and the connecting structure of carbides in the lower location of the blade facilitated the failure process. In the later stage of cracks propagation, the weakened interdendrite area rotate to accommodate the increased plastic strain during loading, leading to the hard grain fragmentation and catastrophic failure.
5. The effect of carbides and interdendrite morphology on LCF failure mechanism are examined by GND distribution and evolution. Higher GND density was found around carbides than in γ matrix, and greater values in interdendrite than in dendrite areas. A very high GND density was found at the tip of oxidised

carbides and ahead/tip of small cracks due to volume expansion during oxidation process.

6. During HCF, the crack initiations are determined by grain orientations, microstructure cluster and casting defects. It is observed that most of the facet formed on {111}<1-10> slip system with highest Schmid factor values. Moreover, the cracks initiation during HCF test was defect-sensitive and an easy slip system activation for a slip plane with high Schmid factor is assisted by the presence of porosity.
7. The size of facet is limited by grain size. It is concluded that the number, size and distribution of the grains surrounding facet grain have a great effect on the crack propagation path.
8. Depending on different fatigue initiation and propagation mechanisms in LCF and HCF proposed in this study, it is recommended that LCF resistance for turbine wheel blade can be increased by microstructure modification such as reducing carbides size, disrupting carbide network and connectivity. Whilst for HCF resistance it is highly recommended to reduce the casting defects and controlling the microstructure/microtexture clusters in order to retard crack propagation.

References

[1] H. Matysiak, M. Zagorska, A. Balkowiec, B. Adamczyk-Cieslak, R. Cygan, J. Cwajna, J. Nawrocki, K.J. Kurzydłowski, The microstructure degradation of the IN 713C nickel-Based Superalloy after the stress rupture tests, J. Mater. Eng. Perform. 23(9) (2014) 3305-3313.

[2] M. Coleman, H. Alshehri, R. Banik, W. Harrison, S. Birosca, Deformation mechanisms of IN713C nickel based superalloy during Small Punch Testing, Mater. Sci. Eng. A 650 (2016) 422-431.

[3] D. Gelmedin, K.-H. Lang, Fatigue behaviour of the superalloy IN 713C under LCF-, HCF- and superimposed LCF/HCF-loading, Procedia Engineering 2(1) (2010) 1343-1352.

[4] L. Kunz, P. Lukáš, R. Konečná, High-cycle fatigue of Ni-base superalloy Inconel 713LC, Int. J. Fatigue 32(6) (2010) 908-913.

[5] L. Kunz, P. Lukáš, R. Konečná, S. Fintová, Casting defects and high temperature fatigue life of IN 713LC superalloy, Int. J. Fatigue 41 (2012) 47-51.

[6] M. Petrenec, K. Obrtlík, J. Polák, Inhomogeneous dislocation structure in fatigued INCONEL 713 LC superalloy at room and elevated temperatures, Mater. Sci. Eng. A 400-401 (2005) 485-488.

[7] N. Boutarek, D. Saïdi, M.A. Acheheb, M. Iggui, S. Bouterfaïa, Competition between three damaging mechanisms in the fractured surface of an Inconel 713 superalloy, Mater. Charact. 59(7) (2008) 951-956.

[8] M. Goto, D. M. Knowles, Initiation and propagation behaviour of microcracks in Ni-base superalloy Udimet 720 Li, Eng. Fract. Mech. 60(1) (1998) 1-18.

[9] Z.K. Chu, J.J. Yu, X.F. Sun, H.R. Guan, Z.Q. Hu, High cycle fatigue behavior of a directionally solidified Ni-base superalloy DZ951, Mater. Sci. Eng. A 496(1–2) (2008) 355-361.

[10] H.S. Kitaguchi, H.Y. Li, H.E. Evans, R.G. Ding, I.P. Jones, G. Baxter, P. Bowen, Oxidation ahead of a crack tip in an advanced Ni-based superalloy, Acta Mater. 61(6) (2013) 1968-1981.

[11] T. Connolley, P.A.S. Reed, M.J. Starink, Short crack initiation and growth at 600 °C in notched specimens of Inconel718, Mater. Sci. Eng. A 340(1–2) (2003) 139-154.

[12] A. Pineau, D.L. McDowell, E.P. Busso, S.D. Antolovich, Failure of metals II: Fatigue, Acta Mater. 107 (2016) 484-507.

[13] P. Kontis, E. Alabort, D. Barba, D.M. Collins, A.J. Wilkinson, R.C. Reed, On the role of boron on improving ductility in a new polycrystalline superalloy, Acta Mater. 124 (2017) 489-500.

[14] P. Kontis, D.M. Collins, A.J. Wilkinson, R.C. Reed, D. Raabe, B. Gault, Microstructural degradation of polycrystalline superalloys from oxidized carbides and implications on crack initiation, Scr. Mater. 147 (2018) 59-63.

[15] S. Birosca, F. Di Gioacchino, S. Stekovic, M. Hardy, A quantitative approach to study the effect of local texture and heterogeneous plastic strain on the deformation micro-mechanism in RR1000 nickel-based superalloy, Acta Mater. 74 (2014) 110-124.

[16] M. Calcagnotto, D. Ponge, E. Demir, D. Raabe, Orientation gradients and geometrically necessary dislocations in ultrafine grained dual-phase steels studied by 2D and 3D EBSD, Mater. Sci. Eng. A 527(10) (2010) 2738-2746.

[17] P.S. Karamched, A.J. Wilkinson, High resolution electron back-scatter diffraction analysis of thermally and mechanically induced strains near carbide inclusions in a superalloy, Acta Mater. 59(1) (2011) 263-272.

[18] T. Benjamin Britton, A.J. Wilkinson, Stress fields and geometrically necessary dislocation density distributions near the head of a blocked slip band, Acta Mater. 60(16) (2012) 5773-5782.

[19] J. Jiang, J. Yang, T. Zhang, J. Zou, Y. Wang, F.P.E. Dunne, T.B. Britton, Microstructurally sensitive crack nucleation around inclusions in powder metallurgy nickel-based superalloys, Acta Mater. 117 (2016) 333-344.

[20] J. Jiang, J. Yang, T. Zhang, F.P.E. Dunne, T.B. Britton, On the mechanistic basis of fatigue crack nucleation in Ni superalloy containing inclusions using high resolution electron backscatter diffraction, Acta Mater. 97 (2015) 367-379.

[21] J. Nye, Some geometrical relations in dislocated crystals, Acta Metall. 1(2) (1953) 153-162.

[22] M. Ashby, The deformation of plastically non-homogeneous materials, Philos. Mag. 21(170) (1970) 399-424.

[23] A. Arsenlis, D. Parks, Crystallographic aspects of geometrically-necessary and statistically-stored dislocation density, Acta Mater. 47(5) (1999) 1597-1611.

[24] W. He, W. Ma, W. Pantleon, Microstructure of individual grains in cold-rolled aluminium from orientation inhomogeneities resolved by electron backscattering diffraction, Mater. Sci. Eng. A 494(1-2) (2008) 21-27.

[25] A.J. Wilkinson, D. Randman, Determination of elastic strain fields and geometrically necessary dislocation distributions near nanoindents using electron back scatter diffraction, Philos. Mag. 90(9) (2010) 1159-1177.

[26] J. Jiang, T.B. Britton, A.J. Wilkinson, Measurement of geometrically necessary dislocation density with high resolution electron backscatter diffraction: Effects of detector binning and step size, Ultramicroscopy 125 (2013) 1-9.

[27] T.M. Pollock, S. Tin, Nickel-based superalloys for advanced turbine engines: chemistry, microstructure, and properties, J. Propul. Power 22(2) (2006) 361-374.

[28] F.P.E. Dunne, A.J. Wilkinson, R. Allen, Experimental and computational studies of low cycle fatigue crack nucleation in a polycrystal, Int. J. Plast 23(2) (2007) 273-295.

[29] L. Engel, H. Klingele, An atlas of metal damage, Wolfe Publishing Ltd. (1981) 271.

[30] A. Bhambri, T. Kattamis, J. Morral, Cast microstructure of Inconel 713C and its dependence on solidification variables, Metall. Trans. B 6(4) (1975) 523-537.

[31] J. Jiang, T. Britton, A. Wilkinson, Evolution of dislocation density distributions in copper during tensile deformation, Acta Mater. 61(19) (2013) 7227-7239.

[32] A.N. Stroh, A theory of the fracture of metals, Adv. Phys. 6(24) (1957) 418-465.

[33] V.V.C. Wan, J. Jiang, D.W. MacLachlan, F.P.E. Dunne, Microstructure-sensitive fatigue crack nucleation in a polycrystalline Ni superalloy, Int. J. Fatigue 90 (2016) 181-190.

[34] L.G. Zhao, J. Tong, M.C. Hardy, Prediction of crack growth in a nickel-based superalloy under fatigue-oxidation conditions, Eng. Fract. Mech. 77(6) (2010) 925-938.

[35] J. Miao, T.M. Pollock, J.W. Jones, Crystallographic fatigue crack initiation in nickel-based superalloy René 88DT at elevated temperature, Acta Mater. 57(20) (2009) 5964-5974.

[36] I. Bantounas, D. Dye, T.C. Lindley, The role of microtexture on the faceted fracture morphology in Ti–6Al–4V subjected to high-cycle fatigue, Acta Mater. 58(11) (2010) 3908-3918.

[37] P. Peralta, C. Laird, Fatigue fracture at bicrystal interfaces: experiment and theory, Acta Mater. 46(6) (1998) 2001-2020.

[38] C. Blochwitz, J. Brechbühl, W. Tirschler, Analysis of activated slip systems in fatigue nickel polycrystals using the EBSD-technique in the scanning electron microscope, Mater. Sci. Eng. A 210(1) (1996) 42-47.

Chapter 6: Deformation Mechanism of IN713C during Standard Fatigue Tests

Abstract

The polycrystalline IN713C produced via investment casting is one of the widely-used nickel-based superalloy in automotive and aerospace industries. This alloy, however, has an apparent inhomogeneous microstructure generated during casting and contains dendritic structure that gives rise to strain localisation during loading. Yet, the effect of dendrite structure formed during solidification on γ', carbides, TCP precipitations and morphologies, which directly influence strain distribution in the components, is rarely studied. In the present study, IN713C cast bars are tailored with three different grain structures, *i.e.*, transition, equiaxed and columnar, with a substantial grain size differences. The produced bars are tested using both strain controlled LCF (Low Cycle Fatigue) and stress controlled HCF (High Cycle Fatigue) at 650 °C. The results showed that most of fatigue cracks initiated from casting porosities and fatigue life extended in the microstructure with a small grain size during both HCF and LCF loadings. It is also demonstrated that fatigue striations are mainly observed within dendrite areas during crack propagation, whereas the higher GND (Geometrically Necessary Dislocation) density were predominantly observed in the interdendrite areas. Here, we propose a concept of 'Crack Path Unit (CPU)', to describe the deformation micromechanism. By combining fracture surface characteristic methodology and dislocation distribution analyses within the dendrite structural unit size. Furthermore, this model to understand the deformation micromechanism can provide a new perspective on the interpretation of Hall-Petch relationship in casting materials that contain dendritic structure. This is based on the findings in the current study of observing the high crack propagation resistance in the fine grains due to crack path divergence rather than the dislocation pile-up at the grain boundary or in-between the γ/ γ' channels. Moreover, by utilising serial sectioning method followed by layered EBSD scanning, quasi-3-D grain orientation mappings were obtained, and crystallographic texture information were directly correlated with the fracture surface observations. This allowed an investigation of the influence of orientation of individual grains and micro/macro texture on crack propagation rate. This research underlines the critical stage of crack propagation in

fatigue life and its correlations with microstructural parameters, offering potential practical applications by controlling these parameters during IN713C alloy casting process.

6.1 Introduction

Directionally cast nickel-based superalloy, usually referred to as secondary generation superalloys, generally exhibits higher strength at elevated temperatures due to their possession of higher volume fraction of strengthening phase of γ′ (around 70%) compared to forged first generation superalloy which contains around 30% of γ′ [1, 2]. Moreover, superalloy produced via investment casting also has the advantage of minimising machining process compared to the forged alloys, which is of significant economic efficiency and enable massive industrial production. IN713C has been widely used as turbocharger turbine wheel materials in the automotive industry for decades [3, 4]. However, casting has an inherent problem of porosity formation (shrinkage and/or gas pore) and usually results in relatively large grains, which degrades the alloy's fatigue property to a great degree. The fatigue failure is counted for 90% of the total component failures used in critical applications, thus both LCF and HCF in superalloys have received considerable academic and industrial interests [5]. The general concepts and theories of fatigue developed from other metals also have been successfully applied to newly developed superalloys. Although from the fracture mechanics point of view, the crack propagation is the fatigue determining step rather than crack initiation, especially for the alloys used in high temperature applications, however, still more literature on crack initiation are available than on crack propagation stage [6, 7]. Those studies mainly focused on slip bands formation, porosities, inclusions [8, 9] or special grain boundary characteristics [10, 11]. Indeed, the crack nucleation stage covers large portion of the total fatigue life, particularly in HCF regime where the alloy is subjected to low external stresses. It is well established that the crack initiation time is directly related to the presence of the defects such as porosity, pre-existing cracks and inclusions. However, with the technological advancements in the alloys processing routes, these defects that acts as local stress concentration sites, are largely minimised which can delay crack initiation greatly [6]. Nonetheless, defects cannot be eliminated completely even using most advanced processing methods including powder metallurgy, thus stress

concentration points and crack initiation sites are always available. Therefore, fatigue life should be controlled in crack propagation stage via designing an optimum microstructure for crack growth resistance.

The lack of 3-D and non-destructive crack observation in most of the studies in the literature added further difficulty in correlating crack path interaction with individual microstructure features. For instance, fatigue striation, a unique indicative feature in fatigue propagation process that able to provide detailed information about deformation mechanism, can only be observed and analysed after complete fracture. Although striation usually is used as indication of fatigue process occurrence and sometimes quantitatively correlated with propagation rate [12, 13], very few reports have analysed the distribution of striations and their interaction with local microstructures, which is critical in understanding the effects of microstructure on crack propagation process. In general, multi-phenomena occurs during alloy casting, including element partitioning, dendrite formation and second phase precipitation, leading to heterogeneous overall microstructure. This produced microstructure in the solidified alloy allows strain localisation during fatigue loading [14]. The authors of this study believe that in order to obtain complete description of deformation mechanism during fatigue crack propagation stage in cast materials, the effects of dendritic structure, grain size and microtexture should be thoroughly addressed.

The pioneering work about the possible effects of dendrite structure on fatigue life was conducted by Horstemeyer et al. [15] in a die cast magnesium alloy. They demonstrated that the HCF life might be affected by average secondary dendrite arm spacing in addition to the drastic difference in nucleation site size and average grain size. In our earlier work [3] we proposed a strain accommodation model via lattice rotation of interdendrite area in the late stage of crack propagation in IN713C superalloy. However, the question of to what extend the dendrite structure affects crack propagation and overall deformation mechanism remained unanswered.

The effect of grain size on mechanical properties and in particular on fatigue crack growth is another topic studied extensively [16]. The classical empirical Hall-Patch relationship which implies the benefit of small grain size in increasing material strength, has been successfully applied to many metals/alloys. The classical explanation for this

relationship is either dislocation pile-up at grain boundaries as crack barriers in small size grains or large local stress by dislocation accumulation causing neighbouring grain slip activation in large size grains [16]. Many recent researches on slip transmission [17, 18] or dislocation transmission [19] across grain boundary confirmed and further developed this theory. Furthermore, gradient grain size structure has been developed and showed enhanced fatigue crack growth resistance [13]. Nevertheless, Hall-Patch relationship usually apply to homogeneous single-phase materials. In the current investigation we examine to what extent this relationship can be valid in heterogeneous multi-phase system such as in solidified IN713C superalloy and how dislocation accumulation and behaviour can govern Hall-Patch relationship and overall deformation micromechanism during LCF and HCF Loading.

The individual grain crystallographic orientation, microtexture, macrotexture and mesotexture are also significant parameters in determining crack initiation sites as well as crack propagation path. Moreover, it is well established that both grain boundary's tilt and twist misorientation angles should be considered in crack growth investigation [20, 21]. This is due to the significant role of grain boundaries that act as a barrier to slip or crack transfers. However, recognising the grain boundary plane, which is critical for complete grain boundary characterisations, is not straightforward without obtaining 3-D information. Thus, obtaining micro/meso-texture information in 3-D is important to observe the crack path. One difficulty of such study is to provide such 3-D vision of orientation distribution. Moreover, it is important to correlate these microstextures to the crack propagation route and features in 3-D perspective, as striations are essentially formed by the alternative slip activation and blunting on different slip systems which depend on crystallographic orientations [23, 24].

The background of this research is the relationship between fatigue property and microstructure/microtexture in turbine blade used for turbocharger at elevated temperature. The turbine blade produced via investment casting consists of two distinctive grain size structure in different positions. In the current study, standard fatigue test samples have been elaborately refined with different grain structures and standard LCF and HCF tests have been conducted in a controlled way. In addition to crack initiation stage, we pay more attention to the crack propagation stage and its relationship with local microstructural features such as dendrite structure, grain size

and micro/macro/meso-texture, to portray exact deformation mechanism in IN713C nickel-based superalloy.

6.2 Materials and Experiment Procedures

6.2.1 Bars Produced by Investment Casting

The materials used in this study was IN713C nickel-based superalloy with the chemical composition shown in Table 1. As described in Section 1, in the casting process for turbocharger turbine blades, complex geometrical configuration leads to local different solidification parameters such as cooling rate, resulting in disparity of grain structure across the blade, i.e., large columnar grain area, fine equiaxed grains at the tip of blades and transition area between the two [4, 14]. In order to study the effects of all three grain structures on fatigue property, three different microstructures of columnar, equiaxed and transition bars were produced via investment casting at Cummins Turbo Technologies at Huddersfield, UK. The initial LCF property of these bars are recently reported [4]. The detailed manufacturing process for the bars can be found in [4]. Furthermore, based on the experience of first batch samples, the casting parameters have been optimised and better distinguished grain structures were produced in this trail reported here. The produced bars of the three distinctive microstructures, i.e., transition, equiaxed and columnar, are shown in Fig. 6.1a. The EBSD orientation mapping were conducted in the bar area indicated in Fig. 6.1b and shown in Figs. 6.1c, 6.1d, 6.1e for Transition (T), Equiaxed (E) and Columnar (C), respectively. For transition bar, the average grain size transit from ~ 635 μm (upper part in Fig. 6.1c) to ~ 2145 μm (lower part in Fig. 6.1c), while for equiaxed and columnar samples, the average grain size are ~ 1745 μm (Figs. 6.1d and 6.1f) and ~ 2960 μm (Figs. 6.1e and 6.1f), respectively. The IPFs (Inverse Pole Figures, Figs. 6.1c-e) show no strong texture in any of the bars. A typical microstructure that existed in all three bars consisted of dendritic structure (Fig. 6.2a), MC-type carbides mainly distributed within interdendrite area (Fig. 6.2b) and precipitate strengthening phase γ′ in both dendrite area (Fig. 6.2c) and interdendrite area (Fig. 6.2d) with average size of ~ 500 nm. It should be emphasised here that all three bars show no significant variation in dendrite, carbides and γ’ shape, size and morphologies.

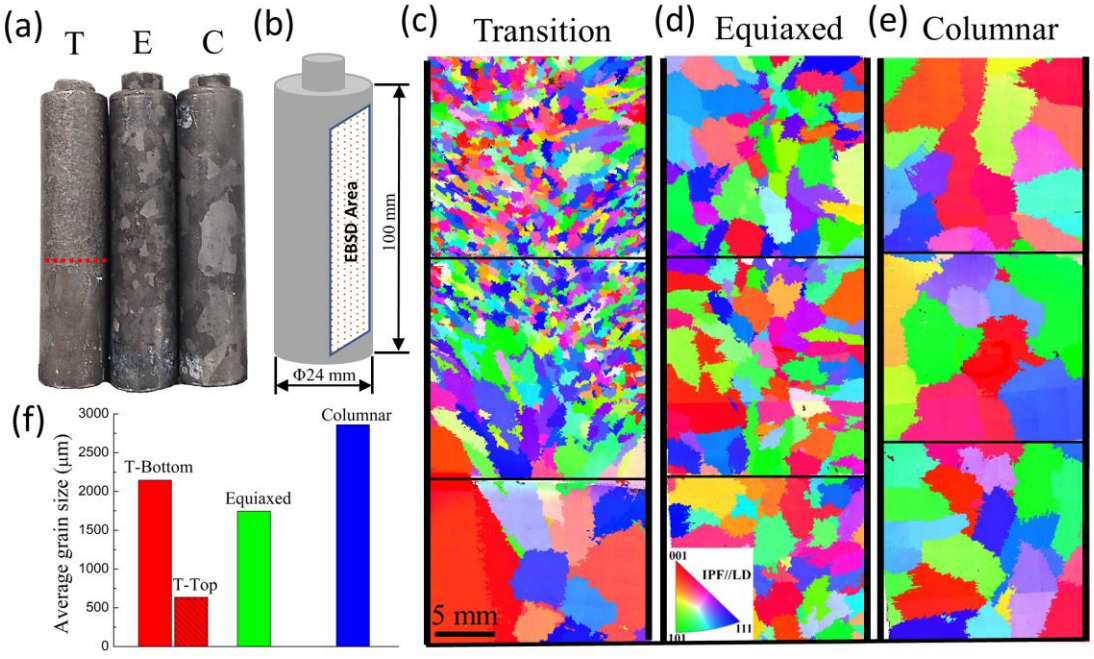

Fig. 6.1 Received bars with three different grain structures: T(Transition), E(Equiaxed) and C(Columnar). (a) and (b) are real size material and schematic bars, respectively; (c-e) IPFs (Inverse Pole Figures) of these bars show grain structures. Scanned areas are shown in (b) and notice that they are cut and separately scanned due to very large area; (f) average grain size of these structures.

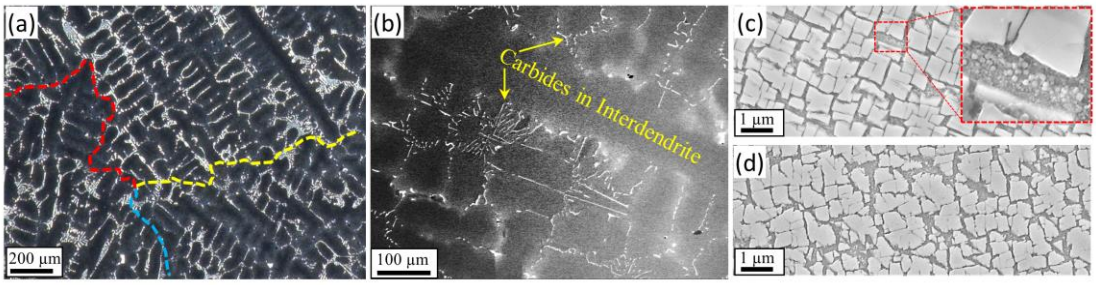

Fig. 6.2 Representative microstructure in received materials: (a) dendrite structure within three grains, dashed lines show grain boundaries; (b) carbides segregating in interdendrite area; (c) and (d) γ′ in dendrite area and interdendrite area, respectively; Magnified area in (c) shows very small γ′ in γ channels.

6.2.2 Fatigue Testing

The cylindrical fatigue test specimen with geometry is shown in Fig. 6.3a and a gauge length of 18 mm and a gauge diameter of 6 mm were machined from as-received bars. The LCF tests were conducted according to ASTM E606 standards and under strain control with maximum strain of 0.4%. The HCF tests were conducted according to ASTM E466 standards and under stress control. The maximum stress values were obtained by tensioning the samples up to 0.2% strain and was ~ 335 MPa for all the samples. The test frequency for LCF and HCF were 0.5 Hz and 30 Hz, respectively. Both LCF and HCF tests were conducted at the R-ratio of -1, with sinusoidal waveform and at 650 °C to simulate the turbocharger wheel operating conditions.

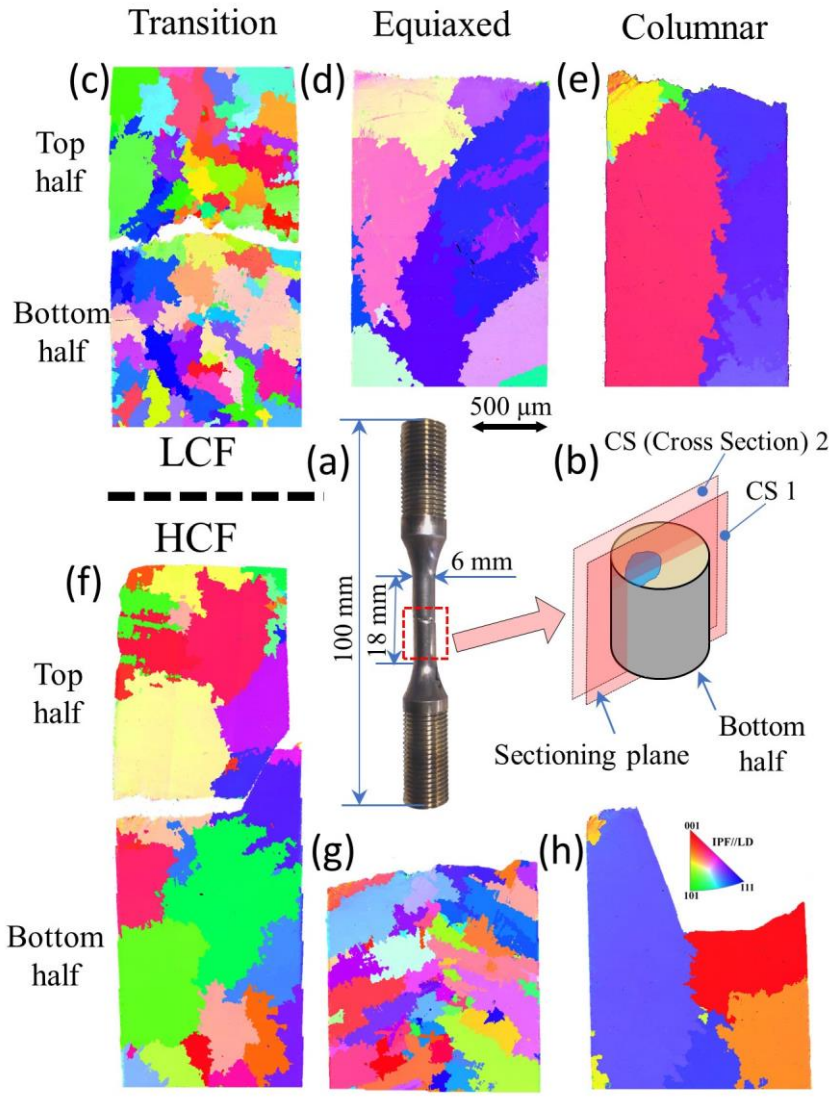

Fig. 6.3 Grain structure around actual fractured area in tested bars: IPFs in (c-e) for LCF and (f-h) for HCF; (a) a representative failed bar (L-C) with major dimension size; (b) schematic

half fractured sample with sectioning planes showing EBSD scan position (only two CSs shown here). To examine assumed transition structure, both half fractured samples are characterised and displayed. The results show no transition structure in the centre of the bar with 'nominal' transition structure. And the actual grain size might not fit well with assumed grain structure compared to Fig. 6.1.

6.2.3 Microstructure Characterisations

Following the fatigue tests, the fracture surfaces of failed sample were cleaned by ultrasonic bathing in detergent solution for 20 minutes and then in ethanol for 20 minutes. Fractography observations were then carried out using Keyence light microscope and Scanning Electron Microscope (SEM), using Zeiss (EVO) and Jeol 7800F Field Emission Gun (FEG) microscopes. After complete fracture surface characterisation, serial sectioning of the failed fatigue samples along Loading Direction (LD) were performed in order to correlate the fracture surface with microstructure and microtexture beneath the fracture surface in three dimensions (3-D). A schematic graph in Fig. 6.3b shows the sectioning process with only two sectioning planes (CS (Cross Section) 1 and CS 2) displayed. The 3-D sectioning procedures were as follows: The first flat plane along LD was made by carefully grinding the cylindrical sample to nearly parallel to the central crack growth direction from initiation sites with the help of optical microscope during grinding process. Then the sample was mounted with conductive bakelite with the flat surface been further grinded, polished and culminated with 0.05 μm colloidal silica for 20 min, followed by EBSD scanning. After first layer characterisation (microstructure and EBSD mapping), the sample was further grinded and polished by removing 300~500 μm in depth according to the average grain size of the cast specimen followed by EBSD scanning. This subsequent layer-by-layer 'grinding-polishing-EBSD scanning' was carried out with the sample dismounting in between every two sections for SEM observation to align the fracture surface with the EBSD scanned planes. In the meantime, after each EBSD scanning, the mounted sample was electrolytically etched using 10% phosphoric acid at 3-5V for 3-5s to γ', carbides, oxides and secondary cracks.

High resolution imaging and EBSD mapping were performed using JEOL 7800F FEG-SEM equipped with AZTEC data acquisition and analysis software with a Nordlys

EBSD detector. The SEM operating voltage used was 10-20 kV for imaging and 20 kV for EBSD scan with a current of ~ 14nA. For layer-by-layer and large EBSD mapping, a binning of 8×8 and step size of 8 µm were used to balance the time consumed and quality required. Whilst for High Resolution (HR) scanning used for GND calculation, a binning of 4×4 and step size of 100 nm were selected, with an exposure time of 150 ms per pattern. The EBSD data analysis was conducted using standard HKL-EBSD Channel 5 software package. The GND and slip trace mapping were calculated using in-house python code. The principles and details of the calculations are reported previously in [3, 25]. Furthermore, the dislocation accumulations close to initiation sites and beneath fatigue striations were studied using Focus Ion Beam (FIB)-Transmission Electron Microscopy (TEM) and FEI 200F Scanning Transmission Electron Microscopy (STEM)-High Angle Annular Dark field (HAADF). Further TEM specimens close to initiation sites were cut out as thin plate along LD and then grinded and polished to ~ 100 µm in thickness. After punching into 3 mm diameter foils, they were further polished to ~50 µm, followed by twin-jet electronic polishing using Struers Tenupol III. For this, an electrolyte of 10% perchloric acid in methanol was used at -20 ^{o}C and 20 V. The dislocations on {111} planes were observed and STEM-HAADF mode was used as they can give better contrast for dislocation observation in TEM [26].

6.3 Results

6.3.1 General Description of Crack Initiation and Propagation during LCF and HCF.

6.3.1.1 Fatigue Life and Overview of Fracture Surface

The cross-section microstructure beneath the fracture surface for the LCF and HCF tested samples are shown in Fig. 6.3. The fracture surface of each tested sample together with fatigue life for LCF and HCF are shown in Fig. 6.4 and Fig. 6.5, respectively. Figs. 6.3c-h shows EBSD-derived IPF // LD maps, revealing the grain size, shape and orientation in the cross-section planes that are indicated by the red dashed lines on each sample in Figs. 6.4a, d, g and Figs. 6.5a, d, g. Given the relatively uniform grain size distribution in Equiaxed (E) and Columnar (C) grain structures, only half of the failed samples (bottom half) were prepared for EBSD mapping. However, for Transition (T)

structure, both halves of the fractured samples have been mapped to try to identify transition area, see Figs. 6.3c and 6.3f. From Fig. 6.3, it is clear that the columnar microstructure exhibited largest grain sizes among the three produced microstructures. However, the grain size in equiaxed bar tested under HCF condition (Fig. 6.3g), is significantly smaller than those of equiaxed bar tested under LCF condition in Fig. 6.3d. Thus, there are some grain size disparities in the bars. However, the main purpose of achieving small equiaxed grains to be compared to a large columnar microstructure was produced from the investment casting trails. Moreover, transition area could not be found around failure area in transition samples. This is expected as producing transition area in the centre of the cast bar to be machined as a centre of the testing specimen is very difficult. Also, there is some discrepancy in the grain sizes in bars of transition microstructure, see Figs. 6.3a and 6.3f. Thus, the produced transition bars cannot be representative of actual transition microstructure in turbine wheel blades. Therefore, due to the inconsistency between actual produced microstructures and expected grain sizes, the present study will focus on the effects of grain size in individual bars on fatigue properties. However, here we use the initial notation of originally designated microstructure for simplicity purposes, e.g., T stands for Transition structure although it does not demonstrate the fatigue failure in transition area. For clarity purpose L and H notations are used for the samples tested in Low and High cycle fatigues, respectively. For example, L-T, L-E and L-C stand for LCF-Transition, LCF-Equiaxed and LCF-Columnar, respectively, see Figs. 6.4 and 6.5.

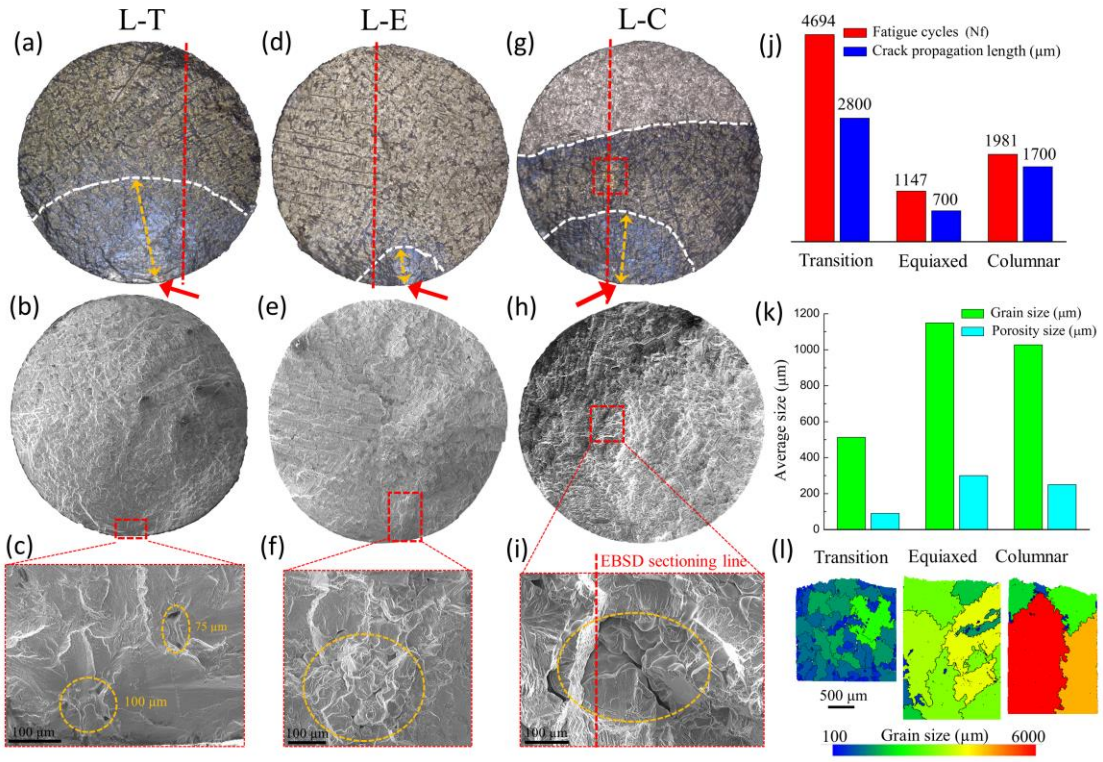

Fig. 6.4 Fracture surface in LCF samples by optical microscope and SEM. (a-c) for L-T (LCF-Transition), (d-e) for L-E and (g-i) for L-C. Red arrows in (a) (d) (g) indicate crack initiation sites, white dashed lines distinguish crack propagation stages, yellow double arrows show crack propagation distance and red dashed lines indicate EBSD position. (c) and (f) show porosities in initiation sites (highlighted by yellow dashed circles) and (i) shows a large pore in the middle of fracture surface in L-C. (j) Fatigue life (cycles) for each sample and the crack propagation distance measured by the yellow double arrows; (k) Average grain size of each sample and average porosity size; (l) Grain structure with all Euler color for each sample.

The overview of the fracture surface investigation using from both optical and scanning electron microscope is presented in Figs. 6.4 and 6.5. Nearly all the samples failed from subsurface casting pores during both LCF and HCF testing conditions. The crack initiation sites are identified as indicated by the red arrows and dashed boxes in Figs. 6.4 and 6.5. For instance, L-T sample failed in an area where three small pores with size of 70~100 μm are present, see Fig. 6.4c; whereas, in L-E sample, the failure started on a site exhibiting a cluster of porosities with size of ~ 250 μm, see Fig. 6.4f. Similarly, in HCF samples, the size of subsurface porosities in H-T and H-E are ~ 290 and 140 μm, respectively, see Figs. 6.5c and 6.5f. The average grain and porosity sizes where the crack initiated are shown in Figs. 6.4k and 6.5k. It seems there is correlation

between the size of porosity and grain sizes and they scaled up accordingly, i.e., the larger the grain, the larger the porosity. It should be emphasised here, although the crack in L-C initiated on the sample surface, i.e., not a sub-surface crack, a very large porosity in a size of ~ 300 μm was found in the central part of fracture surface, see Figs. 6.4h and 6.4i. A similar large porosity was found in the centre of the columnar sample in HCF, i.e., H-C, see Figs. 6.5h and 6.5i. This will be further discussed in Section 3.1.2 and Section 4.2.

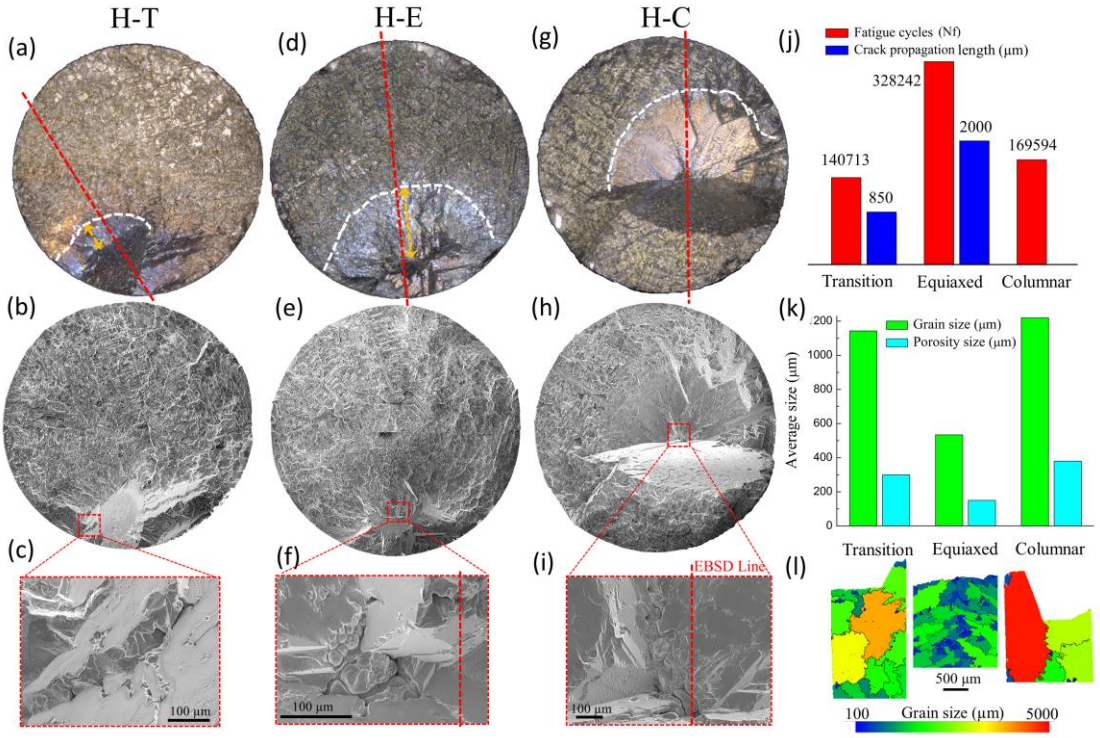

Fig. 6.5 Fracture surface in HCF samples by optical microscope and SEM. (a-c) for H-T (HCF-Transition), (d-e) for H-E and (g-i) for H-C. White dashed lines in (a) (d) (g) distinguish crack propagation stages, yellow double arrows show crack propagation distance and red dashed lines indicate EBSD position. (c) and (f) show porosities in initiation sites (highlighted by yellow dashed circles) and (i) shows a large pore in the middle of fracture surface in L-C. (j) Fatigue life (cycles) for each sample and the crack propagation distance measured by the yellow double arrows; (k) Average grain size of each sample and average porosity size; (l) Grain structure with all Euler color for each sample.

In general, the fatigue failure process during both LCF and HCF conditions consisted of three distinctive stages: crack initiation (mainly from casting porosity), propagation and overload regimes. This is consistence with our previous reports on actual failed

turbine blades [3]. It is well established that the fatigue property of superalloy is sensitive to mean stress level at elevated temperature [5, 16]. Effectively, this leads to the major differences in crack initiation sites between LCF and HCF. During HCF test, with low mean stress applied, the crack will grow crystallographically along {111} planes (termed 'mode II' [16]), leading to the formation of 'facet' immediately after crack initiation from a defect, see Fig. 6.5. The authors of the current study believe that facet formation is an integral part of the crack initiation stage during HCF as the pore's initiation point will be within the facet that is created straight afterward. The crack propagation stage is characterised as a relatively flat surface and fatigue striations which will be quantitatively analysed in detail in following sections. The overload (final rupture) regime, however, is featured with rough fracture surface and visible dendrite structures. The primary dendrite arms can be clearly seen in overload areas, see Fig. 6.4d as an example.

It is interesting to notice that the colour contrast in optical images is very useful in distinguishing all the three stages of crack formation, propagation and rupture. The crack propagation areas are usually covered by shinny dark blue colour due to oxidation occurrence at 650°C, whereas the overload areas by yellow or whitish colours. The white dashed lines in Figs. 6.4 and 6.5 are used to separate the propagation area from the overload area. The exception is L-C sample where there are 2 white dashed lines as there is a 'mixed area' between the lines consisting both crack propagation and overload features, which will be further discussed in Section 4.3.

It is evident from Figs. 6.4j-I and 6.5j-I that both LCF and HCF longer fatigue lives benefit from smaller grain size. Specifically, during LCF, L-T sample with ~510 μm average grain size have more than four times longer life (4694 cycles) than L-E sample (1147 cycles) with ~ 1150 μm grain size, and double life times than L-C sample (1981cycles) with ~ 1030 μm grain size, see Figs. 6.4j, 6.4k. Similarly, during HCF, small grain sample (H-E) has much higher fatigue cycles than large grain samples (H-T and H-C), see Figs. 6.5j-i. The crack propagation distance, defined and measured from initiation site to the centre of division line between propagation and overload areas (i.e., the white dashed line in Figs. 6.4 and 6.5), are indicated by the yellow dashed lines on the same figures. This type of analyses mainly shows that the higher fatigue life in small grain samples are partially and directly resulted from longer fatigue crack propagation stage, in addition to smaller porosity size in small grain sample can

contribute to higher fatigue life [27, 28]. The relationship between grain size, porosity size and crack propagation distance will be further discussed in Section 4.

6.3.1.2 Crack Initiation: Shrinkage Cavity (Porosity)

Fig. 6.6 presents three examples of porosities in cross-section profile with Fig. 6.6a-c showing for H-C, Fig. 6.6d-f for L-C, and Fig. 6.6g for H-E bars. In order to reveal the pores in the cross section, the EBSD mapping was performed along the cross-section lines as shown in Figs. 6.5i, 6.4i and 6.5f, respectively, indicated as red dashed lines. It should be noted that pores shown in H-C and H-E cross-section images are the actual crack initiation sites, while the pore in L-C sample is within the propagation area as indicated by red boxes in Figs. 6.4g and 6.4h. For H-E sample, the cross-section plane in which the EBSD mapping was performed is slightly missed the pore during grinding process, see Fig. 6.5f, thus the pore morphology is not available in this sample, see Fig. 6.6g. The curvy shaped surface morphology of the pores in the samples, as shown in Figs. 6.6b and 6.6e, indicates that most of the porosities observed, especially those initiated cracks, are casting pores rather than gas pores [6]. Moreover, the imposed EBSD-IPF maps on SEM images as shown in Figs. 6.6a, d and g suggest that most of porosities formed on the grain boundaries. Furthermore, the GND mapping in Fig. 6.6c showed a high GND density around the crack-initiated porosity and the GND intensity is varying depending on the pore segment curvature degree. This high GND distribution reflect the dislocation evolution and accumulation during the crack nucleation period, and consistent with the modelling result from [29]. It is interesting to note the relatively low GND density around the porosity in crack propagation area in Fig. 6.6f, compared to the ones in Fig. 6.6c. This dislocation density disparity indicates different effects of porosity in crack initiation and propagation stages. Further GND density distribution analyses revealed: (a) very low GND density in large γ′, see Fig. 6.6b, c, indicating the 'hard' nature of γ′. This is consistent with the report in [30]; (b) high GND density around carbides, see Figs. 6.6e, f, showing carbides/crack direct interaction as reported in [3, 31]; (c) high GND density ahead of secondary crack tip, see Figs. 6.6e, f, this is considered to be one of the essential criteria for crack propagation according to recent studies by Jiang et al. [8] and Liu et al. [3].

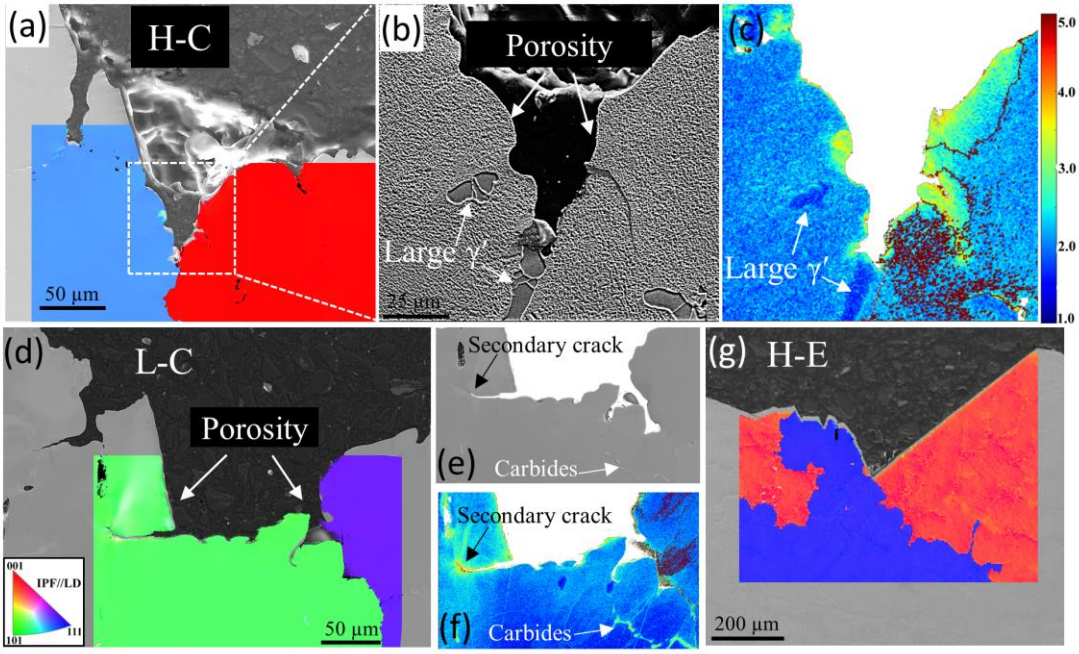

Fig. 6.6 Cross section of porosities. (a-c) porosity of initiation site in H-C, sectioning line is shown in Fig.6.5i with red dashed line, (b) The magnified area of white dashed rectangular area in (a), and (c) GND map of (b). (d) The large middle porosity in Fig. 6.4i (EBSD position is shown with red dashed line), (e) and (f) show the EBSD area and GND map, respectively. (g) The position very close to initiation porosity in H-E, the sectioning position is shown with the red dashed line in Fig. 6.5f. IPFs are superimposed on scanning surface in (a), (d) and (g). Step size for GND mapping is 200 nm.

6.3.1.3 Crack Propagation Stage

A general description of crack propagation process is shown macroscopically in Figs. 6.7b, c and microscopically in Figs. 6.7d-k for L-E sample. The major propagation areas are divided into low and high ΔK (range of stress intensity factor) according to the crack advancement distance from the crack initiation site (porosity here) [15]. Between crack propagation and overload areas, a transition or 'mixed area' are also schematically shown in Fig. 6.7a. This transition area is characterised with a mixed striation (common feature in propagation area) and rough dendrite structure (common feature in overload area). This is clearly presented as a striation 'valley' located between two interdendrite 'hills' in Fig. 6.7f. It is generally believed that fatigue striation is the most distinguishable feature in fatigue crack propagation are on fracture surface. Here, we assume that the striations were produced based on cycle-by-cycle mode and determine

the crack propagation rate by measuring the average spacing between the adjacent striations. This assumption has been previously verified for wide stress amplitudes [12] and in very low stress amplitude [24]. In the current study, the Backscatter (BS) electron mode in high-resolution SEM system was used to characterise the unclear striation lines as it provides higher contrast compared to Secondary Electron (SE) mode. This was especially useful at very early stage of propagation when crack propagation rate is low and striation spacing is very small. An example of such a faded striation in low ΔK region (100 μm away from initiation point) is shown in Fig. 6.7d, and the propagation rate was measured to be ~ 200 nm per cycle. As the crack further propagated, the propagation rate increased to 0.8 μm / cycle in the high ΔK region and 1.8 μm / cycle in the transition area, see Fig. 6.7e and Fig. 6.7f, respectively.

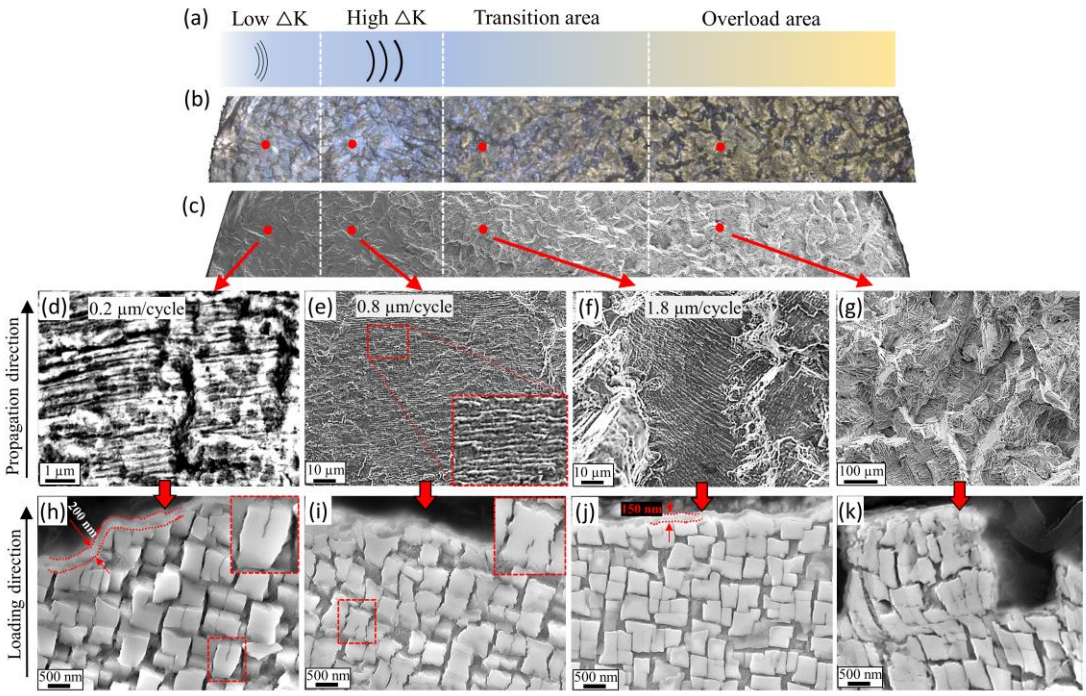

Fig. 6.7 General features in sequential crack propagation stages, exemplified from sample L-T. (a) schematically showing different propagation stages with striations (black curved lines) superimposed. (b) and (c) Part of whole fracture surface by OP and SEM, respectively. (d-g) Fatigue striations as major characteristics are shown in each stage corresponding to the area in (c). (h-k) γ′ morphology immediately beneath the fracture surface in (d-g) individually. Very thin oxidation layer can be noticed, and the thickness are indicated by double dotted lines in (h) and (j).

The effects of loading stress during the crack propagation stage and loading history can be further revealed by microstructure evolution beneath the fracture surface. Fig. 6.7h-k present the evolution of γ' morphology immediately under the fracture surface in the 4 regions in Fig. 6.7d-g. At low ΔK region when stress is low, the cubic γ' almost keep its original shape except very few γ' are slightly deformed with curvy γ′ boundaries, as highlighted in the inset of Fig. 6.7h. Whereas, at high ΔK region when stress is sufficiently high and propagation process (loading period) is long (because propagation rate is not the highest at this stage), most of γ′ have been distorted with 'hard toothed saw edge' boundaries, as magnified in the inset in Fig. 6.7i. It should be noted that at overload region the γ′ also have been deformed but with elongated shape (Fig. 6.7k), which explains the tensile rupture mode in final catastrophic overload stage as expected. However, the γ′ at transition region was found (unexpectedly) undeformed, see Fig. 6.7j, similar to that in untested samples (Fig. 6.2c). This is might partly because the propagation rate at this region is relative high so that there was not enough time for deformation happened (although the stress is relatively high).

The fatigue tests were conducted at 650 ºC in air and as explained in Section 3.1.1, the oxidation effects were observed via blue colour contrast in the optical images shown in Figs. 6.4, 6.5, and 6.7b. This oxidation occurrence could also be confirmed by a shallow oxide scale observed on the samples' cross-section, see the double red dashed lines in Figs. 6.7h-j. The thickness of the oxide scale in low ΔK area (~200 nm, see Fig. 6.7h) is slightly higher than in transition area with ~150 nm in thickness (Fig. 6.7j) due to longer air exposure at low ΔK location. Furthermore, the effects of oxidation on crack propagation was further revealed by oxidised carbides. Fig. 6.8a shows the role of oxidised carbides in inducing and facilitating secondary crack growth. Figs. 6.8b and 6.8c show the oxidised carbides on the fracture surface, i.e., primary crack plane. It is evident from the figures that MC-type carbides oxidation played an important role in fatigue crack diversion and propagation at elevated temperature. This particular effect on carbide oxidation on crack growth has been reported previously in [3, 11, 32].

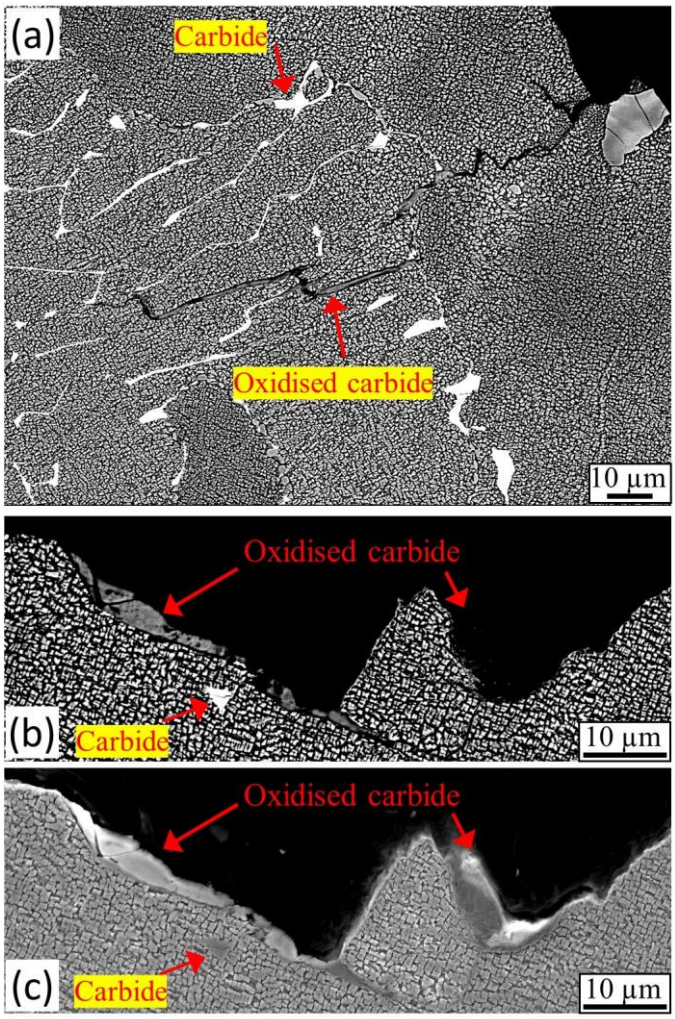

Fig. 6.8 oxidation assisted crack propagation: oxidised carbides along secondary crack (a) and primary crack ((b) and (c)).

6.3.2 Fatigue Striation and GND Local Accumulations

6.3.2.1 Fatigue Striation within Dendritic Structure

The detailed fatigue striations were characterised using HR-SEM. A very interesting relationship between striation distribution and dendrite structure was found. It is established that the fatigue striation was only limited in dendrite core areas (including both primary dendrite area and secondary dendrite area) during both LCF and HCF. Fig.6. 9 shows three examples of striations within secondary dendrite areas: Fig. 6.9a-d, Fig. 6.9e-h and Fig. 6.9i obtained from sample L-C, H-E and L-T, respectively. The optical images (Figs. 6.9a, e, i) show that the fracture surface in propagation areas were

covered by small intermittent blocky shape areas with blue colour and narrow brownish channels separating them. On a macroscale level, these individual blocky areas present a wave-like shape along crack propagation direction, see in Figs. 6.9e and 6.9f. The brownish and bluish parts however, are the interdendrite and secondary dendrite areas, respectively, see Fig. 6.9i. This dendrite structure can be further confirmed by measuring the size of blue area in SEM image (see Fig. 6.9b) and dendrite arm size in polished optical image (see Fig. 6.9d), which shows the equivalent dimensions in both imaging modes (~70 µm in width and 100-200 µm in length). Moreover, the higher magnification observation of these dendritic areas (bluish areas) which exhibit well defined striations (Fig. 6.9c, h) leads to an empirical conclusion that where there was a blue area, there was a striation.

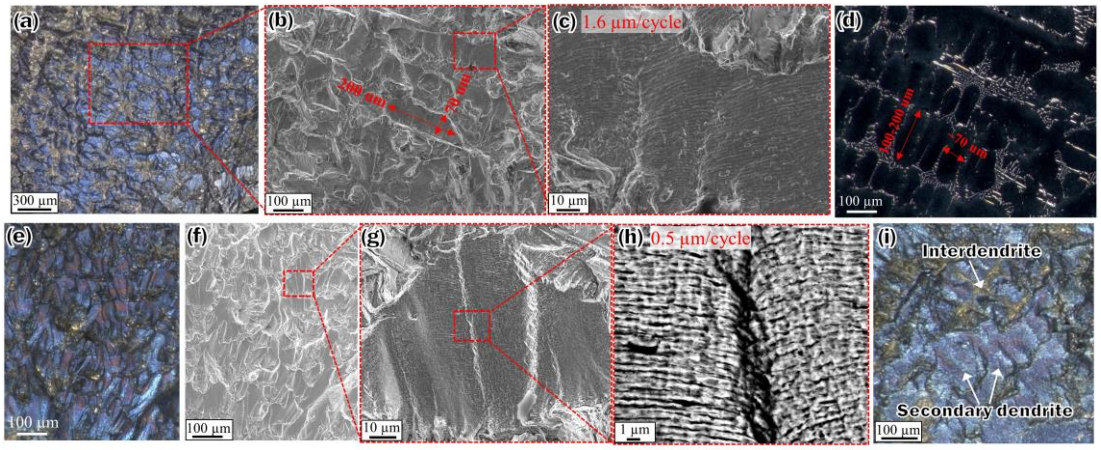

Fig. 6.9 Secondary dendrite structure and striation distribution. (a-d) from L-C, (e-h) from H-E and (i) from L-E. (a, b) and (e-g) show the dendrite structure on fracture surface; (c) and (h) show the striations in dendrite area; (d) Dendrite structure in the sample and the average size of secondary dendrite is comparable to dendrite size on fracture surface in (b).

For better understanding the direct correlation of fatigue striation lines and dendrite structure, representative striations located within primary dendrite cores are further characterised as shown in Fig. 6.10. A primary dendrite arms is indicated by red dashed box in Fig. 6.10a, b. This example was taken from the early crack propagation area, i.e., low ΔK region in the L-T sample, see Fig. 6.7 which is very close to initiation site and obtained from sample L-T. Whilst the primary dendrite arms can be easily observed in the late crack propagation area, i.e., high ΔK region, see an example in Fig. 10d taken from H-C sample. As expected, the blue dendrite areas contained striation lines with

very low crack propagation rate of ~ 360 nm / cycle in the very early crack propagation stage, see the shadowy striation lines in Fig. 10c which is the high magnified image of the red point in Fig. 6.10b. A high crack propagation rate of 0.9~1.3 μm / cycle in high ΔK region are shown in Figs. 6.10f and 6.10h which are the high magnified areas in Figs. 6.10e and 6.10g, respectively. Moreover, in the low ΔK region, the slow crack propagation and the flat nature of the characterised primary dendrite surface area assisted in measuring the γ' size (~ 400 nm) on the fracture surface, see Fig. 10c. Considering the morphology of these intact cubic aligned γ', it is clear that this striation area is in fact within the dendrite area, see also Figs. 6.2c and 6.2d. Furthermore, it is interesting to observe the striation lines 'cutting through' these γ′ without any kind of diversion or obstructions. Given the theory that striation produced by alternating activation of {111} slip planes [23], this fracture surface feature can be correlated with the distorted γ′ in Fig. 6.7i to give a 3D view of fatigue loading process.

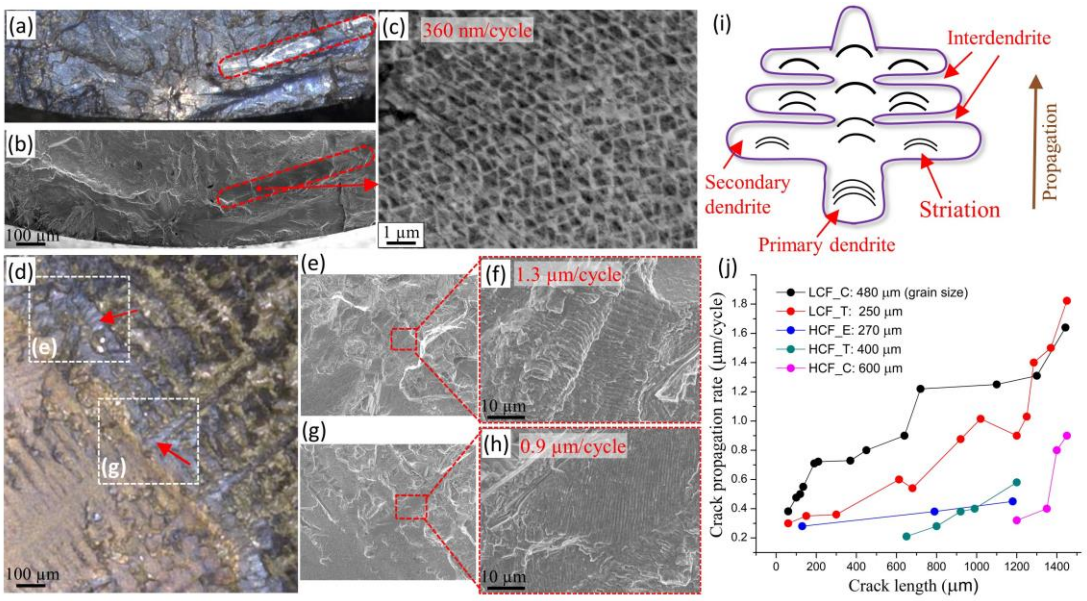

Fig. 6.10 Primary dendrite structure and striation distribution. (a-c) from L-T, (d-h) from H-C. Primary dendrite are shown in red dashed circles in (a, b) and representative fine striations close to initiation site is shown in (c). Primary dendrites are shown by color contrast in (d) and striations are magnified in (f, h) from white dashed rectangular areas. (i) Schematically illustration of dendrite structure (both primary and secondary) and striation distribution. (j) Grain size dependence of crack growth rate, obtained from measurement of width of striations, as displayed in (c, f, h) and in other figures for example.

Based on the results summarised above, a simplified model of striation line distribution within the dendrite structure is schematically presented in Fig. 6.10i. It shows the fatigue striation, which represents the trace of fatigue crack propagation process, is only limited in primary and secondary dendritic areas that are separated by interdendrite areas. Moreover, the crack propagation rate increases as the crack advances, signified with increasingly wider striation spacing along the propagation direction in the same figure.

Based on the elaborate measurement of striation spacings across the whole fracture surface for each sample, the crack propagation rate vs crack length (distance from initiation point) data is displayed in Fig, 6.10j. As we try to focus on the effect of grain size rather than porosity, the information from L-E is not included as the crack started from a large porosity cluster (Fig. 6.4f) and the sample failed rapidly. For further clarification, the average of grain size for each sample are also listed in the same figure. It is evident that the crack propagation rate in LCF samples are much higher than in HCF samples after crack initiation stage. This can be explained by the much higher loading stress applied in LCF test condition (~630 MPa) than in HCF (~335 MPa). Importantly, it is clear that the crack propagation rate in the large grain size sample is higher than in the small grain size samples during both LCF and HCF tests. For LCF, this aspect is more attributed to the faster rate increase in the initial crack growth stage. For instance, the faster crack propagation rate was found in the L-C sample in between 80 μm and 200 μm compared to the rate in L-C sample in the same crack length. As for HCF, a significant difference in facet size in each sample within the initiation zone was found which might affect the starting point of striation occurrence. Therefore, considering the rate ratio (slope) of the crack propagation rate in HCF might be more indicative. It is showed that the slope of large grain (~ 400 μm) sample H-T is higher than the small (~ 270 μm) sample H-E. Also, the longer crack propagation 'distance' in H-E is consistent with the result in Figs. 6.5a, b, j. A special notice should be given to H-C, for which the term 'crack propagation distance' should be used cautiously and will be further discussed in Section 4.3. However, with the largest grain size in H-C, it should be highlighted that the propagation stage with striation only covered a distance of ~200 μm and showed a large slope of propagation rate. More examples of crack propagation rate determination in L-T, L-C, H-T, H-E and H-C samples are shown in Supplement Fig. 6.1.

6.3.2.2 EBSD-based GND Analyses

It is generally believed that geometrically necessary dislocation (GND) represent an extra storage of dislocations required to accommodate the lattice curvature resulted from non-uniform plastic deformation such as in two-phase system or polycrystalline material [33]. In contrast, the rest of dislocations which evolve from random trapping process and produce no long-range curvature in the lattice are termed as 'statistically stored dislocations (SSD)' [33]. It is also believed that GNDs act as obstacles to the motion of other SSDs and hence contribute to the work hardening of the material [34]. The EBSD-based GND calculation that is based on misorientation data can offer quantitative information on GND type dislocation distribution in micro-scale but cannot count for SSD type as they are not contributing to the lattice curvature, i.e., misorientation data. The GND mapping for large areas are shown in Fig. 6.11for L-T and H-E sample. The mapping sites are immediately beneath the small crack propagation stage of fracture surface (blue areas) and parallel to the loading direction. Samples with highest fatigue life, largest crack propagation area and smallest grain size under both LCF and HCF conditions, L-T (Figs. 6.11a-c) and H-E (Figs. 6.11d-f), respectively, are particularly chosen. The Nb EDS mapping was used to signify carbides distribution and dendrite structure, see Figs. 6.11b and 6.11e. The grain boundaries are extracted from IPF maps in Figs. 11a and 11d are superimposed on the EDS mapping and GND 2-D mappings, see the white lines in Figs. 6.11b-c and 6.11e-f. The most striking feature in the GND maps is that the GND density distributions are nearly the reflection of dendrite structure in both examples. The high GND density (3×10^2 um^{-2}) was in the interdendrite areas while lower density (~ 25 um^{-2}) was found in the dendrite areas. In contrast, it seems that GND density have no apparent relationship with grain boundaries, especially in sample L-T, although the grains in the EBSD mapped area have different orientations. Furthermore, comparing the average GND density within each individual grain suggested that the average GND density is not affected by crystallographic orientations and hence the Schmid factors, see Figs. 6.11a, c, d, f. This is probably due to the relatively low stress level used during the fatigue test, including LCF stress level of 630 MPa whereas the yielding strength of IN713C is ~ 718 MPa. We believe the direct correlations between GND and grain

orientation can be better investigated above yield strength of the material in order to induce observable changes; Or the changes caused by orientations, if exist, are negligible compared to the change caused by dendrite structure. However, unexpectedly, a slightly higher GND density was found in H-E than in L-T, see Figs. 6.11c and 6.11f, although higher loading stress in LCF (~ 630 MPa) than in HCF (~ 335 MPa). This is probably because more intense dendrite structure (smaller dendrite size) at this location of H-E sample than in the selected area for L-T. This indicate that the critical role of dendritic structure can overlay the influence of orientation factor in this particular stress levels used in the current study. It is therefore, concluded here that GND density accumulation and distribution is more affected by the existing dendritic structure rather than grain boundary or orientation. The GND relationship with striation distribution and hence on fatigue crack propagation will be discussed in detail in Sections 4.1 and 4.2.

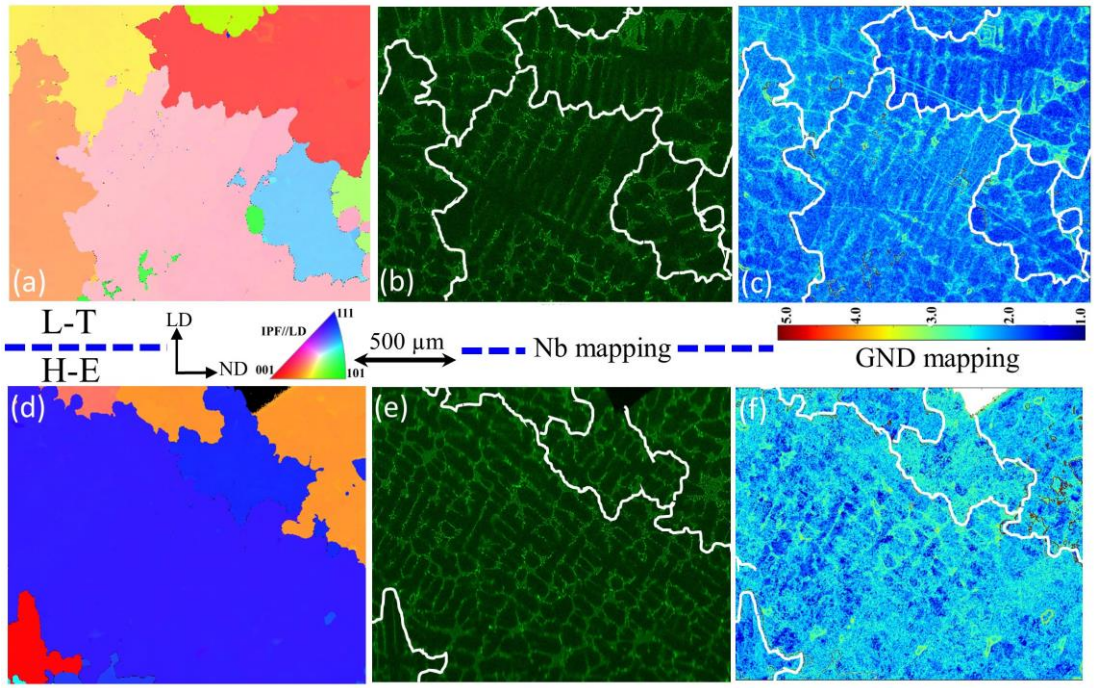

Fig. 6.11 Dendrite structure dependence GND density distribution based on EBSD datas. (a-c) from L-T and (d-f) from H-E. (a, d) IPFs show grain orientation grain structure; (b, e) Element mapping of Nb showing dendrite structure in the same area in (a, d), respectively; (c, f) GND density mapping with grain boundaries superimposed by white lines, step size of 200 nm was used.

6.3.2.3 STEM-based Dislocation Analyses

The dislocation density correlation with the dendritic structure is further studied via TEM-BF (bright field) and STEM-HAADF. The area of interests (AOIs) were extracted using FIB technique as well as conventional thin TEM foil sample preparation. The exact FIB-extract sites are indicated on the SEM image and GND density map shown in Figs. 6.12a and 6.12b. The two extracted areas are carefully extracted from dendrite and interdendrite zones. The TEM-BF images of interdendrite and dendrite area are shown in Fig. 6.12c and Fig. 6.12d, respectively. Fig. 6.12c clearly shows high dislocation density within the interdendrite area along the γ channels. In contrast, almost free dislocation zone is found in dendrite area that featured an intact shape and orderly γ', see Fig. 6.12d. These TEM images also confirmed irregular morphology and slightly larger γ' in the interdendrite area compared with those in the dendrite area. Further dislocation distribution investigation was carried out using conventional thin foil specimens beneath crack propagation area of fracture surfaces.

Figs. 6.12e-f and 6.12g show dislocation density and morphology in typical interdendrite and dendrite area, respectively. Moreover, STEM-HAADF mode have been employed here as this technique provides high resolution and contrast for dislocation observation as reported in [35]. Again, it shows much higher dislocation density in interdendrite area than dendrite area. It appears that the dislocations in interdendrite area are mostly accumulated around γ′ and especially between narrow γ channels, see Fig. 6.12e (BF) and Fig. 6.12f (HAADF). Fig. 6.12h-j directly compare the dislocation density in an adjacent interdendrite / dendrite area. According to the measurement method from Pesicka et al., [36], it is evaluated that the average dislocation density in interdendrite area and dendrite area are ~250 and ~25 μm^{-2}, as shown in Fig. 6.12i and Fig. 6.12j, respectively. These dislocation density values are comparable to and in an agreement with the result from EBSD-based GND calculations. It should be remembered that the dislocations observed by TEM are consist of both GND-type and SSD-type dislocations. This indicates that most of the entangled dislocations observed in the interdendrite area in Fig. 6.12i are GND types.

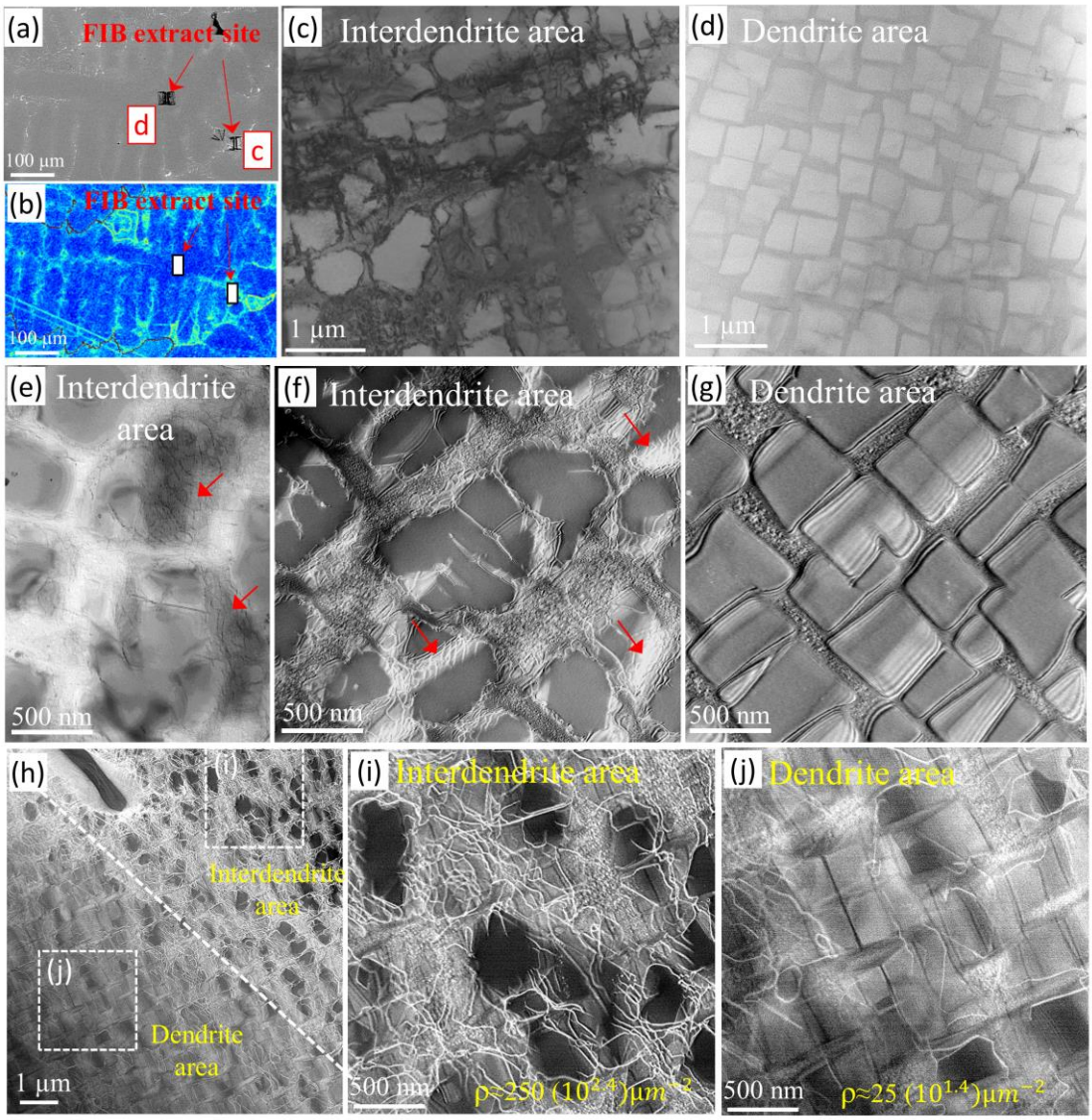

Fig. 6.12 Dendrite structure dependent dislocation distribution based on TEM and STEM-HADDF. (a-d) Specimen from FIB (Focused Ion Beam) extracted site; (e-j) Specimen from electric polishing. (c, d) BF (Bright Field) images of dislocation in interdendrite area and dendrite area, respectively; (e, f) BF and STEM-HADDF images showing dislocation around γ′ in a typical interdendrite area, respectively; (g) HADDF image in a typical dendrite area. (h-j) HADDF images in an adjacent interdendrite/dendrite area showing much higher dislocation density in interdednrite. Some dislocations are indicated by red arrows in (e, f).

6.3.3 Micro/Macro/Meso-Texture and Failure Correlations

6.3.3.1 Facet Formation and Growth during HCF Loading

Serial sectioning technique together with EBSD for all post-test samples have been utilised to reveal the grain size and crystallographic orientation distributions as well as their direct influence on crack initiation and propagation mechanisms. Parts of EBSD mapped sections that could reveal the key features have been presented in Figs. 6.13 and 6.14 for HCF samples, and in Fig. 6.15 for LCF samples. All the EBSD mapping (IPFs // LD) without rotation for each cross section in all the samples are shown in Supplement Figs. 6.2-6.7. As stated in Section 3.1, the most predominant feature during HCF loading in polycrystalline alloys is the facet formation and growth in crack initiation stage. This is clearly demonstrated in the IPF//LD maps in Figs. 6.13 and 6.14. From the obtained EBSD data, the individual facet grain orientation with reference to the loading direction (LD) as well as the specific activated slip system and hence the Schmid Factor (SF) of the individual slips can be resolved. The calculated slip traces and the highest SF values for each slip plane are also superimposed on the Figs. 6.13c, 6.13d and 6.14d. The results from overall serial sectioning data suggest that there is only one facet plane activated immediately after crack initiation (porosity in this case) in sample H-T (Grain 1 (G1) in Fig. 6.13c) and sample H-C (G5 in Fig. 6.14d). While there are two facet planes in sample H-E (G3 and G4 in Fig. 6.13d) intersecting at the initiating porosity site (Fig. 6.5f and Fig. 6.13b). It is not surprised that in a small grain and pore size sample such as in H-E, both facet planes were activated along a slip system with highest SF values, i.e., 0.43 of (1-11) slip plane in G3 and 0.44 of (-111) slip plane in G4, which have been highlighted in red colour and the red slip traces in Fig. 6.13d. However, in the samples with large grain and pore sizes, such as in H-T and H-C, the activated slip plane has the third highest SF values, 0.39 of (-111) in G1 and even as small as 0.28 of (-111) in G5, as highlighted in yellow colour in Figs. 6.13c and 6.14d, respectively. It should be noted here that Schmid factor calculation is based on the validity of the external uniaxial stress state within individual grains without considering additional local stresses. However, it has been reported that the effective SFs might be affected by local stress states generated by precipitates, adjacent grains or residual stress [37]. The large grain size in the order of 0.5 mm which limit the influence of adjacent grains in sample H-T and H-C as well as similar carbide size and distribution

might have minimum effect on the local stress variation. However, the porosity on other hand with large size and non-homogenously distributed may influence the stress state locally. Indeed, the high GND density in the vicinity of large pore sizes as shown previously in Fig. 6.6c can act as a stress raiser for crack initiation, which effectively validate the local stress state role on deformation mechanisms. Therefore, it is concluded that when the size of porosity is large enough to induce large local stress changes, the slip that actually activated is not necessarily has the highest nominal SF value.

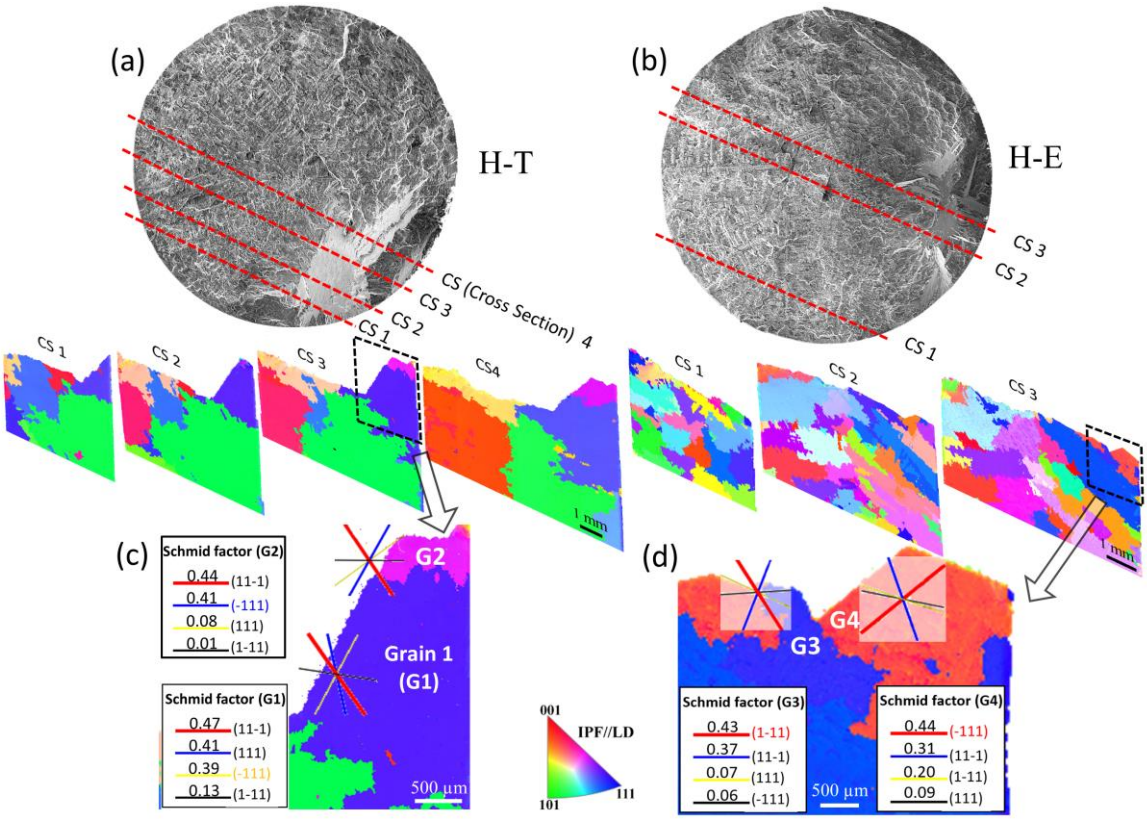

Fig. 6.13 Grain orientation and structure distribution across the fracture surface revealed by serial sectioning method in sample H-T (a, c) and H-E (b, d), parts of IPFs // LD are displayed corresponding to the red dashed sectioning lines in (a, b). Calculated slip traces for {111} slip planes in facet grain(s) are superimposed and the highest Schmid factor value for each slip plane are displayed for each facet grain in (c, d).

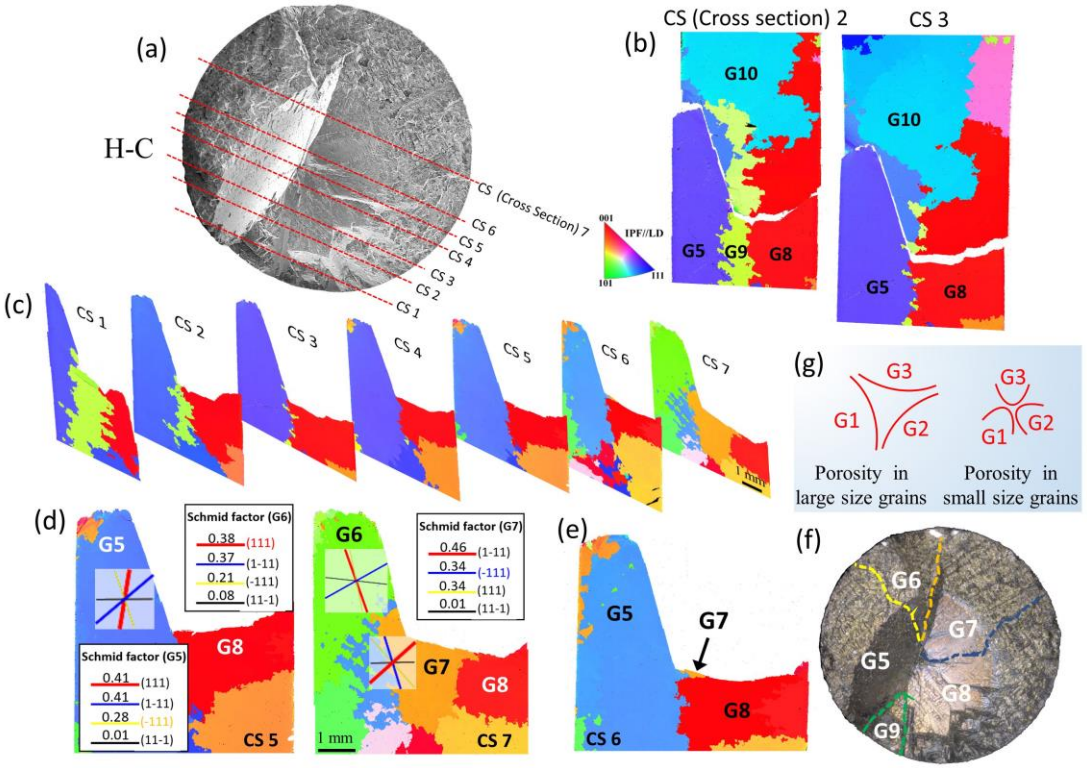

Fig. 6.14 Grain orientation and structure distribution across the fracture surface in sample H-C. Parts of IPFs // LD (c) are displayed corresponding to the red dashed sectioning lines in (a). (d-e) IPFs // LD of cross section (CS) 5, 7 and 8 without image distortion. Calculated slip traces for {111} slip planes in facet grains (G5, G6 and G7) are superimposed and the highest Schmid factor value for each slip plane are displayed for each facet grain in (d). (b) Both top and bottom half of fractured sample at some locations are sectioned and EBSD scanned to reveal the whole facet grain. (e) Intersection of three grains that produce the porosity; (f) Spatial grains position around fracture surface. (g) schematically shows grain size dependence of porosity size in the materials.

It is interesting to note that the slip transfer across the facet planes in H-T sample, Fig. 6.13a and H-C sample, Fig. 6.14. The slip transfer in sample H-T from (-111) plane in G1 (<111>//LD orientation) to (-111) plane with a relative high SF (0.41) in G2 (<112>//LD orientation), see cross-section (CS) 3 and CS 4 in Figs. 6.13a and 6.13c. Whereas, in H-C sample, the slip plane (-111) in G5 transfer (or extend) to (111) in G6 with highest SF (0.38) and partly to (-111) in G7, see Fig. 6.14. It should be emphasised here that the three faceted grains, i.e., G5, G6 and G7, have shared almost the same facet plane as macroscopically shown in Fig. 6.14a. Using the definition of tilt and twist angles in [20, 21] and the 3-D optical imaging, the tilt angle and twist angle are ~ 45°

and ~ 50° between G1 and G2, 0° and 0° between G5 and G6, respectively. This is in an agreement with the results by Larrouy et.al. [21] that twist angle less than 60° facilitates direct slip transfer between the grains. Moreover, it seems when the outcoming plane (in G6) which has the highest SF is aligned with incoming plane (in G5) in H-C sample, this slip transfer occurred without changing direction which require the minimum energy.

Fig. 6.14b shows the EBSD maps of two parallel cross section for both halves of the failed bars sectioning both half of failed bars. This quasi 3-D view was needed to validate that the facet size is limited by faceted grain size. As shown in Fig. 6.14b. the facet length is determined by the grain size. In CS 2, the facet plane is constrained in between G10 and G9. Whereas in CS 3 the same facet length is constrained by G10 and G8 (Fig. 6.14b). The similar observation was found in other two HCF samples. For example, in CS 2 of H-T sample (Fig. 6.13a), the facet plane in G1 is restricted by the grain beneath it that has a <101>//LD orientation, and in CS 3 of H-E, the facet plane in G4 is restricted by G3 (Fig. 6.13d). This also agrees with our previous report on turbine blade when failed in HCF mode where faceting occurred [3].

In addition to obtaining orientation information and distribution in 3-D, another advantage of serial sectioning technique is to reveal some specific microstructure features in detail. For instance, the quasi 3D-EBSD mapping for sample H-C (Fig. 6.14c), revealed that the fracture surface consists only of 5 grains, i.e., G5-G9, see Fig. 6.14f. However, the large porosity that initiated crack (Fig. 6.5i) is located at the triple junction of three grains, G5, G7 and G8, as shown in CS 6 and CS 7 in Fig. 6.14c and Fig. 6.14e. From theoretical point of view, finding casting porosity at the triple junction is not uncommon during solidification process as it represents a weak point, especially in between 3 or 4 completely different orientated grains. Furthermore, geometrically and due to larger constrain can present in between the larger grains, it is anticipated the larger the size of neighbouring grains, the larger pore size in between them is created at a given stress level. A simplified schematic graph in Fig. 6.14g demonstrates that larger grains have low grain boundary curvature and thus during solidification they will form a relative larger pore at the triple junction compared to the pore formed in between small grain that have much greater boundary curvatures.

6.3.3.2 Crack Propagation during LCF

Representative cross sections (CS) of three LCF samples are shown in Fig. 6.15. By layer-by-layer sectioning, crack initiation sites (porosities) can be exactly identified and examined just as in HCF samples. For instance, the porosities cluster in sample L-E (Fig. 6.4f) is assumed to form by a triple junction of three grains, i.e., G3 (Grain 3), G4 and G5, as indicated in CS 4 of Fig. 6.15b. It is observed that grain boundary affects the final propagation stop site where crack transit from crack propagation (Stage II) to overload stage (Stage III). An example is shown in Fig. 6.15c, two intersection sites between CS2, CS4 and crack transition line (indicated as white line) are identified as grain boundary points, as indicated by two red arrows in IPFs of these two CSs. Another two examples in HCF samples are further displayed in Supplement Fig. 6.8, showing the barrier effect of grain boundary on the final stage of crack propagation. Moreover, it is important to be pointed out that both in LCF and HCF samples, combining fracture surface and beneath IPFs, crack propagation stage in small grain samples such as L-T (Fig. 6.15a) and H-E (Fig. 6.13b) covered 4-5 grains whilst large grain samples such as L-C (Fig. 6.15c) and H-T (Fig. 6.13a) covered 1-2 grains.

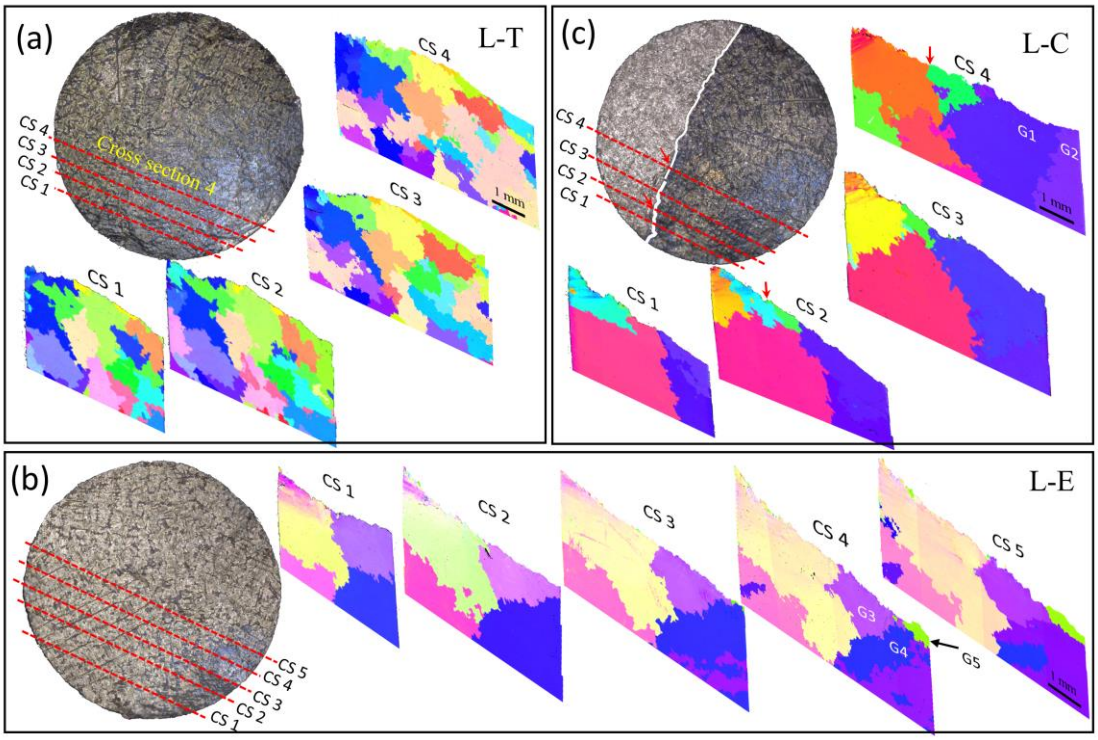

Fig. 6.15 Grain orientation and structure distribution across the fracture surface in sample L-T (a), L-E (b) and L-C (c). Parts of IPFs // LD (c) are displayed corresponding to the red dashed sectioning lines.

6.4 Discussion

6.4.1 On the Role of Dendrite Structure during Crack Propagation Stage

The results showed that fatigue striations, the unique traces of crack propagation process, are only limited in dendrite core area which includes primary and secondary dendrite arms. In other words, intermittent striation areas are separated by interdendritic areas (Fig. 6.9 and Fig. 6.10). It appears that the dendrite core area provided a path unit for crack propagation direction so that it is termed “Crack Propagation Unit (CPU)” here given the critical role of dendritic structure in crack propagation stage. Fig. 6.10i has schematically showed the striation distribution and dendrite structure in directing the crack propagation path. The complete set of microscopic and macroscopic data and images in the current study were collected to describe the exact crack propagation mechanism in IN713C alloy and it is summarised in Fig. 6.16. The striation structure during different stages of crack growth are schematically shown in Fig. 6.16. The grain size effect on crack path is also considered, however, no significant dendrite/crack propagation correlation differences was found in an individual large grain or in a small multi-grain cluster, see Figs. 6.16a-c and 6.16d-f, respectively. It should be emphasised here that there is no significant difference in the effect of loading mode, LCF and HCF, on the striation distribution and dendrite structure relationship during crack propagation stage. Thus, the discussion below is suitable for general fatigue tests.

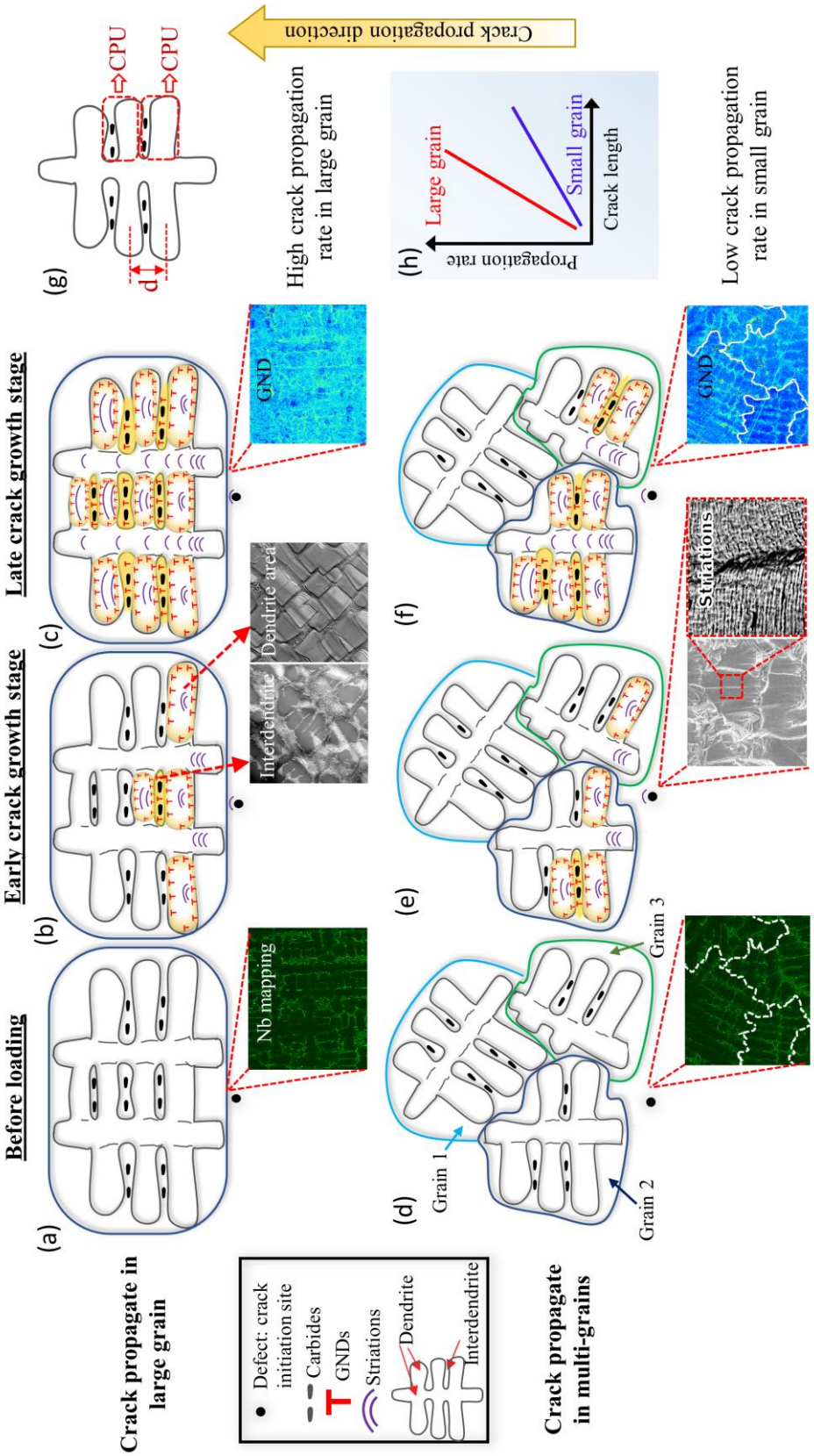

Fig. 6.16 Schematic showing the grain size dependence of crack propagation rate and the dendrite structure dependence of dislocation distribution. (a-c) for large single grain; (d-f) for small multi-grains. The real dendrite structures are shown in the highlight of (a, d) and the real

striation within dendrite area is shown in the highlight of (e). Dislocation segregated in interdendrite areas are proved both by GND mapping (the highlight in (c, f)) and HAADF images (the highlight in (b)). (g) Schematic illustration of crack propagation unit (CPU), and the diameter of CPU, 'd'. (h) Schematic illustration of crack propagation rate versus crack length in different grain size samples.

It is anticipated to have a minimum GND density prior to the fatigue loading in the original untested IN713C alloy in both large grain and small grain cluster, see Figs. 6.16a and 6.16d, respectively. As demonstrated in Figs. 6.16b and 6.16e, after the initial fatigue loading a crack is initiated from a casting defect, i.e., pore. During the early stage of crack growth, the GND were accumulated within interdendrite areas, which has been demonstrated by both EBSD-based GND calculation (the highlight in Fig. 6.16c, f, and Fig. 11) and TEM observation (the highlight in Fig. 6.16b and Fig. 6.12).

The high GNDs density in interdendrite areas are largely generated around carbides as shown in Supplement Fig. 6.9 and reported in our previous investigation [3] and partly around irregular shape γ′. This is because most of carbides are segregated in interdendrite area and there are contrasting deformation ability between carbides and γ matrix, resulting in tremendous strain gradient and GNDs around carbides when imposed to cyclic loading [3, 31]. Moreover, the high lattice misfit between γ′ and γ in interdendrite area (compared to those in dendrite area) that is represented by the irregular γ′ morphology leads to high stress field which effectively resist further dislocation motion via dislocation entanglement mechanism causing strain hardening. Thus, the high GNDs density together with lower dislocation mobility that contribute to the interdendrite area strengthening, creat a microstructure unit of "hard" interdendrite area with much "softer" dendrite area. This explains the crack preferential propagation through the "soft" dendrite area in a "low" propagation rate and leaving observable fatigue striation in this area, as schematically shown in Figs. 6.16b and 6.16e.

As cyclic loading continues, the crack advances following: interdendrite area hardening and dendrite facilitating easy crack propagation mechanisms. This particular mechanism creates a "Crack Propagation Unit (CPU)" and with increasing ΔK, the crack propagation rate increases which is represented by wider striation spacing, as shown in Figs. 6.16c and 6.16f.

The relationship between fatigue striation distribution (morphology) and dendrite structure proposed here is in agreement with our study on actual turbine blade component [3]. From [3] it was clear that the large area of fine long striations was observed during HCF failed location where weak dendrite structure present. Whereas, only local and separated striation lines during crack propagation stage was observed in LCF failed location where obvious dendrite structure exhibited [3].

6.4.2 On the Role of Grain Size during Crack Propagation Stage

The results from fatigue tests in this study show a significant beneficial effect of smaller grain size on fatigue life during both LCF and HCF loadings (Fig. 6.4j and Fig. 6.5j). Moreover, a slower crack propagation rate in smaller grain size samples has also been observed (Fig. 6.10j). This is generally attributed to the Hall-Petch effect, i.e., material strength increases with decreasing grain size or fits a simple inverse scaling law according to Dunstan and Bushby [38]. Both mentioned functions are more related to the fact that the grain boundary is not only block the dislocation movement leading to dislocation pile up, but also acts as source of dislocation nucleation [39]. The interaction between dislocation and grain boundary has been studied widely using FIB and TEM to direct observation [19] or EBSD for strain mapping [17] and reviewed recently [39]. In general, they agreed that grain size and strength have inversely proportional relationship. Meanwhile, it is believed that fatigue crack propagation rate increases with increasing grain size [15]. This is due to the free slip length that depends on the alloy grain size and geometry. In coarse grain size materials, the free slip length cab be as large as the grain size and accommodate large numbers of dislocations. This in effect generate significant strain incompatibility with the adjacent grains, and hence promoting slip and later crack transfers across the grain boundaries. Both mentioned hypothesis above anticipated large numbers of dislocations along grain boundaries, which, however, is not the case in the present study. Instead, a large amount of dislocations (GNDs) distributed in interdendrite areas rather than grain boundaries, as described in Section 4.1 and schematically illustrated in Fig. 6.16. This is in addition due to the difference between single phase materials where the above theorises mainly applied and γ’ precipitated hardened IN713C alloy, where the dislocation mainly generate and accumulate in the γ channel before moving toward interdendritic area and

grain boundaries. However, it appears that the stress level used during both LCF and HCF loading was not high enough to push a mass of dislocation from the interdendritic area toward the grain boundaries.

As described in Section 4.1, the concept of CPU was proposed for individual dendrite areas, rather than individual grains. If strength of materials including fatigue crack propagation resistance is closely related to dislocation patterns during deformation, it would be reasonable to designate "d" in the Hall-Petch Equation (Equ.1) for cast alloys to CPU size (secondary dendrite arm spacing) instead of grain size, as indicated in Fig.15g.

$$\sigma_y = \sigma_0 + k_y d^{-1/2} \qquad (1)$$

where σ_0 is a material constant representing the stress required to cause dislocation motion within a grain and the slope k_y measures the propensity of the unit boundaries to resist the transmission of slip. However, the CPU size or secondary dendrite arm spacing is in the same order in all the samples investigated, regardless of different grain size. Therefore, a plausible explanation for the higher resistance to fatigue propagation in smaller grain size sample is the complex configuration of dendrite structure across different grains, as schematically explained in Fig. 6.16.

For comparison purposes, the same surface crack propagation area, i.e., same crack front length, in only one single large grain in Figs. 6.16a-c (representing crack in large grain size sample) and three small grains in Figs. 6.16d-f (representing crack in multi-grains sample) is shown. In the latter case, the small grains have different orientations and form different dendrite structure during solidification process, as shown in Fig. 6.16d. At the early crack growth stage, the crack grows along CPUs and there is no significant difference in propagation rate between large grain and small clustered grains, as shown in Figs. 6.16b and 6.16e, respectively. However, in the later stage, the crack growth continues without changing directions in large single grain, see Fig. 6.16e, and decelerate in multiple grains case, see Fig. 6.16f. This deceleration in the latter case is attributed to the dendrite direction changes in the adjacent grains. As the crack fronts within individual dendrite area have to adjust to accommodate the abrupt change of direction and maintain continuity. Frequent such accommodation hence hinder the crack propagation, as shown in Fig. 6.16f and Fig. 6.16h. It should be noted here, this is a simplified model with a small grain numbers and demonstrated only in 2-D, thus,

the effect of grain size in 3-D will be even greater. For instance, in only one-dimension (1-D) situation, it showed that crack propagation area in smaller grain size sample covered ~5 grains (L-T, see Fig. 6.15a), in contrast with ~2 grains in large grain size sample (L-C, see Fig. 6.15c). However, this difference in grain numbers becomes 25 (5×5) versus 4 (2×2) after realising that the crack propagation is at least a 2-D event.

This model proposed here signify the beneficial effect of smaller grain size on fatigue crack propagation resistance, validating one more Hall-Petch effect. However, this model can be used in inhomogeneous microstructure containing dendrite structure and carbides in cast superalloys. Therefore, specific microstructure features and local stress conditions must be taken into account when applying Hall-Petch relation to precipitation hardened cast polycrystalline alloys such as IN713C.

6.4.3 On the Role of Crystal Orientation during Crack Propagation Stage

According to Neumann model [40], fatigue crack propagation process is dominated by alternate activation of slip systems and leads to the formation of striations on the fracture surface. In nickel-based supealloy (fcc structure) these slip systems are {111} slip systems, and the propagation process is essentially orientation related. The example shown in Fig. 6.17 clearly demonstrates the effect of grain orientation on fatigue crack path. The fracture surface study for H-C sample in Fig. 6.17a (same sample in Figs. 6.5g, 6.10d and 6.14f) shows that there is a unique large flat area immediately after initiation porosity site crossing two grains (G7 and G8 in Fig. 6.14f) on which dendrite structure is apparently visible as indicated in Fig. 6.17a. Between this area and overloading area there is a narrow ‘propagation area’ identified via striations lines analyses. This boundary area indicated in Fig. 6.17a is further magnified in Fig. 6.17b showing 3 points of interest. This narrow area is only 200 μm in width as indicated by two red dashed lines in Fig. 17a and again shows colour contrast (see Fig. 6.17b). Within the area, it is observed that only few faded striation lines were found at the interfacing area (Area 1 as indicated in Fig. 6.17b) and very fine striation lines as propagation ‘starts’ with small striation spacings (0.4 μm / cycle) in Area 2, quickly followed by large propagation rate (0.8 μm / cycle) in Area 3. The large flat area featured with visible dendrite structure is termed here as ‘brittle cracking area’ due to its rapid cracking (brittle) without alternate slip systems activating process. This

phenomenon is believed to be related with the grain configuration with respect to the loading direction (grain orientation). In the model proposed by Bowles and Broek [23], it is assumed that the crack propagation occurs by a slip decohesion mechanism with at least two acting planes. The crack plane is the plane bisecting the two operating {111} slip planes and can be either (001) or (110) crack planes. In the case of (001) crack plane, for instance, two slip planes, as schematically shown in Fig. 6.17e, (111) in the upper unit and (11-1) in the lower cell will result in the new (001) crack plane if taking effective Burgers vector into account [41]. Therefore, when the (001) plane is perpendicular to loading direction (<001>// LD), i.e., Cube orientation, the (111) family slip should be on 45 degrees angle with the loading direction to facilitates a pure shear condition, thus Cube is generally believed to be soft and easy to activate octahedral (111) slip system. However, the shear condition for both (1-11) and (-111) slip plane care active will allow a crack propagation perpendicular to the LD which is <001> in this case.

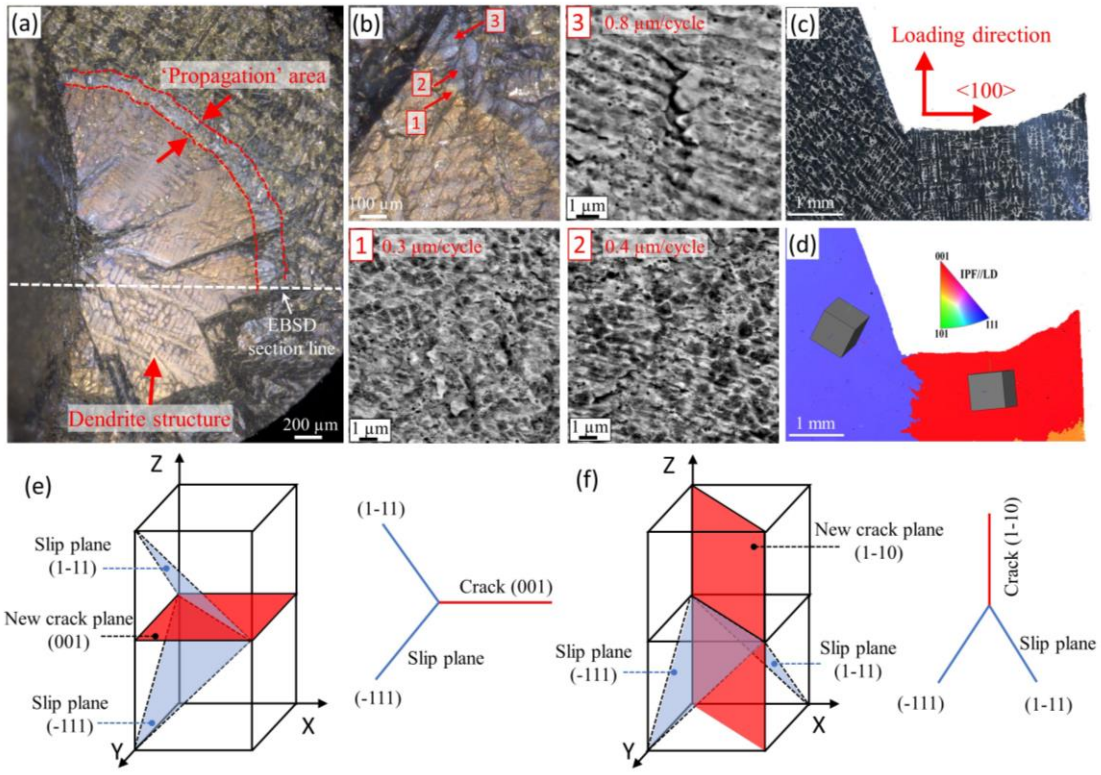

Fig. 6.17 Orientation dependence of crack propagation rate, an example from sample H-C. (a) Between initiation porosity and real 'propagation' area there is a large flat area where dendrite structure is visible. (b) the mirror surface of (a) in another half sample, and striations in different position of the narrow propagation area are magnified in 1-3. (c) and (d) cross section showing

the dendrite structure by OP and crystallographic orientation, respectively. The sectioning line is shown with white dashed line in (a). (e) and (f) schematically shows the mechanism of macroscopic fatigue crack propagation directions.

It has also been reported that the preferable and fast-growing direction for dendrite growth during solidification for nickel-based superalloy is <001> direction [42]. This is confirmed by the dendrite structure and morphology shown in Figs. 6.17c and 6.17d. This dendrite growth direction parallel to crack direction (perpendicular to loading direction) might also contribute to the significant large crack propagation rate in this brittle cracking area. Overall, it is concluded that grains with Cube orientation (<001>//LD) will tremendously facilitate crack propagation by offering readily propagation planes along dendrite growth direction.

6.5 Comments

6.5.1 Creative Characterisation Fracture Surface Using Conventional Techniques

Optical microscope (OM) and Scanning electron microscope (SEM) are two conventional techniques that have been widely used for fractography characterisation. The crack propagation model proposed here (Fig. 6.16) is mainly inspired by the correlation of colour contrast in OM with the striation observation in SEM, confirming the relationship between dendrite structure and striation distribution. Furthermore, the high-resolution backscatter electron (BSE) mode in SEM successfully resolve the striation even at very early crack growth stage with tens of nanometres spacing (e.g., Fig. 6.7d and Fig. 6.10c), making the quantitative characterisation of crack propagation rate possible. Although fractography is a quite old and ‘old-fashioned’ topic and technique, it is believed that instead of only satisfying with locating crack initiation site and a few locations of striation, an exhaustive characterisation of fracture surface combining different techniques (e.g., OM and SEM) will help shed some lights on the specific fatigue deformation micromechanism.

6.5.2 3-D Correlating Fracture Surface Features with underneath Microtexture and Microstructure by Serial Sectioning Method

In-situ test and three-dimensional (3-D) characterisation are the trend of materials research. And it is easy to understand that an exhaustive analysis of (short) fatigue cracks would require information on microstructure, microtexture (grain shape and orientation) and crack propagation rate in 3-D. By combining diffraction and phase-contrast X-ray tomography technique, Herbig et al. [43] made the first attempt to correlate fracture surface and grain orientation and propagation rate in 3-D in an in-situ and non-destructive way. Amongst destructive and post-mortem way for fatigue research, serial sectioning method can give 3-D information either by focussed ion beam (FIB) milling [44] or mechanical serial polishing [45], from which 3-D images of short cracks can be reconstructed. But FIB technique has the disadvantage of very limited studied volume [44] and for mechanical polishing way, to the best of the authors' knowledge, the current study together with our recent report [3] are the first kind of studies to correlate fracture surface with underneath microtexture and microstructure in 3-D or semi-3-D by using manual serial sectioning method. There is no need to section through the whole surface with very small distance between each section due to relative large grain size and relative symmetric crack propagation in round bar shape sample, neither the reconstruction of the 3-D image. But we do need conduct several mounting-scanning-dismounting procedures in the middle to precisely locate the scanning position and alignment for accurate correlation. Particularly, with the help of colour contrast due to oxidation and striation spacing, fatigue stages and crack propagation rate are relatively easy to be identified. However, still, some local information, such as the effect of orientation on striation spacing (propagation rate) in different propagation direction, cannot be obtained using this method, which may need the help of FIB for site analysis. Moreover, for the application to small grain size sample, smaller section distance is needed. Overall, the serial section / 3-D (or semi-3-D) method shown here offer a quick way to probe the deformation mechanism based on fractography and 3-D characterisation in fatigue crack research.

6.6 Conclusions

IN713C nickel-based superalloy produced via investment casting were tested under LCF and HCF conditions at 650°C. An exhaustive characterisation and analysis were conducted on fractured samples surface in 2-D and quasi 3-D, utilising SEM, TEM and HR-EBSD. Here, a fatigue crack propagation micromechanism in cast alloy is proposed in terms of dendrite structure, grain size and crystallographic orientation. The major conclusions from this study are:

1. Small grain size is recommended for both LCF and HCF properties.
2. Fatigue striations are only found in dendrite areas, separated by interdendrite channels.
3. The individual dendrite volume is considered to be a critical parameter in fatigue crack propagation and acted as crack propagation unit (CPU).
4. EBSD-based GND mapping and STEM-HAADF imaging showed that dislocation density in hard interdendirte area is much higher than in the soft dendrite area.
5. Large grain size microstructure shows higher crack propagation rate than small grain microstructure. This beneficial effect of small grain size is believed to be due to the frequent change of propagation directions in the CPU rather than to be controlled by dislocation accumulation at the grain boundary.
6. Under HCF condition, it appear that when the size of porosity is small, the faceting happened on activated slip plane with highest Schmid Factor value. Whereas in the case of large pore size and hence large local stress around pore, it is not necessary for the facet to occur on the highest SF plane.
7. Having large volume fraction of <100> // LD, i.e., Cube orientation within crack propagation area will facilitate crack propagation as <100> direction is the bisection plane of two {111} slip planes and is the preferable direction for dendrite growth.
8. Higher LCF life in fine grain microstructure is largely due to the deceleration of the crack propagation rate. Whilst during HCF test, in addition to slower growth rate, the smaller grain size samples also generate smaller facet size which assist greatly in crack growth constrain.

References

[1] Y. Xu, Q. Ran, J. Li, J. Peng, X. Xiao, X. Cao, G. Jia, Strengthening behavior of Nb in the modified Nimonic 80A, Mater. Sci. Eng. A 569 (2013) 27-40.

[2] S. Birosca, G. Liu, R. Ding, C. Rae, J. Jiang, B. Britton, C. Deen, M. Whittaker, The dislocation behaviour and GND development in nickel-based superalloy during creep, Int. J. Plast (**Submitted**)

[3] G. Liu, J. Salvat Cantó, S. Winwood, K. Rhodes, S. Birosca, The effects of microstructure and microtexture generated during solidification on deformation micromechanism in IN713C nickel-based superalloy, Acta Mater. 148 (2018) 391-406.

[4] J.S. Cantó, S. Winwood, K. Rhodes, S. Birosca, A Study of Low Cycle Fatigue Life and its correlation with Microstructural Parameters in IN713C Nickel Based Superalloy, Mater. Sci. Eng. A (2018).

[5] T.M. Pollock, S. Tin, Nickel-based superalloys for advanced turbine engines: chemistry, microstructure and properties, J. Propul. Power 22(2) (2006) 361-374.

[6] K.S. Chan, Roles of microstructure in fatigue crack initiation, Int. J. Fatigue 32(9) (2010) 1428-1447.

[7] A. Pineau, D.L. McDowell, E.P. Busso, S.D. Antolovich, Failure of metals II: Fatigue, Acta Mater. 107 (2016) 484-507.

[8] J. Jiang, J. Yang, T. Zhang, J. Zou, Y. Wang, F.P.E. Dunne, T.B. Britton, Microstructurally sensitive crack nucleation around inclusions in powder metallurgy nickel-based superalloys, Acta Mater. 117 (2016) 333-344.

[9] Y. Liu, Y. Wu, M. Kang, M. Wang, M. Li, H. Gao, J. Wang, B. Sun, Y. Ning, Fracture mechanisms induced by microporosity and precipitates in isothermal fatigue of polycrystalline nickel-based superalloy, Mater. Sci. Eng. A (2018).

[10] J. Miao, T.M. Pollock, J.W. Jones, Crystallographic fatigue crack initiation in nickel-based superalloy René 88DT at elevated temperature, Acta Mater. 57(20) (2009) 5964-5974.

[11] J.C. Stinville, E. Martin, M. Karadge, S. Ismonov, M. Soare, T. Hanlon, S. Sundaram, M.P. Echlin, P.G. Callahan, W.C. Lenthe, V.M. Miller, J. Miao, A.E.

Wessman, R. Finlay, A. Loghin, J. Marte, T.M. Pollock, Fatigue deformation in a polycrystalline nickel base superalloy at intermediate and high temperature: Competing failure modes, Acta Mater. 152 (2018) 16-33.

[12] F. Riemelmoser, R. Pippan, H. Stüwe, An argument for a cycle-by-cycle propagation of fatigue cracks atsmall stress intensity ranges, Acta Mater. 46(5) (1998) 1793-1799.

[13] C.W. Shao, P. Zhang, Y.K. Zhu, Z.J. Zhang, J.C. Pang, Z.F. Zhang, Improvement of low-cycle fatigue resistance in TWIP steel by regulating the grain size and distribution, Acta Mater. 134 (2017) 128-142.

[14] M. Coleman, H. Alshehri, R. Banik, W. Harrison, S. Birosca, Deformation mechanisms of IN713C nickel- based superalloy during Small Punch Testing, Mater. Sci. Eng. A 650 (2016) 422-431.

[15] M.F. Horstemeyer, N. Yang, K. Gall, D.L. McDowell, J. Fan, P.M. Gullett, High cycle fatigue of a die cast AZ91E-T4 magnesium alloy, Acta Mater. 52(5) (2004) 1327-1336.

[16] U. Krupp, Fatigue crack propagation in metals and alloys: microstructural aspects and modelling concepts, John Wiley & Sons2007.

[17] T. Benjamin Britton, A.J. Wilkinson, Stress fields and geometrically necessary dislocation density distributions near the head of a blocked slip band, Acta Mater. 60(16) (2012) 5773-5782.

[18] Z. Zheng, D.S. Balint, F.P.E. Dunne, Investigation of slip transfer across HCP grain boundaries with application to cold dwell facet fatigue, Acta Mater. 127 (2017) 43-53.

[19] R. Ding, J. Gong, A.J. Wilkinson, I.P. Jones, A study of dislocation transmission through a grain boundary in hcp Ti–6Al using micro-cantilevers, Acta Mater. 103 (2016) 416-423.

[20] T. Zhai, A.J. Wilkinson, J.W. Martin, A crystallographic mechanism for fatigue crack propagation through grain boundaries, Acta Mater. 48(20) (2000) 4917-4927.

[21] B. Larrouy, P. Villechaise, J. Cormier, O. Berteaux, Grain boundary–slip bands interactions: Impact on the fatigue crack initiation in a polycrystalline forged Ni-based superalloy, Acta Mater. 99 (2015) 325-336.

[22] Lee, I. Robertson, H. Birnbaum, AnIn Situ transmission electron microscope deformation study of the slip transfer mechanisms in metals, Metall. Trans. A 21(9) (1990) 2437-2447.

[23] C. Bowles, D. Broek, On the formation of fatigue striations, Int. J. Fract.Mech. 8(1) (1972) 75-85.

[24] H. Cai, A. McEvily, On striations and fatigue crack growth in 1018 steel, Mater. Sci. Eng. A 314(1-2) (2001) 86-89.

[25] S. Birosca, F. Di Gioacchino, S. Stekovic, M. Hardy, A quantitative approach to study the effect of local texture and heterogeneous plastic strain on the deformation micromechanism in RR1000 nickel-based superalloy, Acta Mater. 74 (2014) 110-124.

[26] J. Pešička, A. Aghajani, C. Somsen, A. Hartmaier, G. Eggeler, How dislocation substructures evolve during long-term creep of a 12% Cr tempered martensitic ferritic steel, Scr. Mater. 62(6) (2010) 353-356.

[27] M.F. Horstemeyer, N. Yang, K. Gall, D.L. McDowell, J. Fan, P.M. Gullett, High cycle fatigue of a die cast AZ91E-T4 magnesium alloy, Acta Mater. 52(5) (2004) 1327-1336.

[28] A. Cervellon, J. Cormier, F. Mauget, Z. Hervier, Y. Nadot, Very High Cycle Fatigue of Ni-Based Single-Crystal Superalloys at High Temperature, Metallurgical and Materials Transactions A (2018) 1-13.

[29] S. Dezecot, V. Maurel, J.-Y. Buffiere, F. Szmytka, A. Koster, 3D characterization and modeling of low cycle fatigue damage mechanisms at high temperature in a cast aluminum alloy, Acta Mater. 123 (2017) 24-34.

[30] P. Kontis, E. Alabort, D. Barba, D.M. Collins, A.J. Wilkinson, R.C. Reed, On the role of boron on improving ductility in a new polycrystalline superalloy, Acta Mater. 124 (2017) 489-500.

[31] P.S. Karamched, A.J. Wilkinson, High resolution electron back-scatter diffraction analysis of thermally and mechanically induced strains near carbide inclusions in a superalloy, Acta Mater. 59(1) (2011) 263-272.

[32] T. Connolley, P.A.S. Reed, M.J. Starink, Short crack initiation and growth at 600 °C in notched specimens of Inconel718, Mater. Sci. Eng. A 340(1–2) (2003) 139-154.

[33] M. Ashby, The deformation of plastically non-homogeneous materials, Philos. Mag. 21(170) (1970) 399-424.

[34] H. Gao, Y. Huang, Geometrically necessary dislocation and size-dependent plasticity, Scr. Mater. 48(2) (2003) 113-118.

[35] Q. Ding, S. Li, L.-Q. Chen, X. Han, Z. Zhang, Q. Yu, J. Li, Re segregation at interfacial dislocation network in a nickel-based superalloy, Acta Mater. 154 (2018) 137-146.

[36] J. Pešička, R. Kužel, A. Dronhofer, G. Eggeler, The evolution of dislocation density during heat treatment and creep of tempered martensite ferritic steels, Acta Mater. 51(16) (2003) 4847-4862.

[37] P. Peralta, C. Laird, Fatigue fracture at bicrystal interfaces: experiment and theory, Acta Mater. 46(6) (1998) 2001-2020.

[38] D.J. Dunstan, A.J. Bushby, Grain size dependence of the strength of metals: The Hall–Petch effect does not scale as the inverse square root of grain size, Int. J. Plast 53 (2014) 56-65.

[39] J. Kacher, B.P. Eftink, B. Cui, I.M. Robertson, Dislocation interactions with grain boundaries, Curr. Opin. Solid State Mater. Sci. 18(4) (2014) 227-243.

[40] P. Neumann, Coarse slip model of fatigue, Acta Metall. 17(9) (1969) 1219-1225.

[41] O. Düber, B. Künkler, U. Krupp, H.J. Christ, C.P. Fritzen, Experimental characterization and two-dimensional simulation of short-crack propagation in an austenitic–ferritic duplex steel, Int. J. Fatigue 28(9) (2006) 983-992.

[42] Y.Z. Zhou, A. Volek, N.R. Green, Mechanism of competitive grain growth in directional solidification of a nickel-base superalloy, Acta Mater. 56(11) (2008) 2631-2637.

[43] M. Herbig, A. King, P. Reischig, H. Proudhon, E.M. Lauridsen, J. Marrow, J.-Y. Buffière, W. Ludwig, 3-D growth of a short fatigue crack within a polycrystalline microstructure studied using combined diffraction and phase-contrast X-ray tomography, Acta Mater. 59(2) (2011) 590-601.

[44] S. Zaefferer, S.I. Wright, D. Raabe, Three-Dimensional Orientation Microscopy in a Focused Ion Beam–Scanning Electron Microscope: A New Dimension of Microstructure Characterization, Metallurgical and Materials Transactions A 39(2) (2008) 374-389.

[45] H. Pirgazi, S. Ghodrat, L.A.I. Kestens, Three-dimensional EBSD characterization of thermo-mechanical fatigue crack morphology in compacted graphite iron, Mater. Charact. 90 (2014) 13-20.

Supplement figures:

L-T

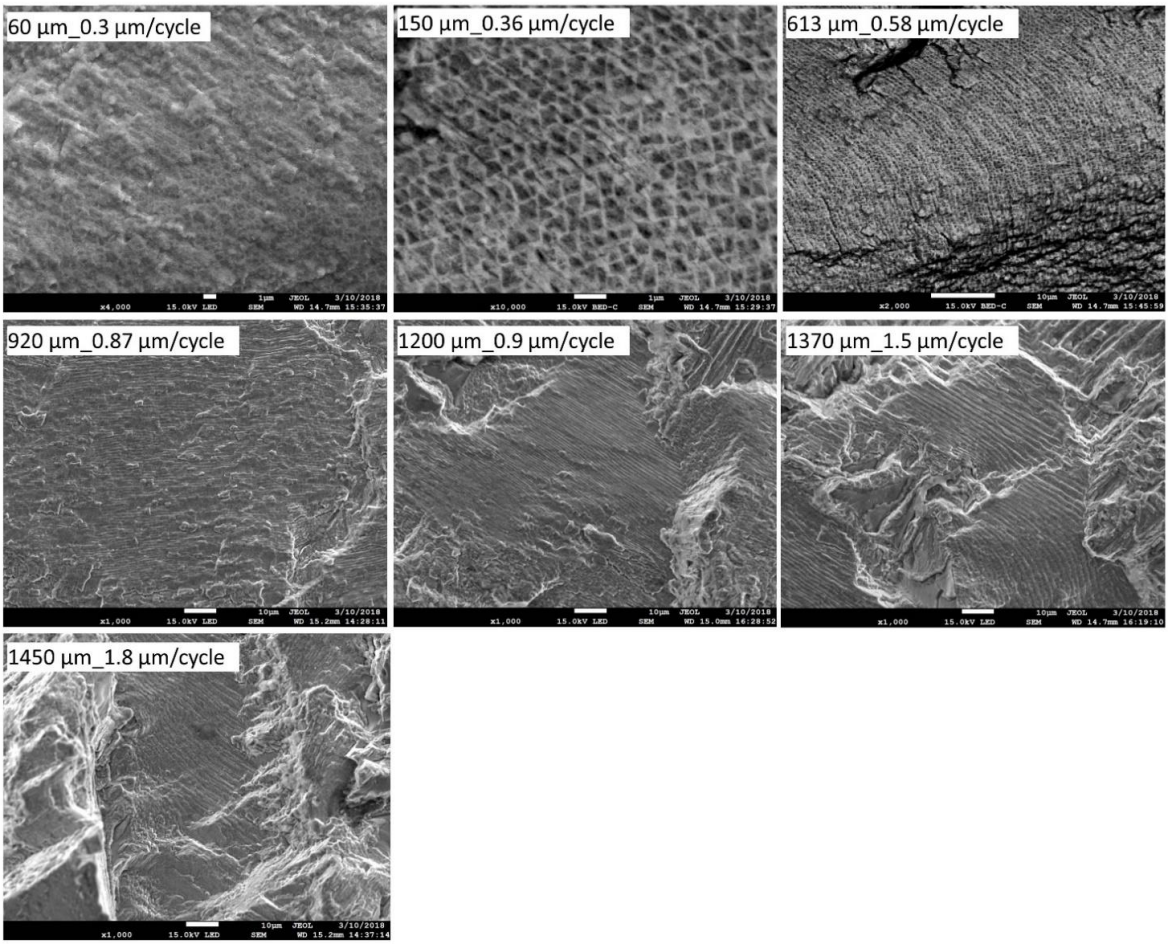
60 µm_0.3 µm/cycle
150 µm_0.36 µm/cycle
613 µm_0.58 µm/cycle
920 µm_0.87 µm/cycle
1200 µm_0.9 µm/cycle
1370 µm_1.5 µm/cycle
1450 µm_1.8 µm/cycle

L-C

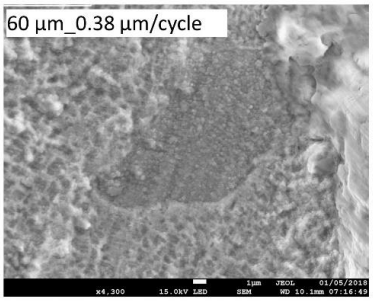
60 µm_0.38 µm/cycle

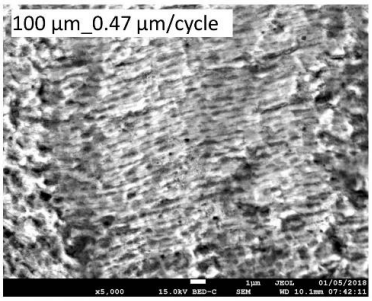
100 µm_0.47 µm/cycle

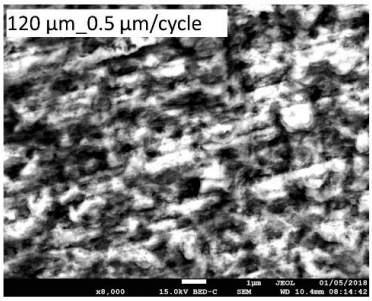
120 µm_0.5 µm/cycle

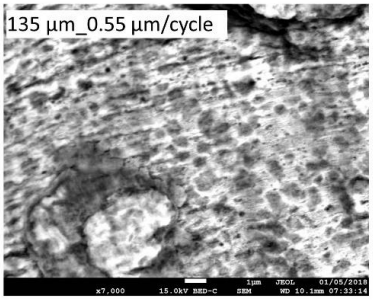
135 µm_0.55 µm/cycle

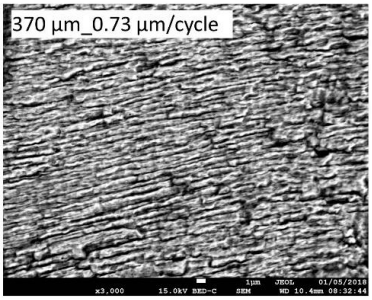
370 µm_0.73 µm/cycle

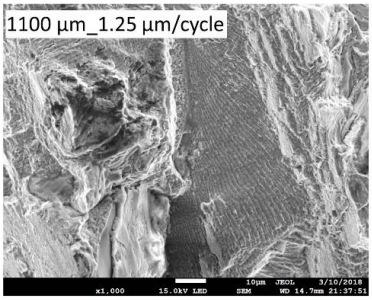
1100 µm_1.25 µm/cycle

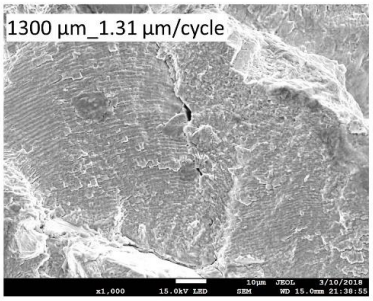
1300 µm_1.31 µm/cycle

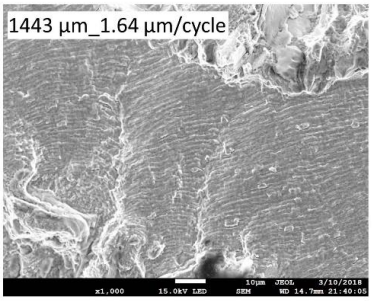
1443 µm_1.64 µm/cycle

H-T

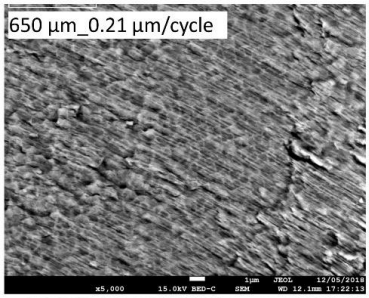
650 µm_0.21 µm/cycle

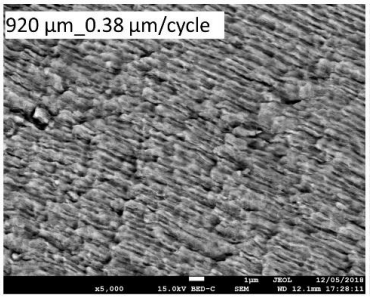
920 µm_0.38 µm/cycle

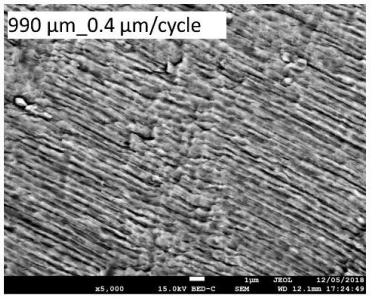
990 µm_0.4 µm/cycle

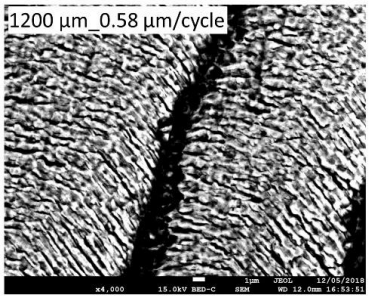
1200 µm_0.58 µm/cycle

H-E

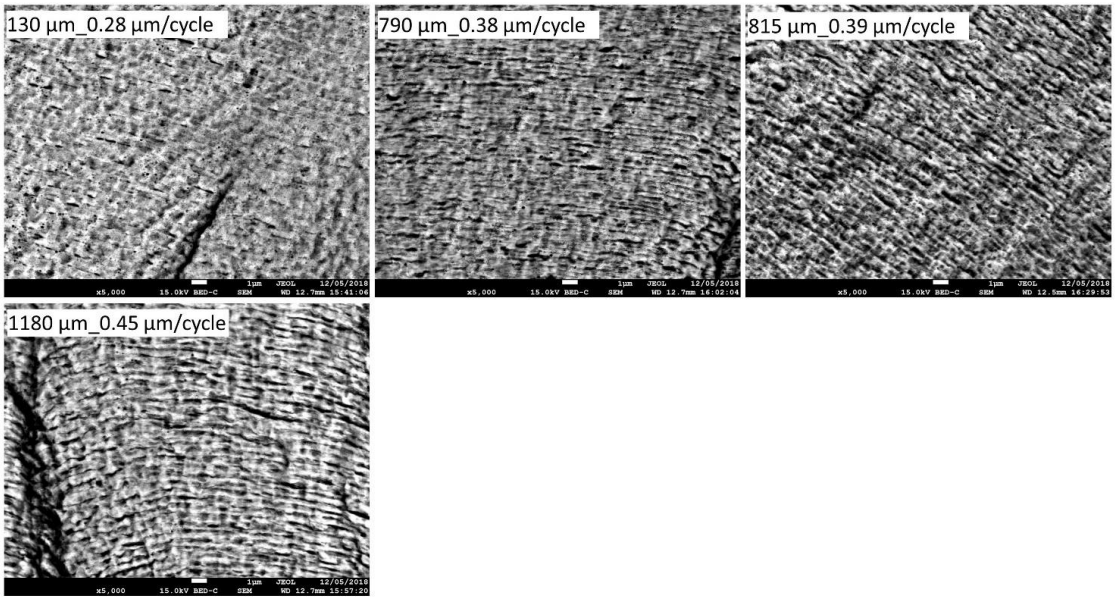

H-C

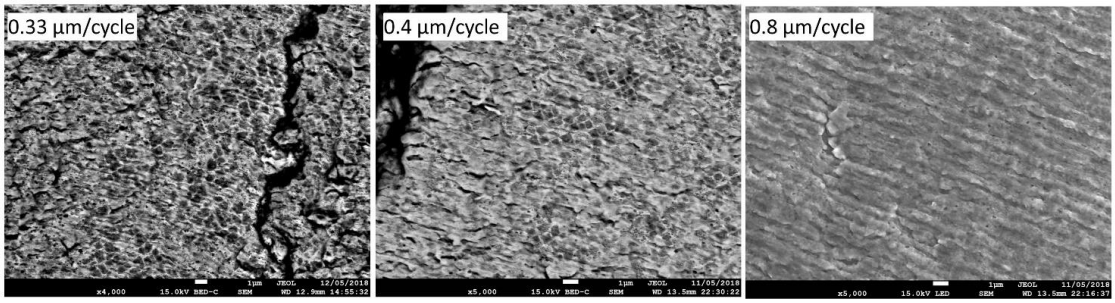

Supplement Fig. 6.1 Examples of striation spacing measurement and crack propagation rate determination in sample L-T, L-C, H-T, H-E and H-C. distance from the crack initiation point (first value) and crack propagation rate for each site are shown in each figure. There is no distance value in H-C sample as the special fracture surface feature in this case as explained in text.

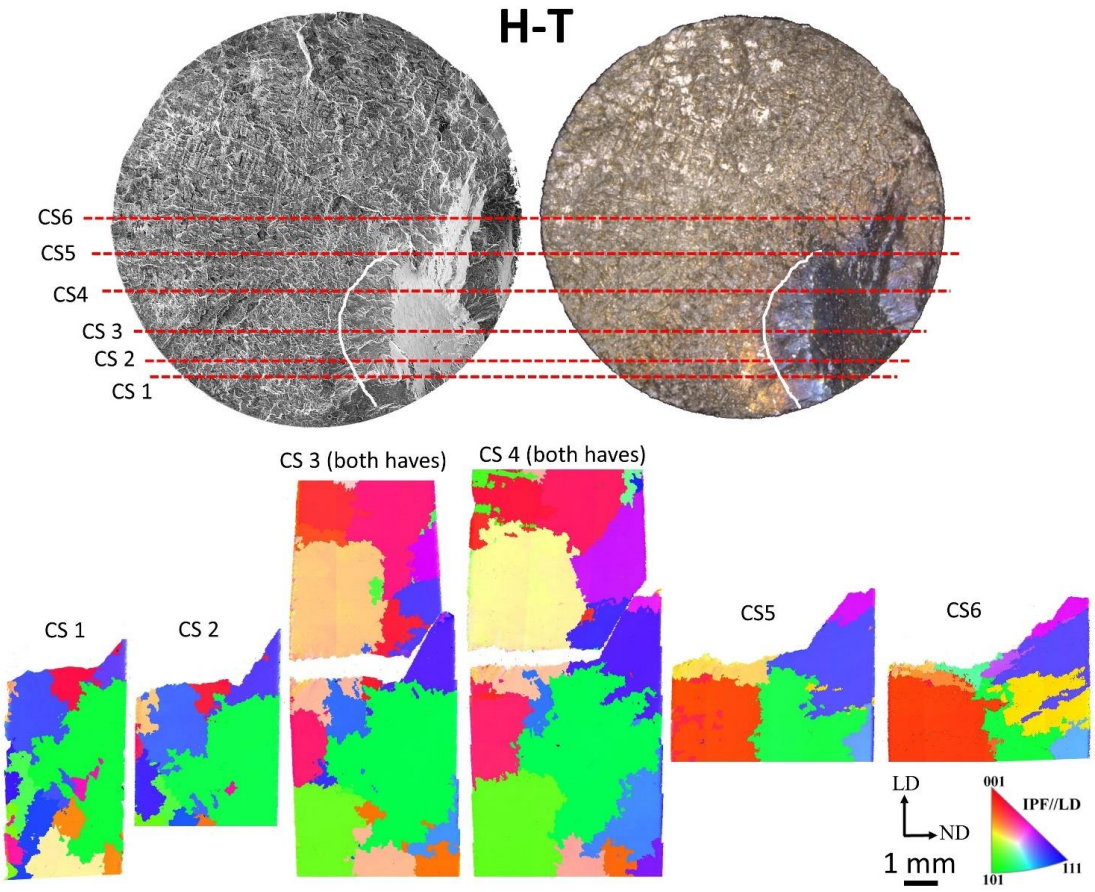

Supplement Fig. 6.2 IPF//LD (Y) without rotation of each cross sections of H-T sample, compared to Fig. 6.13a.

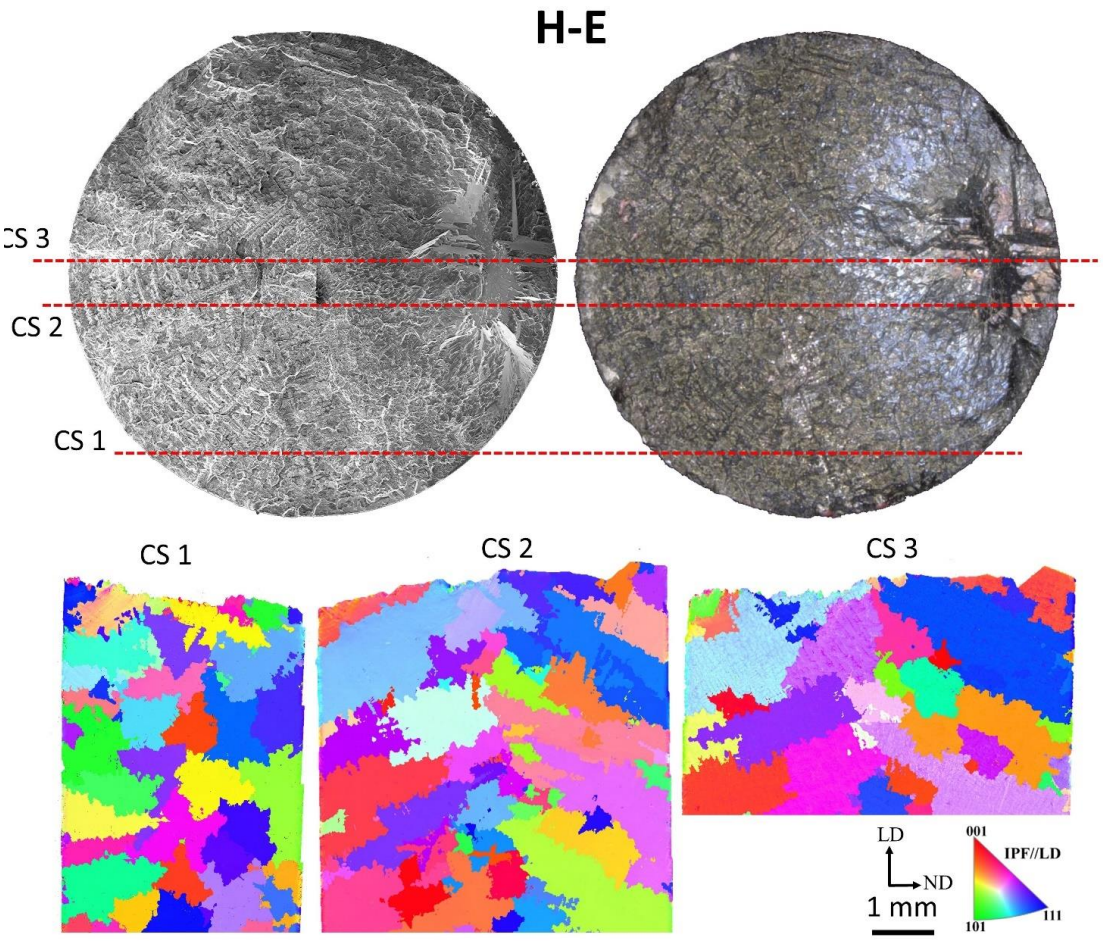

Supplement Fig. 6.3 IPF//LD (Y) without rotation of each cross sections of H-E sample, compared to Fig. 6.13b.

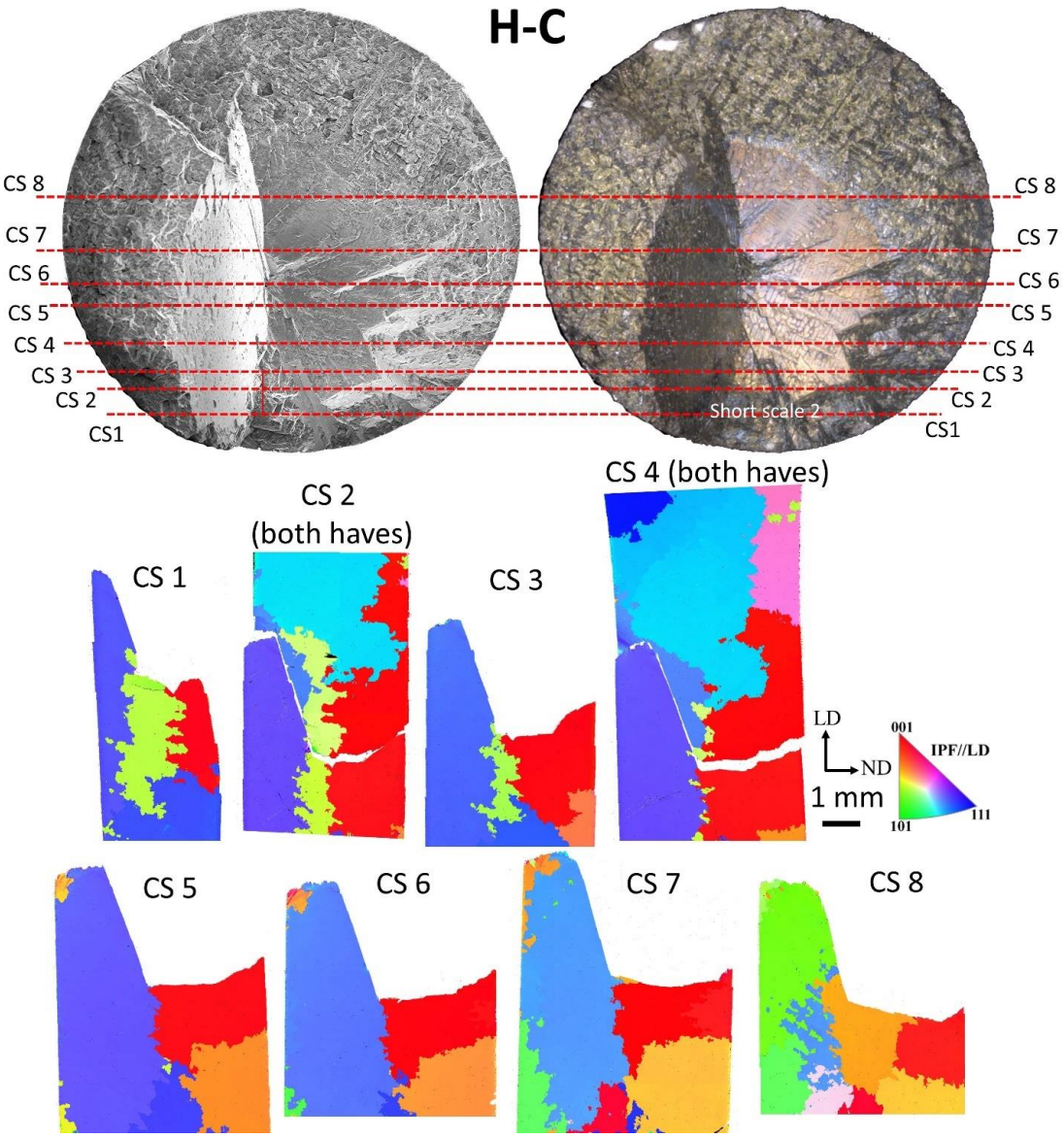

Supplement Fig. 6.4 IPF//LD (Y) without rotation of each cross sections of H-C sample, compared to Fig. 6.14c.

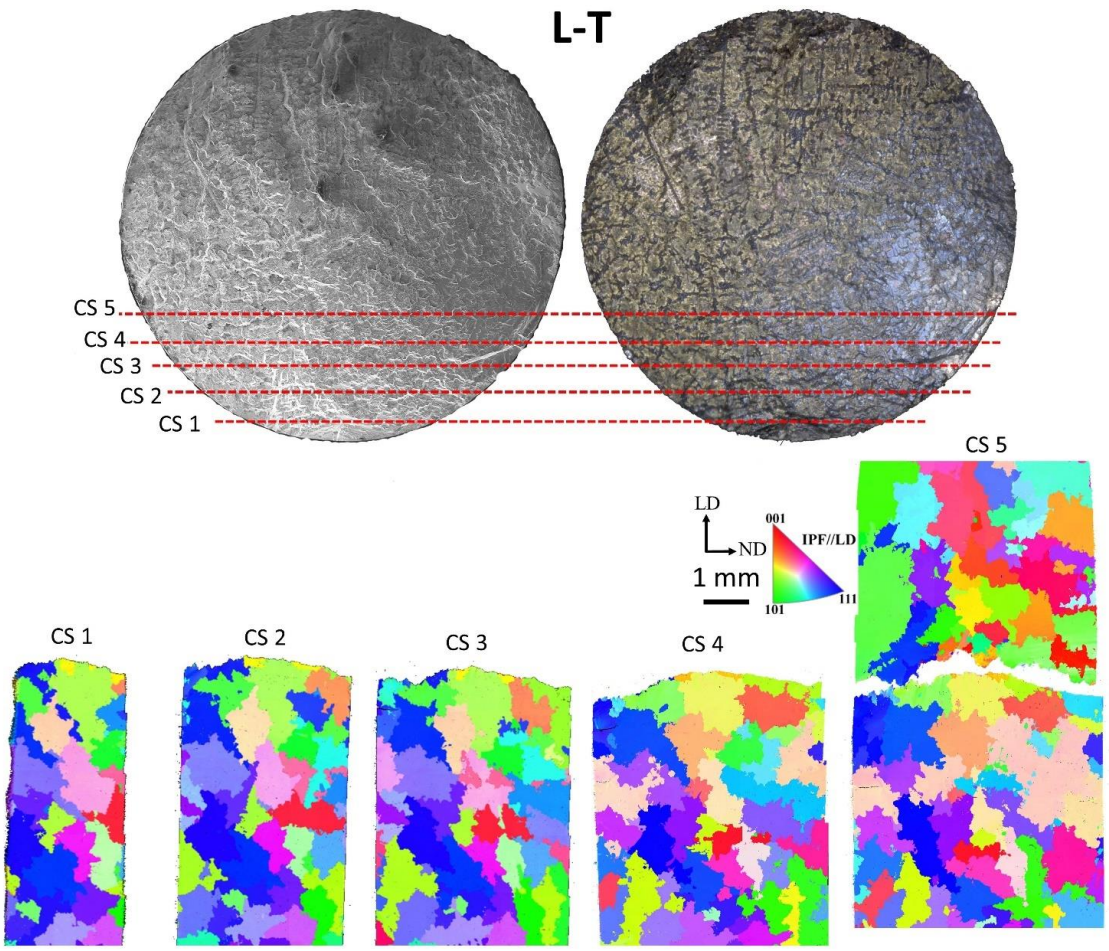

Supplement Fig. 6.5 IPF//LD (Y) without rotation of each cross sections of L-T sample, compared to Fig. 6.15a.

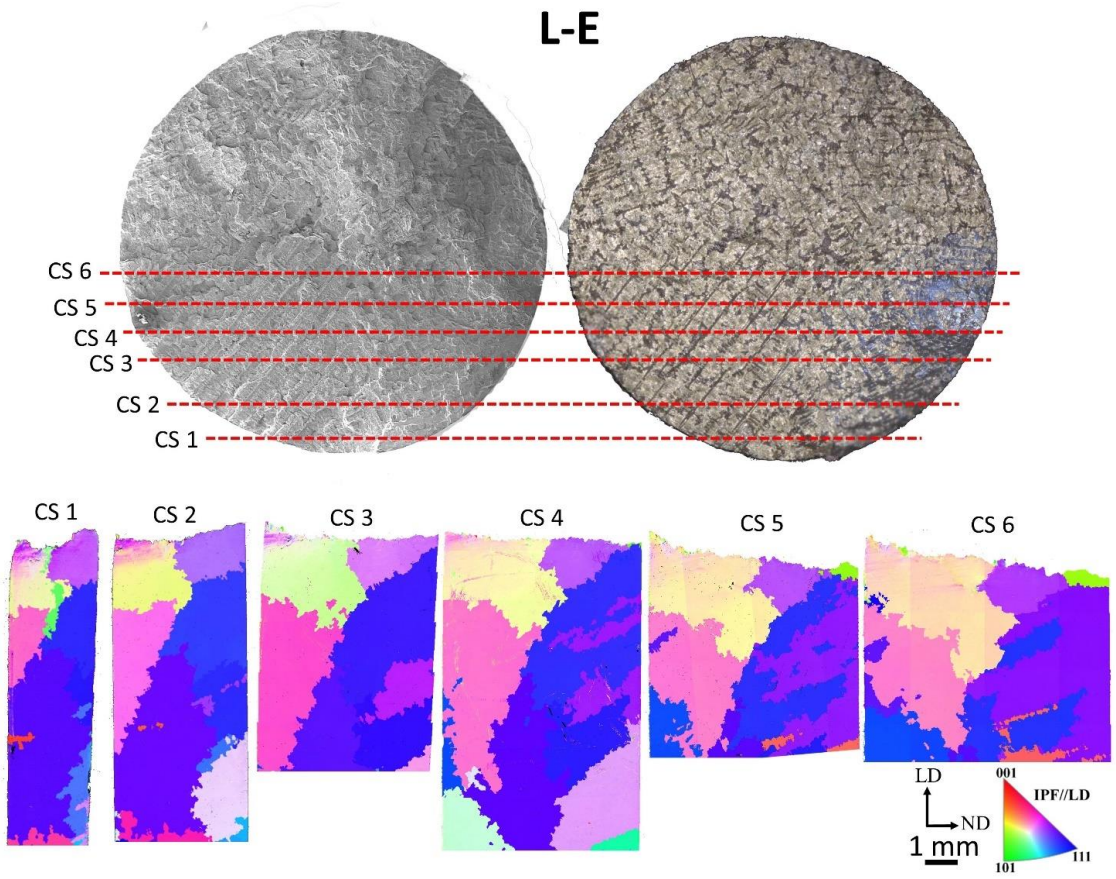

Supplement Fig. 6.6 IPF//LD (Y) without rotation of each cross sections of L-E sample, compared to Fig. 6.15b.

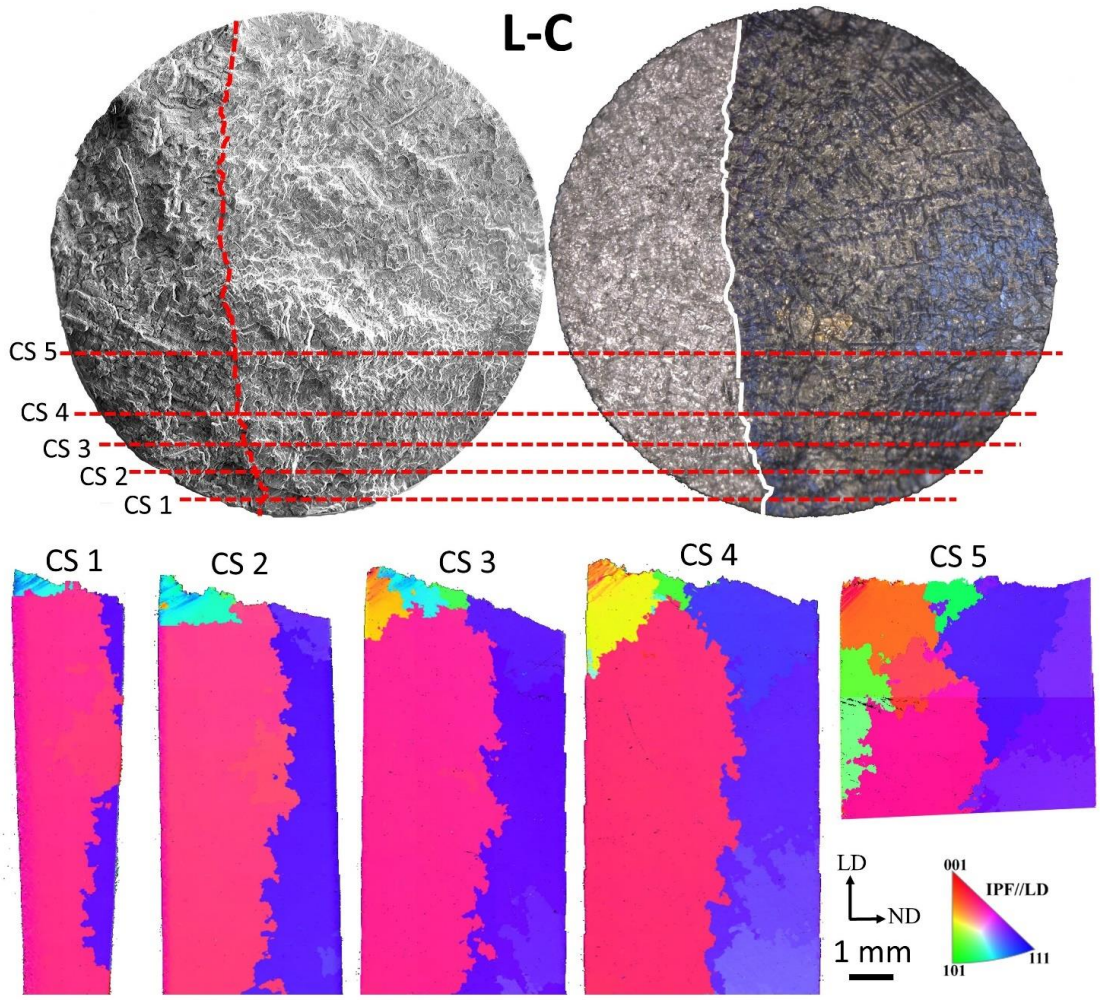

Supplement Fig. 6.7 IPF//LD (Y) without rotation of each cross sections of L-C sample, compared to Fig. 6.15c.

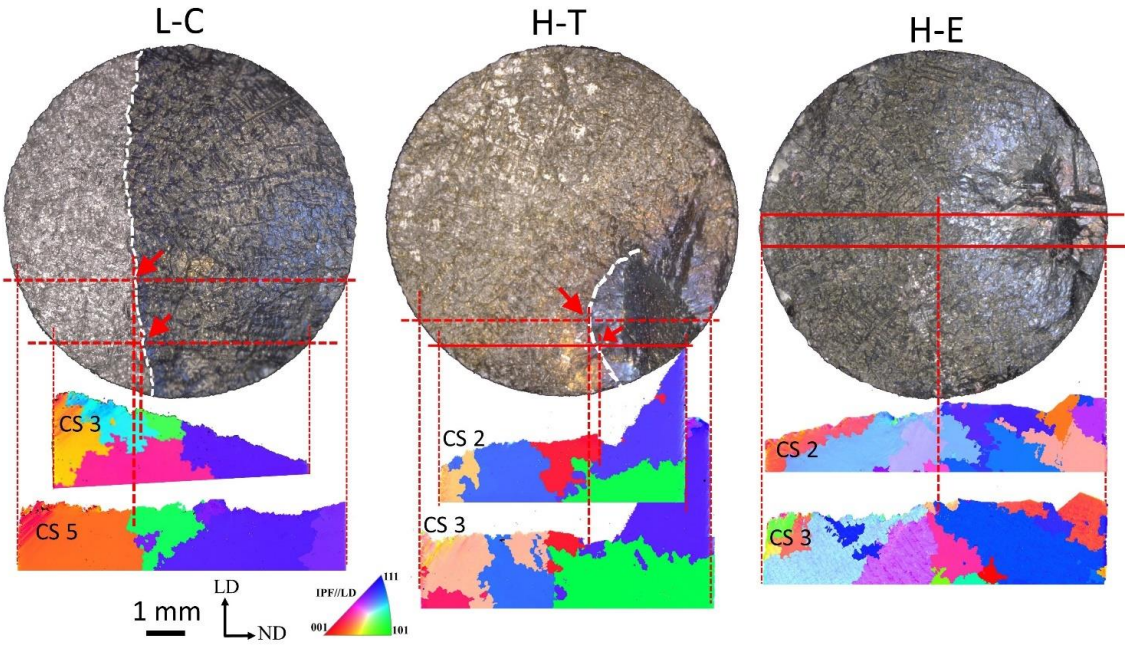

Supplement Fig. 6.8 The effect of grain boundary on the final stage of crack propagation

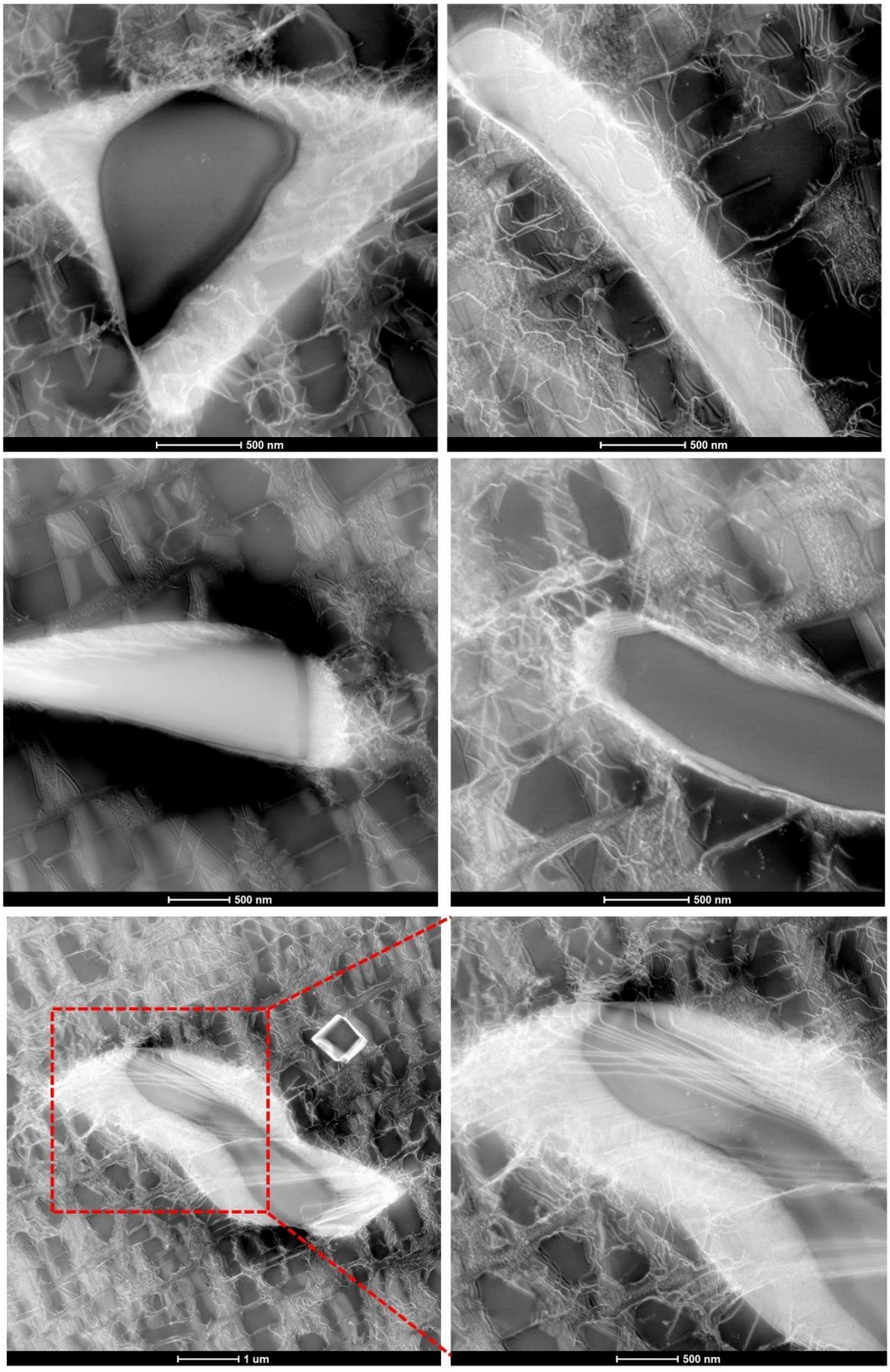

Supplement Fig. 6.9 High dislocation density around carbides in L-E imaged by STEM-HAADF.

Chapter 7: The Effects of Cooling Rate on the Microstructure Developments of IN713C Nickel-based superalloy During Solidification

Abstract

The effects of cooling rate on microstructure and microtexture development during solidification of IN713C nickel-based superalloy have been studied with a range of cooling rate from 0.3 °C/s to 4°C/s (air cooling). The results showed an increase in grain size (from 140 μm to 2 mm) and carbides volume fraction (1.3% to 2%) with increasing cooling rate. It was also found that primary γ' size decreased with increasing cooling rate. Furthermore, it was demonstrated that the dendrite structure was weakened with decreasing cooling rate. The dendrite structure was nearly eliminated at slowest cooling rate applied here (0.3 °C/s). An eutectic cluster that mainly consisted a large γ', Ni_7Zr_2, M_3B_2 type boride and/or MC-type carbide precipitates is identified. This undesirable clusters were always associated with dendrite structure and their volume fraction was found to decrease with decreasing cooling rate. Moreover, predominant phase separation of γ' is observed in the slowest cooling sample and in interdendrite areas in the fastest cooling sample. Hardness test result showed a slight decrease in hardness with decreasing cooling rate. This may result from the balanced effects of detrimental effect of larger γ' and beneficial effect of smaller grain size in slowest cooling sample.

7.1 Introduction

The previous two chapters (Chapter 5 and Chapter 6) have presented and discussed the importance of role of microstructure and microtexture on the fatigue crack initiation and propagation process, especially the role of dendrite structure and gamma grain size. During the investment casting of IN713C nickel- based superalloy, cooling rate is a critical solidification parameter that can be relatively easily controlled both in industrial scale and campus-based lab scale. Therefore, it is interesting to know the microstructure and microtexture changes with different cooling rates, which is of practical significance.

The information obtained can be further used to modify the materials and finally improve their fatigue property.

Many researches have been conducted on the cooling rate correlation with microstructure alterations in nickel-based superalloy [1-11]. Some general trends of these microstructure changes with varying cooling rate have been introduced in the literature review part (Chapter 2 and section 2.5). Particularly, Bhambri et al. [1] have studied the effect of cooling rate on the microstructure of the same material, IN713C, a few decades ago. They focused on the carbide, γ', dendrite structure and element segregation. However, the advancement of characterisation technique nowadays, such as high-resolution SEM, and the development of EBSD, make the characterisation of the microstructure on micro/macro scale possible.

In the current investigation, a few solidification trials have been undertaken in the laboratory. HR-SEM, TEM, STEM-HAADF and HR-EBSD was used for the microstructure and microtexture complete charaterisaion. Further attention was paid on grain size, dendrite structure and the associated phase precipitation. Moreover, the hardness test was conducted to reveal the effects of varying microstructures features and crystallographic grain orientation on hardness.

7.2 Experiment Procedures

To simulate and study the effects of cooling rate during solidification on the microstructure (dendritic, grains, carbides and gamma prime), solidification experiment was undertaken with different cooling rate using induction furnace with Ar gas protection. The specimen was first heat up to 1550°C within 15 mins and hold for 15 minutes, then cooled down with different cooling rate (controlled by heating system) in a crucible ring with the size of Ø12×24 mm, see Fig. 3.3a. The materials used for this study are IN713C nickel-based superalloy and the chemical composition are listed in Table 2.2. Afterwards, the solidified sample were cut through the longitudinal direction (solidification direction). The cross-section surface was then mounted, grinded and polished and further for harness test and EBSD scanning. The grinding and polishing procedures are detailed in Chapter 3 and Sections 5.2 and 6.2. During EBSD scanning, for large area of the cross-section, a large step size of 8 μm and 8 × 8 binning are used

for fast scanning. Smaller step size ranging from 200 nm to 2 μm for hardness loading area and 4 × 4 binning are chosen for high resolution mapping. Procedure for etching (both chemical and electric) for SEM imaging and for TEM specimen preparation have also been reported in Section 6.2.

The hardness test use Vickers hardness, and the loading force of 3Kgf was chosen. The loading holding time is 15s.

7.3 Results and Discussion

7.3.1 Effect of Cooling Rate on Grain Structure, γ' and Carbides

In the current research, the samples that are solidified at four cooling rates, i.e., 4 °C/s (air cooling, noted as AC, the highest cooling rate in the trials), 2.8 °C/s (noted as 2C), 1.2 °C/s (noted as 3C) and 0.3 °C/s (the slowest cooling rate, noted as 4C) are selected for detailed characterisations. Fig. 7.1 shows IPFs // Y (solidification direction) for each cooling rate sample. It shows grain size decrease with decreasing cooling rate, from around 2 mm in air cooling (AC) sample (Fig. 7.1a), 350 μm in 2C sample (Fig. 7.1b), 210 μm in 3C sample (Fig. 7.1c) to around 140 μm in 4C sample (Fig. 7.1d). According to the orientation distribution function (ODF) in 3C and 4C samples, there is no predominant texture formed during solidification when the grain size decreased whilst the grain numbers increased.

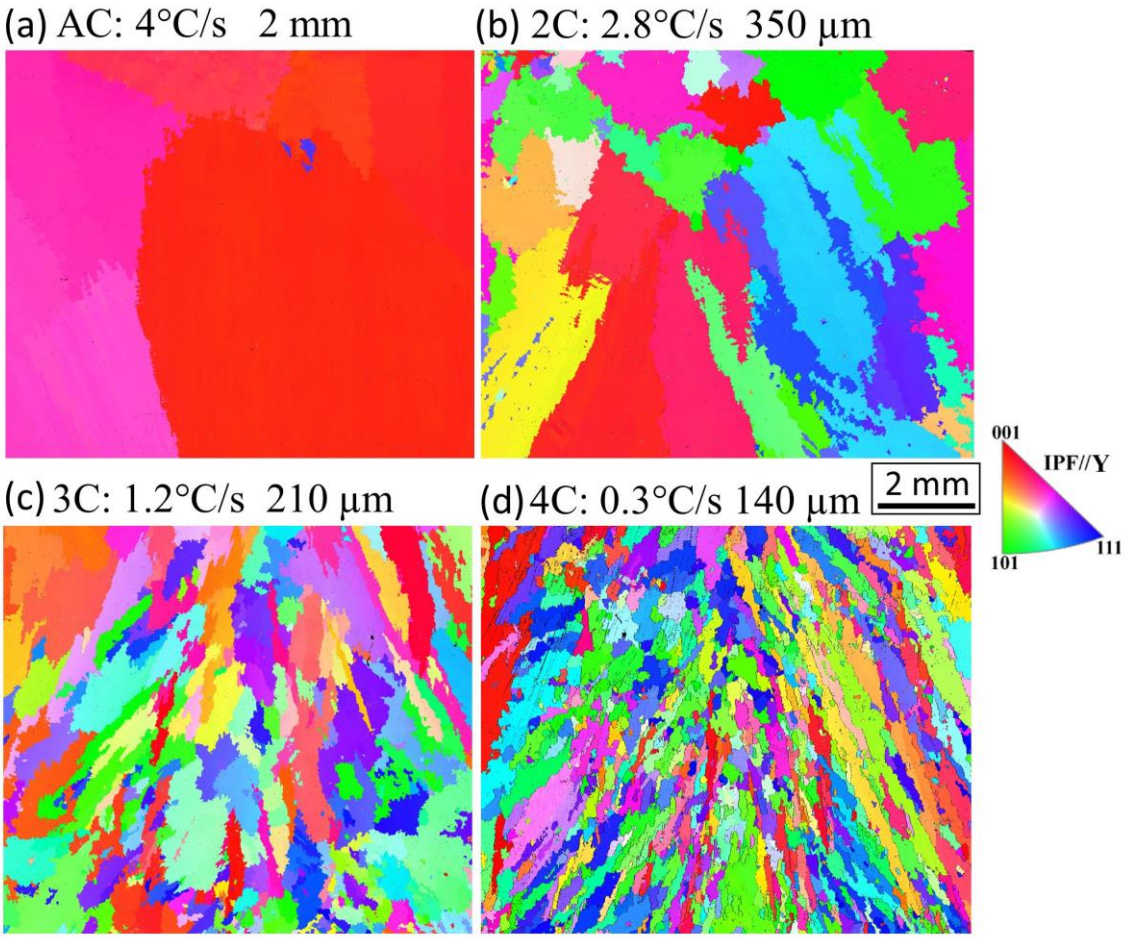

Fig. 7.1 IPFs // solidification direction (Y direction) showing grain size and structures varying with different cooling rate: (a) 4°C/s, noted as AC, (b) 2.8°C/s, noted as 2C, (C) 1.2°C/s, noted as 3C and (d) 0.3°C/s, noted as 4C. The average grain size for each structure are also listed on the figures.

Fig. 7.2 shows the primary γ' size and morphology evolutions with varying cooling rate. The results showed that there were two sets of γ' precipitation observed in the cast alloy, i.e., the large size (200-700 nm) precipitating around 810 °C which are termed 'primary γ'' here, and the small size (10-30 nm) precipitating during lower temperature period of cooling, which is termed 'secondary γ''. The morphology and size of secondary γ' are shown and discussed in Fig. 7.3 and Fig. 7.4. The result from Fig. 7.2 indicates a larger primary γ' size with decreasing cooling rate. This is in an agreement with studies in [3-7]. Specifically, the average primary γ' size changed from around 160 nm in AC, 240 nm in 2C, 380 nm in 3C to around 720 nm in 4C. The morphology of primary γ' in all samples are essentially cubic shape, except a bit small round corner is observed

in primary γ' in AC sample. For primary γ' in 4C sample, in addition to the cubic shape, some large γ' seem to be cut through by two perpendicular lines in the centre, see Fig. 7.2d. This is called phase separation phenomenon [12-15] and will be introduced in Fig. 7.5 in detail.

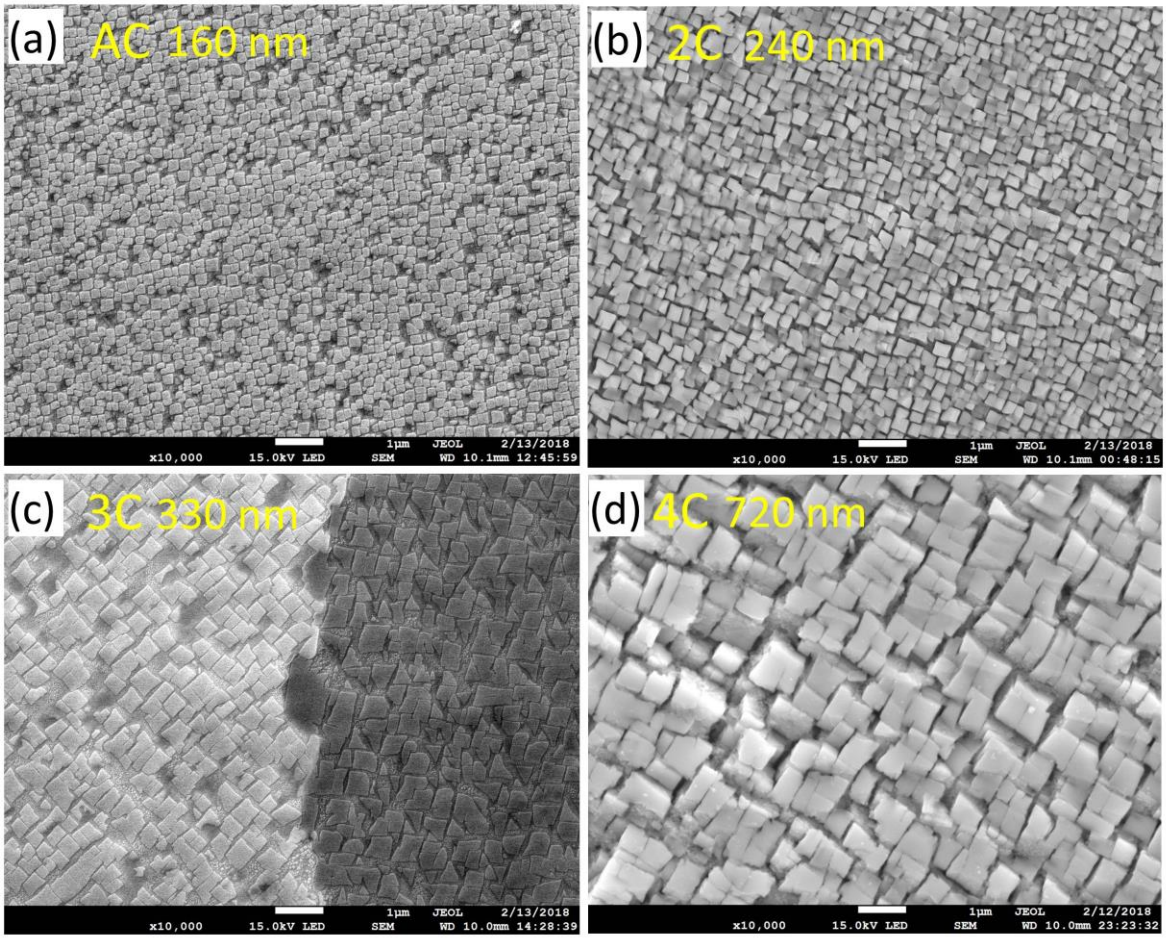

Fig. 7.2 Size and morphology of primary γ' varying with different cooling rate: (a) AC, (b) 2C, (C) 3C and (d) 4C. The average γ' for each cooling rate are also listed on the figures. The images are selected from dendrite area if there is apparent dendritic structure in the solidification samples.

It should be noted that the γ' are imaged from dendrite area where the sample has predominant dendrite structure, such as AC sample which will be discussed in the next section. Fig.7.3 present an example of the difference of primary γ' in dendrite area and interdendrite area in AC sample. A bit larger size of γ' and non-uniformed distribution of γ' can be found in interdendrite area compared to dendrite area. Moreover, the phase

separation can also be observed in interdendrite area as indicated by red dotted circles in Fig. 7.3b.

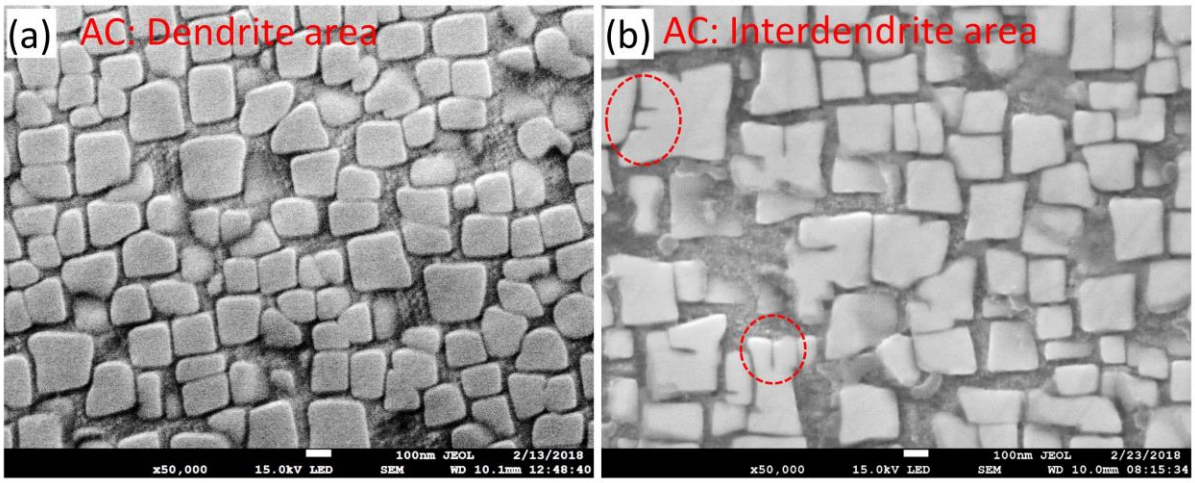

Fig. 7.3 Difference in size and morphology of primary γ' in dendrite area (a) and interdendrite area (b) in AC sample. Some of phase separation sites are indicated by red dotted lines in (b).

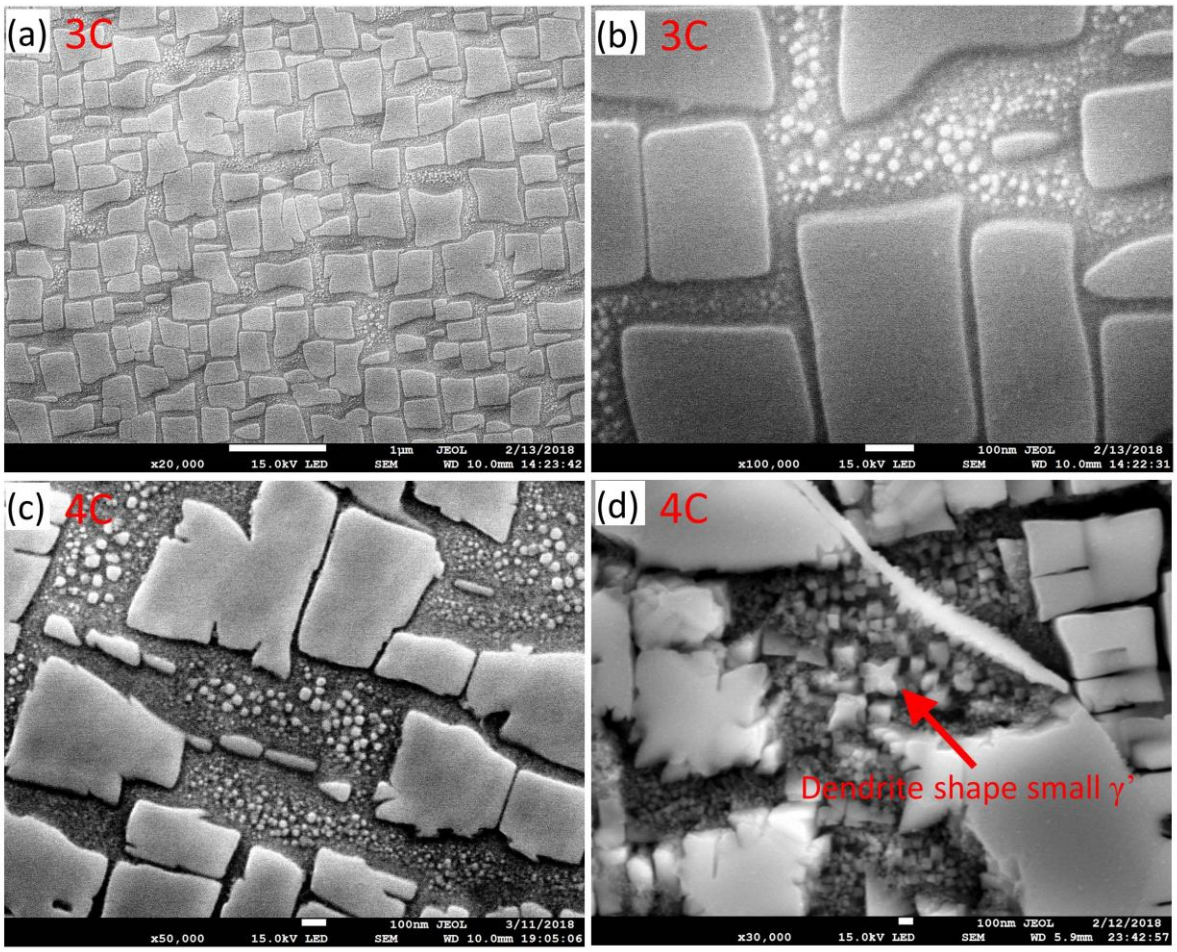

Fig. 7.4 Effect of cooling rate on the size and morphology of secondary γ'. (a) (b) in 3C and (c) (d) in 4C

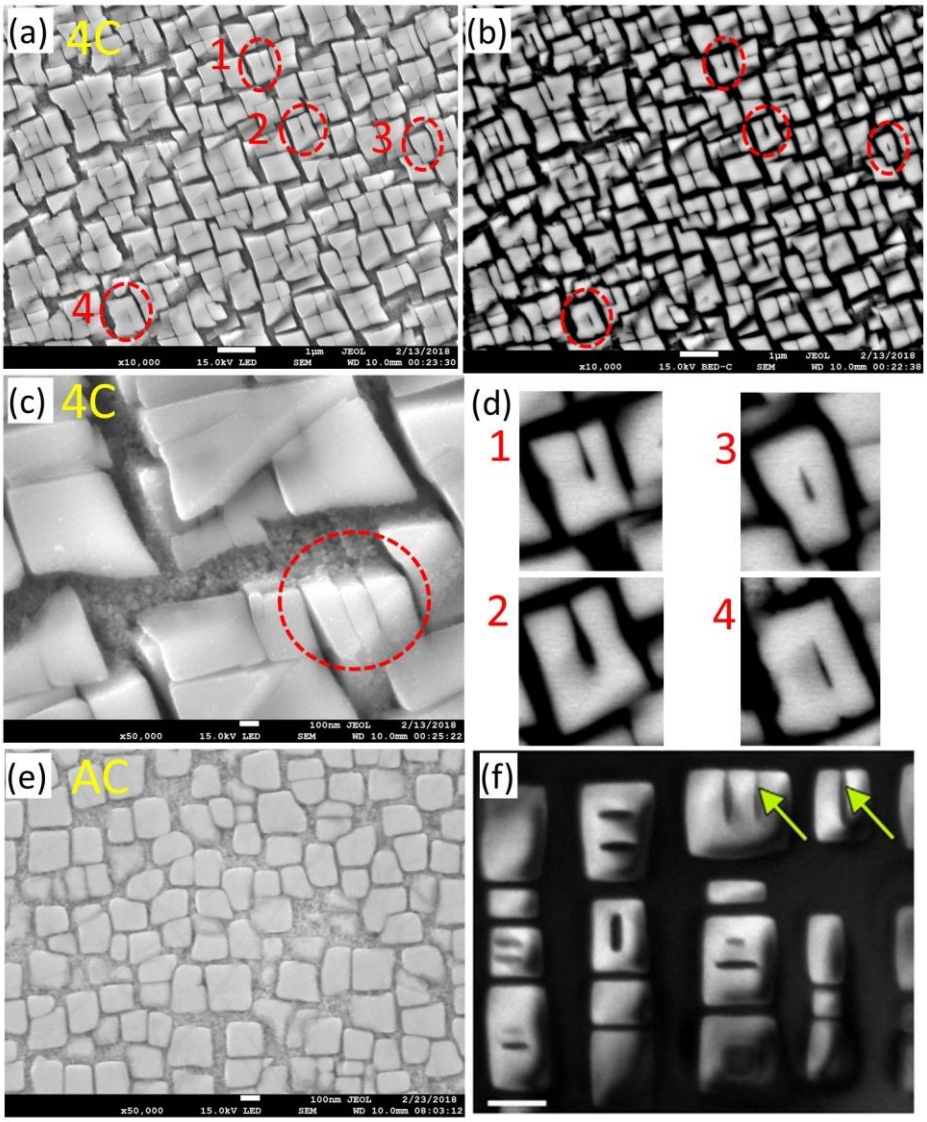

Fig. 7.5 Effect of cooling rate on phase separation. (a-d) in 4C, (e) in AC and (f) from ref. [13]. (a) (b) show the same area with different imaging mode: (a) SE (second electron) and (b) BS (backscatter). Some of phase separation sites are highlighted with red dashed circles in (a, b) and magnified in (d). (c) shows a 3-D phase separation perspective by deep etching.

The effect of solidification cooling rate on secondary γ' is exemplified in Fig. 7.4. In 3C sample, very fine spherical secondary γ' particles with 10-30 nm in size are uniformly distributed in the γ channel (Fig. 7.4a, b). Whilst in 4C sample with slower cooling rate, not only are the size of these uniformed spherical secondary γ' particles a little larger (20-60 nm) than in 3C (Fig. 7.4c), some dendritic shape secondary γ' with around 200 nm in size can be observed along the grain boundaries in 4C sample (indicated by red arrow in Fig. 7.4d). According to the hierarchy of γ' shape evolution

[16], it is concluded that slower cooling rate produce much higher misfit between γ' and γ than high cooling rate samples.

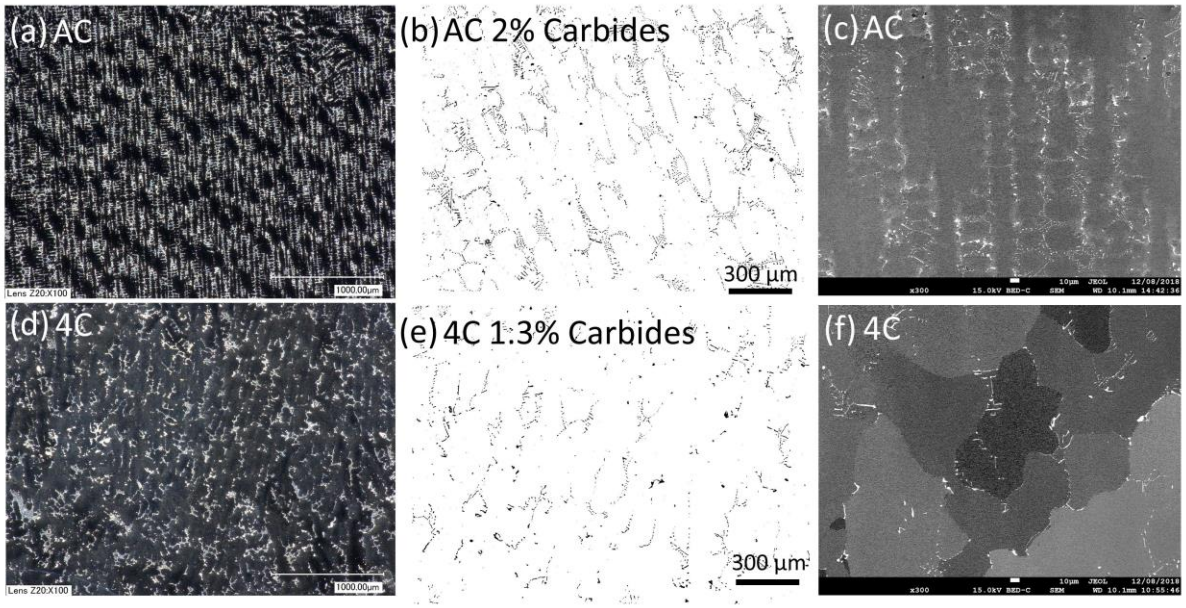

Fig. 7.6 Effect of cooling rate on carbides volume fraction and distribution. (a-c) in AC and (d-f) in 4C. (a, d) optical images showing carbides distribution with white contrast; (b, e) optical images after image processing showing carbides distribution and volume fraction with black contrast; (c, f) SEM images showing carbides distribution.

As discussed above, phase separation occurred in both in 4C sample and interdendrite area of AC sample. Some detailed examples in 4C are shown in Fig. 7.5a-d where phase separation sites are highlighted by red dashed circles and numbered in 1-4. The dendritic area in AC where there is no phase separation is displayed in Fig. 7.5e. The phase separation in nickel-based superalloy is also reported in literature [5] and it is shown in Fig. 7.5f as an example. It shows that phase separation initiated either on the edge of primary γ' (1, 2 in Fig. 7.5d) or in the centre of primary γ' (3, 4 in Fig. 7.5d), which agrees with [5], see Fig. 7.5f. During slow cooling rate, solute elements, especially heavy atomic elements such as Ta, Mo and Nb have more time to diffuse uniformly, which provides an excessive amount to the formation of γ'. This is also a reason of large γ' size in slower cooling sample (4C). However, this high element containing condition of γ' also leads into a super-saturation status, therefor facilitate the occurrence of phase separation [13, 15]. The same situation applies to the interdendrite area in dendrite structures, where most of heavy atomic element are partitioned to

interdendrite areas, as shown in Table 5.1. The specific effects of this phase separation on the mechanical property of superalloy are yet to be examined [13, 15].

The microstructure witnesses a weakening dendrite structure with slowing cooling rate. Fig. 7.6 shows the representative dendrite structure in AC (Fig. 7.6a-c) and corresponding area in 4C (Fig. 7.6d-f). The result shows a clear dendrite structure in AC (Fig. 7.6c) and almost elimination of dendrite structure in 4C (Fig. 7.6f). By utilising BS (backscatter electron) mode in SEM, it is easy to identify the distribution of carbides by the white contrast in SEM images, i.e., in interdendrite area in AC (Fig. 7.6c) and long grain boundary in 4C (Fig. 7.6f). Also, the contrast in optical images can be used to calculate the volume fraction of carbides. It should be pointed out here that not only are carbides located in the interdendrite area and the other phases such as boride and Ni_7Zr_2 exhibit the same contrast with carbides in optical and SEM images. Therefore, calculation of the volume fraction for AC and 4C is a rough estimation and a slightly overestimation, especially in AC. However, it is still safe to claim that slower cooling rate leads to decrease in the precipitation of carbides, with 1.3% volume fraction of carbides in 4C and nearly 2% in AC.

7.3.2 Effect of Cooling Rate on Second Phase Precipitation

As in other nickel-based superalloy, the general phases in cast IN713C include γ matrix, γ’ strengthening phase (primary, secondary and probably tertiary γ’) and carbides (mainly MC-type carbides here). In addition to these phases, there are other two phases, Ni_7Zr_2 and M_3B_2-type boride might present. Although these two phases have been reported by Matysiak et.al [17], their precipitation location, morphology, and their relationship with other phases have rarely been reported. Here, we present a full characterisation of phases in IN713C and compare the difference with varying cooling rate, utilising the various scale of SEM images, TEM, STEM-HAADF and EDS from both SEM and TEM.

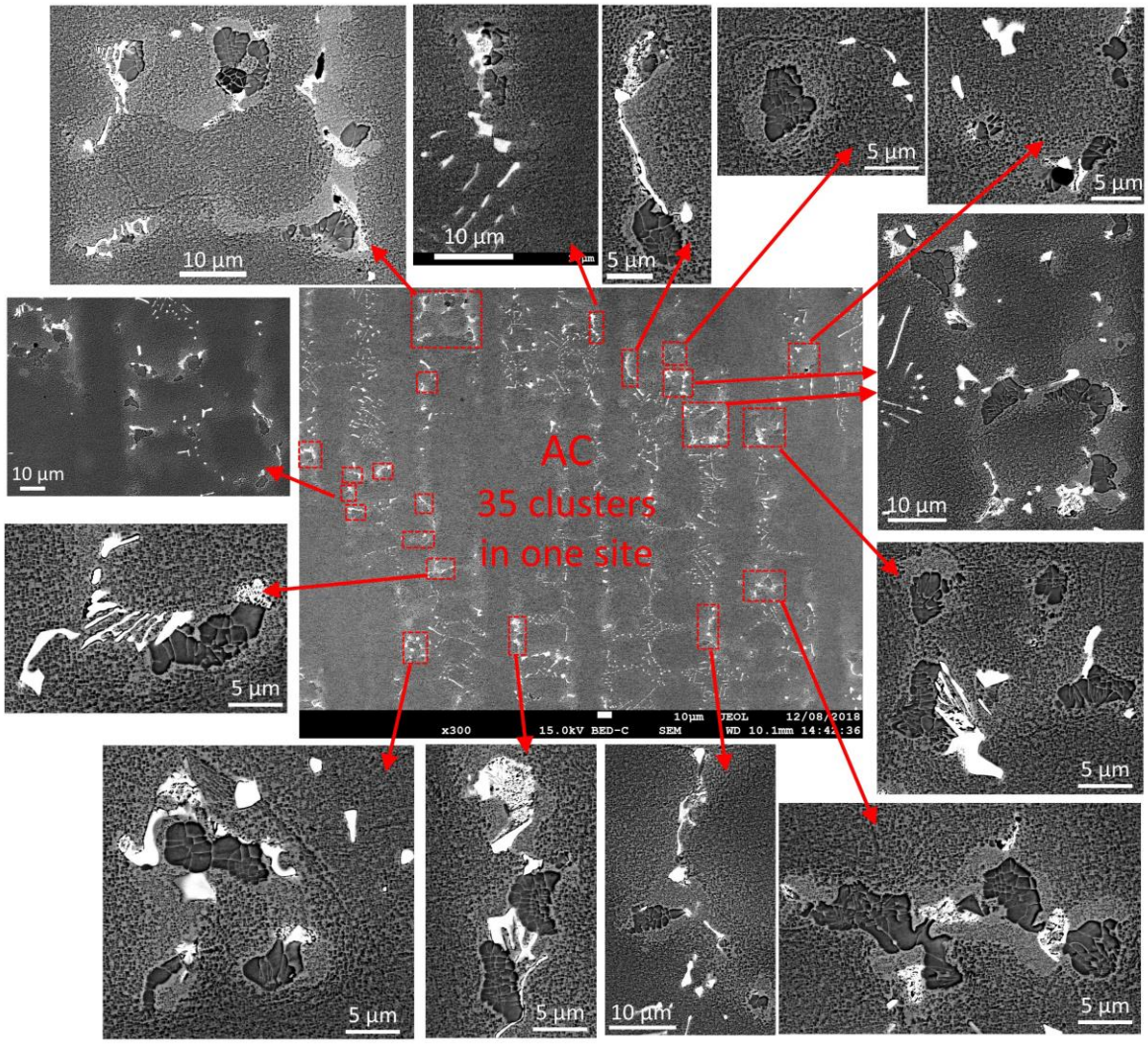

Fig. 7.7 Example of density and structure of eutectic clusters in one site in AC sample. The definition of eutectic cluster can be found in text.

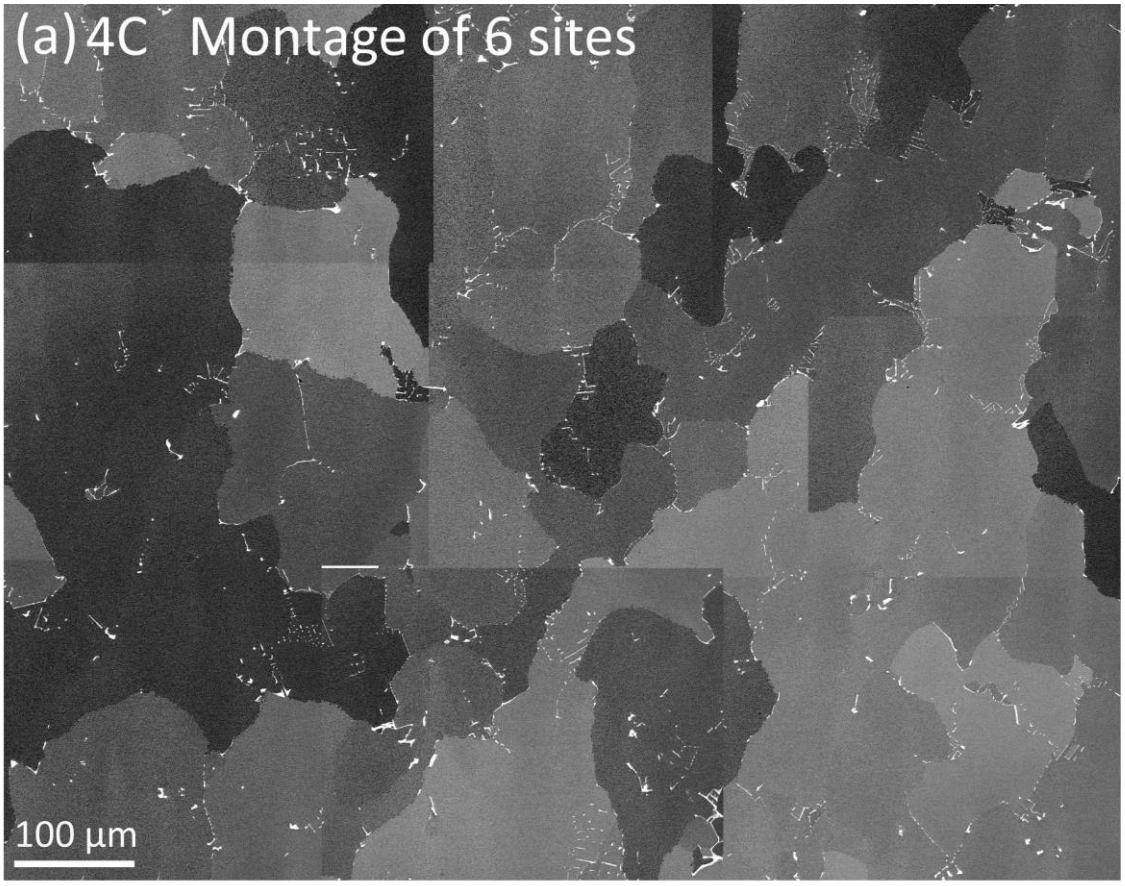
(a) 4C Montage of 6 sites
100 µm

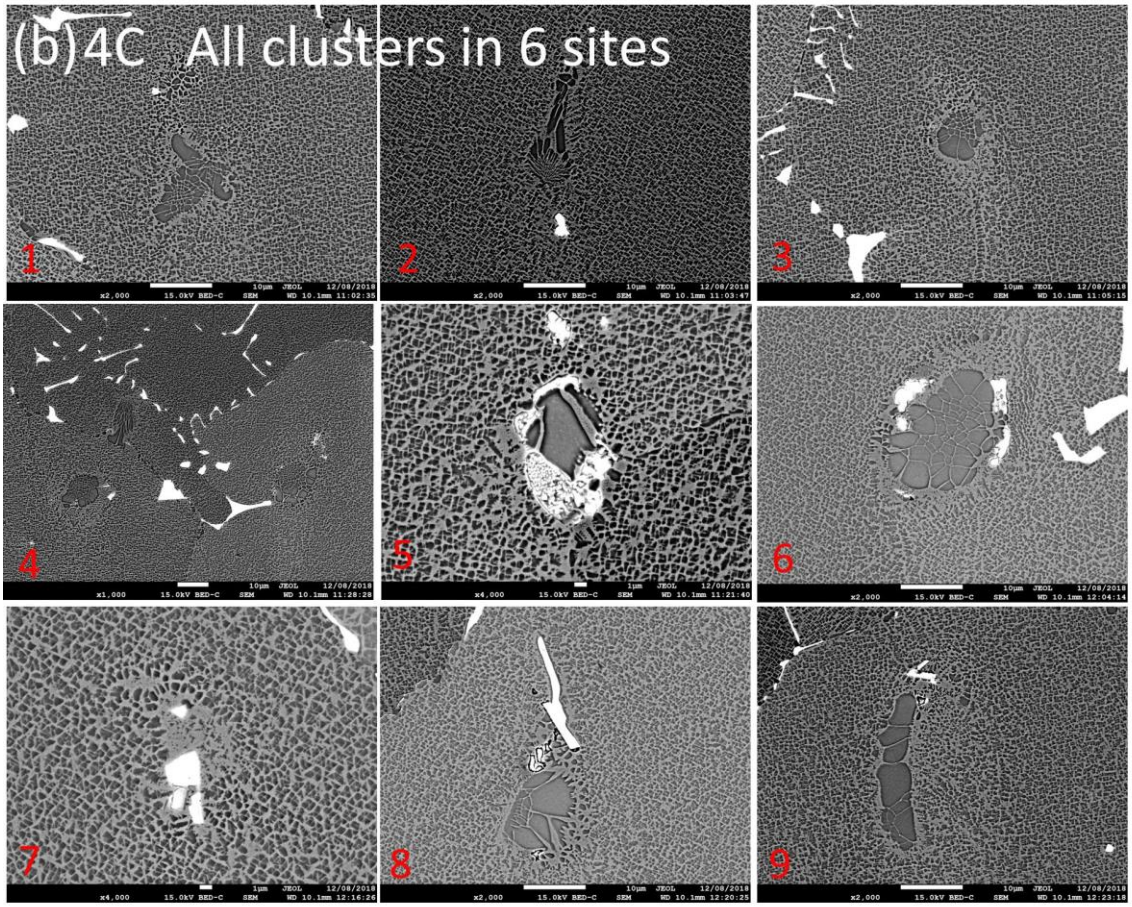
(b) 4C All clusters in 6 sites
1
2
3
4
5
6
7
8
9

Fig. 7.8 Example of density and structure of eutectic clusters in 6 sites (compared one site in Fig. 7.7 in AC) in 4C sample.

The representative microstructure including these phases are shown in Fig.7.7 and Fig.7.8 for AC and 4C, respectively. In interdendrite area in AC sample, in addition to carbides, other phases with complicated precipitation structure are also observed to segregate in the area. In the current study, we define the 'eutectic cluster' as the basic precipitation unit for three or four phases. The most predominant feature of this cluster is one large γ' associated with Ni_7Zr_2 and/or M_3B_2-type boride and/or carbides. This cluster unit is counted for a few large areas in both AC and 4C samples to compare the precipitation density. In an area of 400 × 300 μm^2, there are totally 35 eutectic clusters (Fig. 7.7), whilst in an area in 4C almost 6 times larger than in Fig. 7.7, 930 × 750 μm^2 (Fig. 7.8), there are totally 5 these clusters with very weak precipitation (some sites only consist of large γ' without other phases and will not be classified as a cluster, such as 1, 2, 3 and 4 in Fig. 7.8b). The average cluster density ratio was found to be ~ 35:1 in AC: 4C.

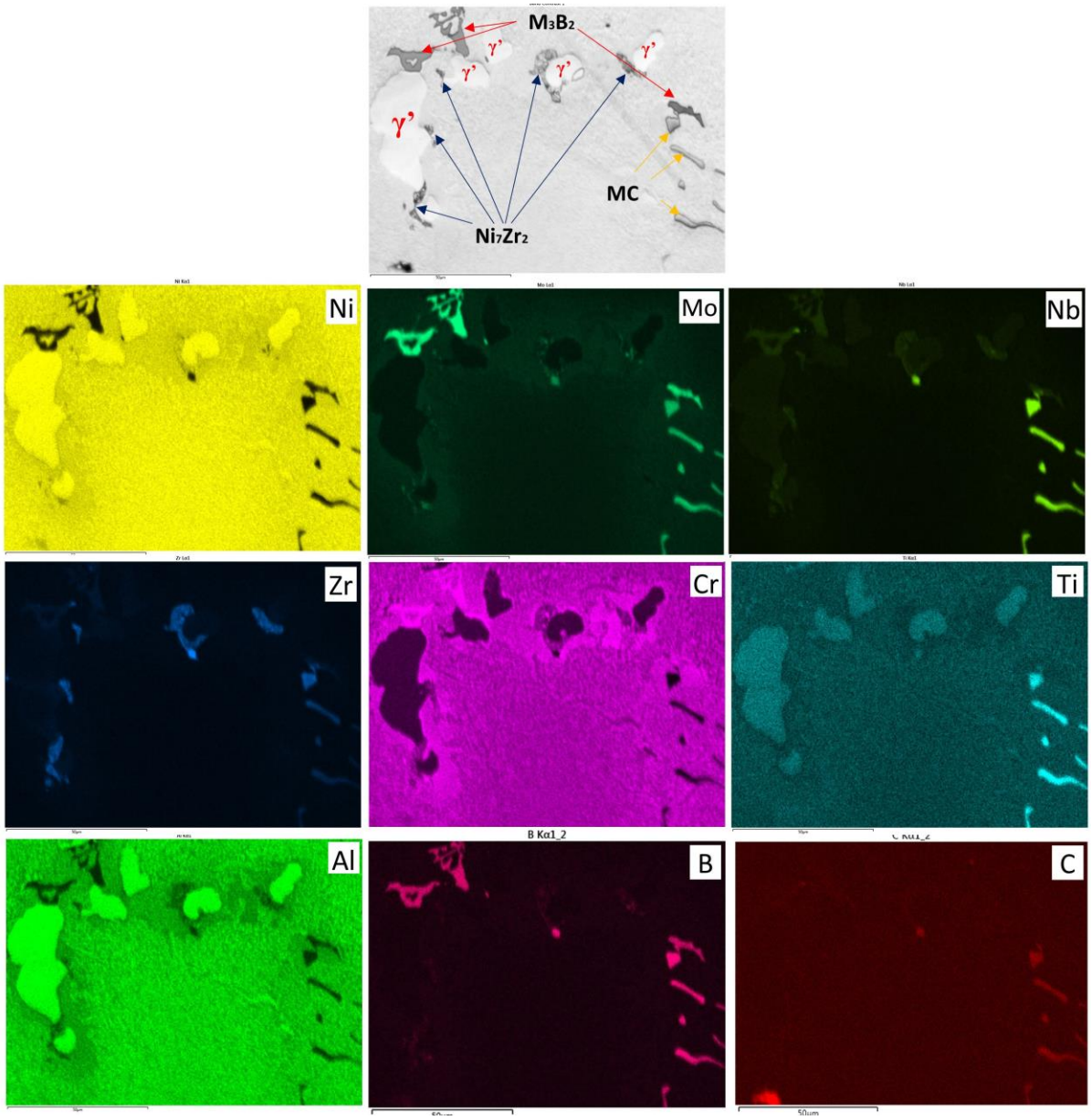

Fig. 7.9 Representative SEM image (band contrast image) of a eutectic cluster and EDS mapping in AC, showing the structure, morphology and elements distribution of four phases in the cluster: large γ', MC, Ni_7Zr_2 and M_3B_2

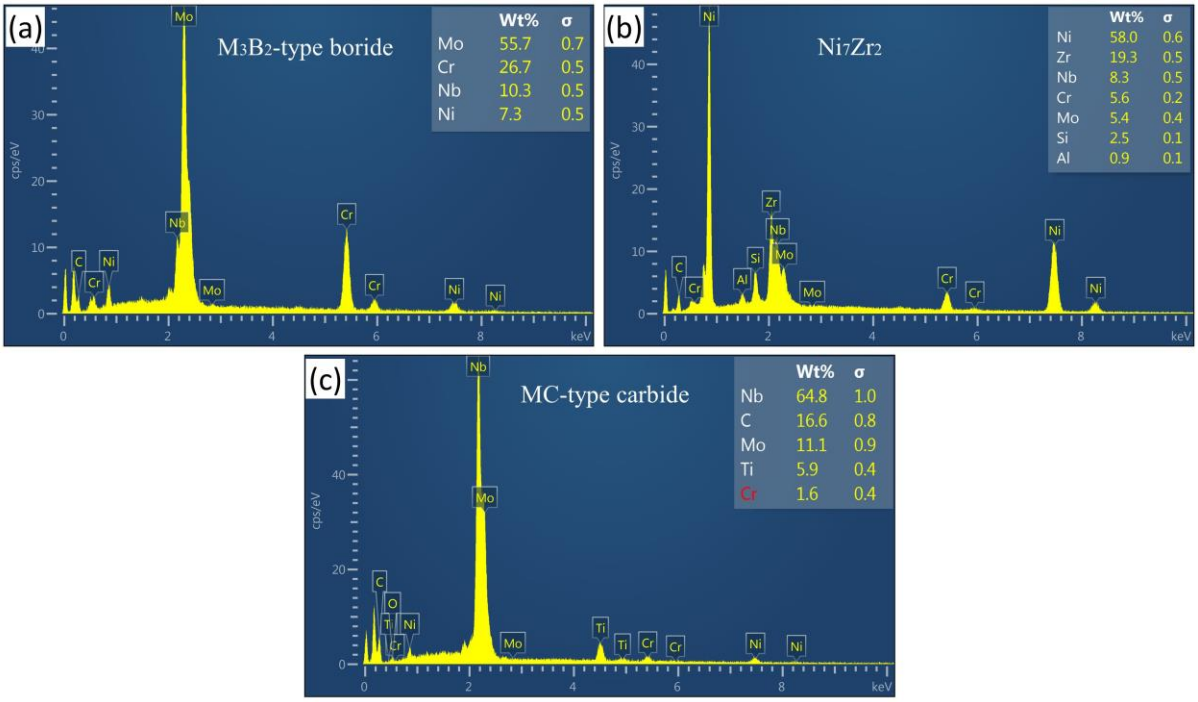

Fig. 7.10 Representative SEM-EDS spectrum for three common phases associated with eutectic cluster: (a) M_3B_2-type boride, (b) Ni_7Zr_2 (c) MC-type carbide

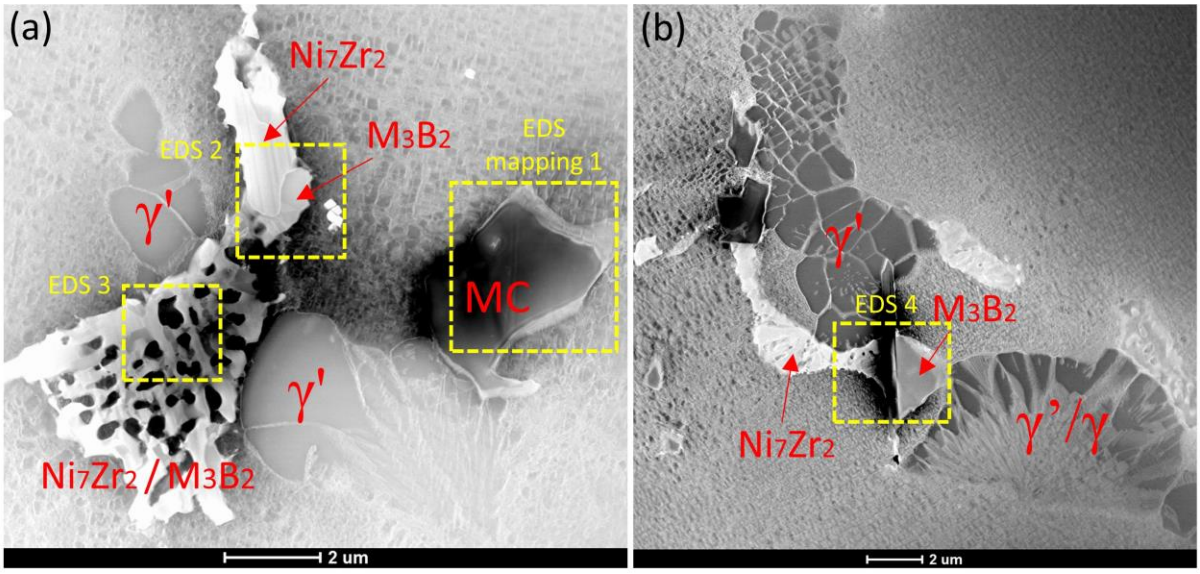

Fig. 7.11 Two representative STEM-HAADF images showing the eutectic cluster. Different phases are indicated or highlighted. Yellow rectangular areas are EDS-mapped and showed in following figures.

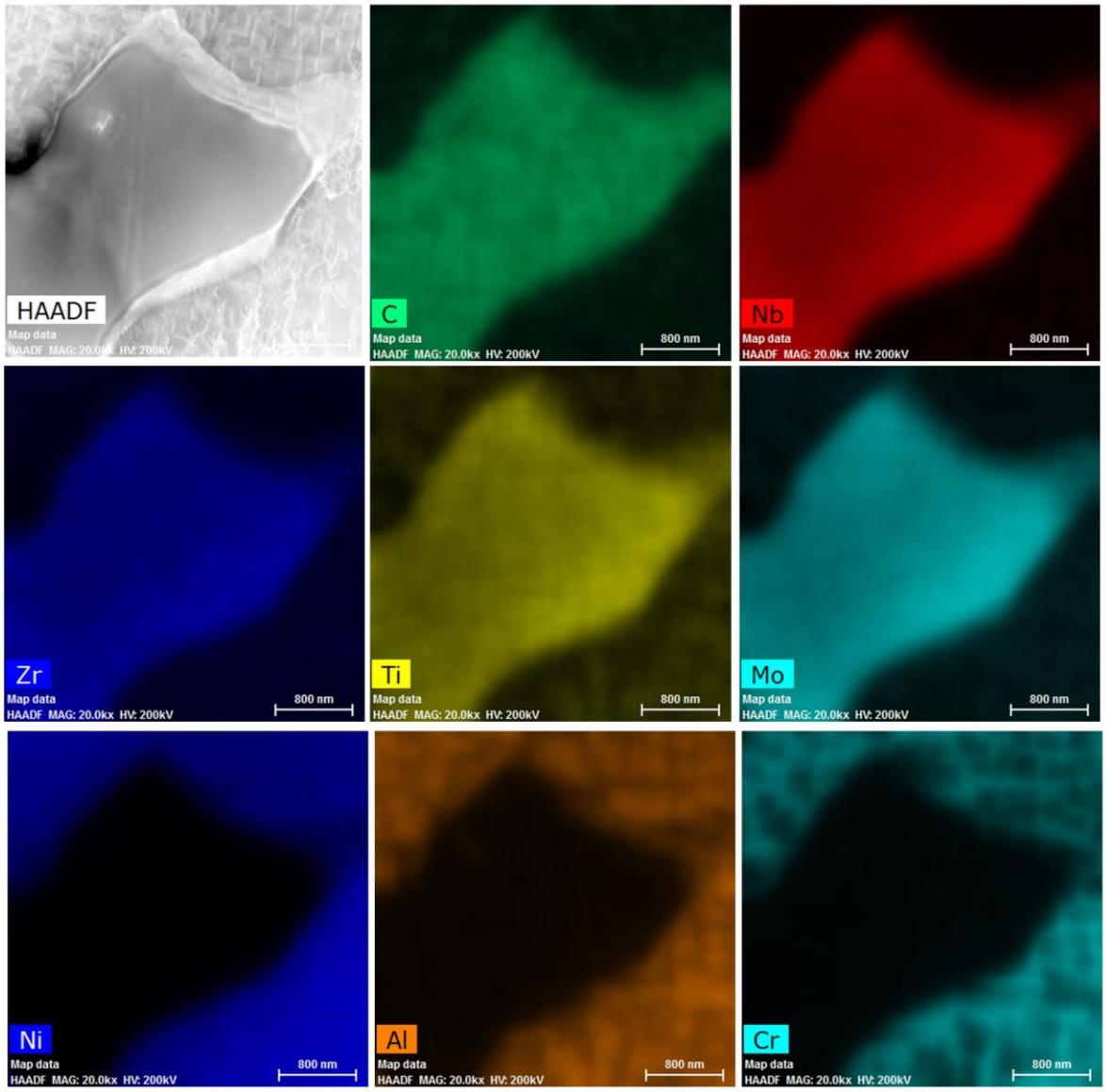

Fig. 7.12 EDS mapping of MC-type carbide which is mapped in the area of ‘EDS 1’ in Fig. 7.11a.

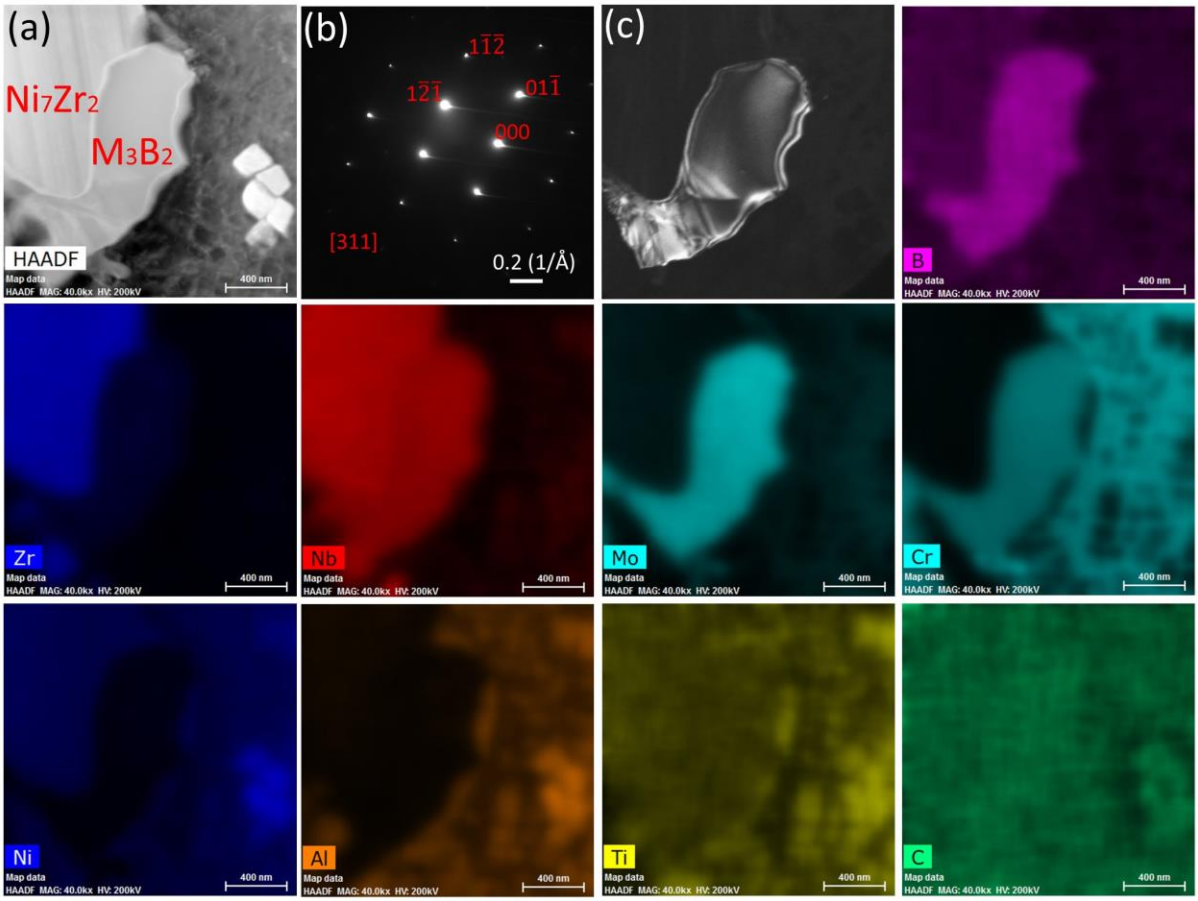

Fig. 7.13 EDS mapping of M_3B_2-type boride and Ni_7Zr_2 which were mapped in the area of 'EDS 2' in Fig. 7.11a. The Diffraction Pattern (DP) and dark field (DF) image of boride are showed in (b) and (c), respectively.

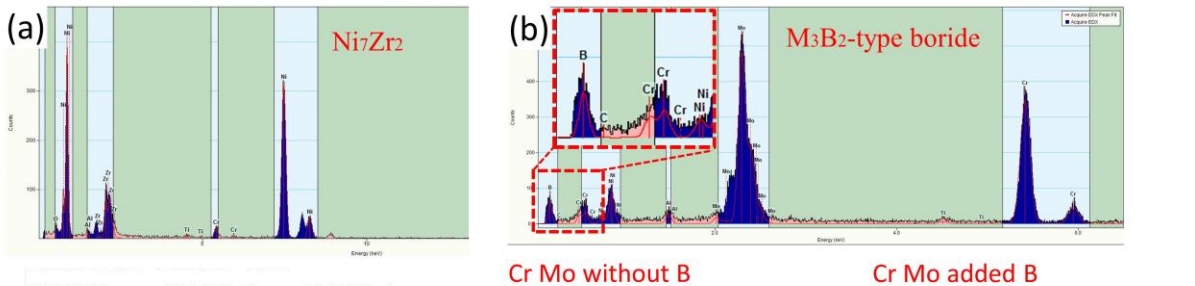

Element	Weight %	Atomic %
C(K)	0.44	2.23
Al(K)	0.76	1.71
Ti(K)	0.57	0.72
Cr(K)	3.94	4.60
Ni(K)	76.23	78.75
Zr(K)	14.89	9.90
Nb(K)	3.14	2.05
Mo(K)	0.00	0.00

Cr Mo without B

Element	Weight %	Atomic %
C(K)	0.00	0.00
Al(K)	1.41	3.28
Ti(K)	0.42	0.55
Cr(K)	47.60	57.20
Ni(K)	14.23	15.15
Zr(K)	0.15	0.10
Nb(K)	6.76	4.54
Mo(K)	29.39	19.14

Cr Mo added B

Element	Weight %	Atomic %
B(K)	30.51	71.87
C(K)	0.00	0.00
Al(K)	1.08	1.02
Ti(K)	0.51	0.27
Cr(K)	31.93	15.64
Ni(K)	9.40	4.08
Zr(K)	0.43	0.12
Nb(K)	5.18	1.42
Mo(K)	20.91	5.55

Fig. 7.14 Representative TEM-EDS spectrum for (a) Ni_7Zr_2 and (b) M_3B_2-type boride, the element list with and without element of B are both included.

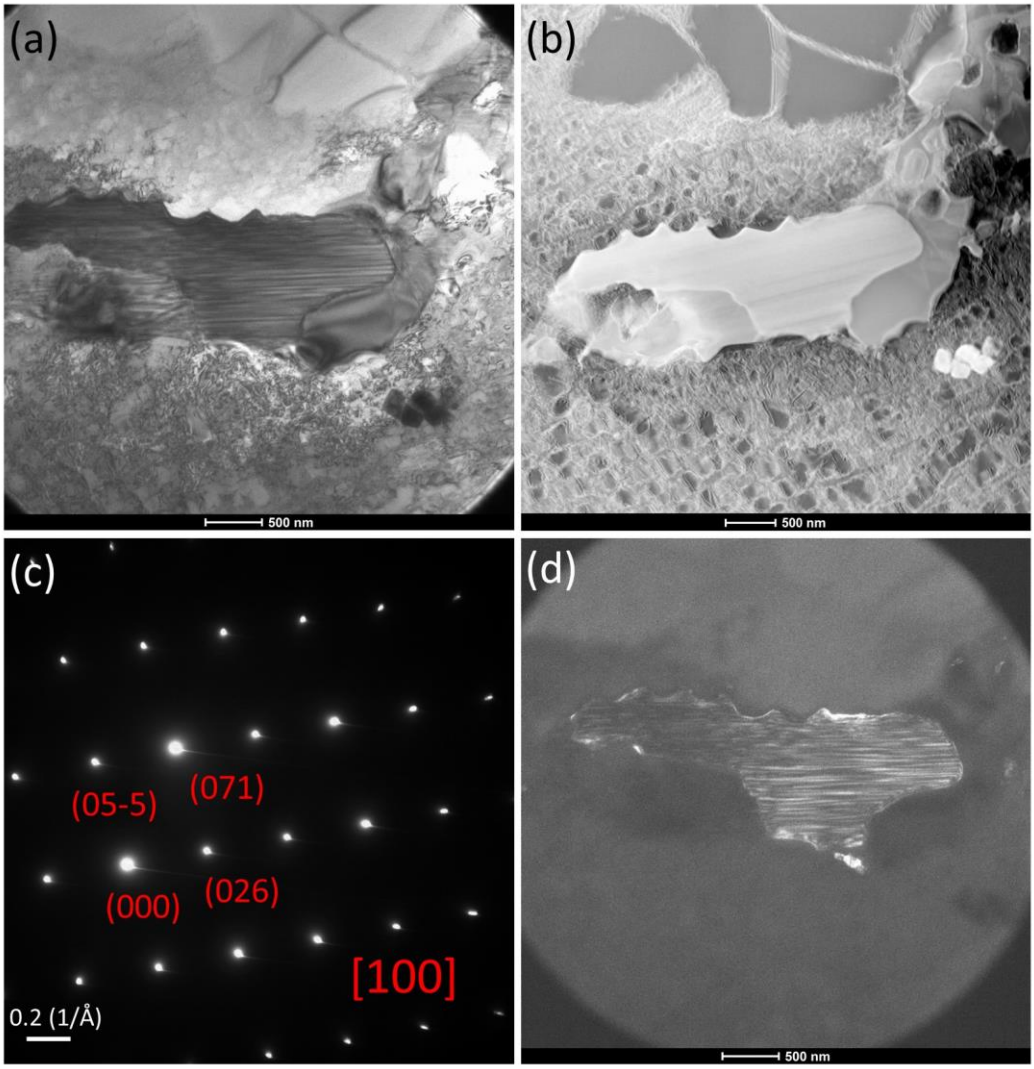

Fig. 7.15 Images of Ni_7Zr_2 in Fig. 7.11a. (a) BF image, (b) STEM-HAADF image, (c) DP of Ni_7Zr_2 and (d) DF image of Ni_7Zr_2.

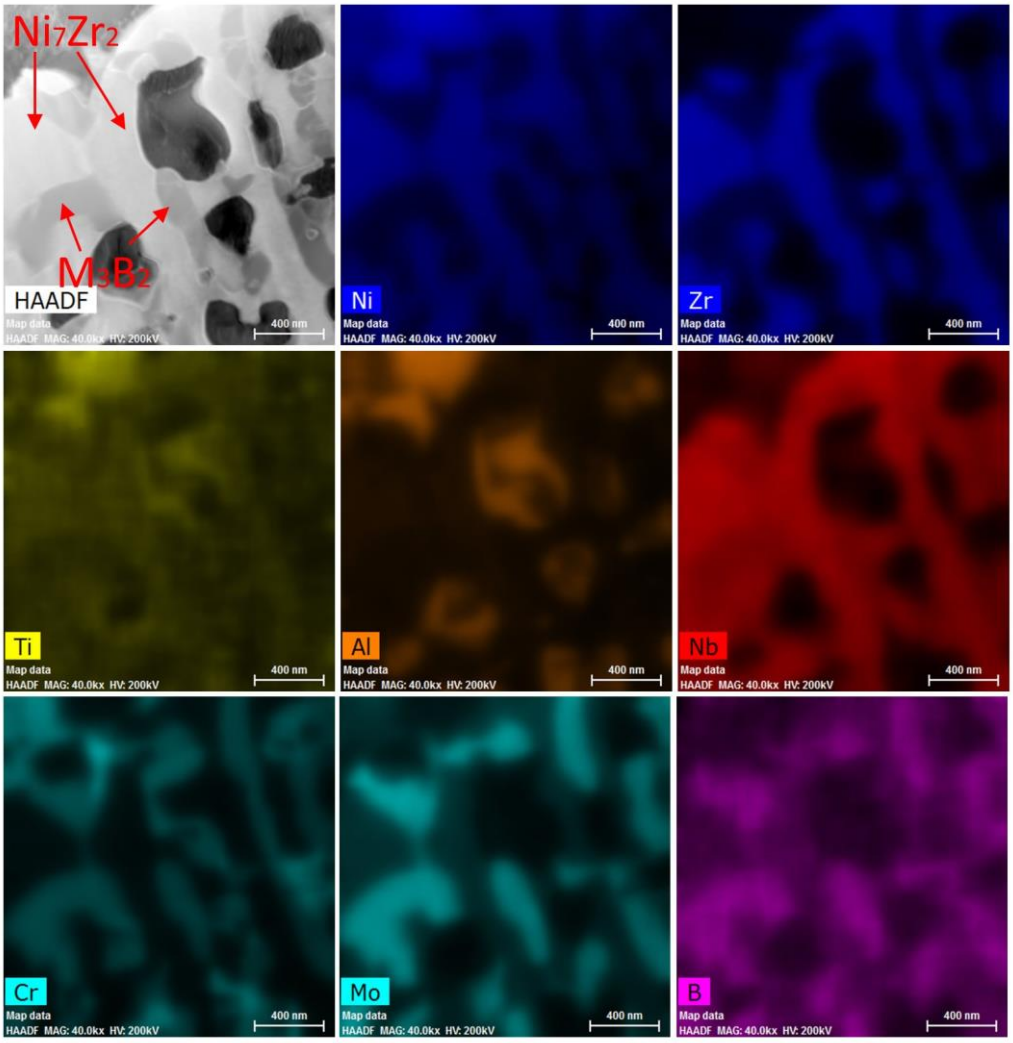

Fig. 7.16 EDS mapping of Ni_7Zr_2 and M_3B_2-type boride which were mapped in the area of 'EDS 3' in Fig. 7.11a. Note the weaved structure of these two phases.

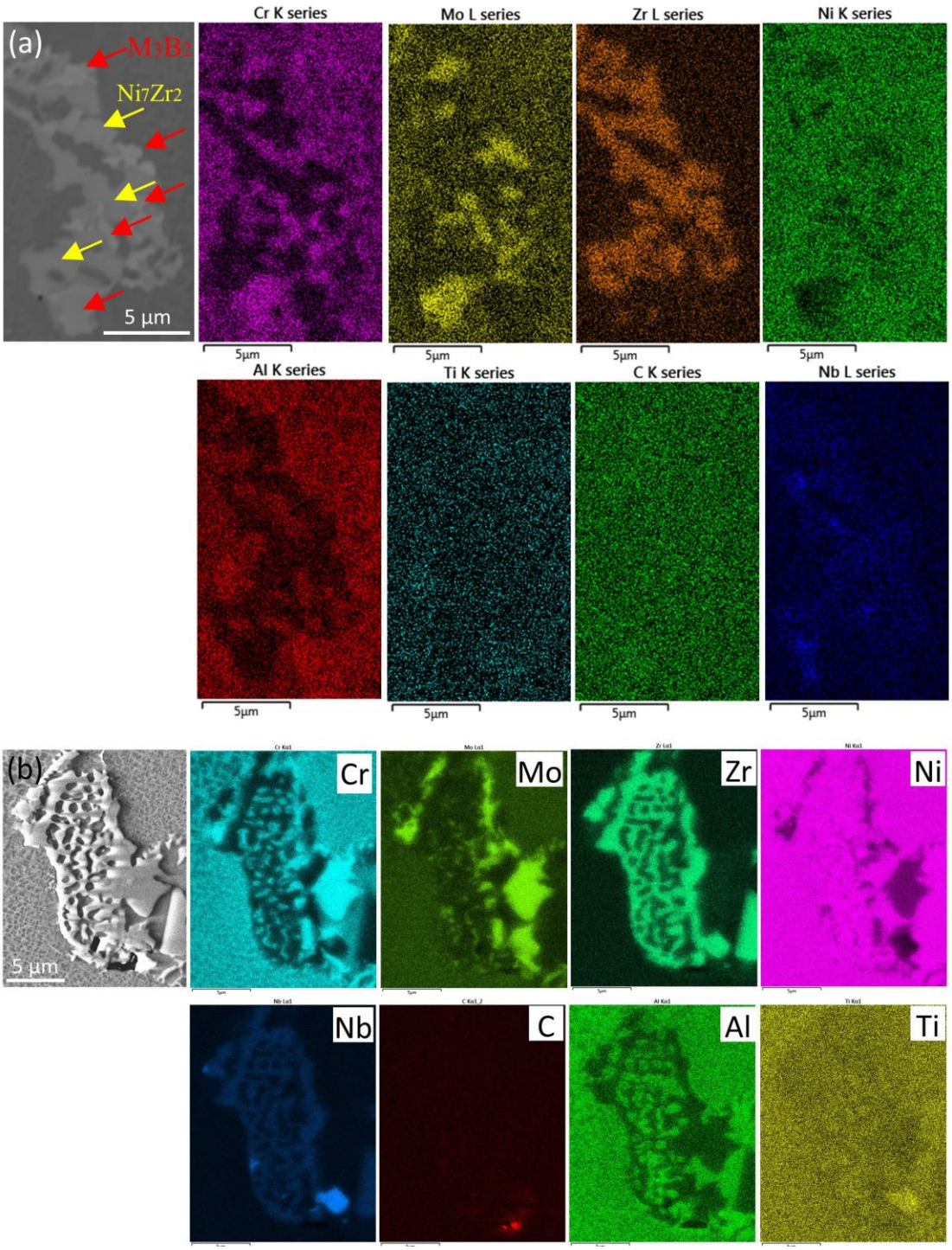

Fig. 7.17 Another two examples (a, b) of the weaved structure of Ni_7Zr_2 and M_3B_2-type boride by SEM in AC, together with their element mappings.

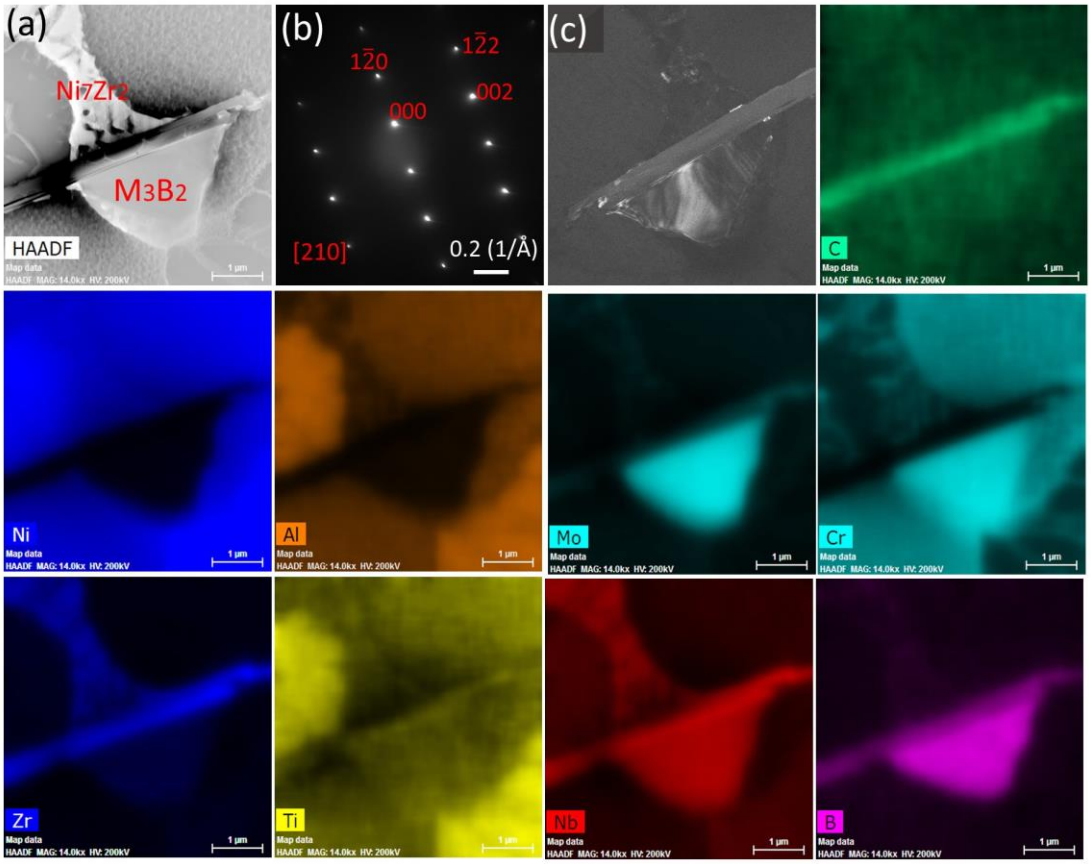

Fig. 7.18 EDS mapping of M_3B_2-type boride and Ni_7Zr_2 which were mapped in the area of 'EDS 4' in Fig. 7.11b. The diffraction pattern (DP) and dark field (DF) image of boride are showed in (b) and (c), respectively.

Fig. 7.9-7.18 present examples of clusters and reveal their chemical compositions, general morphology and distribution.

Fig. 7.9 shows a large serial of clusters consist of a few large γ', a few carbides, Ni_7Zr_2 and M_3B_2-type borides, which are indicated in band contrast image in Fig. 7.9. As defined above for cluster, it shows Ni_7Zr_2 and borides precipitate around large γ', and borides exhibit blocky script shape while Ni_7Zr_2 shows dotted connected morphology. The typical point EDS spectrum of each precipitate are shown in Fig. 7.10. Combined with point spectrum and EDS mapping, it is confirmed that Ni_7Zr_2 majorly rich in Ni, Zr and very slightly in Nb, Cr and Mo; Carbides majorly rich in Nb, Mo, Ti, C and very slightly in Zr, which is line with the results in Chapter 5; M_3B_2-type borides majorly rich in Mo, Cr, B and very slightly in Nb, Ni. It should be noted that cautious was taken in choosing Boron (B) element during EDS mapping due to its detection difficulty for

low atomic number elements in EDS. For instance, EDS system failed to distinguish the element of C and B in the mapping in identifying carbides, see Fig. 7.9. The result shows that there are elements segregation around the cluster according to the EDS mapping. For instance, a rich in Mo, Cr, a slight deletion in Ni and severe deletion in Al are observed along the cluster phases.

Another two examples of clusters imaged by HAADF are given in Fig. 7.11. The diffraction patterns (DP) analysis, EDS mapping (point) for each phase(s) are presented from Fig. 7.12-7.18.

Fig. 7.12 shows the high-resolution element EDS mapping of MC-type carbide in Fig. 7.11a (EDS mapping 1) and further confirms that the carbides are rich in C, Nb, Mo, Ti and Zr. Fig. 7.13 shows the element EDS mapping of two blocky Ni_7Zr_2 and M_3B_2-type boride, and the DP (Fig. 7.13b) and correspondingly DF image of boride (Fig. 13c). It also confirms that the Ni_7Zr_2 are majorly rich in Ni, Zr, and slightly in Nb and probably very slightly in Cr according to the TEM spectrum in Fig. 14a, and there is no Mo detected. For boride, it largely rich in Mo, Cr and slightly rich in Ni and Nb according to EDS point (Fig. 7.14b) which agrees well with SEM-based EDS result. It needs to be pointed out again that it should be cautious to choose the element of B as it is on the forbidden list of elements in the TEM software. However, combined with DP identification, the phase is very likely to be M_3B_2-type boride and mainly riches in Mo and Cr. The crystallographic structure is tetragonal with lattice parameter a=b=5.8 Å, c=3.1 Å. Fig. 7.15 further shows the BF image (Fig. 7.15a), STEM-HAADF image (Fig. 7.15b), DP (Fig. 7.15c) and DF image (Fig. 7.15d) of Ni_7Zr_2 in Fig. 13a. Based on the EDS spectrum of both TEM and SEM and DP information, it is confirmed that this elongated phase is Ni_7Zr_2 and the crystallographic structure is monoclinic with lattice parameter a=4.7 Å, b=8.2 Å, c=12.2 Å and β=95.8º.

Fig. 7.16 shows another set of precipitation phases of Ni_7Zr_2 and boride, and their EDS mapping of 'EDS 3' in Fig. 7.11a. It is interesting to note that they precipitated not only together as was observed in Fig. 7.13, but also in a weaved way with each other. They show a slightly different contrast in HAADF image as indicated in Fig. 7.16, and can be further distinguished by EDS mapping, i.e., phases rich in Mo and Cr are boride while in Ni and Zr are Ni_7Zr_2. This particular precipitation morphology of these two phases can be verified by two more examples shown in Fig. 7.17. Again, they

precipitated closely together and Ni_7Zr_2 present ‘meshed net’ shape while boride present dotted, separated and small blocky shape.

Another eutectic cluster imaged by HAADF in Fig. 7.11b (EDS 4) is further analysed in Fig. 7.18. Ni_7Zr_2 / boride / carbide precipitated immediately beside large γ’ or γ’- γ eutectic. Ni_7Zr_2 and boride precipitated together but not in a ‘weaved’ way. Ni_7Zr_2 again shows a ‘meshed’ morphology and boride shows a blocky morphology. Moreover, there is an elongated thin carbide precipitating in the middle of Ni_7Zr_2 and boride. The DP (Fig. 7.18b) and DF image (Fig. 7.18c) of boride are also shown in the figure.

According to the detailed characterisation for the above representative eutectic clusters and the phases within them, it is concluded that the most common cluster consist of a large γ’ associated with Ni_7Zr_2 and/or boride precipitating together. There are two spatial distribution for Ni_7Zr_2 and boride when they coexist, i.e., either precipitating in close neighbourhood or in a weaved mixture way. However, Ni_7Zr_2 usually has the meshed, connected morphology and boride usually has separated blocky morphology. These precipitation and morphology features can be used as a rule of thumb to quickly identify the type of phase without further chemical or crystal examination, such as used in the Fig. 7.7 and Fig. 7.8.

7.3.3 Effects of Cooling Rate on Hardness

Hardness tests have been carried out for all samples produced with varying cooling rates. The results show that crystallographic orientation and grain size generated by different cooling rates have specific effects on hardness. Fig. 7.19 shows the effect of grain orientation on slip system activated during loading and hardness. In the AC sample with only a few grains (Fig. 7.1a), there is evident orientation dependence of hardness, i.e., the hardness from Goss orientation (110)<001>, 430 HV (Fig. 7.19a) is higher than that of near Cube orientation (001)<100>, 387 HV (Fig. 7.19a, site 1). This is expected as Cube orientation is usually regarded as ‘soft’ orientation that is easy for slip systems activation [18]. This aspect can be further clearly explained by the following slip traces analysis and Schmid factor calculations. A hardness has been loaded in a single grain with Brass orientation (<111>//LD) in 4C sample. The brass orientation is usually regarded as ‘hard’ grain with less slip system activated. The slip

traces both from experiment and calculations confirm this. There are majorly two slip planes: (-111) with the highest SF of 0.45 in red line (Fig. 7.19c) and (11-1) with also the highest SF of 0.45 in blue line in blue line (Fig. 7.19c) that have been activated. The blue line corresponds to the slip traces lines in the bottom left (have been magnified in Fig. 7.19c) and up right areas in Fig. 7.19b, and the red line corresponds to the slip trace lines in the bottom right and up left areas in Fig. 7.19b. In contrast, in the loading site in 4C sample (Fig. 7.19e), only majorly (1-11) planes with the highest SF of 0.43 (red line in Fig. 7.19e) has been activated, see the slip traces line in the bottom left and up right areas in Fig. 7.19e. Moreover, besides these activated slip planes, the SF of other possible slip planes in near Cube grain are averagely higher than in Brass grain, e.g., 0.40 of (1-11) plane and 0.39 of (111) plane in the near Cube grain against 0.28 of (11-1) plane, 0.15 of (111) plane and 0.14 of (-111) plane in the Brass grain. It should be mentioned that the hardness of Brass grain (380 HV) in 4C sample is very close to the near Cube grain (387 HV) in AC sample. However, the size of primary γ' in 4C is much larger than that in AC. It is generally believed that with the similar γ' volume fraction, superalloys with smaller size of γ' possess higher strength [19, 20]. Therefore, it is assumed this close hardness values in these two grains is the balance of effect of γ' size and crystallographic orientation. As the loading site is within the single grain and the loading area is relatively small compared to the grain size, the effect of grain size on the hardness is assumed to be negligible in both cases.

The deformation produced by loading in hardness test in relation with the dendrite structure has also been attempted to analyse by using GND calculation. The results are shown in Fig. 7.20. This new testing site is in the same near Cube grain in AC sample as in Fig. 7.19b, and the slip trace directions (Fig. 7.20g, i and j) and SF values (Fig. 7.20g) are very close to the Fig. 7.19a-c as expected (because they belong to the same grain). The GND density distribution has been calculated both before loading (Fig. 7.20c) and after loading (Fig. 7.20f) in the same area (Fig. 7.20a-f) for comparison. It shows an increase in GND density around loading area after loading as expected. Interestingly, this dislocation density increasement shows a dendrite structure dependence, i.e., higher density in interdendrite area than in dendrite area (Fig. 7.20f). Moreover, the GND map (Fig. 7.20h) of the magnified interdendrite/dendrite area (Fig. 7.20g) shows not only this dendrite-related disparity, but also slight density fluctuation across slip trace lines. It is also observed that a dendrite structure dependence of slip

trace distribution, i.e., there are clear slip trace lines in dendrite area and these lines terminate in interdendrite areas, see Fig. 7.20j. These dendrite structure dependent GND and slip lines distributions are very similar to the situation of fatigue deformation as reported in Chapter 6. In fatigue deformation, we have reported fatigue striations are only limited in dendrite areas while high GND density are limited in interdenrite areas. It should be pointed out that the loading deformation in hardness test is different from the deformation mode of cyclic loading in fatigue. However, the result here combined with the results from Chapter 6 on fatigue seem to indicate the common function of dendrite structure and its interaction with movement of dislocations. Generally, the interdendrite areas act as 'hard' unit to hinder dislocation movement, no matter in cyclic loading or plane slipping. This 'hard' nature is attributed to the element segregation during solidification and the resulting phases precipitation (carbides and eutectic phases), and probably the high misfit of γ/γ' in interdendrite areas.

Fig. 7.21 presents two examples of hardness tested on grain boundary in 4C to reveal the effect of grain structure (size) on hardness and slip activation. Slip transfer can be observed from grain 3 (G3) in Fig. 7.21c, d (site 3 in 4C sample). One predominant feature of slip systems activated are their deviation (to different degrees) of actual slip planes from the calculated ones (the highest SF value lines), see Fig. 7.21a, c, which is believed to have been affected by neighbouring grains. According to classical Hall-Petch relations, the strength of materials will benefit from smaller grain size because of the dislocation pile-up on grain boundaries [21, 22]. In hardness test, this strengthening effect by larger grain numbers (smaller grain size) is believed to the geometrically compatibility needed for slip transfer in neighbouring grains. The average hardness of all samples in Fig. 7.21e shows a slight decrease in hardness with decreasing cooling rate. This possible explanation is the balance effect of significant increase in γ' size (decrease hardness) and decrease in grain size (enhance hardness) with the former playing a more determining role. After all, the loading area is relatively a small area compared to grain size in the sample and involve few grains even in 4C sample with smallest grain size.

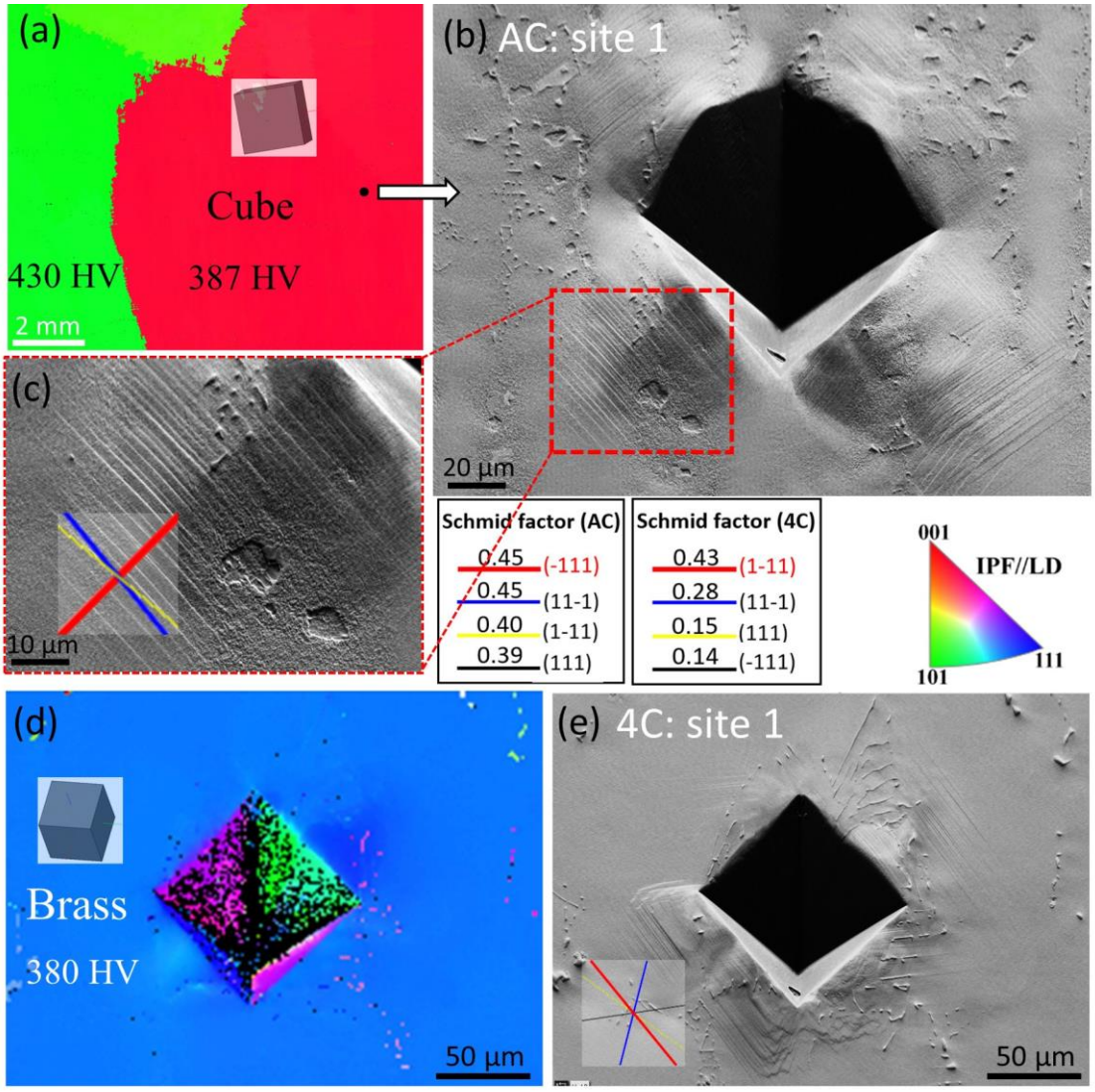

Fig. 7.19 Effects of crystallographic orientation on hardness. (a-c) in AC sample and (d, e) in 4C sample. (b, c) are hardness test in Cube grain in AC, and (d, e) are hardness test within a single grain with Brass orientation. (a, d) are IPFs // loading direction (Z). (b) (c) and (e) are FSD (Forward scatter detector) images showing actual slip traces. The calculated slip traces are superimposed on the figures together with Schmid factor calculations.

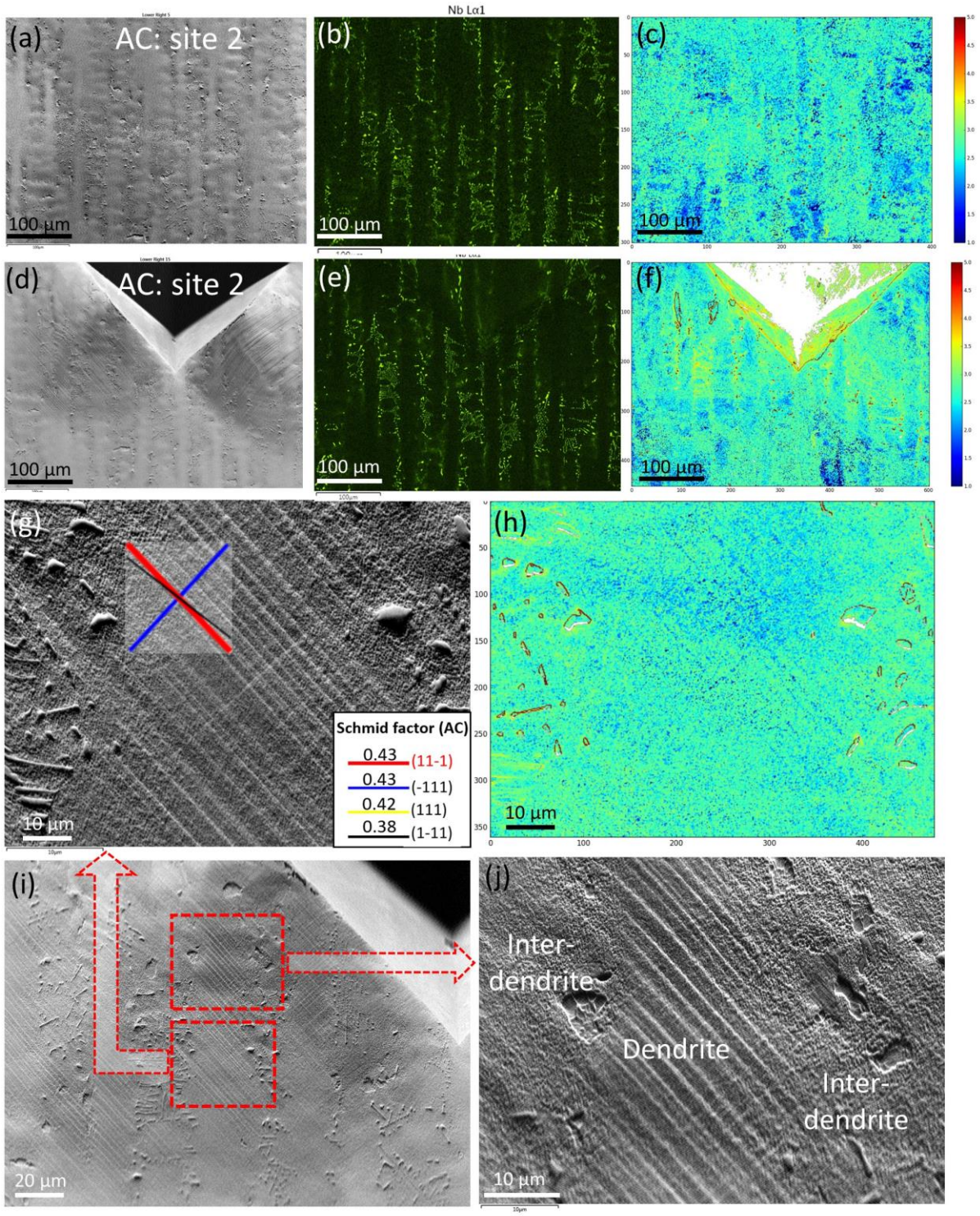

Fig. 7.20 Hardness test on another site in the Cube grain in AC to show the GND distribution and slip traces in terms of dendritic structure. (a-c) before loading and (d-f) after loading. (g, j) two magnified dendritic areas showing the slip traces. Element mapping of Nb were used to show the dendrite structure in (b, e); GND mapping of (c), (f) and (h) correspond to area of (a), (d) and (g), respectively.

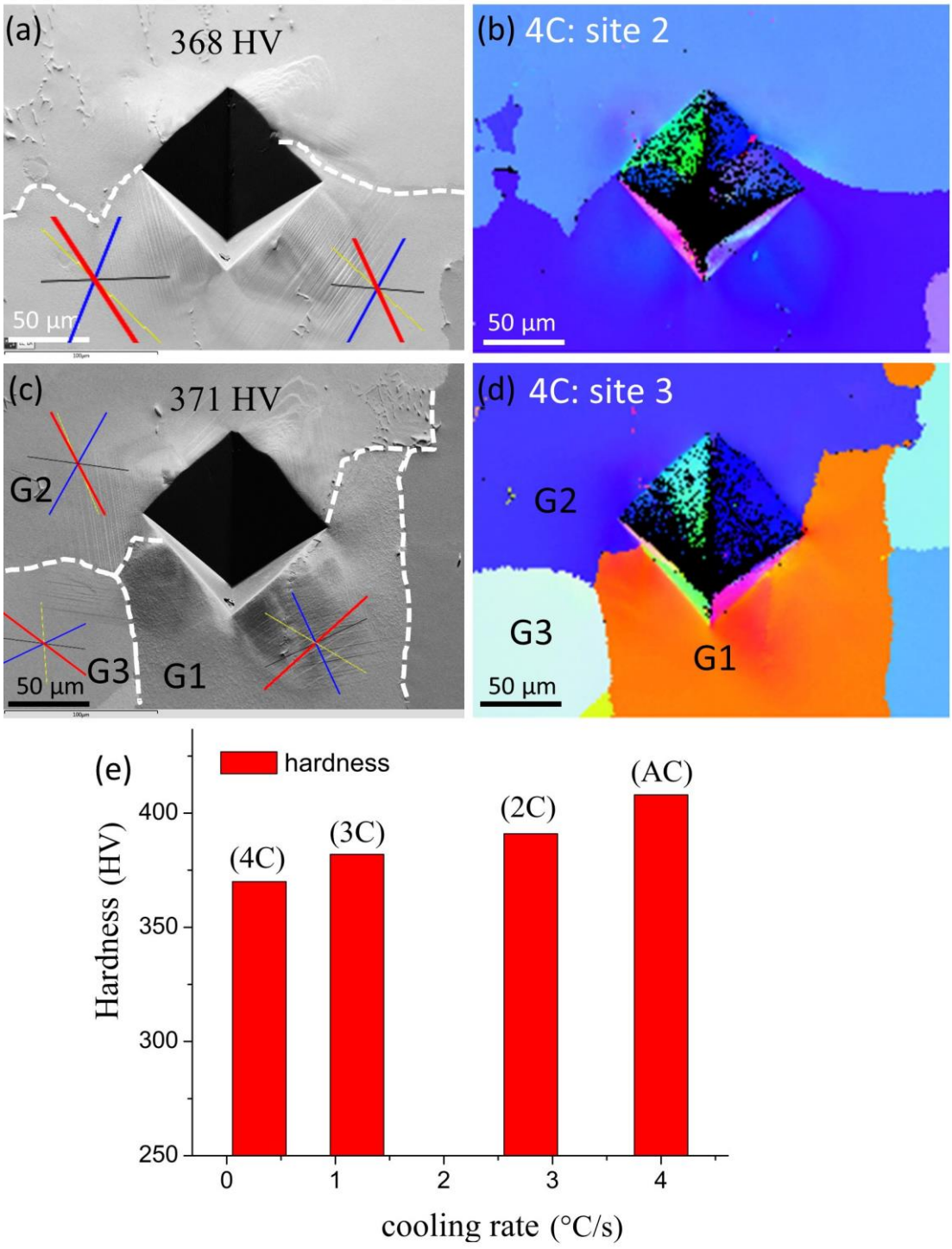

Fig. 7.21 Effects of neighbouring grains on slip activation and hardness. Another two hardness tests in 4C sample. (a, c) FSD images of two sites after loading; (b, d) corresponding IPFs//LD. The calculated slip traces are superimposed on the figures. (e) the hardness of samples with four cooling rates.

7.4 Conclusions

In this chapter, effects of cooling rate on microstructure and microtexture after solidification in IN713C nickel-based superalloy have been studied. The grain structure, phases precipitation, dendrite structure and hardness tests have been characterised in detail. We paid more attention to precipitates formation and deformation of hardness in relation with dendrite structure. Particularly, we defined a term of 'eutectic cluster' to reveal the precipitation rule of other phases such as Ni_7Zr_2 and M_3B_2-type boride, and to present the density of these phases in a statistic way. Based on the results and analyses, following conclusion could be reached:

1. Decreasing cooling rate leads to smaller grain size, larger size of both primary and secondary γ' as well as weakening the dendrite structure formed during solidification.
2. Decreasing cooling rate slightly changed the morphology of primary γ', from round cubic shape in AC (Air cooling) sample to cubic shape (4C sample with lowest cooling rate); some secondary γ' change from spherical shape to dendritic shape.
3. Phase separation of primary γ' was observed in 4C sample and interdendrite area of AC sample, because of more numbers of heavy atomic element been diffused to γ' phase.
4. The volume fraction of carbides decreased in interdendrite area with decreasing cooling rate. At the lowest cooling rate (0.3°C/s), no dendrite structure was found. Most carbides are found to segregate in interdendrite areas and when there is no dendrite structure, they precipitate along grain boundaries.
5. Typical eutectic cluster observed in the interdendrite area of high cooling rate sample (e.g. AC sample) consisted of an relatively very large size γ' associated with Ni_7Zr_2 and/or M_3B_2-type boride, and sometimes with MC-type carbides.
6. Ni_7Zr_2 precipitates were rich in Ni and Zr, slightly in Nb and Cr, has monoclinic crystal with lattice parameter a=4.7 Å, b=8.2 Å, c=12.2 Å and β=95.8º, and usually present a meshed connected morphology. The blocky, separated phase are assumed to be M_3B_2-type boride, rich largely in Mo and Cr, and slightly in Ni and Nb. This boride has tetragonal structure with lattice parameter a=b=5.8 Å, c=3.1 Å.

7. Ni_7Zr_2 and M_3B_2-type boride usually precipitate closely together, either in a weaved connected way or in the neighbourhood.
8. Crystallographic orientation has significant effect on the hardness. Cube orientation has low hardness with a ‘soft’ nature and multiple slip planes activation; Whereas Goss or Brass orientation have high hardness with a ‘hard’ nature and limited slip plane(s) activation.
9. There is a dendrite structure dependent GND density distribution and slip trace lines distribution after loading. A higher GND density were found in interdendrite areas than in dendritic areas and the slip trace lines were limited to the dendrite areas. These slip distribution is very similar to the striation distribution in fatigue test even though they have different deformation modes.
10. Neighbouring grains have effects on the slip plane activations. Loading within single grain, the actual activation plane (slip trace lines) fit well with the calculated slip lines; while loading on multi-grains, there is deviation of actual slip lines with calculated ones.
11. There is a slight decrease in hardness in the samples with lowering cooling rate. This is assumed to be the balanced effects of larger γ’ and smaller grain size, with the former playing a determining role.

References

[1] A. Bhambri, T. Kattamis, J. Morral, Cast microstructure of Inconel 713C and its dependence on solidification variables, Metall. Trans. B 6(4) (1975) 523-537.

[2] F. Binczyk, J. Śleziona, A. Kościelna, Effect of modification and cooling rate on the macrostructure of IN-713C alloy, Arch. Foundry Eng. 9(3) (2009) 13-16.

[3] D.U. Furrer, H.-J. Fecht, γ′ formation in superalloy U720LI, Scr. Mater. 40(11) (1999) 1215-1220.

[4] S.S. Babu, M.K. Miller, J.M. Vitek, S.A. David, Characterization of the microstructure evolution in a nickel base superalloy during continuous cooling conditions, Acta Mater. 49(20) (2001) 4149-4160.

[5] J. Mao, K.-M. Chang, W. Yang, D.U. Furrer, K. Ray, S.P. Vaze, Cooling precipitation and strengthening study in powder metallurgy superalloy Rene88DT, Mater. Sci. Eng. A 332(1–2) (2002) 318-329.

[6] S. Behrouzghaemi, R.J. Mitchell, Morphological changes of γ′ precipitates in superalloy IN738LC at various cooling rates, Mater. Sci. Eng. A 498(1–2) (2008) 266-271.

[7] R. Mitchell, M. Preuss, S. Tin, M. Hardy, The influence of cooling rate from temperatures above the γ′ solvus on morphology, mismatch and hardness in advanced polycrystalline nickel-base superalloys, Mater. Sci. Eng. A 473(1-2) (2008) 158-165.

[8] A.R.P. Singh, S. Nag, J.Y. Hwang, G.B. Viswanathan, J. Tiley, R. Srinivasan, H.L. Fraser, R. Banerjee, Influence of cooling rate on the development of multiple generations of γ′ precipitates in a commercial nickel base superalloy, Mater. Charact. 62(9) (2011) 878-886.

[9] S. Milenkovic, I. Sabirov, J. Llorca, Effect of the cooling rate on microstructure and hardness of MAR-M247 Ni-based superalloy, Mater. Lett. 73 (2012) 216-219.

[10] Y. Zhang, Y. Huang, L. Yang, J. Li, Evolution of microstructures at a wide range of solidification cooling rate in a Ni-based superalloy, J. Alloys Compd. 570 (2013) 70-75.

[11] M. Li, J. Coakley, D. Isheim, G. Tian, B. Shollock, Influence of the initial cooling rate from γ′ supersolvus temperatures on microstructure and phase compositions in a nickel superalloy, J. Alloys Compd. 732 (2018) 765-776.

[12] M. Doi, D. Miki, T. Moritani, T. Kozakai, Gamma/Gamma-Prime microstructure formed by phase separation of gamma-prime precipitates in a Ni-Al-Ti alloy, Superalloys 2004 (2004) 109-114.

[13] F. Vogel, N. Wanderka, Z. Balogh, M. Ibrahim, P. Stender, G. Schmitz, J. Banhart, Mapping the evolution of hierarchical microstructures in a Ni-based superalloy, Nature communications 4 (2013) 2955.

[14] F. Vogel, N. Wanderka, Z. Balogh, M. Ibrahim, P. Stender, G. Schmitz, T. Fedorova, J. Banhart, Evolution of nanoscale clusters in γ′ precipitates of a Ni–Al–Ti model alloy, Ultramicroscopy 159 (2015) 278-284.

[15] F. Vogel, S. Ngai, K. Fricke, M. McKechnie, N. Wanderka, T. Hentrich, J. Banhart, G. Thompson, Tracing the three-dimensional nanochemistry of phase separation in an inverse Ni-based superalloy, Acta Mater. (2018).

[16] R. Ricks, A. Porter, R. Ecob, The growth of γ′ precipitates in nickel-base superalloys, Acta Metall. 31(1) (1983) 43-53.

[17] H. Matysiak, M. Zagorska, A. Balkowiec, B. Adamczyk-Cieslak, R. Cygan, J. Cwajna, J. Nawrocki, K.J. Kurzydłowski, The Microstructure Degradation of the IN 713C Nickel-Based Superalloy After the Stress Rupture Tests, J. Mater. Eng. Perform. 23(9) (2014) 3305-3313.

[18] S. Birosca, F. Di Gioacchino, S. Stekovic, M. Hardy, A quantitative approach to study the effect of local texture and heterogeneous plastic strain on the deformation micromechanism in RR1000 nickel-based superalloy, Acta Mater. 74 (2014) 110-124.

[19] Y. Xu, C. Yang, X. Xiao, X. Cao, G. Jia, Z. Shen, Strengthening behavior of Al and Ti elements at room temperature and high temperature in modified Nimonic 80A, Materials Chemistry and Physics 134(2-3) (2012) 706-715.

[20] Y. Xu, C. Yang, X. Xiao, X. Cao, G. Jia, Z. Shen, Evolution of microstructure and mechanical properties of Ti modified superalloy Nimonic 80A, Materials Science and Engineering: A 530 (2011) 315-326.

[21] E. Hall, The deformation and ageing of mild steel: III discussion of results, Proc. Phys. Soc. London, Sect. B 64(9) (1951) 747.

[22] N. Hansen, Hall–Petch relation and boundary strengthening, Scr. Mater. 51(8) (2004) 801-806.

Chapter 8: General Discussion

8.1 The Effects of Geometry on Deformation Micromechanism: Turbine Wheels and Standard Cast Bars

This project studied the fatigue deformation behaviour of IN713C using both actual turbine wheel blades and standard fatigue test bars. The author believe that this is the first time to directly study the deformation in turbine wheel blades via correlating the microstructure beneath the fracture surface to the fracture surface features in addition to the standard fractography characterisation [1]. The turbine wheel blades used here were failed in in-house testing which was specially designed for simulation of failures in actual service. It is useful and interesting to compare the different deformation behaviour in these two materials (turbine blade and bar) resulted from their respective microstructures and testing conditions. Both turbine blades and bars are produced via investment casting and possess relatively large grains (except small grain area in bars of Transition structure). All the fatigue tests were tested in around 650°C. However, they experienced different loading modes and conditions. For standard bars in standard fatigue tests, they experienced uniaxial cyclic loading force, with different stress in different fatigue modes (~650 MPa for LCF and ~350 MPa for HCF) and they were exposed to high temperature air condition. Whilst for turbine blades in in-house testing, loading force was resulted from centrifugal stress of high speed rotating wheels and resonance in LCF and HCF, respectively. These relatively low stresses in turbine wheels and the different dimension size and shape of wheels (see Fig. 5.1a) from bars (see Fig. 3.2d) determined the much longer fatigue life in turbine wheels (days and weeks) than in bars (less than 4 hours test). Although oxidation assisted crack propagation due to carbides oxidation have been observed in LCF of both blades (Fig. 5.6) and bars (Fig. 6.8), the oxidation-induced cracking mechanism was the determining mechanism for crack propagation only in LCF of blades, as illustrated in Chapter 5 and in Fig. 5.14. This is probably because the long fatigue life in blades compared to bars, in which oxygen has more time to diffuse and oxidise carbides. Moreover, the high temperature gas used in in-house test was real exhausted gas which

contained other elements such as carbon dioxide, sulphides. These harsh detrimental gases probably further accelerated the oxidation process in tests for blades.

Further differences between the real turbine blade and cast bar testing were observed in the fatigue striations morphologies. In the study of turbine blades, it was found the long continuous striations during HCF mode (Chapter 4 and Fig. 5.3) and local separated striation (Chapter 4 and Fig. 5.4) in LCF mode. However, studies on bars showed the striation morphology was more associated with dendrite structure. Moreover, there were similar dendritic structures in all standard cast bars used for LCF and HCF tests. In all failed bars, the striations were local and separated. These observation and correlation can be applied to turbine blades as LCF failed area showed obvious dendrite structure while HCF failed location in blade showed weak dendrite structure. These variation in microstructures across the turbine blade are due to the complicated configuration of turbine wheel which results in different solidification conditions. Whilst in bars, although different grain structure (transition, equiaxed and columnar) have been produced by controlling casting parameters, the dendrite size as well as γ' were unchanged. This is probably due to the small dimension of the bar and relatively fast cooling rate used.

8.2 The Effects of Fatigue Modes (HCF and LCF) on Deformation Micromechanism

The difference in loading modes, i.e., HCF and LCF, results in different crack initiation sites and affect the crack propagation process. It has been mentioned in Chapter 3 that the definitions of HCF and LCF in in-house testing for turbine blades are different from tradition definition due to their loading force causes (centrifugal stress and resonance for LCF and HCF, respectively). For standard fatigue bars, the difference between strain-controlled LCF and stress-controlled HCF is directly reflected in different stress levels. Although turbine blades and bars have different materials geometries and were tested in different conditions as mentioned above, LCF in both test forms exhibits feature of high stress level while HCF in both test forms exhibits feature of low stress level. This low stress level in HCF might explain the faceting phenomenon observed both in blades and bars despite their different materials geometries and testing conditions. The relatively low external loading stress results in the fewer dislocation

and slip activation in limited slip planes. The results in both tests showed that these slip plane(s) in faceting grain(s) usually was the {111} slip planes with the highest Schmid factor value(s), and in most of cases (Fig. 5.11, Fig. 5.12, Fig. 6.13 and Fig. 6.14), with the presence of casting porosity which provide local stress concentration. On the contrary, the relatively high loading stress in LCF both in blades and bars make the multiple slip activation in a number of slip planes possible. Once the crack initiated, the crack would propagate in a way less dependent on crystallographic orientation and without the faceting phenomenon in LCF tests.

The effect of different loading stress level on fatigue crack propagation is directly reflected in the crack propagation rate graph (Fig. 6.10j) for standard fatigue tests in bars where the microstructure (dendrite structure and γ') are similar in LCF and HCF samples. This propagation rate data is based on the detailed measurement of well-defined individual striation spacing in the crack propagation stage. It demonstrated in Chapter 6 that, in general trend, the average crack propagation rate in LCF samples were higher than in HCF samples even though the rates vary with different grain structures (such as higher rate in LCF-Columnar than LCF-Transition). The results showed that the overall higher fatigue crack growth rate in LCF was due to high loading stress compared to those in HCF samples.

8.3 The Effects of Carbides and Oxidised Carbides on Fatigue Crack Propagation

The role of carbides and carbides oxidation is important in the current studied material, IN713C nickel-based superalloy. This is because on the one hand, this material contains relatively high concentration of C (0.12%) and Nb (2.2%, Table 2.2) which leads to the high-volume fraction (2%) of MC-type carbides during solidification process. On the other hand, carbides mainly precipitate in interdendrite areas which contributes the major part of microstructure heterogeneity in this alloy. Section 2.3.3 in Chapter 2 has reviewed the recent progress on the effects of carbides and oxidised carbides on fatigue property, especially the crack initiation induced by carbides oxidation which was first reported by Conolley et al [2]. It is now generally believed that these inhomogeneous distributed carbides have detrimental effects on fatigue property in causing crack either by their brittle nature or by their oxidation when exposed to high temperature. However, the details of how the carbides oxidation induce small crack initiation and how the

oxidation proceed with oxygen channelling process are first reported here. Moreover, how the dendrite structure (carbides distribution) affect the oxidation and crack propagation process is also investigated in this study for turbine blades (LCF mode), see Chapter 5. This research mainly utilised the HR-EBSD and related GND calculation. It was found that the high GND density around oxidised carbides (partly generated by oxidation process as volume expansion-induced plasticity) facilitated the small crack nucleation and propagation. Moreover, the connectivity of the carbide network structure in LCF failed area of blades further accelerated the oxidation process and crack propagation rate. This carbides-oxidation-assisted crack initiation and propagation model is schematically shown in Fig. 5.14a-d.

This carbides oxidation assisted crack initiation and propagation process was predominantly observed in LCF in turbine blade where there were obvious dendrite structures. The oxidation induced cracking was regarded as the determining process for fatigue propagation in LCF of blades. Whilst there was no such process been observed in HCF of turbine blade where there were very weak dendrite structure and small size carbides. During the bars tests, however, this carbides oxidation assisted crack initiation and propagation process has been observed in both LCF and HCF (Fig. 6.8) but not taken as determining mechanism for crack propagation. It should be noted that bars possess the significant dendrite structure with large size carbides, the same case as in LCF failed areas in blades. As mentioned in Section 8.1, single fatigue test for blades last much longer time than for bars, which indicates longer oxidation process in blades than in bars. Therefore, a number of factors such as microstructure and specific testing condition should be taken into account when evaluating to which degree this carbides oxidation determine the fatigue crack initiation and propagation process.

8.4 The Effects of Dendrite Structure on Fatigue Crack Propagation

Dendrite structure is the predominant feature in cast alloys. In the current study, IN713C superalloy was produced by investment casting method. The dendrite structure featured chemical elements (such as Mo. Cr) segregation and carbides precipitation in interdendrite areas. This dendrite structure and the large amount of carbides within interdendrite areas contributed greatly in microstructure heterogeneity in this material.

Two different roles of dendrite structure in fatigue crack propagation were first reported in this project.

The first one is the rotation of interdendrite area to accommodate strain inhomogeneity during deformation in the late stage of crack propagation in LCF of blades. As shown in Fig. 5.13 and schematically shown in Fig. 5.14e-f, only interdenrite area rather than the whole grain rotated from Brass orientation to Cube to further facilitate (or cause) crack propagation. This rotation was evidenced by the high GND density in interdendrite areas.

The second one is general fatigue crack propagation morphology based on dendrite structure. This is mainly based on the observation in LCF and HCF bars that fatigue striations were only limited to dendrite areas and high dislocations (GNDs) segregated in interdendrite areas. A novel concept of 'Crack Propagation Unit (CPU)' was therefore proposed to describe this basic role of dendrite structure in crack propagation process. Based on this concept, similar to the Hall-Patch relationship in single phase alloy that strength inverse to the grain size, it is assumed that the resistance of fatigue crack growth would be inverse of the size of dendrite (dendritic spacing). The possible effects of dendrite structure on fatigue life has been reported by Horstemeyer et al. [3] in a die cast magnesium alloy. They noticed the variation in HCF life might be affected by average secondary dendrite arm spacing in addition to the drastic difference in crack nucleation site size (defects) and average grain size. However, this effect of dendrite structure on crack propagation is further elucidated here with detailed microstructure examined and sub-microstructure deformation mechanism explained.

8.5 The Effect of Crystallographic Orientation on Fatigue Crack Initiation and Propagation

Crystallographic orientation has an significant effect on the fatigue crack initiation in HCF which is evidenced by the faceting phenomenon. This faceting phenomenon has been observed in both tests for blades and bars. The calculation of slip trace and Schmid Factor (SF) for each slip plane based on EBSD data and serial sectioning technique have revealed that faceting (or slip) are mostly activated in one of the {111}<1-10> slip system with the highest SF value, as shown in the case of Fig. 5.11, Fig. 5.12 and Fig.

6.13b, d. In this sense, Cube orientation has higher probability of faceting than Brass or Goss as it has more slip planes with relatively high Schmid factors. However, it should be pointed out here, the specific faceting occurrence depends more on the SF value of individual slip plane than the average SF value of a grain. Therefore, it is not surprising that both faceting in the example of Fig. 5.11 and Fig. 5.12 happened in Goss grains. Moreover, effective SF value is influenced by several factors such as local stress status and surrounding grains. Although most of the faceting were observed coexist with porosities which help to increase local stress concentration and therefore, facilitate crack initiation. The size of porosity is related to casting process and suspected closely related to grain size (Fig. 6.14g). However, when the defects (porosity) is large enough which produce significant local stress concentration, the nominal highest SF value is no longer necessary for slip activation in a grain. This is evidenced by sample H-T (Fig. 6.13c) and H-C (Fig. 6.14d) where in the former case, slip activated in (-111) plane with SF of 0.39 (third highest SF in the grain) and in the latter case in (-111) plane with SF of 0.21 (third highest SF in the grain). And the high local stress is confirmed by the high GND density around porosity by cross section, see Fig. 6.6c.

The Cube orientation is found to facilitate fatigue crack propagation. On the one hand, the faster growth direction during solidification process in nickel-based superalloy is <100> direction, which is parallel to the crack propagation direction in stage II of fatigue process and perpendicular to the loading direction. This will facilitate crack propagate along interdendrite area or interface of dendrite/interdendirte which are the relatively weak area due to microstructure inhomogeneity. On the other hand, from the point of alternative slip activation during fatigue crack propagation (and the cause of striation), the <100> direction is also parallel to the effective slip activation direction, as shown in Fig. 6.17e. Therefore, fatigue crack propagation would be accelerated in the grain with Cube orientation.

8.6 The Effect of Grain Size on Fatigue Property in IN713C Alloy

The effects of grain size on fatigue property and deformation behaviour have been investigated in standard fatigue tests for cast bars. These bars have been specially designed with three different grain structures, i.e., transition, equiaxed and columnar. However, more attention has been focused on the effect of size of these bars due to the

deviation of casting structure from the ideal designs. The results showed beneficial effect of small grains in both LCF and HCF. The major contribution of small size grain is to divert crack propagation directions in different grains with different orientation. This is different from classical explanation of Hall-Patch relations that materials are strengthened by the dislocation pile-ups at grain boundaries. As mentioned in 8.4, the crack propagation unit in the current alloy is influenced by individual dendrite size, and the dislocations (GNDs) are mainly accumulated within the interdendrite areas rather than at grain boundaries. These findings provide another perspective to expand the usability of the Hall-Patch relations. In addition, it is found that large size grains lead to large porosity during casting process, which will cause fatigue crack initiation. Furthermore, in HCF particularly, the size of facet is observed the same size of faceting grain, which leads to the conclusion that small grain material benefit fatigue property partly by causing small size facet.

8.7 The Effect of Solidification Cooling Rate on Microstructure and Microtexture Development of IN713C Nickel-Based Superalloy

As mentioned above, microstructures such as grain size, carbides, dendrite structure and microtexture have specific and different effects on fatigue properties. The solidification trials with different cooling rates have been carried out to investigate the evolution of the microstructures and microtexture in IN713C. Similar studies of cooling rates have been carried out for other alloys and superalloys [4-7]. And the results obtained here are generally in line with other studies in [4-7]. For instance, with increasing cooling rate, the size of γ' decreased. Moreover, the morphology of γ' changed from cubic to spherical and dendrite structure became more evident with increasing solidification cooling rate. In addition to these findings, the dendrite structure and the phases precipitation within interdendrite areas have been characterised and analysed in great detail. The composition, morphology and precipitation distribution of these phases are identified and summarised. In particular, two unique precipitation morphologies of two phases, Ni_7Zr_2 and M_3B_2-type boride, were observed. They either precipitated closely together in neighbourhood with blocky shape of boride or precipitated in a weaved way together with netting shape. Their formation in interdendrite area during fast cooling process are attributed to the significant chemical

element segregation. Moreover, the M_3B_2-type boride has the very similar element concentrations and rich in Mo and Cr, which are typical TCP phase formation elements. Therefore, this boride is suspected to have close relationships with TCP formation during microstructure degradation in service or high temperature exposure. Overall, lower cooling rate tend to weaken or diminish dendrite structure which decease the microstructure inhomogeneity and decrease grain size which is in general is good for property. However, at the same time, slowing cooling rate increase the size of γ' which is usually a disadvantage for property. Therefore, the finally effects of cooling rate on fatigue property is yet to be examined. Here, the deformation behaviour of different structure after solidification trails in hardness tests has been analysed and compared to the behaviour of fatigue, which further showed that the interdendrite area has the function of separating slip bands. Overall, the important and different role of dendrite structure have been revealed and need to further be verified, which can provide guidelines to modify the material accordingly.

Reference

[1] N. Boutarek, D. Saïdi, M.A. Acheheb, M. Iggui, S. Bouterfaïa, Competition between three damaging mechanisms in the fractured surface of an Inconel 713 superalloy, Mater. Charact. 59(7) (2008) 951-956.

[2] T. Connolley, P.A.S. Reed, M.J. Starink, Short crack initiation and growth at 600 °C in notched specimens of Inconel718, Mater. Sci. Eng. A 340(1–2) (2003) 139-154.

[3] M.F. Horstemeyer, N. Yang, K. Gall, D.L. McDowell, J. Fan, P.M. Gullett, High cycle fatigue of a die cast AZ91E-T4 magnesium alloy, Acta Mater. 52(5) (2004) 1327-1336.

[4] A. Bhambri, T. Kattamis, J. Morral, Cast microstructure of Inconel 713C and its dependence on solidification variables, Metall. Trans. B 6(4) (1975) 523-537.

[5] F. Binczyk, J. Śleziona, A. Kościelna, Effect of modification and cooling rate on the macrostructure of IN-713C alloy, Arch. Foundry Eng. 9(3) (2009) 13-16.

[6] D.U. Furrer, H.-J. Fecht, γ′ formation in superalloy U720LI, Scr. Mater. 40(11) (1999) 1215-1220.

[7] S.S. Babu, M.K. Miller, J.M. Vitek, S.A. David, Characterization of the microstructure evolution in a nickel base superalloy during continuous cooling conditions, Acta Mater. 49(20) (2001) 4149-4160.

Chapter 9: Conclusions

In this PhD project, the effects of microstructure and microtexture generated during solidification on fatigue deformation have been studied in IN713C nickel-based superalloy. Based on the exhausted characterisation of microstructure and microtexture that is related to deformation process, such as carbides, oxides, dendrite structure, crystallographic orientation and fatigue striations, particularly, by utilising the concept and tool of GND calculations, the deformation modes for different testing samples (wheel blades and standard bars) in different testing conditions (in-house test for wheel blades and standard fatigue test for bars) have been proposed respectively.

In Chapter 4, the features of fracture surface failed in in-house testing for wheel blades have been exhaustedly examined both macroscopically and microscopically. It is observed that the predominant faceting phenomenon and long, clear striations in HCF (VHCF) mode against the local, separated striations and rough fracture surface in LCF are the major differences in fractography feature of LCF and HCF. Based on these feature differences, a step-by step guide to distinguish fracture mode by fracture surface have been developed.

In Chapter 5, the further characterisation of microstructure and microtexture have been undertaken on the cross-section of the wheel blades failed in in-house testing. Particularly, serial sectioning technique combined with EBSD has been used to reveal the activated slip systems and the effects of surrounding grain structures. In LCF, it is observed that oxidised carbides have the significant role of initiating and deflecting secondary cracks. Much higher GND density was found surrounding oxidised carbides and assumed to facilitate crack initiation. Furthermore, in the later stage of crack propagation, interdendrite area was observed to rotate to accommodate strain and deformation heterogeneity. In HCF, faceting was usually initiated from slip planes with the highest Schmid factor values, sometimes with the assistance of small porosity when SF was not high enough. Based on these observations and calculations of GND and slip traces, a microstructure sensitive crack initiation and propagation mode for LCF and a microtexture sensitive crack initiation and propagation mode for HCF of wheel blades in in-house testing have been proposed.

In Chapter 6, we conducted standard fatigue tests (strain control for LCF and stress control for HCF) on standard bars with three different grain structures (transition, equiaxed and columnar). As most of crack initiated from casting defects (porosities), more attention has been paid to crack propagation process. By the distinguished colour contrast in optical images combined with SEM examination and statistically determination of striations, it is found that fatigue striations majorly located in dendrite areas. Higher dislocations segregated in interdendrite areas which has been calculated by EBSD-based GND and verified by STEM-based dislocation obvervation. Therefore, we propose the concept of 'crack propagation unit (CPU)' to model the fatigue crack propagation process and this unit is dendrite area, separated by interdendrite network. Moreover, it is found that samples with smaller grain size have slower crack propagation rate, which is fitted with the classical Hall-Patch relations. However, instead of dislocation pile-up around grain boundaries, this beneficial effect of small grain size is majorly attributed to the crack propagation divergence in smaller grain size samples.

In Chapter 7, solidification trials have been carried out to study the effects of cooling rate on the microstructure and microtexture during casting in IN713C nickel-based superalloy. In addition to the differences in grain size, size and morphology of primary and secondary γ', carbides (volume fraction) with varying cooling rate, we also noticed the phase separation of primary γ' in slowest cooling sample (4C) and interdendrite area of fastest cooling sample (AC). More attention has been focused on the dendrite structure formation with cooling rate. It is demonstrated slowing cooling rate will effectively weaken the dendrite structure and even eliminate it in the lowest cooling sample (4C). In AC sample with predominant dendrite structure, a term of 'eutectic cluster' is coined to express the phase precipitation features. A typical eutectic cluster consists of a very large γ' and Ni_7Zr_2 and/or M_3B_2-type boride precipitating closely together. Following the solidification trials, hardness tests were undertaken to study the effect of grain size and orientation on the slip activation and hardness. It is demonstrated that when the grain size is comparable to the loading area, neighbouring grains would slightly deviate the activating slip plane from calculated slip plane with the highest SF value. And the slightly decrease in hardness with cooling rate is attributed to the balanced effect of larger γ' size and smaller grain size with decreasing cooling rate. Moreover, slip traces lines were evident in dendrite area than in interdendrite area and

much higher GND density was found in interdendrite areas around deformed areas after loading.

The major contribution of the whole research is to try to elucidate the determining factor(s) that affect the fatigue deformation, and furthermore, the deformation micromechanism for each fatigue mode in different testing conditions. Here, the role of dendrite structure on fatigue deformation have been highlighted through the project. The dendrite structure contributes the major part of microstructure heterogeneity and is closely related to the chemical segregation during solidification process. Understanding this role of dendrite structure and therefore modifying the related microstructure is believed to useful in improve the fatigue property.

The other contribution in terms of experiment technique is the 3-D or quasi-3-D characterisation that combined serial sectioning technique and EBSD, providing a precise relationship between the fracture surface details and beneath grain structure and orientations in 3-D and in a large scale. This method can be applied not only in the study of fatigue in superalloy, but also for general fatigue study and even for other mechanical testing such tensile or creep, especially when large size grains are involved.

Chapter 10: Suggestions for Future Work

The possible future work based on this project can be divided to sections: one is to further verify the mechanism proposed here and another is to study the microstructure stability such phase precipitation during long term exposure in high temperature and their effects on properties.

1. By further controlling the casting defects and further refine the grain structure. In Chapter 6 we propose the crack propagation mechanism by minimising the effect of porosity (for instance, we did not measure the propagation striation in sample L-E due to their cluster of porosities in initiation site and quick failure). However, the effects of defects are not negligible when the size of pores are large enough or even it is hard to evaluate to how much degree the effect of defect does on crack propagation. The ideal situation is a sample of defect free which is still very hard to obtain in the current technique.
2. To adjust the size of dendrite size while keep other microstructure such as grain size, γ' size, volume of carbides, etc., at the same time, and then conduct standard fatigue test. This will be the direct way to verify the model of 'crack propagation unit (CPU)' proposed in this research.
3. To conduct interrupted fatigue test using double flat sample, shown in Fig. 9.1a, to in-situ study the crack initiation and crack propagation in relation with grain structure (size and orientation), dendrite structure and carbides. Notched sample also can be used specialised for crack study (Fig. 9.1c). an example of EBSD IPF//X of transition sample is shown in Fig. 9.1b.
4. To conduct microstructure stability during long term exposure in high temperature to study the phases evolution, with more attention been paid to TCP phase initiation and growth. This is of significance as turbine wheels are expected to exposure higher temperature to improve efficiency in the upcoming decades, and microstructure degradation and TCP phase precipitation are believed to deteriorate materials property severely. Fig. 9.2 shows an example of needle like TCP phase (riches in Mo and Cr) precipitation and growth after aging at 820 °C for 2000 hours.

5. It is also interesting to know the fatigue property and deformation difference in the sample produce by different cooling rate, which is the further work on Chapter 7.

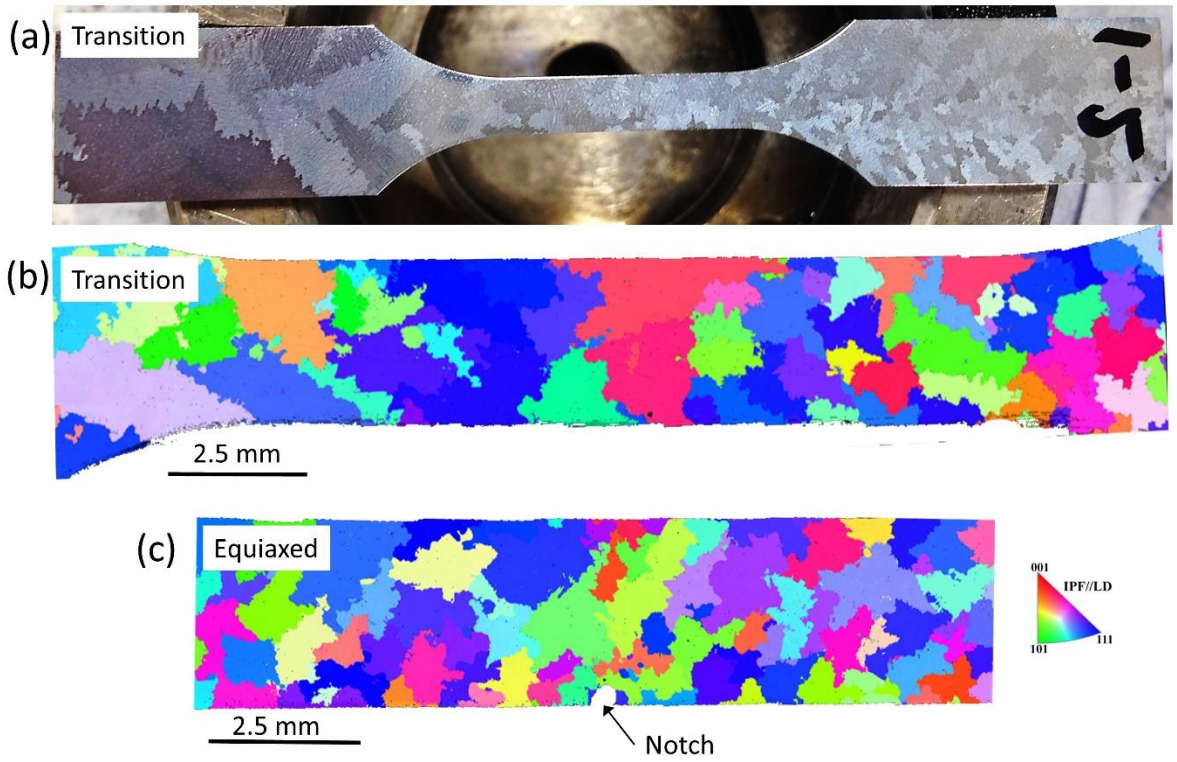

Fig. 9.1 Example of double flat sample for interrupted fatigue test. (a) A transition grain structure sample after polishing with grain structure and grain size visible on the surface. (b) An example of IPF//LD (X) showing transition grain structure. (c) IPF//LD showing a notched sample with equiaxed grain structure.

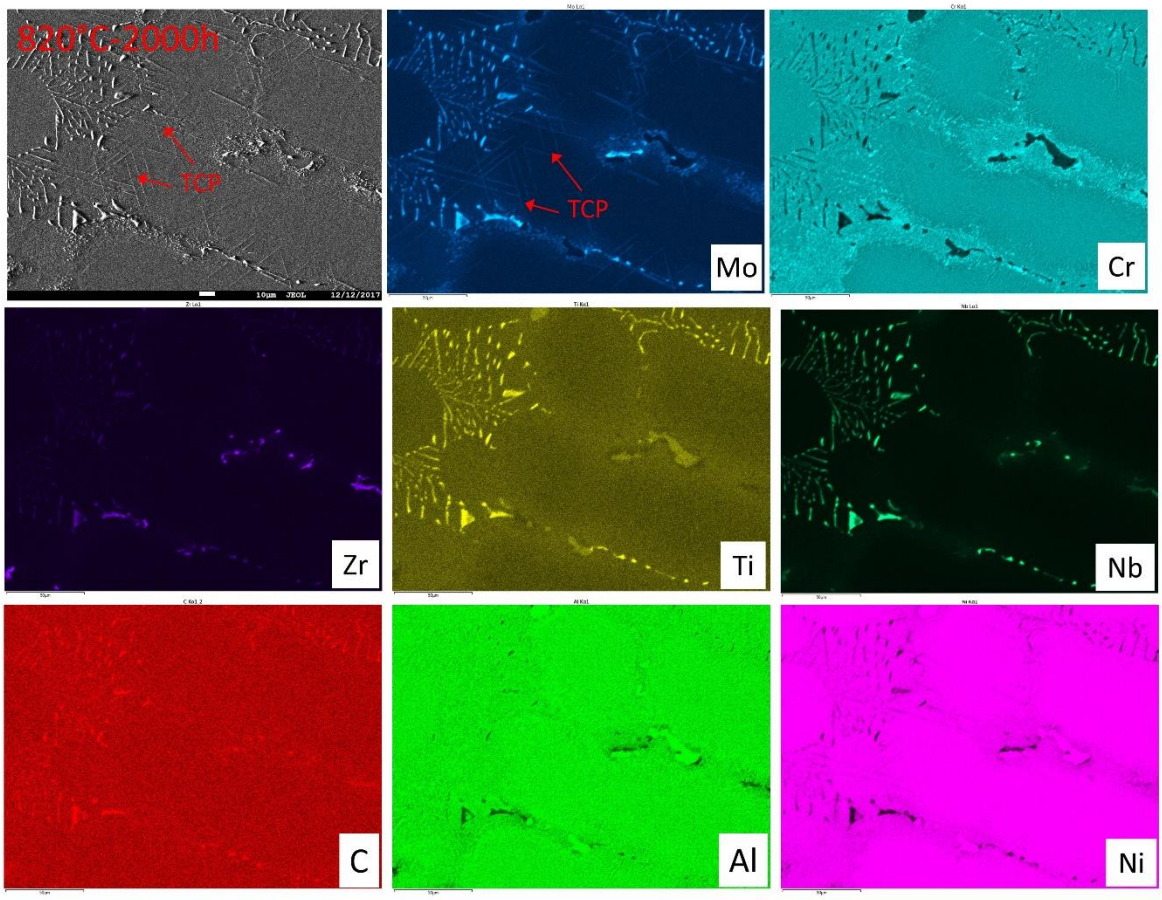

Fig. 9.2 An example of TCP phase precipitation and growth after aging at 820 °C for 2000 hours. The EDS element mapping confirm that this needle like TCP phase (indicated by red arrows) are rich in Mo and Cr.